SINGLE-PARTICLE TRACKING ASSAYS AND COMPUTATIONAL TOOLS FOR STUDYING VIRUS-MEMBRANE INTERACTIONS

A Dissertation

Presented to the Faculty of the Graduate School of

Cornell University

In Partial Fulfillment of the Requirements for the Degree of

Doctor of Philosophy

by

Donald Won Lee

May 2016

SINGLE-PARTICLE TRACKING ASSAYS AND COMPUTATIONAL TOOLS FOR STUDYING VIRUS-MEMBRANE INTERACTIONS

Donald Won Lee, Ph. D.

Cornell University 2016

This dissertation discusses recent developments in single-particle tracking (SPT) assays and computational tools for studying the interaction between viruses and lipid membranes. Lipid membranes of host cells are effective barriers against foreign entities, but viruses have evolved strategies to bind to and penetrate through these membranes. The infection process involves a series of virus-host interactions such as 1) activation of viral proteins via host cell proteases, 2) binding of virus proteins to specific host cell receptors, 3) conformational changes of viral fusion proteins near the cell membrane, and 4) fusion of the cell and viral membranes. Building assays that can study these interactions is useful for expanding our knowledge on viruses and confirming the activity of antiviral compounds. With the combined usage of high-resolution microscopy and supported lipid bilayers, individual viruses can now be tracked as they undergo sequential steps of the virus infection process. Yet, the utility of this assay is limited by experimental design, image processing, and data analysis challenges. We have thus developed 1) an assay that can trigger virus membrane fusion rapidly, 2) a stochastic simulation model that explains major kinetics steps of the fusion process, 3) an image restoration algorithm that reveals virus particles in noisy SPT videos, and 4) a kinetic model that describes the “adhesion-strengthening” mechanism that viruses use to stably bind to membranes. We have tested the utility of these tools as we dissected the kinetics steps involved with the influenza virus and parvovirus infection process.

BIOGRAPHICAL SKETCH

Donald Lee was born in Vallejo, CA in 1987 and was raised in Japan for 7 years and in Korea for 9 years. He did his studies inside U.S. military oversea bases and benefitted from a multicultural learning environment. After graduating Seoul American High School in 2005, he returned to the U.S. and did his undergraduate studies at U.C. Berkeley. He majored in chemical engineering and joined Professor Jhih-Wei Chu's simulation group to learn about all-atom simulation research. In 2009, he graduated with a B.S. degree in chemical engineering and searched for potential graduate schools to attend. The Swine Flu Pandemic of 2009 influenced Donald's decision to pursue virus research at Cornell, and he joined Susan Daniel's research group to study factors that govern the ability of influenza viruses to target and enter cells. He became a fellow for the National Science Foundation GK-12 program starting in 2011 and had the opportunity to teach high school students about viral infection and various science topics through activities that he created. In 2015, he began his work in Gary Whittaker's research group to develop bioinformatics software that facilitates DNA sequence analysis and diagnosis of feline infectious peritonitis virus in cats.

I dedicate this dissertation to family and friends who have supported me unconditionally. Thanks Mom, Dad, and Nuna for everything – the care packages, cards, advices, being there for me – couldn't have done it without you! Thank you Lin family for taking care of me while I was Berkeley, feeding delicious food in SF, the colorful pajamas for Christmas (I still have 3!), and showing how to live the life! To the teachers from SAHS – Mrs. and Mr. Beckham, Ms. Pell, Ms. Park – thank you for providing me the tools and guidance to make it all the way through graduate school – that was a crazy amount of studying! To my friends from Berkeley – thanks for helping me out through college, making study groups super fun, and arranging our yearly chaotic reunion dinners!

To Susan, thank you for the opportunity to do all the exciting research shown in this dissertation! To Gary, thank you for helping me get through my last year in graduate school and adopting me into your FCoV team! To Colin, thank you for the opportunity to work with parvovirus and getting a paper in the spotlight! To Paulette, Julie, Shivaun, and Nev, thank you for opportunity to be a part of GK12 – had lots of fun teaching science at high schools! To Fernando and Jhih-Wei, thank you for teaching me about computational research!

And finally to my colleagues at Cornell who made graduate school so much fun and are now my life-long friends – you guys are the BEST!

Hope to work with you all again!

ACKNOWLEDGMENTS

The research presented here was made possible through the generous support from:

National Science Foundation (NSF)
- Grant DGE-1045513 to D.W.L. via GK12 Grass Roots Fellowship
- Grant DGE-0841291 to D.W.L. via GK12 Cornell's Learning Initiative for Medicine and Bioengineering (CLIMB) Fellowship
- Grant CBET-1263701 to S.D.

National Institute of Health (NIH)
- R01 Grant AI48678 to G.R.W.
- R01 Grant GM8496821 to C.R.P.
- R01 Grant AI092571 to C.R.P.

National Institute of Allergy and Infectious Diseases (NIAID)
- Grant F32AI100545 to A.B.A. via NRSA post-doctoral fellowship

Semiconductor Research Corporation
- Contract #2012-VJ-2272 to V.T.

NIAID Centers of Excellence for Influenza Research and Surveillance (CEIRS)
- Virus research fund and reagents

New York Influenza Center of Excellence (NYICE)
- Grant 414529-G to S.D. and L.P.

Intel Corporation
- Provided computer equipment and support

Cornell Engineering Learning Initiative (ELI)
- Funds for K.B.B. via Genentech and Proctor & Gamble donations

Cornell NanoScale Facility (CNF)
- CNF is funded by NSF grant ECCS-0335765.

Nanobiotechnology Center at Cornell University
- Provided research fund to L.P., G.R.W., and S.D.

I thank the following people for their support and help with the various projects:

Committee members
Susan Daniel
Gary Whittaker
Fernando Escobedo

PI Collaborators
Paulette Clancy
Colin Parrish
David Eliezer

NSF GK12
Nevjinder Singhota
Shivaun Archer
Chris Schaeffer
Julie Nucci
Jon Shaut
Ellen Schneider
Paula Jones
Kathy Rogers
Jason Boock

Colleagues
Andrew Allison
Angela Hsia
Ashley Macner
Beth Licitra
Charles Wisler
Chun-ti Chang
Deirdre Costello
Eugene Choi
Hung-Lun Hsu
James Xia
Javier Olaya
Jean Millet
Jun Yan
Kaitlyn Bacon
Kevin Vasquez
Lakshmi Nathan
Ling Chao
Lisa Bolin
Marco Straus
Mark Richards
Nicole Andre
Rohit Singh
Sijun Yang
Victor Tse
Yueting Zhang

TABLE OF CONTENTS

LIST OF FIGURES

PREFACE

CHAPTER 1

CHAPTER 2

CHAPTER 3

CHAPTER 4

CHAPTER 5

CHAPTER 6

LIST OF TABLES

PREFACE

CHAPTER 1

CHAPTER 3

CHAPTER 4

CHAPTER 5

LIST OF ABBREVIATIONS

Reagents

CA	Citric Acid
MES	1 mM 2-*(N*-morpholino*)*ethanesulfonic acid
oNBA	o-nitrobenzaldehyde
R110C18	Octadecyl Rhodamine 110 Chloride
R18	Octadecyl Rhdoamine B
SRB	Sulforhodamine B

Virus

CPV	Canine Parvovirus
FCoV	Feline Coronavirus
FECV	Feline Enteric Coronavirus
FIPV	Feline Infectious Peritonitis Virus
IAV	Influenza A Virus
VSV	Vesicular Stomatitis Virus

Lipids

aG_{M1}	asialoganglioside
Chol	Cholesterol
DOPC	1,2-dioleoyl-*sn*-glycero-3-phosphocholine
G_{M1}	monosialotetrahexosylganglioside
G_{M3}	monosialodihexosylganglioside
G_{D1A}	disialoganglioside
POPC	1-palmitoyl-2-oleoyl-*sn*-glycero-3-phosphocholine
POPG	1-palmitoyl-2-oleoyl-*sn*-glycero-3-phospho-(1'-*rac*-glycerol

Miscellaneous Terms

Ab(s)	Antibody(ies)
AFM	Atmoic Force Microscopy
asyn	alpha-synuclein
FRAP	Fluorescence Recovery After Photobleaching
HPI	Hydropathy Index
NMR	Nuclear Magnetic Resonance
SLB	Supported Lipid Bilayers
SPR	Surface Plasmon Resonance
SPT	Single-particle Tracking
SSA	Stochastic Simulation Algorithm
SUV	Small Unilamellar Vesicles
TIRF	Total Internal Reflection Fluorescence
TFR	Transferrin Receptors
VDWV	Van der Waals Volume
STAWASP	Segmented Temporal Averaging While Avoiding Synced Pixels

LIST OF SYMBOLS

Virus membrane fusion

w	Number of HA trimers in fusible unit
q	Number of HA trimers in fusible unit that underwent conformation change
N	Number of HA trimers that actively change conformation for fusion

Virus binding

N	Number of binding events
N_+	Accumulated number of binding events since the movie started
N_-	Accumulated number of unbinding events since the movie started
t	Time elapsed in the movie
t_{res}	Binding residence time of virus to receptor
t_{cutoff}	Minimum binding residene time required for a binding event
t_{movie}	Total duration of a binding movie
R_{on}	Binding rate dN_+/dt
A_{cam}	Field of view of the camera

PREFACE

THESIS OVERVIEW

The interaction between proteins and lipid membranes is critical for a variety of biological processes, particularly virus infection. Lipid membranes act as the host cell's first barrier against foreign entities, but viruses have evolved strategies to penetrate the membrane and initiate infection. Using the influenza virus as a model, the viral entry process requires a series of successful virus-host interactions such as 1) activation of viral proteins via host cell proteases [1], 2) binding of virus proteins to specific host cell receptors [2-5], 3) conformational changes of viral fusion proteins near the cell membrane [6-9], and 4) fusion of the cell and viral membranes (see review by Skehel et al. [10]). A thorough understanding of all of these interactions is critical for developing antiviral targets and satiating our unending curiosity about viruses.

Much research has been targeted at understanding the cell-entry mechanisms of viruses. The emergence of single-particle tracking (SPT) microscopy has enabled detailed studies of multiple major steps of the virus infection pathway within a single assay. Yet, the utility of SPT is limited by experimental design, image processing, and data analysis challenges. This dissertation discusses advancements in both SPT assays and data analysis strategies in the context of studying virus-membrane interactions. In detail, we have investigated the kinetics of the enveloped influenza virus and the non-enveloped parvovirus binding to their putative receptors, which are respectively sialic acid and transferrin receptor. We have also studied the membrane fusion process of influenza virus using both simulations and experiments. The next steps would be to use these tools for testing and screening antiviral drug candidates.

THE VIRUS INFECTION CYCLE

The influenza A virus (IAV) is often used as a model for virus infection, and we discuss its cell-entry process in detail. The virus infection begins with the binding of the virions to host cell sialic acid receptors found on glycosylated membrane proteins or glycolipids. Attachment is mediated by viral surface proteins called hemagglutinin (HA), which is a homotrimer glycoprotein [11]. Prolonged attachment of the virus to receptors can trigger *de novo* endocytosis [12], internalizing the virus inside endosomes. The endosome contain proton channels that lower the pH, which is originally intended to activate proteases that degrade foreign entities, but can be exploited by viruses to activate viral proteins. If the HA proteins have not already been activated via external serine proteases [1, 13], then endosomal proteases could potentially cleave the HA for activation. An activated HA contains a HA_1 and HA_2 subunits, referred to as the receptor-binding domain and the membrane fusion domain, respectively. At low pH conditions, these activated HA proteins undergo a major conformational change that exposes hydrophobic residues, called fusion peptides, towards the endosomal membrane [6-9]. These fusion peptides insert into the host membrane hydrophobic layer and are critical for advancing the virus-host complex into a "hemifusion" intermediate where the outer leaflets of the host and viral membranes are connected [14-15]. After a further lag time, a full pore forms [14-16], enabling the viral inner genome and proteins to diffuse into the host cytoplasm.

When the viral genome reaches the cytoplasmic space and nucleus, new progeny viruses can be produced using the host cell machinery. The viral capsid assembles at the host membrane, packages necessary viral RNA segments and proteins, and eventually, forms a progeny virion that buds off the cell membrane [17-18]. The egress of the influenza virus is

facilitated with the presence of another virus membrane protein called neuraminidase (NA) [19], which cleaves sialic acid receptors and prevents viruses from rebinding to the infected host cells.

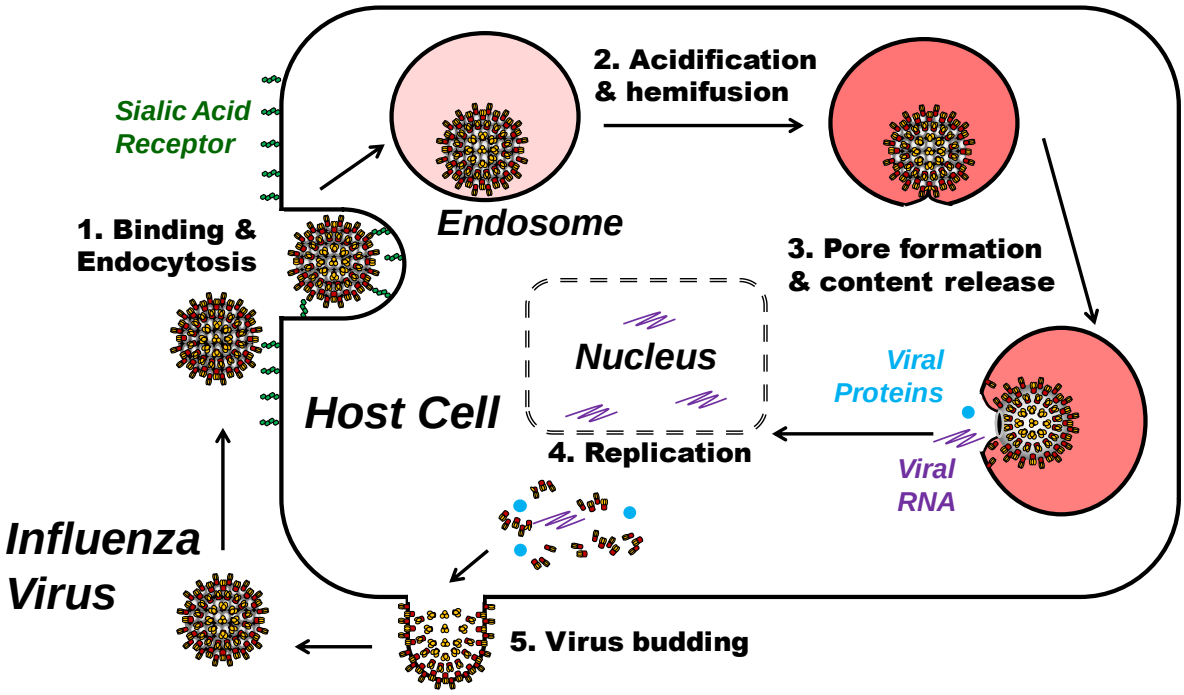

Figure 1 Infection cycle of influenza virus.

The infection cycle is generally similar for different viruses. Parvovirus, a nonenveloped virus that infects mainly carnivore species and domestic pets, binds to host cell membrane transferrin receptors using its surface protein VP2[20]. Contrary to influenza virus though, parvovirus may not always initiate endocytosis *de novo*, but rather it gets trapped in a coated pit while it is forming for other reasons [21]. After internalization via endocytosis, the viral genome is released inside the cytoplasm, though the exact mechanism is still unknown.

GRAND MOTIVATION OF VIRUS CELL-ENTRY STUDIES

The grand goal of most virus-host interaction studies is to develop antiviral drugs. The swine flu pandemic of 2009 demonstrated the limitations of current medicine technology to control viral outbreaks against one of the most-studied virus in literature. Antiviral drugs Osletamivinr [22] and Zanamir [23] that block NA function were sparsely administered in fears that overuse of these drugs will select drug-resistant strains. However, resistant strains emerged regardless[24-26], and studies have shown NA is not a critical for localized viral infection [27]. Considering limited success of NA-targeting antivirals, HA-targeted antiviral therapy opens up new opportunities to block the flu virus.

A theoretical, but noteworthy, advantage of anti-HA drugs is that by preventing viral entry, the virus cannot replicate and mutate inside the host to develop drug-resistant strains. Broadly neutralizing antibodies against HA have been promising, as these target highly-conserved HA stem regions associated with membrane fusion functions [28-29], and some target conserved regions of the HA binding domain [30-31]. Another promising solution is to block binding using sialic acid decoys. Decoy receptors may be able to confer protection from future variations of the flu virus because mutated viruses that cannot bind to the decoy would also not be able to bind to our cells. Recent studies have proved the feasibility of using decoy liposomes to inhibit infection in mouse models [32]. Building an assay that can quickly quantify and screen various anti-binding and anti-fusion compounds is expected to be of high value in the near future.

ASSAYS FOR STUDYING HOST-VIRUS INTERACTIONS

Numerous assays have been developed to dissect the different steps of the cell-entry mechanism exploited by viruses. We categorize the assays into two categories: binding and fusion assay. Binding assays measure attachment efficiency of viral proteins to host receptors where as fusion assays that measure the efficiency at which enveloped viruses fuses with the host membranes. These assays can be subdivided into two approaches: ensemble versus stochastic. The ensemble approach measures the collective binding or fusion behavior of many virions with host membranes, whereas the stochastic approach measures each virion's binding or fusion events. The high-throughput capabilities of ensemble approach assays may be appealing for some applications, whereas the high-level of detail provided by the slower stochastic approach assays is more useful for dissecting the cell-entry mechanisms of viruses. Table 1 and 2 lists common binding and fusion assays, respectively, along with their advantages and disadvantages.

Table 1 Comparison of different binding assays. E = ensemble assay. S = stochastic assay.

Technique - Description	Advantages	Disadvantages
SPT[33-35] (S)– track particles using fluorescence microscopy	Decouple binding from fusion. Visual confirmation. Kinetic data of direct binding.	Image processing is slow. Requires dyes.
SPR[36] (E)– track adsorbed mass based on laser reflection angle that changes with surface thickness	0.91 pg/mm^2 sensitivity [37]. Does not need dyes. Automation capable.	No visual confirmation. Cannot measure fusion. Indirect measure of binding.
QCM[38] (E)– track adsorbed mass based on frequency response of oscillating surface	10 pg/mm^2 sensitivity [39]. Does not need dyes. Measure material softness.	No visual confirmation Cannot measure fusion. Indirect measure of binding.
Glycan Array[40-41] (E)– detect binding of virus to receptors attached onto an array chip	Screens many candidate receptors. Fast assay.	No kinetic data.
Hemagglutination [3, 42] (E)– detect aggregation of cells when mixed with virus.	Mimics *in vivo* system better. Can see results with eyes.	Qualitative data. Hard to control cell membrane.
Cell Infection (E)– detect death of cells in presence of infectious particles	Finds infectious particle count. Closer to *in vivo* system.	Cannot decouple infection steps. Qualitative. Hard to control cell membrane. Indirect measure of binding.
NMR[43] (E)– electron spin shift of protein and receptors caused by binding.	Extracts binding equilibrium data	Requires solubilized proteins. Indirect measure of binding. No visual confirmation.
AFM[44-45] (S)– measure binding force of virus to receptors using AFM tip.	Extract binding force.	Hard to sample many viruses. No visual confirmation.

Table 2 Comparison of Fusion Assays. E = ensemble assay. S = stochastic assay.

Technique - Description	Advantages	Disadvantages
Fluoremetry[46] (E)– Detect fusion by fluorescence dequenching in a cuvette with virus + liposomes + fusion-trigger agent	Cuvette-based simple setup.	Cannot decouple binding & fusion. Blurred fusion event data. Requires concentrated samples. Need dyes.
SPT w/ acid flow[16] (S)– detect individual fusion event upon acid flow trigger	Measures fusion lag time. pH is easier to control. Visual confirmation. Can study binding too.	Data analysis is slow. Fusion trigger is slower (>1s). Shearing force from fluid flow. Need dyes.
SPT w/ uncaging acid[47] (S)– detect individual fusion event upon instant acidification via proton uncaging technique	Measures fusion lag time. Fusion trigger is fast (<50ms). No shearing effect. Can study binding too.	pH is harder to control. UV laser photobleaches dyes. Need dyes.
Electrical Conductance [48] (S)– measure changes in cell conductance when fusion occurs	No need for dyes. Measure pore-formation.	Needs electrode attachment to cell. Hard for testing many viruses. Not designed for binding studies.
CryoEM [49-50] (S)– takes frozen EM images of viruses in the middle of undergoing membrane fusion	Sees fusion intermediates.	No kinetic data.

The binding residence time (or contact time of virus to membranes) and fusion lag time (time from fusion-triggering event to actual fusion event) distributions are important to know for characterizing the cell-entry process of viruses. These data can only be obtained using the stochastic approach. The binding residence time of a virus to a receptor provides important information about the virus uptake probability via endocytosis. For instance, viruses that bound longer than the clathrin-mediated endocytosis time scale (~3 min [12]) will have a high chance of being internalized to attempt infection. The fusion lag time data correlates with sequential steps involved with membrane fusion, such as protein conformation change, membrane bending, and membrane merging. Given a lag time distribution, one could simulate the membrane process to dissect which sequential steps and which proteins are hindering the fusion rate. The lag time distributions are also useful for evaluating the efficacy of fusion-inhibitor molecules by tracking the shift in mean lag times. SPT assays are advantageous because they can decouple these infection steps and provide clarity about at what steps do the antiviral molecules inhibit infection.

THE SPT VIRUS BINDING AND FUSION ASSAY

Stochastic assays are becoming more accessible due to advancements in high-resolution fluorescence microscopy technology that can track single-fluorophore molecules. Here, we use total internal reflection fluorescence (TIRF) microscopy for SPT studies due to its ability to illuminate just the surface region where the glass and water meets (Figure 2). TIRF exploits evanescent waves that decay exponentially off the glass-water interface when a laser is shined at an incident angle exceeding the critical incident angle (>61° in our case). The next component of our assay requires a target membrane. We use a membrane mimic call supported lipid bilayers (SLBs), which can be formed spontaneously on the glass surface

(Figure 3) by rupturing lipid vesicles. SLBs are ideal for studying virus-membrane interactions under a 100-nm thick evanescent wave, and the bilayer composition can easily be changed during the lipid vesicle preparation step to study how host membrane properties affect the virus cell-entry process. These bilayer modifications would otherwise be difficult to control using cell-based assays.

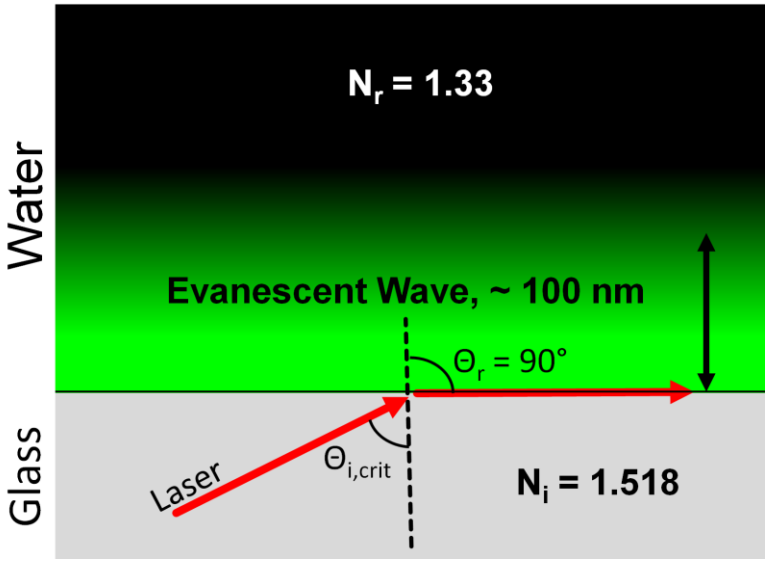

Figure 2 Mechanics of total internal reflection. Total internal reflection is achieved with $\theta_{i,crit}$ is at least 61°, as solved using Snell's Law, $N_i \sin\theta_i = N_r \sin\theta_r$.

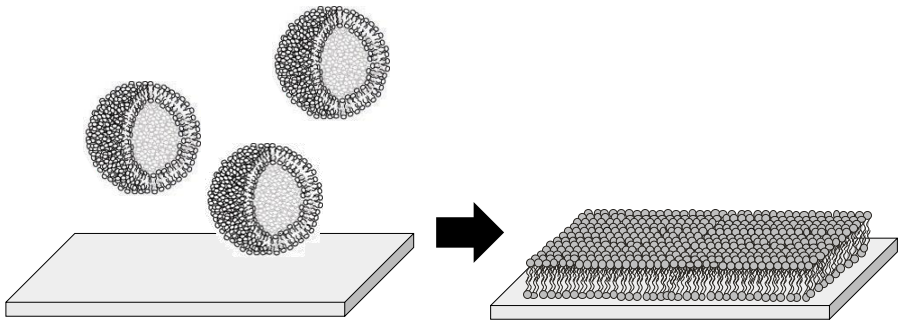

Figure 3 Supported lipid bilayer formation process. Lipid vesicles spontaneously rupture on hydrophilic glass to form bilayers. The bilayer contains roughly 1 nm of water gap from the glass, allowing the lipids to be laterally mobile. Images adapted from Johnson et al.'s work [51].

Combining TIRF and SLBs, we can build a SPT assay for studying virus-membrane interactions (Figure 4). Experiments are conducted inside microfluidic devices as they provide good control over the SLB formation process, virus loading steps, and fusion-

triggering events. Membrane fusion is triggered by lowering the pH, and we provide two methods to do this. One method is to use microfluidic channels to withdraw acidic solution over the viruses that are pre-bounded to a membrane [16, 52]. This excels in preserving the pH level, but there exists a time delay for pH to drop to occur due to the buffer exchange rate. Additionally, shear forces over the virus while flowing in the acid buffer may have unknown effects on the fusion process by straining the viral protein. Hence we developed a second method to lower the pH using photolytic compounds that release protons upon exposure to UV light [47]. For this method, the virus can be instantly acidified under stagnant conditions, but limitations include difficulty controlling the pH right after acidification.

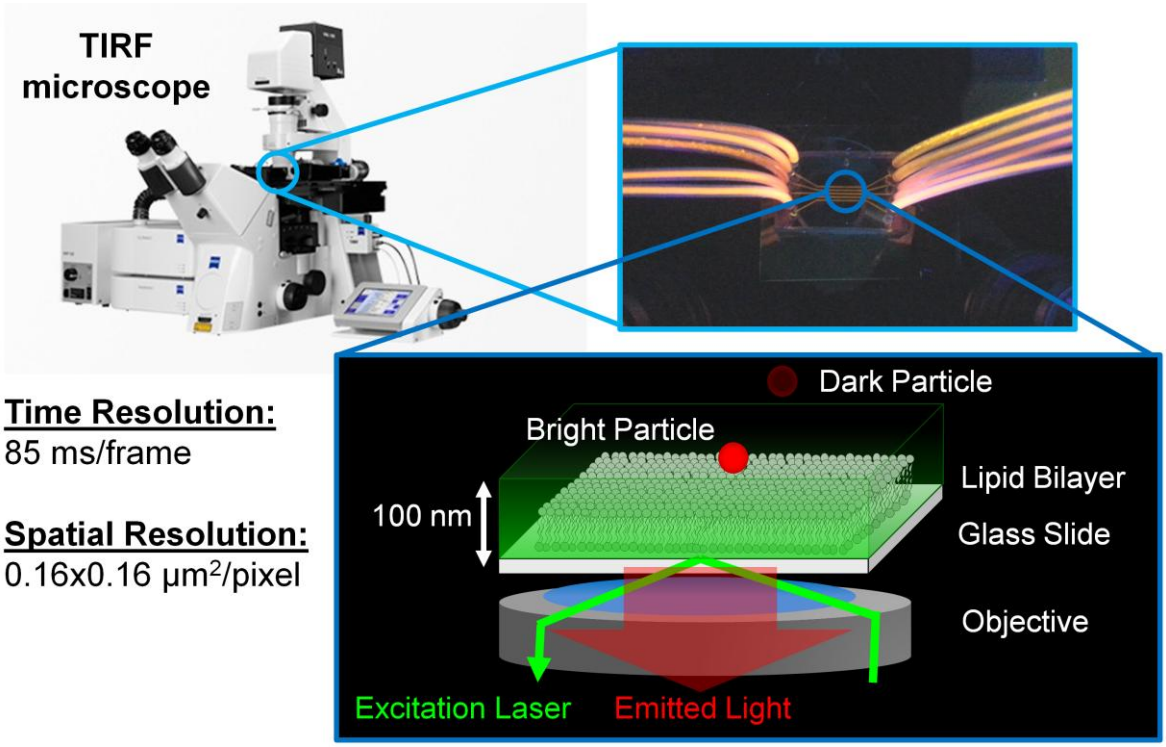

Figure 4 Microfluidic device setup for single-particle tracking experiments.

RESEARCH INTEREST: SPT IMAGE PROCESSING

Stochastic assays contain a variety of other limitations that prevent their usage in a more standardized setting. For instance, extracting data from images is not simple. Unlike

ensemble assays that output a single measurable signal (eg fluorescent intensity like from fluoremetry), stochastic assays generally outputs a noisy image of particles that must be analyzed using complex software. Complicating matters further is the low signal-to-noise ratio of most images from SPT microscopy that renders image analysis difficult. Dim fluorescent particles can be merely 4 pixels large and are almost indistinguishable from noise. Most image restoration strategies used for SPT studies have been intended for other image applications where features of the object are much larger than that of noise [53-56]. These tend to underperform for SPT studies, and hence, developing proper SPT image restoration algorithms [57] is required for extracting useful, quantitative data from noise microscopy videos.

RESEARCH INTEREST: MULTIVALENT BINDING

An under-studied aspect in binding literature is the analysis of contact time distributions for multivalent binding systems. Relevant studies of bivalent binding with antibodies hinted at unique binding behaviors that do not reflect thermodynamic binding models [58].Other studies [33, 35], including ours, obtained similar perplexing discrepancies between expected and actual dissociation curves when dealing with multivalent binding systems. The unbinding kinetics is particularly interesting for influenza viruses because they can bind fairly permanently to cell membranes despite having a weak HA-SA dissociation constant. The dissociation constant, K_d, is 3.2 mM for α2,3 SA in complex with HA from H3 serotype virus [43] – as a reference point, HIV's GP41 protein in complex with CD4 receptor has a dissociation constant of 5 nM [59]. This could provide a rational explanation for the need for influenza viruses to maintain a high surface density of viral protein (~400 per virion [60]) than HIV (~10-100 per virion [61]), in order to achieve sufficient binding residence times for

infection via multivalent bonds. We are interested in how the interplay between fast unbinding kinetics of weak monovalent HA-SA bonds versus slow formation time of stronger multivalent bonds could give rise to unusual overall unbinding kinetics.

RESEARCH INTEREST: HOST ADAPTATION OF VIRUSES

Influenza virus binds to specific sialic acid receptor structure found on host cells. Frequently, literature distinguishes between the α2,6 and α2,3 sialic acid as the human and avian receptor respectively. The α2,6 SA is found commonly in human adult lungs [62-64] whereas the latter is found in avian intestines [3-4], providing a rational theory that H5N1 avian flu outbreaks is a result of HA mutations that switch receptor preference from α2,3 to α2,6 SA[64]. However, several evidences suggest that this linkage is not the sole factor governing host target, and topology (or peripheral structure of the SA) could play a large role [65]. We are interested in quantify by how much the binding kinetics can change upon slight variation in receptor structure or slight variations in viral binding protein residues. These data would be important for explaining the ability of viruses to switch host targets.

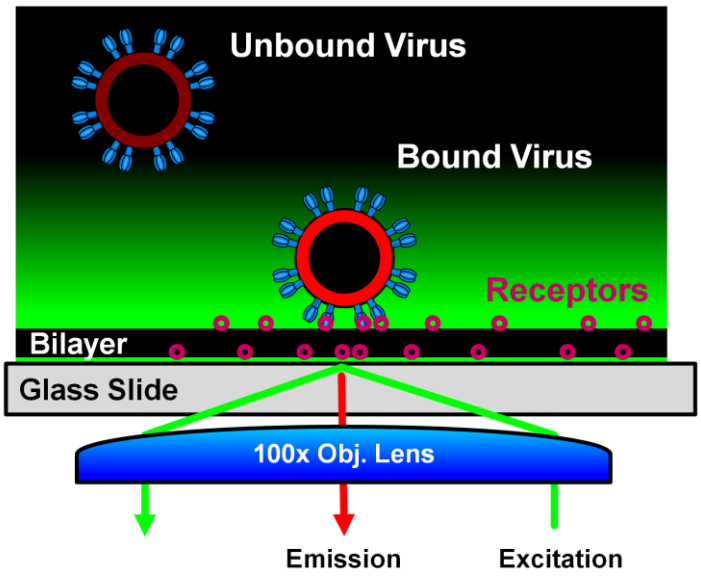

Figure 5 Single-virion binding experiment setup.

RESEARCH INTEREST: FUSION MECHANISM

For enveloped viruses, the following step after receptor binding is membrane fusion. An on-going debate starting since the 1980's is how many HA proteins are actually needed to induce membrane fusion. By knowing cooperativity levels of viral proteins, one could estimate the ratio of antibody to virus titer required to inhibit viral infection. For instance, a highly cooperative system would essentially be inhibited with few Abs, whereas a non-cooperative system would require an excessive amount of Ab to stop viral infection. Considering influenza virus is used as a model virus for other viruses, the uncertainty in HA cooperativity for membrane fusion propagates uncertainties about other viruses such as HIV and VSV. Past studies have obtained conflicting evidences that HA act [16, 66-71] and do not act cooperatively [72-75], leading to a series of inconsistent hypothesis pertaining to virus membrane fusion mechanism. These in turn led to several inconsistent simulation models [70-71, 76] and data interpretation issues. Resolving these issues is an important goal towards better understanding the fusion mechanism of influenza and other similar viruses.

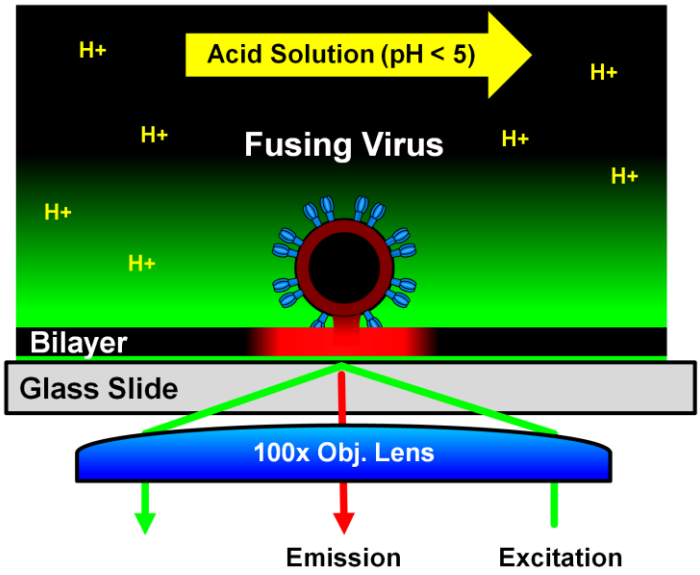

Figure 6 Single-virion fusion experiment setup.

REFERENCES

1. Böttcher, E., T. Matrosovich, M. Beyerle, H.-D. Klenk, W. Garten, and M. Matrosovich, *Proteolytic Activation of Influenza Viruses by Serine Proteases TMPRSS2 and HAT from Human Airway Epithelium.* JOURNAL OF VIROLOGY, 2006. **80**(19): p. 9896-9898.
2. Rogers, G.N., J.C. Paulson, R.S. Daniels, J.J. Skehel, I.A. Wilson, and D.C. Wiley, *Single amino acid substitutions in influenza haemagglutinin change receptor binding specificity.* Nature, 1983. **304**(5921): p. 76-78.
3. Rogers, G.N., T.J. Pritchett, J.L. Lane, and J.C. Paulson, *Differential sensitivity of human, avian, and equine influenza a viruses to a glycoprotein inhibitor of infection: Selection of receptor specific variants.* Virology, 1983. **131**(2): p. 394-408.
4. Rogers, G.N., R.S. Daniels, J.J. Skehel, D.C. Wiley, X.F. Wang, H.H. Higa, and J.C. Paulson, *Host-mediated selection of influenza virus receptor variants. Sialic acid-alpha 2,6Gal-specific clones of A/duck/Ukraine/1/63 revert to sialic acid-alpha 2,3Gal-specific wild type in ovo.* Journal of Biological Chemistry, 1985. **260**(12): p. 7362-7.
5. Rogers, G.N. and B.L. D'Souza, *Receptor binding properties of human and animal H1 influenza virus isolates.* Virology, 1989. **173**(1): p. 317-322.
6. Skehel, J.J., P.M. Bayley, E.B. Brown, S.R. Martin, M.D. Waterfield, J.M. White, I.A. Wilson, and D.C. Wiley, *Changes in the conformation of influenza virus hemagglutinin at the pH optimum of virus-mediated membrane fusion.* Proceedings of the National Academy of Sciences, 1982. **79**(4): p. 968-972.
7. Doms, R.W., A. Helenius, and J. White, *Membrane fusion activity of the influenza virus hemagglutinin. The low pH-induced conformational change.* Journal of Biological Chemistry, 1985. **260**(5): p. 2973-2981.
8. Gething, M.J., R.W. Doms, D. York, and J. White, *Studies on the mechanism of membrane fusion: site-specific mutagenesis of the hemagglutinin of influenza virus.* The Journal of Cell Biology, 1986. **102**(1): p. 11-23.
9. Ruigrok, R.W., N.G. Wrigley, L.J. Calder, S. Cusack, S.A. Wharton, E.B. Brown, and J.J. Skehel, *Electron microscopy of the low pH structure of influenza virus haemagglutinin.* EMBO Journal, 1986. **5**(1): p. 41-49.
10. Skehel, J.J. and D.C. Wiley, *Receptor binding and membrane fusion in virus entry: the influenza hemagglutinin.* Annual Review of Biochemistry, 2000. **69**(1): p. 531-569.
11. Wilson, I.A., J.J. Skehel, and D.C. Wiley, *Structure of the haemagglutinin membrane glycoprotein of influenza virus at 3 [angst] resolution.* Nature, 1981. **289**(5796): p. 366-373.
12. Rust, M.J., M. Lakadamyali, F. Zhang, and X. Zhuang, *Assembly of endocytic machinery around individual influenza viruses during viral entry.* Nature Structural +ACY- Molecular Biology, 2004. **11**(6): p. 567-573.
13. Garten, W., F.X. Bosch, D. Linder, R. Rott, and H.-D. Klenk, *Proteolytic activation of the influenza virus hemagglutinin: The structure of the cleavage site and the enzymes involved in cleavage.* VIROLOGY, 1981. **115**(2): p. 361-374.
14. Chernomordik, L., A. Chanturiya, J. Green, and J. Zimmerberg, *The hemifusion intermediate and its conversion to complete fusion: regulation by membrane composition.* Biophysical Journal, 1995. **69**(3): p. 922-929.
15. Chernomordik, L.V., V.A. Frolov, E. Leikina, P. Bronk, and J. Zimmerberg, *The pathway of membrane fusion catalyzed by influenza hemagglutinin: Restriction of lipids, hemifusion, and lipidic fusion pore formation.* The Journal of Cell Biology, 1998. **140**(6): p. 1369-1382.

16. Floyd, D.L., J.R. Ragains, J.J. Skehel, S.C. Harrison, and A.M. van Oijen, *Single-particle kinetics of influenza virus membrane fusion.* Proceedings of the National Academy of Sciences, 2008. **105**(40): p. 15382-15387.
17. Rossman, J.S. and R.A. Lamb, *Influenza virus assembly and budding.* VIROLOGY, 2011. **411**(2): p. 229-236.
18. Nayak, D.P., E.K.-W. Hui, and S. Barman, *Assembly and budding of influenza virus.* VIRUS RESEARCH, 2004. **106**(2): p. 147-165.
19. Chen, B.J., G.P. Leser, E. Morita, and R.A. Lamb, *Influenza virus hemagglutinin and neuraminidase, but not the matrix protein, are required for assembly and budding of plasmid-derived virus-like particles.* JOURNAL OF VIROLOGY, 2007. **81**(13): p. 7111-7123.
20. Chang, S., J. Sgro, and C. Parrish, *Multiple amino acids in the capsid structure of canine parvovirus coordinately determine the canine host range and specific antigenic and hemagglutination properties.* Journal of Virology, 1992. **66**(12): p. 6858-6867.
21. Cureton, D.K., C.E. Harbison, E. Cocucci, C.R. Parrish, and T. Kirchhausen, *Limited transferrin receptor clustering allows rapid diffusion of canine parvovirus into clathrin endocytic structures.* Journal of Virology, 2012. **86**(9): p. 5330-5340.
22. Nicholson, K., F. Aoki, A. Osterhaus, S. Trottier, O. Carewicz, C. Mercier, A. Rode, N. Kinnersley, and P. Ward, *Efficacy and safety of oseltamivir in treatment of acute influenza: a randomised controlled trial.* The Lancet, 2000. **355**(9218): p. 1845-1850.
23. Hayden, F.G., A.D. Osterhaus, J.J. Treanor, D.M. Fleming, F.Y. Aoki, K.G. Nicholson, A.M. Bohnen, H.M. Hirst, O. Keene, and K. Wightman, *Efficacy and safety of the neuraminidase inhibitor zanamivir in the treatment of influenzavirus infections.* NEW ENGLAND JOURNAL OF MEDICINE, 1997. **337**(13): p. 874-880.
24. Besselaar, T.G., D. Naidoo, A. Buys, V. Gregory, J. McAnerney, J.M. Manamela, L. Blumberg, and B.D. Schoub, *Widespread oseltamivir resistance in influenza A viruses (H1N1), South Africa.* EMERGING INFECTIOUS DISEASES, 2008. **14**(11): p. 1809.
25. Lackenby, A., O. Hungnes, S. Dudman, A. Meijer, W. Paget, A. Hay, and M. Zambon, *Emergence of resistance to oseltamivir among influenza A (H1N1) viruses in Europe.* Euro surveillance: bulletin europeen sur les maladies transmissibles= European communicable disease bulletin, 2008. **13**(5).
26. Le, Q.M., M. Kiso, K. Someya, Y.T. Sakai, T.H. Nguyen, K.H. Nguyen, N.D. Pham, H.H. Ngyen, S. Yamada, and Y. Muramoto, *Avian flu: isolation of drug-resistant H5N1 virus.* NATURE, 2005. **437**(7062): p. 1108-1108.
27. Liu, C., M.C. Eichelberger, R.W. Compans, and G.M. Air, *Influenza type A virus neuraminidase does not play a role in viral entry, replication, assembly, or budding.* JOURNAL OF VIROLOGY, 1995. **69**(2): p. 1099-1106.
28. Ekiert, D.C., G. Bhabha, M.-A. Elsliger, R.H. Friesen, M. Jongeneelen, M. Throsby, J. Goudsmit, and I.A. Wilson, *Antibody recognition of a highly conserved influenza virus epitope.* SCIENCE, 2009. **324**(5924): p. 246-251.
29. Wei, C.-J., J.C. Boyington, P.M. McTamney, W.-P. Kong, M.B. Pearce, L. Xu, H. Andersen, S. Rao, T.M. Tumpey, and Z.-Y. Yang, *Induction of broadly neutralizing H1N1 influenza antibodies by vaccination.* SCIENCE, 2010. **329**(5995): p. 1060-1064.
30. Krause, J.C., T. Tsibane, T.M. Tumpey, C.J. Huffman, C.F. Basler, and J.E. Crowe, *A broadly neutralizing human monoclonal antibody that recognizes a conserved, novel epitope on the globular head of the influenza H1N1 virus hemagglutinin.* JOURNAL OF VIROLOGY, 2011. **85**(20): p. 10905-10908.

31. Whittle, J.R., R. Zhang, S. Khurana, L.R. King, J. Manischewitz, H. Golding, P.R. Dormitzer, B.F. Haynes, E.B. Walter, and M.A. Moody, *Broadly neutralizing human antibody that recognizes the receptor-binding pocket of influenza virus hemagglutinin.* Proceedings of the National Academy of Sciences, 2011. **108**(34): p. 14216-14221.
32. Hendricks, G.L., K.L. Weirich, K. Viswanathan, J. Li, Z.H. Shriver, J. Ashour, H.L. Ploegh, E.A. Kurt-Jones, D.K. Fygenson, R.W. Finberg, J.C. Comolli, and J.P. Wang, *Sialylneolacto-N-tetraose c (LSTc)-bearing Liposomal Decoys Capture Influenza A Virus.* Journal of Biological Chemistry, 2013. **288**(12): p. 8061-8073.
33. Bally, M., K. Dimitrievski, G. Larson, V.P. Zhdanov, and F. Höök, *Interaction of virions with membrane glycolipids.* PHYSICAL BIOLOGY, 2012. **9**(2): p. 026011.
34. Bally, M., M. Graule, F. Parra, G. Larson, and F. Höök, *A virus biosensor with single virus-particle sensitivity based on fluorescent vesicle labels and equilibrium fluctuation analysis.* Biointerphases, 2013. **8**(1): p. 4.
35. Bally, M., A. Gunnarsson, L. Svensson, G. Larson, V.P. Zhdanov, and F. Höök, *Interaction of single viruslike particles with vesicles containing glycosphingolipids.* Physical Review Letters, 2011. **107**(18): p. 188103.
36. Hidari, K., S. Shimada, Y. Suzuki, and T. Suzuki, *Binding kinetics of influenza viruses to sialic acid-containing carbohydrates.* Glycoconjugate Journal, 2007. **24**(9): p. 583-590.
37. Homola, J., *Surface plasmon resonance sensors for detection of chemical and biological species.* Chemical Reviews, 2008. **108**(2): p. 462-493.
38. Takahashi, T., S. Kawagishi, M. Masuda, and T. Suzuki, *Binding kinetics of sulfatide with influenza A virus hemagglutinin.* Glycoconjugate Journal, 2013. **30**(7): p. 709-716.
39. O'Sullivan, C.K. and G.G. Guilbault, *Commercial quartz crystal microbalances – theory and applications.* Biosensors and Bioelectronics, 1999. **14**(8–9): p. 663-670.
40. Stevens, J., O. Blixt, L. Glaser, J.K. Taubenberger, P. Palese, J.C. Paulson, and I.A. Wilson, *Glycan microarray analysis of the hemagglutinins from modern and pandemic influenza viruses reveals different receptor specificities.* JOURNAL OF MOLECULAR BIOLOGY, 2006. **355**(5): p. 1143-1155.
41. Stevens, J., O. Blixt, J.C. Paulson, and I.A. Wilson, *Glycan microarray technologies: tools to survey host specificity of influenza viruses.* NATURE REVIEWS MICROBIOLOGY, 2006. **4**(11): p. 857-864.
42. Suzuki, Y., Y. Nagao, H. Kato, M. Matsumoto, K. Nerome, K. Nakajima, and E. Nobusawa, *Human influenza A virus hemagglutinin distinguishes sialyloligosaccharides in membrane-associated gangliosides as its receptor which mediates the adsorption and fusion processes of virus infection. Specificity for oligosaccharides and sialic acids and the sequence to which sialic acid is attached.* Journal of Biological Chemistry, 1986. **261**(36): p. 17057-17061.
43. Sauter, N.K., M.D. Bednarski, B.A. Wurzburg, J.E. Hanson, G.M. Whitesides, J.J. Skehel, and D.C. Wiley, *Hemagglutinins from two influenza virus variants bind to sialic acid derivatives with millimolar dissociation constants: a 500-MHz proton nuclear magnetic resonance study.* Biochemistry, 1989. **28**(21): p. 8388-8396.
44. Lee, C.-K., Y.-M. Wang, L.-S. Huang, and S. Lin, *Atomic force microscopy: Determination of unbinding force, off rate and energy barrier for protein–ligand interaction.* MICRON, 2007. **38**(5): p. 446-461.
45. Sieben, C., C. Kappel, R. Zhu, A. Wozniak, C. Rankl, P. Hinterdorfer, H. Grubmüller, and A. Herrmann, *Influenza virus binds its host cell using multiple dynamic interactions.* Proceedings of the National Academy of Sciences, 2012.

46. Clague, M.J., C. Schoch, and R. Blumenthal, *Delay time for influenza virus hemagglutinin-induced membrane fusion depends on hemagglutinin surface density.* Journal of Virology, 1991. **65**(5): p. 2402-2407.
47. Costello, D.A., D.W. Lee, J. Drewes, K.A. Vasquez, K. Kisler, U. Wiesner, L. Pollack, G.R. Whittaker, and S. Daniel, *Influenza virus-membrane fusion triggered by proton uncaging for single particle studies of fusion kinetics.* Analytical Chemistry, 2012. **84**(20): p. 8480-8489.
48. Melikyan, G.B., W.D. Niles, M.E. Peeples, and F.S. Cohen, *Influenza hemagglutinin-mediated fusion pores connecting cells to planar membranes: flickering to final expansion.* The Journal of General Physiology, 1993. **102**(6): p. 1131-1149.
49. Lee, K.K., *Architecture of a nascent viral fusion pore.* EMBO J, 2010. **29**(7): p. 1299-1311.
50. Kanaseki, T., K. Kawasaki, M. Murata, Y. Ikeuchi, and S. Ohnishi, *Structural features of membrane fusion between influenza virus and liposome as revealed by quick-freezing electron microscopy.* The Journal of Cell Biology, 1997. **137**(5): p. 1041-1056.
51. Johnson, J.M., T. Ha, S. Chu, and S.G. Boxer, *Early steps of supported bilayer formation probed by single vesicle fluorescence assays.* BIOPHYSICAL JOURNAL, 2002. **83**(6): p. 3371-3379.
52. Wessels, L., M.W. Elting, D. Scimeca, and K. Weninger, *Rapid Membrane Fusion of Individual Virus Particles with Supported Lipid Bilayers.* Biophysical Journal, 2007. **93**(2): p. 526-538.
53. Balasubramanian, S., S. Kalishwaran, R. Muthuraj, D. Ebenezer, and V. Jayaraj. *An efficient non-linear cascade filtering algorithm for removal of high density salt and pepper noise in image and video sequence*. in *International Conference on Control, Automation, Communication and Energy Conservation, INCACEC 2009.* 2009.
54. Xu, Y., J.B. Weaver, D.M. Healy, Jr., and J. Lu, *Wavelet transform domain filters: a spatially selective noise filtration technique.* IEEE Transactions on Image Processing, 1994. **3**(6): p. 747-758.
55. Esakkirajan, S., T. Veerakumar, A.N. Subramanyam, and C.H. PremChand, *Removal of High Density Salt and Pepper Noise Through Modified Decision Based Unsymmetric Trimmed Median Filter.* IEEE Signal Processing Letters, 2011. **18**(5): p. 287-290.
56. Rudin, L.I., S. Osher, and E. Fatemi, *Nonlinear total variation based noise removal algorithms.* Physica D: Nonlinear Phenomena, 1992. **60**(1–4): p. 259-268.
57. Sage, D., F.R. Neumann, F. Hediger, S.M. Gasser, and M. Unser, *Automatic tracking of individual fluorescence particles: application to the study of chromosome dynamics.* IEEE Transactions on Image Processing, 2005. **14**(9): p. 1372-1383.
58. Nieba, L., A. Krebber, and A. Plückthun, *Competition BIAcore for Measuring True Affinities: Large Differences from Values Determined from Binding Kinetics.* Analytical Biochemistry, 1996. **234**(2): p. 155-165.
59. Myszka, D.G., R.W. Sweet, P. Hensley, M. Brigham-Burke, P.D. Kwong, W.A. Hendrickson, R. Wyatt, J. Sodroski, and M.L. Doyle, *Energetics of the HIV gp120-CD4 binding reaction.* Proceedings of the National Academy of Sciences, 2000. **97**(16): p. 9026-9031.
60. Ruigrok, R.W.H., P.J. Andree, R.A.M. Hooft Van Huysduynen, and J.E. Mellema, *Characterization of three highly purified influenza virus strains by electron microscopy.* Journal of General Virology, 1984. **65**(4): p. 799-802.
61. Chertova, E., J.W. Bess Jr, B.J. Crise, R.C. Sowder II, T.M. Schaden, J.M. Hilburn, J.A. Hoxie, R.E. Benveniste, J.D. Lifson, and L.E. Henderson, *Envelope glycoprotein incorporation, not shedding of surface envelope glycoprotein (gp120/SU), is the primary determinant of SU content of purified human immunodeficiency virus type 1 and simian immunodeficiency virus.* JOURNAL OF VIROLOGY, 2002. **76**(11): p. 5315-5325.

62. Varki, N.M. and A. Varki, *Diversity in cell surface sialic acid presentations: implications for biology and disease.* Lab Invest, 2007. **87**(9): p. 851-857.
63. Barkhordari, A., R.W. Stoddart, S.F. McClure, and J. McClure, *Lectin histochemistry of normal human lung.* JOURNAL OF MOLECULAR HISTOLOGY, 2004. **35**(2): p. 147-156.
64. Shinya, K., M. Ebina, S. Yamada, M. Ono, N. Kasai, and Y. Kawaoka, *Avian flu: Influenza virus receptors in the human airway.* Nature, 2006. **440**(7083): p. 435-436.
65. Chandrasekaran, A., A. Srinivasan, R. Raman, K. Viswanathan, S. Raguram, T.M. Tumpey, V. Sasisekharan, and R. Sasisekharan, *Glycan topology determines human adaptation of avian H5N1 virus hemagglutinin.* Nat Biotech, 2008. **26**(1): p. 107-113.
66. Ellens, H., J. Bentz, D. Mason, F. Zhang, and J.M. White, *Fusion of influenza hemagglutinin-expressing fibroblasts with glycophorin-bearing liposomes: role of hemagglutinin surface density.* Biochemistry, 1990. **29**(41): p. 9697-9707.
67. Stegmann, T., J.M. White, and A. Helenius, *Intermediates in influenza induced membrane fusion.* EMBO J, 1990. **9**(13): p. 4231-4241.
68. Blumenthal, R., D.P. Sarkar, S. Durell, D.E. Howard, and S.J. Morris, *Dilation of the influenza hemagglutinin fusion pore revealed by the kinetics of individual cell-cell fusion events.* The Journal of Cell Biology, 1996. **135**(1): p. 63-71.
69. Danieli, T., S.L. Pelletier, Y.I. Henis, and J.M. White, *Membrane fusion mediated by the influenza virus hemagglutinin requires the concerted action of at least three hemagglutinin trimers.* The Journal of Cell Biology, 1996. **133**(3): p. 559-569.
70. Bentz, J., *Minimal aggregate size and minimal fusion unit for the first fusion pore of influenza hemagglutinin-mediated membrane fusion.* Biophysical Journal, 2000. **78**(1): p. 227-245.
71. Dobay, M.P., A. Dobay, J. Bantang, and E. Mendoza, *How many trimers? Modeling influenza virus fusion yields a minimum aggregate size of six trimers, three of which are fusogenic.* Molecular BioSystems, 2011. **7**(10): p. 2741-2749.
72. Bundo-Morita, K., S. Gibson, and J. Lenard, *Estimation by radiation inactivation of the size of functional units governing Sendai and influenza virus fusion.* Biochemistry, 1987. **26**(19): p. 6223-6227.
73. Gibson, S., C.Y. Jung, M. Takahashi, and J. Lenard, *Radiation inactivation analysis of influenza virus reveals different target sizes for fusion, leakage, and neuraminidase activities.* Biochemistry, 1986. **25**(20): p. 6264-6268.
74. Günther-Ausborn, S., P. Schoen, I. Bartoldus, J. Wilschut, and T. Stegmann, *Role of hemagglutinin surface density in the initial stages of influenza virus fusion: Lack of evidence for cooperativity.* Journal of Virology, 2000. **74**(6): p. 2714-2720.
75. Imai, M., T. Mizuno, and K. Kawasaki, *Membrane fusion by single influenza hemagglutinin trimers.* Journal of Biological Chemistry, 2006. **281**(18): p. 12729-12735.
76. Schreiber, S., K. Ludwig, A. Herrmann, and H.G. Holzhütter, *Stochastic Simulation of Hemagglutinin-Mediated Fusion Pore Formation.* Biophysical Journal, 2001. **81**(3): p. 1360-1372.

CHAPTER 1: Image restoration and analysis for single particle tracking of stochastic virus binding to membrane receptors

Donald W Lee, Hung-Lun Hsu, Kaitlyn B Bacon, and Susan Daniel*
Chemical and Biomolecular Engineering, Cornell University, Ithaca, NY, USA, 14853

ABSTRACT

With the development of single-particle tracking (SPT) microscopy and host membrane mimics called supported lipid bilayers (SLBs), virus-membrane interactions can be studied individually while maintaining control over host receptor type and concentration. However, several major experimental design challenges and quantitative image analysis limitations prevent the widespread use of this approach. One major challenge of SPT studies is the low signal-to-noise ratio of SPT videos, which is inevitable due to small particle sizes, low quantum yield of fluorescent dyes, and photobleaching. These situations render current particle tracking software unable to yield reliable binding kinetic data. Hence, we developed an effective image restoration algorithm for SPT applications called STAWASP that enhances the particle signals while preserving particle features. The algorithm was a critical prerequisite for conducting a variety of single-particle and single-molecule tracking studies involving SLBs. We discuss the experimental design, image restoration performance, and data analysis strategies for SPT studies, in the context of studying the influenza X31virus binding to various α2,3 sialic acid glycolipid analogs. We obtained kinetic data that reflects an adhesion-strengthening mechanism via multivalent bonds that the virus uses to increases its binding energy with the target with prolong contact times. We provide strategies to

interpret such data via empirical models from both SPT and ensemble binding assays such as Surface Plasmon Resonance.

INTRODUCTION

Single-particle tracking (SPT) is a versatile technique for studying protein-protein binding interactions occurring at surfaces, particularly the binding of viruses to host cell membrane receptors [1-5]. Viral adhesion to host membranes is critical for viral infection, and dissecting this process is relevant for predicting virus emergence, determining susceptible hosts, or developing binding-inhibitory antiviral compounds. SPT often deploys the use of imaging techniques such as total internal reflection fluorescence (TIRF) microscopy, which can track fluorescent virions within a 100-nm distance away from a surface. The viral receptor can be loaded onto a flat substrate by tethering to receptors to polymers attached covalently to the substrate [6], adsorbing lipid vesicles containing the receptor lipid/membrane protein [7], or forming supported lipid bilayers (SLBs) containing membrane receptors [4-5, 8-10]. The SLB option is advantageous because 1) the receptor type and surface density can be carefully controlled through bilayer preparation steps, 2) receptors are properly orientated in the membrane [11], 3) viral membrane fusion kinetics can be studied using the same assay [8, 12-15], and 4) mobile lipids allow the virus to recruit receptors and form multivalent bonds. However, the SPT-SLB assay contains many technical challenges with experimental design, image processing, and binding kinetic data analysis that limit its adaptation as a standard analytical tool. To increase the utility of SPT-SLB assays, we explain the cause of and demonstrate solutions to these issues as we study of influenza virus binding to several types of α2,3 sialic acid (SA) glycolipids.

One of the biggest barriers to using SPT for viral research is extracting particle information from images. Manually tracking particles is impractical, hence automated tracking software is needed and its proper performance is critical. Fluorescently-labeled virions appear as white spots on a dark background, but often, dim particles exist that are only few pixels large and resemble bright shot noise. Dim particles are particularly detrimental to SPT binding studies because these are intermittently detected by the software and contribute many short, erroneous particle trajectories that skew the binding data. Increasing the particle fluorescence signal by using a more powerful excitation laser is not an effective solution to the problem because photobleaching destroys the signal before adequate data can be collected. Thus this issue is better resolved using image processing techniques.

The SPT image analysis software usually performs the following three steps: image restoration, particle detection, and particle trajectory linking. While much effort has been invested in improving particle detection [16-22] and particle linking algorithms [18, 22-28], less effort has been focused on developing image restoration algorithms for SPT application [29]. Particle tracking software generally underperforms when the signal-to-noise ratio (SNR) is below 4 [18]. Most SPT studies use image restoration techniques originally designed for standard photographs and videos [30-33], which do not adequately restore dim particles with features barely larger than that of shot noise pixels. To resolve the intermittent particle tracking errors, we developed and provide a SPT image restoration algorithm called STAWASP (Segmented Temporal Averaging While Avoiding Synced Pixels). This algorithm effectively uses both spatial and temporal information from the video pixels to stabilize particle intensities, preserve particle features, and remove substantial noise from videos.

Other challenges of SPT-SLB assays is customizing experiments for studying multivalent binding of viruses to receptor analogs, and interpreting the SPT binding/unbinding kinetic data. There are many experiment design choices to consider that affect the kinetic data, and we explain these choices in the context of designing experiments for studying influenza X31 virus (H3N2 strain), which is a model for other enveloped viruses. Enveloped viruses are often labeled with membrane fluorophores since they do not interfere with protein functions and can be used in membrane fusion/dye-dequenching studies [8, 13-15, 34-35]. Yet, quenched concentrations of membrane dye or inefficient labeling can generate substantial numbers of dim particles that are intermittently observable. Hence, tracking membrane-labeled X31 virus serves as a useful test case for developing our image restoration algorithm and data analysis strategies.

A typical influenza virion surface contains roughly 400-500 hemagglutinin (HA) proteins [36] that govern the multivalent binding of the virus to sialic acid receptors on host cells. In this work, we use SLBs that separately contained glycolipids aG_{M1}, G_{M1}, G_{M3}, or G_{D1a} (Figure 1). Except for aG_{M1}, all glycolipids contain the α2,3 SA linkage but with different peripheral oligosaccharide structures. These structures serve to impart differences in binding behavior that can be resolved when tracking stochastic binding events instead of ensemble-averaged binding events.

Generally, viruses bind better to SA at the terminal position [37-39], but SPR studies have shown that X31 virus does not bind to G_{M3} even though it also has a terminal SA [7]. Contrary to this study, X31 virus can infect chicken red blood cells that have been incubated with G_{M3} receptors [40]. We show that the flu virus does bind weakly to G_{M3}, observable with

the experiment conditions and image restoration used in this work. Additionally, we show that binding residence time distributions reflect the adhesion-strengthening process via multivalent bonds that viruses use to stably bind to host membranes [41-44], and we present strategies to characterize these kinetics.

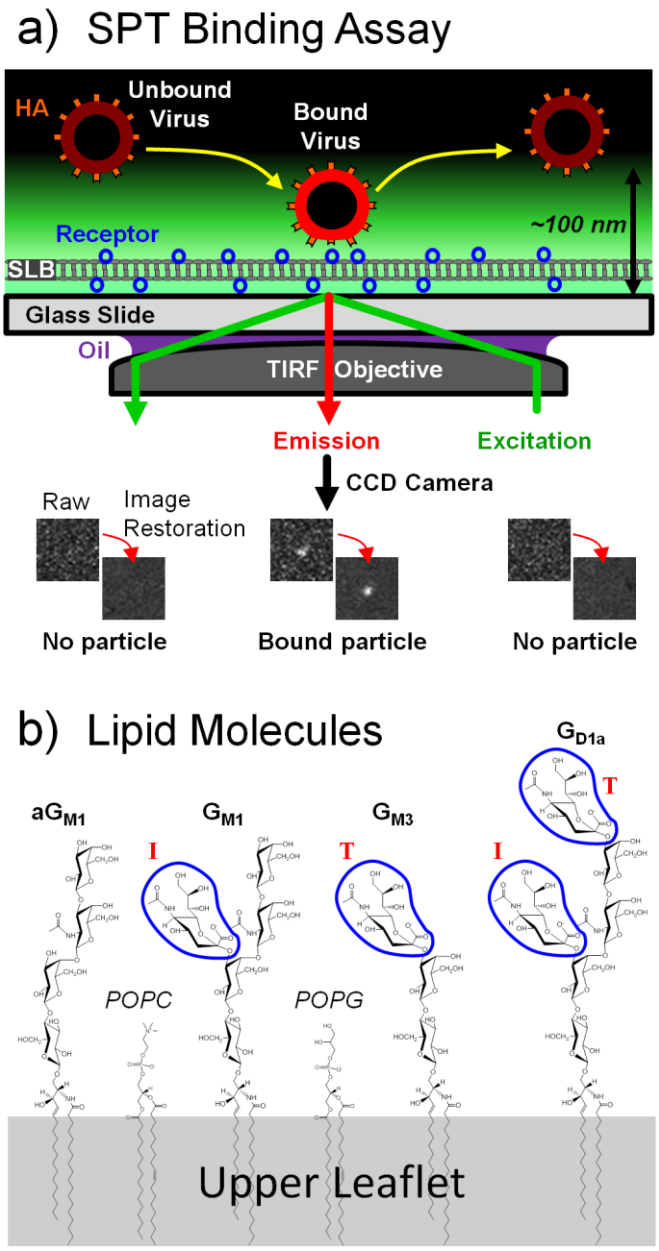

Figure 1 SPT binding assay and receptor structures. a) Setup of SLB on TIRF microscope. Evanescent field illuminate regions where SLB and virus interacts. b) Structure of the sialic acid receptors for X31 tested here. The α2,3-linked sialic acid groups are circled by the blue perimeters. Following the notation by Suzuki et al.[38], sialic acid groups are labeled as either being in the internal (I) or terminal (T) position.

MATERIALS AND METHODS

Producing lipid vesicles for SLBs

Supported lipid bilayers (SLBs) containing glycolipids are made from lipid vesicles. To make the lipid vesicles, 1-palmitoyl-2-oleoyl-sn-glycero-3-phosphocholine (POPC) and 1-palmitoyl-2-oleoyl-*sn*-glycero-3-phospho-(1'-*rac*-glycerol) (POPG) [Avanti Polar Lipids, Alabaster, AL] were separately dissolved in chloroform, while glycolipids monosialotetrahexosylganglioside (G_{M1}) [Avanti Polar Lipids, Alabaster, AL], monosialodihexosylganglioside (G_{M3}), disialoganglioside (G_{D1a}), and asialoganglioside (aG_{M1}) [Sigma-Aldrich, St. Louis, MO] were separately dissolved in a 2:1 chloroform to methanol solution. Glycolipids and POPC solutions were mixed together to yield 1 mol % of glycolipids, while POPG was added when necessary to maintain the same anionic charge density across all lipid samples (equivalent to 2 mol % of monovalent anionic lipids). Lipids were dried under vacuum for 3 hours and rehydrated in MES buffer (1 mM MES, 150 mM NaCl, pH 7) such that the final lipid concentration was 1 mg/mL. Lipids were extruded 10 times using a 1-directional, 20-mL lipid extruder [Northern Lipids Inc., Burnaby, Canada] and a 50 nm pore-size polycarbonate membrane [GE Healthcare, Pittsburgh, PA] to yield 100 nm-diameter vesicles as determined by dynamic light scattering [Malvern Instruments, Worcestershire, UK]. Extruded lipids were collected in a new vial to ensure all lipids have passed the filter.

Measuring surface charges of vesicles and viruses

To ensure long-range electrostatic forces do not influence binding, the surface charges of the vesicles and lipid vesicles were measured using a zeta potential analyzer [Malvern Instruments, Worcestershire, UK]. Lipid vesicles at 0.25 mg/mL dilutions or X31 virus (dye-

labeled and unlabeled) at 0.008 mg/mL dilutions were added to zetacells (model DTS 1061) and subjected to light scattering measurements under an electric field. Triplicate measurements were performed at pH 7, 150 mM NaCl.

Assembling the microfluidic device

Virus binding experiments were performed inside a microfluidic device as shown elsewhere [15]. Glass coverslip slides (No. 1.5 thickness) [VWR, Radner, PA] were cleaned for 10 min using a piranha solution composed of 30 vol % hydrogen peroxide solution (contains 50 wt % H_2O_2) [Sigma-Aldrich, St. Louis, MO] and 70 vol% concentrated sulfuric acid [VWR, Radner, PA]. Glass slides were stored in deionized water until use. A polydimethylsiloxane (PDMS) [Dow Corning, Midland, MI] mold of microfluidic channels (135 μm wide, 75 μm high, and 1.5 cm long) was prepared on top of a patterned, hydrophobic silica wafer produced at the Cornell Nanofabrication Facility (CNF). An air-dried glass slide and the PDMS mold were annealed together after a 30-second oxygen plasma cleaning step at 700 μmHg oxygen pressure. Tygon tubes (0.02" ID x 0.06" OD) [Saint-Gobain Performance Plastic, Worcester, MA] were attached to the microfluidic device such that one end is submerged into the loading solution and the other end is attached to a syringe pump [Harvard Apparatus, Holliston, MA]. The microfluidic device was setup on an inverted total internal reflection fluorescence (TIRF) microscope with a 100x oil immersion objective and 1.46 numerical aperture [Carl Zeiss, Oberkochen, Germany. Model Axio Observer Z1]. A 561 nm laser was shined at a 70° incidence angle to generate an evanescent wave that illuminates the virus within ~100 nm from the glass-water interface.

Forming SLBs inside microfluidic channels

SLBs that act as host membrane mimics were formed by rupturing lipid vesicle on hydrophilic glass surfaces [9, 45]. Lipid vesicle solutions at 1 mg/mL vesicle concentration were loaded into the microfluidic channels at a flow rate of 100 μL/min for 1 min. Vesicles were incubated in the channels for 4 hours to form high quality, defect-free bilayers . Excess vesicles were rinsed away by flowing MES buffer at a flow rate of 100 μL/min for 3 min.

Storing X31 viruses until use

X31 (H3N2/Aichi/68) influenza were obtained from Charles River [Charles River Laboratories, North Franklin, CT] at a protein concentration of 2 mg/mL, which comes in a frozen state. The stock virus solution was defrosted, aliquoted into 5 μL volumes and stored at -80°C until used. An aliquot of virus was freshly thawed and used for each experiment. While this procedure requires viruses to undergo two thaw cycles that decreases viral infectivity relative to fresh virus, it is repeatable and out-competes the other option to store the virus liquid state until each use. The drop in infectivity for a 2^{nd} thaw cycle has been reported to be from $10^{8.6}$ to $10^{7.0}$, whereas degradation over time at 0°C liquid sate causes a larger drop in infectivity to $10^{6.5}$ [46]. The spherical morphology of virus was fairly preserved after a 2^{nd} thaw cycle, as confirmed in a separate EM study using the same virus batch [47].

Labeling the viral membrane with R18

To label the viral envelope with lipophilic fluorescent dye, 5 μL of the virus solution, 250 μL of MES buffer, and 4 μL of 0.01 mg/mL ethanol-dissolved octadecyl rhodamine B (R18) [Invitrogen, Carlsbad, CA] were mixed together in a vial. The mixed solution was gently sonicated in a water bath for 30 min at 25°C in the dark. Unincorporated R18 dye was filtered out using a G-25 sephadex spin column [GE Healthcare, Pittsburgh, PA] at 3000

RPM (743 RCF), and the eluted virus solution was stored in a LoBind vial [Eppendorf, Hamburg, Germany] to prevent loss of viral particles to vial surfaces while conducting the experiments. Before use, 250 μL of filtered virus solution was diluted with 1 mL of MES buffer. Note the labeling of virus with membrane dyes has already been shown to not affect HA function [48-49].

Determining virus concentration & size using NanoSight

X31 stock virus solution from Charles River at an initial viral protein content of 2 mg/mL was diluted to 0.016 mg/mL. The virus solution was loaded into a flow chamber used in the NanoSight system (Malvern Instrument, Worcestershire, UK). Videos of particles floating in the solution were analyzed using the NanoSight software to extract the virus concentration, as well as their average hydrodynamic diameter.

Setting the camera rate and experiment time

SPT studies face an unusual sensitivity to the image capture rate of SPT microscopy [1]. Sensitivity is attributed to the fact that a continuous time data of binding events, which could last anywhere from 0 to infinite time, are being sampled via a camera taking images at discrete time intervals with a set exposure time. Similar issues are explained by the Shannon Nyquist Sampling Theorem [50] and Bally et al. [1]. Short term binding events will inevitably be lost during the dead time between images, which means the overall binding event data will be affected by the camera setting. Increasing the imaging rate (by shortening the dead time) is not always viable as this would lead to excessive dye photobleaching issues and loss of data about long-term binding viruses. The camera setting was thus set according to the minimum binding residence time resolution desired relative to a reference time scale.

We set the reference time scale based on that of virus-mediated *de novo* clathrin mediated endocytosis (CME), which takes roughly 3 min [51]. To encompass the CME timescale, camera was set to take images at 1 s intervals using a 100 ms exposure time for a total duration of 20 min (t_{movie} = 20 min).

Conducting SPT binding experiments

Labeled viruses were loaded into a SLB-coated microfluidic channel at a flow rate of 100 μL/min for 1 min. The flow was stopped by balancing the tube inlet and outlet pressures, which takes at most 1 minute to equilibrate. Stagnant flow conditions are necessary to prevent shear forces from affecting the binding/unbinding kinetics, especially of concern for weak binding interactions. Videos were recorded 1 min after the virus was introduced and the flow was stopped. The excitation laser was turned off in-between images during the 900 ms dead time to prevent excessive photobleaching of fluorophores while recording the video. After experiments, a 20 vol % bleach solution was sent into the microfluidic channels to inactivate viruses. All experiments were performed at 25°C.

Restoring images and tracking particles in SPT videos

Shot noise from SPT videos was removed using our image restoration algorithm called STAWASP, to stand for Segmented Temporal Averaging While Avoiding Synced Pixels. Details about STAWASP are provided below. Particles were detected using custom algorithm that looks for circular regions that are brighter than the background noise intensities (Supporting Materials 1.4). Particles trajectories were determined using a basic algorithm that links particles from adjacent video frames together that are within 3 pixels away from each other (Supporting Materials 1.5). Any remaining errors in trajectories were corrected

manually. All algorithms were developed using MATLAB (Mathworks, Natick, MA).

Defining a "Binding Event" via visual cues

Unlike SPR/QCM where the adsorbed mass to a surface can be detected, or AFM where binding force can be measured, SPT relies on visual cues that a binding event has occurred. These visual cues are not always obvious as virions can undergo stop-and-go motions. There are two criteria that can be used: Criteria 1 – a visible virus is always considered bound, or Criteria 2 – a visible virus that is immobile for at least a minimum duration time (t_{cutoff}) is considered bound. With Criteria 1, a mobile virus is treated as only 1 binding event regardless if this particle stops at and moves to several places. The concern with Criteria 1 is that the more interesting "stopping" events are ignored and the virus may not always be in contact with the SLB while moving. For instance, the virus could be is rolling along the SLBs, unbinding and rebinding to receptors, or simply floating near the field of view of TIRF without making contact. With Criteria 2, a single mobile virus can generate multiple binding events when it remains temporarily immobilized during the stop-and-go motion.

While Criteria 1 may be more appropriate only when studying the lateral diffusion of viruses into coated pits [52], we used Criteria 2 because an immobile virus is most certainly bound to the SLB. In this regime we are then corresponding most closely to the biological situation of virus binding events that lead to *de novo* CME occurring at stationary sites [53]. However, we must decide a minimum binding time for a binding event (t_{cutoff}), otherwise there would be no visual cue to discern a bound virus from a floating virus. We chose a t_{cutoff} of 5 frames (or 5 s) based on the performance of the automated particle tracking software (Supporting Materials 1.6).

Filtering biased binding events

When analyzing the binding residence time distributions, some binding events must be discarded due to ambiguity or bias. Particles that existed since the first frame (left-censored data) of the video were discarded since the actual binding time is uncertain. Those that bound after half of the movie time (½ t_{movie}) were also discarded because binding events that last longer than ½ t_{movie} cannot be observed in a fair manner as those that last for shorter times. Virions that stayed bound by the end of the movie (right-censored data) were included in the data if they initially bound before ½ t_{movie}. Due to the filtering of biased binding events, binding survival curves are drawn only up to ½ t_{movie}.

RESULTS AND DISCUSSION

Establishing conditions for high-quality SLBs

There are several ways to form SLBs: Langmuir Blodgett, lipid film rehydration, or vesicle rupture [9]. When using microfluidics, the vesicle rupture strategy is an effective means to form SLBs as it simply requires loading solutions of lipid vesicles into the channels. However, such method has previously been reported to cause low-quality SLBs if the devices are plasma cleaned [54]. To overcome this issue, which can be especially problematic when studying weak binding interactions, we determined conditions at which high-quality SLBs form with very minimal defects that viruses bind nonspecifically to by optimizing vesicle concentration and SLB formation time. Some issues with using lower vesicle concentrations are the creation of defective SLBs that induce nonspecific binding and spontaneous virus fusion (Figure 2a), most likely due to interaction with edges of SLB patches. The spontaneous fusion events prove that SLBs are laterally conjoined in 2D space, but lipid mobility does not indicate a pristine SLB has formed. Using at least 1 mg/ml vesicle

concentration worked well. The SLB formation time is also important and can vary based on pH or salt [55], lipid compositions [56], and glass surface treatment [57]. For our SLBs, at least 3 hours were needed to reduce non-specific binding of viruses to negligible levels (Figure 2b).

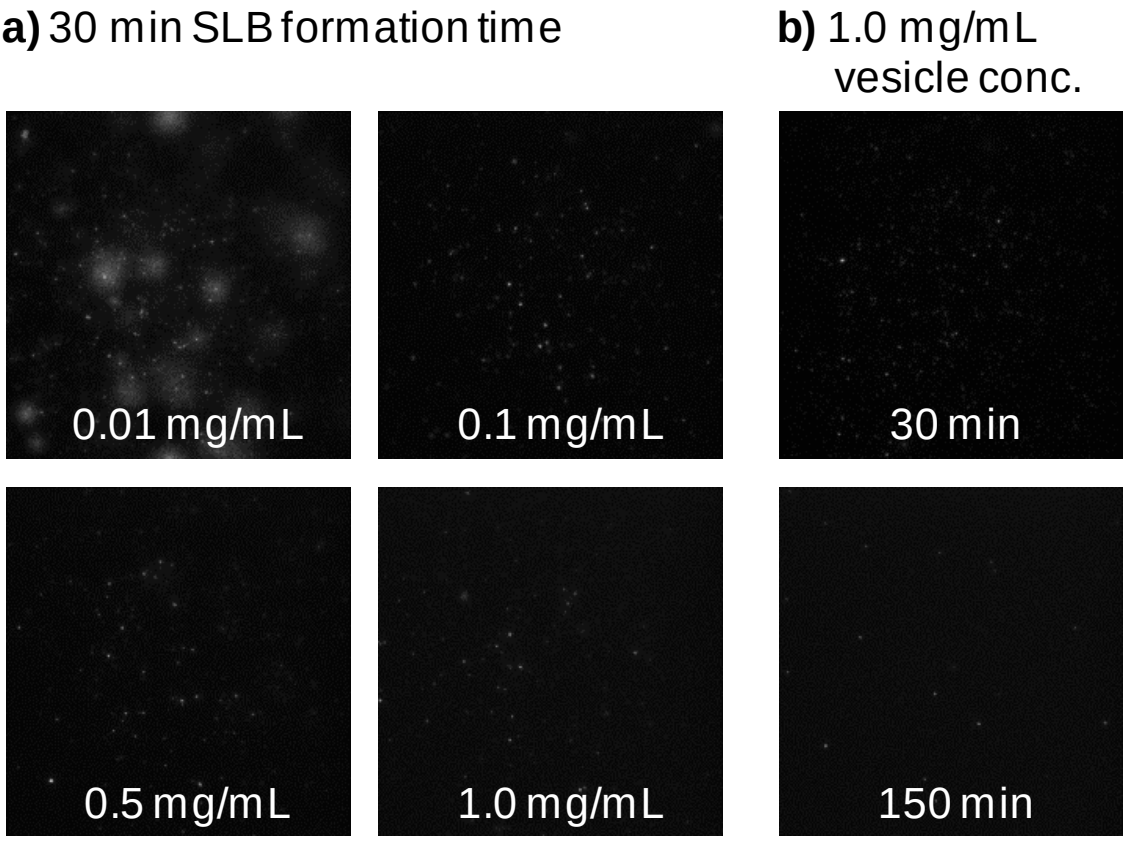

Figure 2 Optimizing SLB formation to reduce nonspecific binding. a) SLBs were formed over 30 min using 1% aGM1 receptor-less lipid vesicles at varying concentrations. X31 nonspecifically bound and spontaneously fused to SLBs (as noted by the radial release and diffusion of R18 into the supported bilayer) formed with low vesicle concentrations. b) The SLB formation time was varied while maintaining a constant 1 mg/mL vesicle concentration. Nonspecific binding was reduced greatly when SLBs are formed over at least 150 min.

Controlling for long-range nonspecific electrostatic binding

Controlling long-range, electrostatic interactions is essential for ensuring that the observed binding events are due to specific interactions. The net charge varies across aG_{M1} (0 charge), G_{M1} (-1 charge), G_{M3} (-1 charge), and G_{D1a} (-2 charge). To maintain the same receptor concentration and charge density of the bilayers, charged lipids must be added. Negatively-

charged POPG lipids were added to equalize the negative charge density across all of the SLBs (Table 1). Positively charged lipids could also be used to neutralize charges from the lipids, but since viruses are negatively charged, clusters of positively charged lipids could potentially induce non-specific binding. The surface charge of the virus must also be monitored, as the usage of too much lipophilic dye R18, which is positively charged, could change the polarity of the virus surface.

The zeta potentials of all lipid vesicles and dye-labeled X31 virus were negative and less than 5 mV in magnitude (Table 1). These magnitudes are much lower than 30 mV zetapotentials that could lead to nonspecific electrostatic attraction/repulsion between the virus and receptors [58]. The high salt content of the buffer also helps screen the charges. Overall, these measurements confirm that long-range, nonspecific electrostatic interactions are not playing a major role in the viral binding kinetics.

Table 1 Zeta potential measurements of vesicles and viruses. suv = small unilamellar vesicles.

Sample	Zeta potential (mV)
1% aGM1 2% POPG 97% POPC suv	-3.45±0.50
1% GM1 1% POPG 98% POPC suv	-3.32±0.59
1% GM3 1% POPG 98% POPC suv	-4.60±1.19
1% GD1a 0% POPG 99% POPC suv	-3.47±0.73
X-31 virus with R18	-2.02±0.26
X-31 virus without R18	-10.11±0.55

Introducing STAWASP image restoration algorithm for SPT

Shot noise is rooted in low-signal, digital images due to the discrete photon collection method of digital cameras and complex electronic signal amplification hardware. In SPT videos, the airy rings of dim particles are barely larger than 2x2 pixels, making them nearly indistinguishable from noise. There are three major image restoration approaches: spatial, temporal, and spatio-temporal filtering. Spatial filtering removes static noise pixels based on

how abnormal a pixel's intensity is compared to neighboring pixels. This method could produce artifacts such as particle blurring. Temporal filtering evaluates how pixel intensity changes over time to remove high-frequency noise fluctuation. However, it can cause particles to become blurred or faded. Spatio-temporal filtering combines aspects from both approaches, but this could become computationally expensive if it requires tracking local spatial regions over time.

Our STAWASP image restoration method can be classified as a spatio-temporal filter, and the algorithm is explained in Figure 3. In short, this algorithm removes noise and preserves particle signals by averaging images (or stacking images) together in spatially and temporally-divided pixel segments. The unique feature of this algorithm is the method at which segments are determined with little input about what is or is not a particle. Segments are determined based on how synchronous a cluster of pixels fluctuate with time. For instance, the chance all 13 pixels in a circular area (Figure 3a) synchronously increase intensity from one frame to the next is improbable due to random noise and highly probably if a particle appears/disappears/moves. Those that do change intensity synchronously are marked as "synced pixels" (Figure 3b). Each pixel in the 2D image is then average through time, but the averaging is done in segments separated by the appearance of synced pixels (Figure 3c). We provide the STAWASP software as a supplemental MATLAB stand-alone and source code files, and the logic and usage of STAWASP are explained in detail in Supporting Materials 1.1-2.

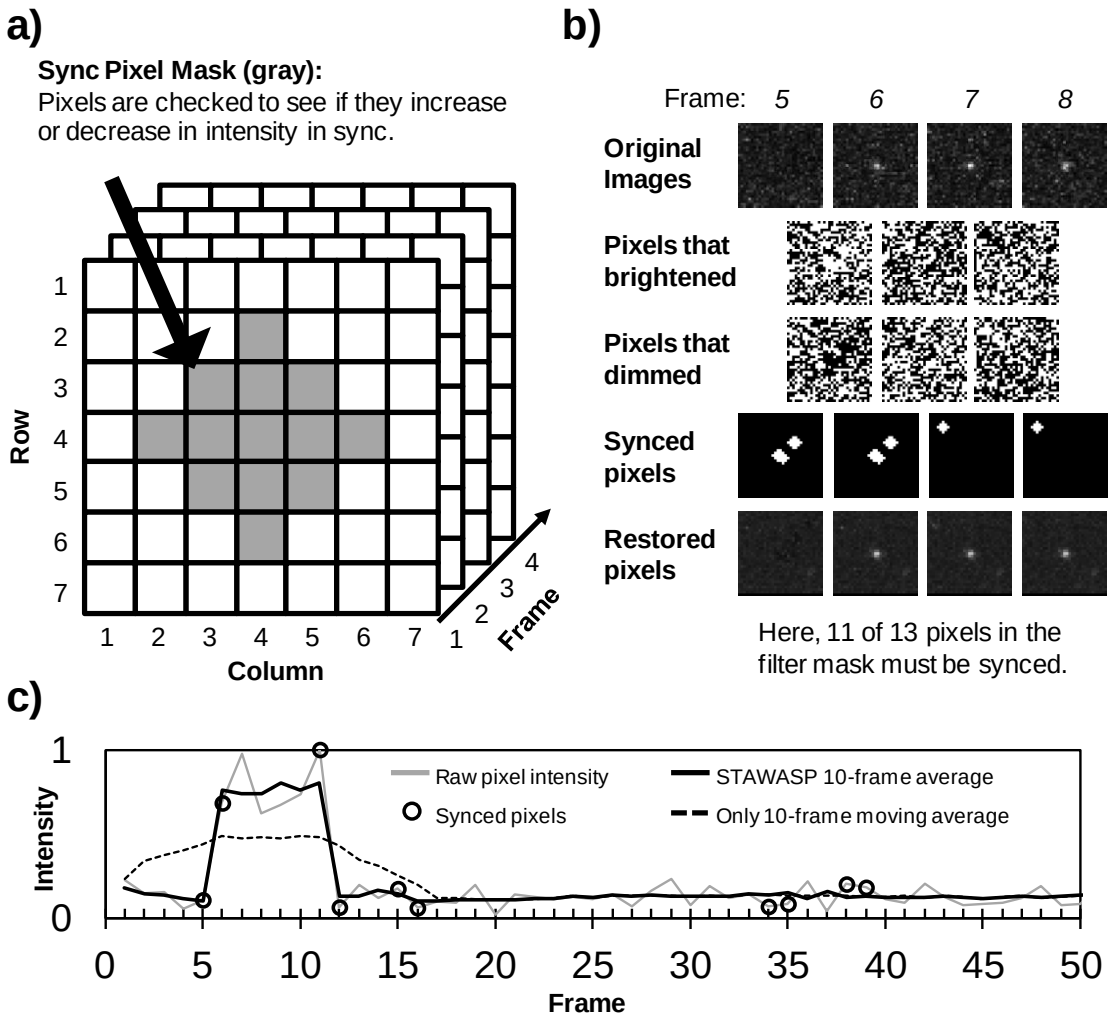

Figure 3 STAWASP algorithm. a) A local cluster of pixels (gray pixels) must either increase or decrease in intensity between consecutive frames to be classified as synced pixels. The pixel cluster size must be larger than a pixel and smaller than the particle of interest. Here, at least 80% of the gray pixels must be synced. b) The steps to determine synced pixels are portrayed here for a particle appearing at frame 6. Since synced pixels are determined using two adjacent frames, synced pixels are marked on both of those frames. Note that false synced pixels can be generated by random noise fluctuations, but these do not necessarily cause a false particle to appear. Also, a stationary particle will not always generate synced pixels since its intensity fluctuation is caused by random noise. c) The intensity trace for the center pixel of the particle images part B is shown when using STAWASP or the regular 10-frame temporal averaging scheme. With STAWASP, temporal averaging is performed in a segmented fashion such that temporally-adjacent, synced pixels are not averaged together.

Comparing performance of STAWASP

The performance of the STAWASP image restoration was compared against other common methods, using a first simulated, noise-ridden video of binding particles (Figure 4). Simulation details are provided in the Supporting Materials 1.3. The signal-to-noise ratios (SNRs, defined here as the particle peak intensity divided by the standard deviation of the noise intensity) were varied between 0.5 to 5. The Mean, Median, and LoG (Laplacian of Gaussian) noise filters intermittently revealed particles with SNRs $\geq$ 2.2, whereas particles with SNRs < 2.2 were undetectable. The 10-frame temporal averaging method was able to reveal particles with SNRs $\geq$ 1.1, but all the particles faded in and out of view. The STAWASP algorithm was able to reveal particles with SNRs $\geq$ 1.1, and it preserved the appearance/disappearance times of particles with SNRs $\geq$ 2.2.

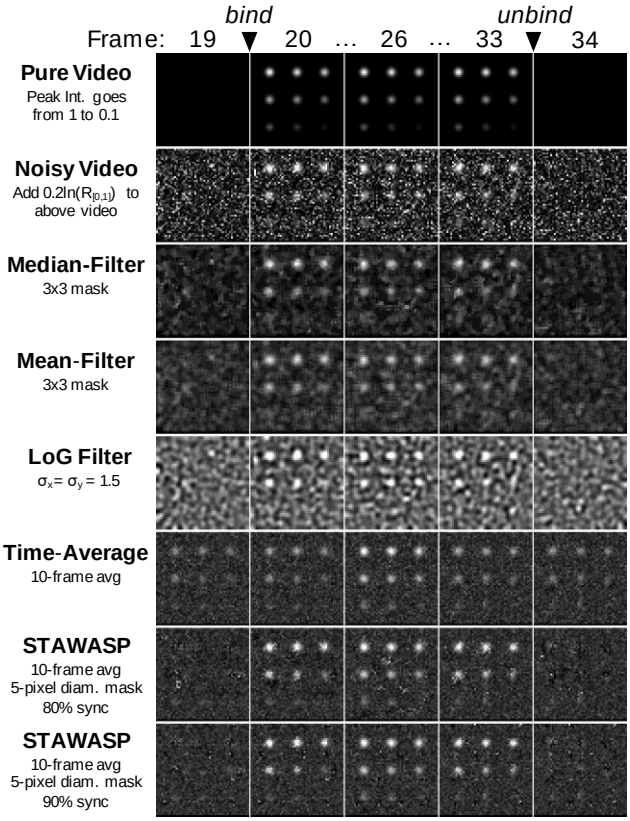

Figure 4 Testing various image restorations on a simulated movie. A simulated movie with noise was generated to compare image restoration performance (see Supporting Materials 1.3 for simulation details). The pure video shows particles with varying intensities appearing at frame 20 and disappearing after frame 33. Noise is added according to the function N = -0.2ln(R), where R is a uniform random number from 0 to 1. The SNRs of the 9 particles, from top left to bottom right are as follows: 5.0, 4.4, 3.9, 3.3, 2.8, 2.2, 1.6, 1.1, 0.5. The LoG (Laplacian of Gaussian) spatial filtering method is described by others[29, 59].

No image restoration is perfect, and a common artifact of the STAWASP algorithm are short-lived bright pixels throughout the movie, which is a result of the inability to distinguish a small cluster of bright noise from an actual particle. These artifacts are dealt with later by the particle detection (Supporting Materials 1.4) and tracking algorithms that filter out false particles (or shot noise that looks like particles) based on the criteria for a real binding event, as discussed above. We use a custom tracking algorithm that links particles together within 3 pixels between frames (Supporting Materials 1.5). The resulting particle detection and tracking performance with and without STAWASP are provided in Supporting Materials

1.6. Note that for actual SPT videos involving X31 viruses, we manually correct remaining erroneous trajectories to increase the accuracy of the data.

Images of viral binding are shown before and after using STAWASP image restoration (Figure 5). The clarity provided by the restored image, which is critical for obtaining accurate number statistics of viral binding. A qualitative assessment of the virus binding microscopy images shows that X31 binds most frequently to G_{D1a}, less frequently to G_{M3}, and negligibly to G_{M1}. The control case shows a minimum level of nonspecific binding of X31 to aG_{M1} SLBs, which confirms high-quality SLBs were formed inside microfluidic channels.

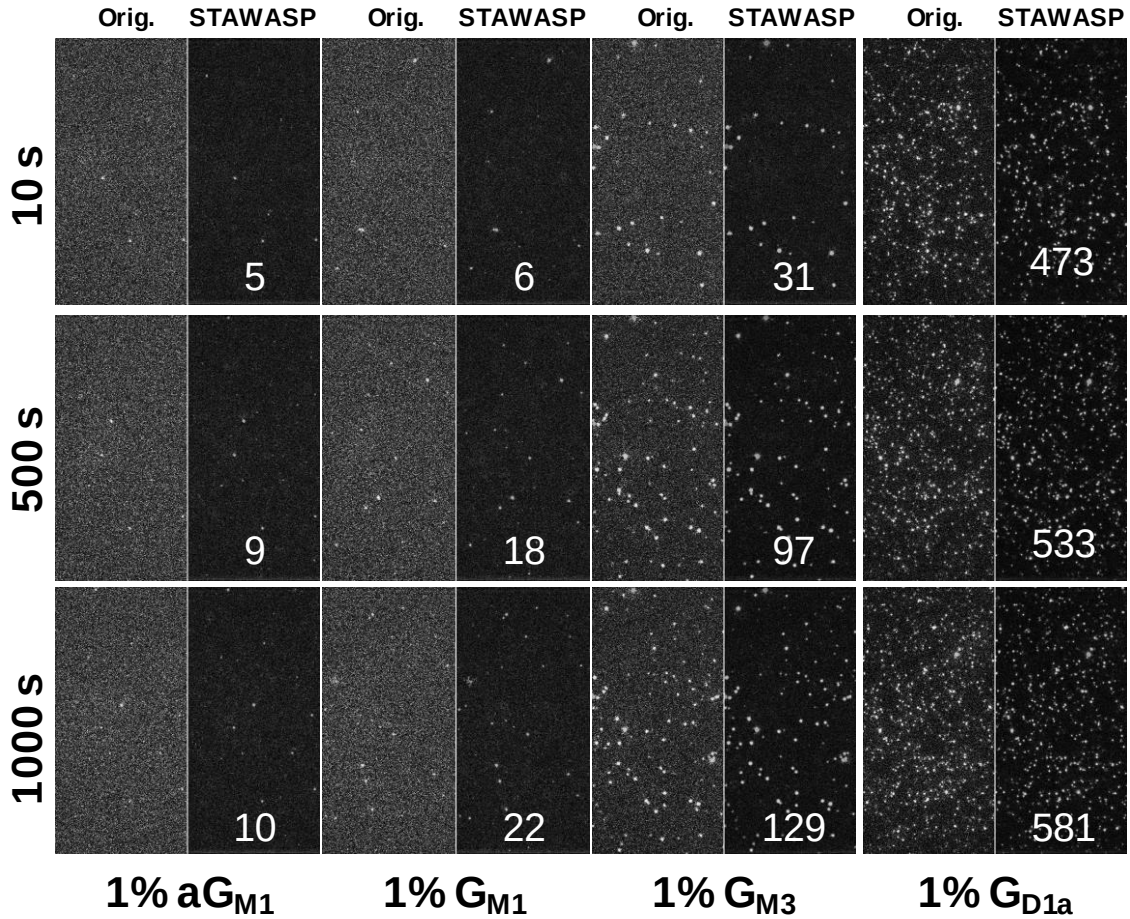

Figure 5 Original (left half) and STAWASP-restored (right half) sample images of X31 influenza binding to 1% glycolipid SLBs. The white number shows the particle count, P_{count}, for the right half of each image, which represent a physical size of 82 μm high x 41 μm wide using 512 x 256 pixels. Note that P_{count} is not the same as N. We show P_{count} for qualitative comparisons only, and a quantitative comparison must be done using N instead, which is determined after the particle linking step. The time on left is the video recording time, which starts ~60 s after the virus is loaded, and therefore some virus exists at time 0. We show images starting at 10 s merely because the performance of STAWASP is optimal after 10 frames. We provide movies of the first 300 s as supplemental files (Videos 1-4), played at 10x real time where 1 frame = 1 sec. STAWASP-enhanced movies are provided only for X31 binding to G_{M3} and G_{D1a} as Videos 3b and 4b respectively. [Image Processing Note: The images here have undergone background subtraction as explained in Figure S4, and intensities were linearly scaled.]

Analyzing binding frequency rate and rate parameter k_{on}

Before discussing the virus binding kinetic data, we must first clearly define variables associated with SPT data analysis (Table 2).

Table 2. Variables involved with SPT data analysis

Variable	Definition
P_{count}	Number of particles detected in an image
N	Number of binding events
N_+	Accumulated number of binding events since the movie started
N_-	Accumulated number of unbinding events since the movie started
t	Time elasped in the movie
t_{res}	Binding residence time (or contact time) of virus to receptors
t_{cutoff}	Minimum binding residence time required for a binding event
t_{movie}	Total duration time of the SPT video

Note that $N \leq P_{count}$ (unless t_{cutoff} = 1 frame) because not all particles seen in the movie satisfy the binding event criteria that a particle must remain immobile for longer than a certain cutoff time. Furthermore, when discussing SPT data, distinguishing normal time t and residence time t_{res} is important. For instance, N vs t plots portray the net number of binding events as a function of time, whereas N vs t_{res} plots portrays how many binding events last longer than t_{res} time (which is a survival function).

We first analyzed the N vs t plots for X31 binding to the SA receptors. N is related to the other variables by the equation $N(t) = N_+(t) - N_-(t) + N_0$, where N_0 is the N when the movie starts. The N(t) data clearly shows that G_{D1a} bilayers have a higher capacity to hold onto viruses (Figure 6a, blue line), versus other receptors. One interpretation of the low and flat curve of G_{M3} (Figure 6a, green line), relative to G_{D1a}'s curve, is to say G_{M3} is not a functional receptor. In fact, SPR studies concluded that G_{M3} is not a receptor for X31 [7], though they studied viruses binding to lipid vesicles instead of SLBs, using half the G_{M3} concentration than what was used here, and while applying a slight hydrodynamic flow that could prevent weak binding events. However, having a $dN/dt \sim 0$ does not mean there is no binding rate, similar to how when a system reaches equilibrium, a forward/reverse reaction still exists.

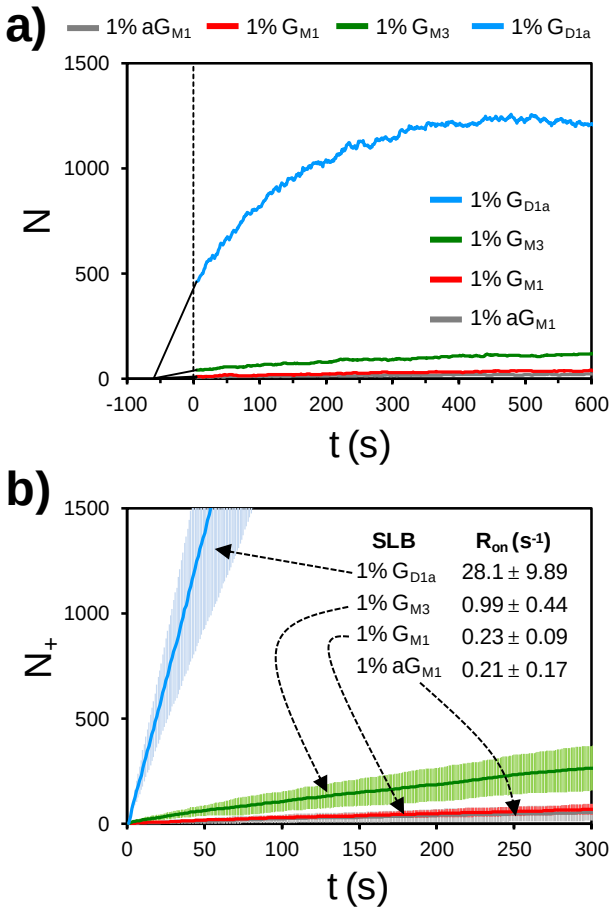

Figure 6 Two types of binding rate data of X31 to various receptors. A) N vs t plots for one representative data set from a triplicate set. Negative time means time before recording, and the solid black lines are just an extrapolation to -60 s when the viruses are estimated to first reach the SLBs. B) N_+ vs t plots, averaged over a triplicate set of data. The slope of this plot corresponds to binding frequency rate R_{on}. The error bars are the standard deviations, computed using 3 different trials.

The N_+ vs t plots (Figure 6b), show that X31 does in fact bind more frequently to G_{M3} than to aG_{M1} and G_{M1}. The slope of the N_+ vs t plots yields the binding frequency rate, R_{on}, and R_{on} for G_{M3} is 3 STDs higher than that of aG_{M1} and G_{M1} cases. This supports that G_{M3} can be a functional receptor for the virus.

Despite G_{D1a} and G_{M3} each having a terminal SA known to promote binding [38], X31 binds to G_{D1a} ~30 fold more frequently than to G_{M3}. This cannot be explained by the presence of 2 SA per G_{D1a} molecule, as spatial distances between SA do not allow them to bind to 2 binding sites of an HA trimer (Figure 7), including alternative binding sites located at the

HA1/HA2 junction [60]. Additionally, the lack of binding of X31 to G_{M1}'s internal SA suggests that the virus is not binding to the same internal SA in G_{D1a}. The extended distance of terminal SA from the SLB hydrophobic layer appears to promote binding. Access to G_{M3}'s internal SA may be sterically hindered by the close proximity of terminal SA to the bilayer.

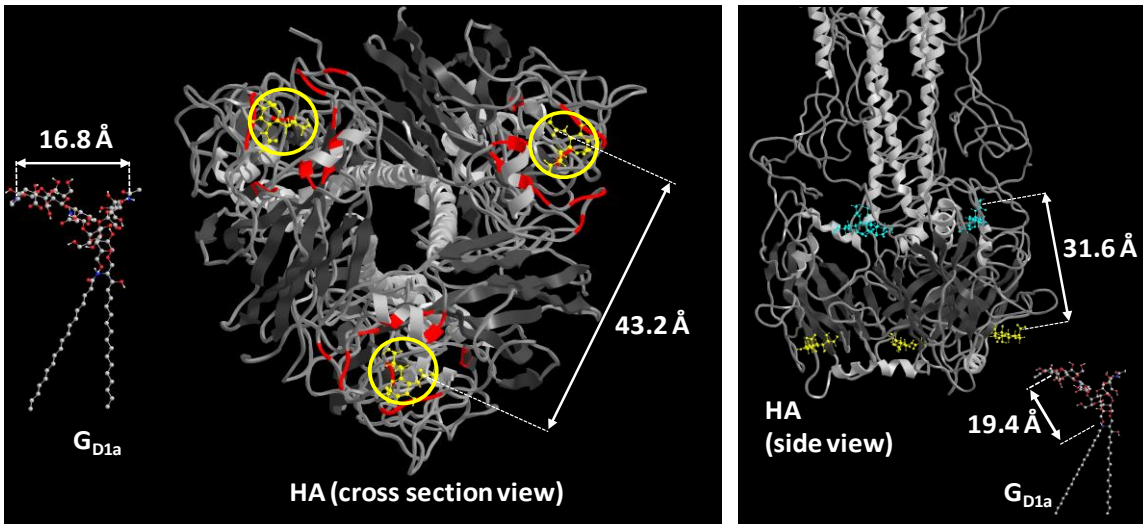

Figure 7 Using structural arguments to understand binding results. Left) View of HA protein head group in relation to G_{D1a}. Red regions show the binding pockets and yellow circles show where sialic acid are located. Right) Side view of HA protein in relation to G_{D1a}. Teal molecules are sialic acids at potential secondary binding sites. The SLB would be on the bottom side of the protein, while the viral membrane would be on the top side. The hemagglutinin structure and sialic acid positions were obtained by Sauter et al.[60] PDB ID: 1HGG.

Binding rates are often characterized via a binding rate constant k_{on}, but SPT data do not provide a single value for k_{on} as we will discuss the reasons for later. Starting with the standard approach for finding a single k_{on} value, the k_{on} parameter can be solved for via the relation $R_{on} = k_{on}[V][SA]A_{cam}$ where A_{cam} is 6274 μm^2 for our camera field of view, [V] is the visible virus concentration in the bulk solution, and [SA] is the surface density of free receptors in the SLB. Since R_{on} is determined using early time points of the experiment, this enables the assumptions that [SA] and [V] are approximately equal to initial values right when the virus is loaded into the channels. Therefore we can treat $[SA] \approx [SA]_{init}$ and $[V] \approx [V]_{init}$ to estimate the binding rate constant k_{on}. The concentration $[V]_{init}$ is ~4.5 pM based on

Nanosight measurements, and the receptor surface density $[SA]_{init}$ is ~16500 μm^{-2} for 1 mol % assuming a lipid occupies 0.65 nm^2 [61]. With these constants, the values for k_{on} are $(4.4\pm3.6)x10^2$, $(5.5\pm2.0)x10^2$, $(2.1\pm0.9)x10^3$, and $(6.0\pm2.1)x10^4$ 1/Ms for aG_{M1}, G_{M1}, G_{M3}, and G_{D1a} respectively, when using the binding event criterion t_{cutoff} = 5s. The k_{on} values for G_{M3} and G_{D1a} are within the expected range found for similar receptors using SPR and QCM binding assays, which have reported k_{on} = $2x10^3$ $M^{-1}s^{-1}$ for multiple HAs binding to fetuin [62], k_{on} = $3.61x10^4$ $M^{-1}s^{-1}$ for soluble HA binding to G_{D1a} [63], and k_{on} = $1.6x10^6$ $M^{-1}s^{-1}$ for X31 virion binding to vesicles containing 0.5 mol% Neu5Acα2-3nLc4Cer [7].

We now discuss why there can be multiple values of k_{on} and caution against the direct comparison of k_{on} from SPT assays to ensemble assays. Both k_{on} (or R_{on}) depend on the choice of t_{cutoff} because t_{cutoff} dictates how many binding events are included in a data set (Figure 8a). For instance, by setting t_{cutoff} to be infinite, no binding events will exist that meets this requirement, hence, k_{on} = 0. Conversely, setting t_{cutoff} to be 0 would make k_{on} seem to diverge to infinite because there will be no distinction between a binding event, elastic collision, or floating virus that is simply visible on the camera. Since the chance for a binding event to exceed a certain t_{cutoff} value is dictated by the binding residence time distribution, this means a relationship between k_{on} and k_{off} exists and the two parameters are not entirely decoupled as one would normally expect. To understand this relationship, we generated a plot for SPT data, that relates R_{on} (which is directly proportional to k_{on}) to the choice for t_{cutoff} (Figure 8b).This plot is useful for comparing binding data taken across various t_{cutoff} settings.

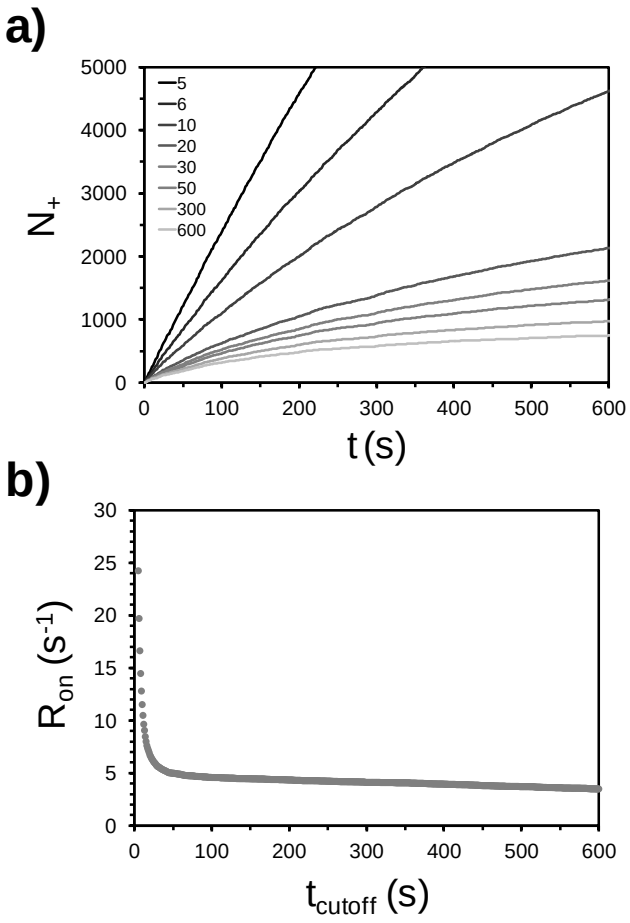

Figure 8 Observing how binding kinetics changes with choice of t_{cutoff} for a 1 % G_{D1a} trial. a) N_+ vs t at varying t_{cutoff} settings shown in the legend. b) R_{on} vs t_{cutoff} plot showing how R_{on} is affected with t_{cutoff} choice.

Analyzing binding residence time distribution and unbinding parameter k_{off}

We next analyze the N vs t_{res} plots that portray information about the binding residence time distribution and unbinding rates (Figure 9a). The unbinding curves did not agree with the 1:1 binding model (Eq. 1), and double exponential fit model (Eq. 2).

Eq. 1 : single binding energy population

$$N = N_0 \exp(-k_{off} t_{res})$$

Eq. 2 : double binding energy populations

$$N = N_{0,A}\exp(-k_{off,A}t_{res}) + N_{0,B}\exp(-k_{off,B}t_{res})$$

Rather, N decays in an unusual logarithmic fashion with respect to t_{res}, as also noticed by norovirus binding kinetics studies [1-2] and our recent work with parvovirus binding to transferrin receptors [44]. Alternative analytical models are generally lacking for multivalent binding systems and recent studies have begun to address this issue [1-2, 5, 44, 64]. Here, we searched for an empirical model to describe the overall unbinding probability of the virus by testing various log plots between N and t_{res} until a linear relationship was found (Figure 9b and 9c). Two possible fit equations for N vs t_{res} are provided (Eq. 3 and 4). Note that Eq. 4 mimics the approach used by Bally et al. [1], while Eq. 3 is developed by us and also describes the binding residence distribution of parvovirus binding to transferrin receptors [44]. These empirical fits can be related to binding force distributions, as discussed next.

Eq. 3 : empirical fit derived from Figure 9b

$N = N_0\exp(B)\left(\ln\frac{t_{res}}{\Delta t}\right)^{-A}$ where Δt is a reference time interval $\leq t_{cutoff}$. We used Δt = 1s based on the time interval between images. Note that all equations here apply only when $t_{res} \geq t_{cutoff}$.

Eq. 4 : empirical fit derived from Figure 9c and proposed by Bally et al [1]

$$N = N_0\left[1-\frac{\exp(B)}{1-A}\left(t_{res}^{1-A}-t_0^{1-A}\right)\right] \quad \text{if } A \neq 1$$

$$N = N_0\left[1-\exp(B)\ln\frac{t_{res}}{t_0}\right] \qquad \text{if } A = 1$$

Unbinding rates are often characterized via an unbinding constant k_{off}, which in turn is related to binding force. Since Eq. 2 and 3 failed to fit our data, this suggests that the unbinding kinetics does not follow a constant k_{off} value. We thus assumed k_{off} is not a constant and could vary with t_{res}. To extract k_{off}, we equated the empirical fits with the 1st order dissociation equation ($dN/dt = -k_{off}t$) and solved for k_{off}. The resulting equations for k_{off} are shown as Eq. 5 or 6 (derivations are in Supporting Materials 2.1).

Eq. 5: $k_{off}(t_{res})$ based on Eq. 3

$$k_{off}(t_{res}) = \frac{A}{t_{res}\ln\left(\frac{t_{res}}{\Delta t}\right)}$$

Eq. 6: $k_{off}(t_{res})$ based on Eq. 4

$$k_{off}(t_{res}) = \frac{\exp(B)t_{res}^{-A}}{1-\frac{\exp(B)}{1-A}\left(t_{res}^{1-A}-t_0^{1-A}\right)} \quad \text{if } A \neq 1$$

$$k_{off}(t_{res}) = \frac{\exp(B)t_{res}^{-1}}{1-\exp(B)\ln\frac{t_{res}}{t_0}} \quad \text{if } A = 1$$

Since k_{off} is a function of t_{res}, this would imply that the binding force changes depending on the contact time between the virus and receptor. Viruses can increase their binding force to host receptors via an adhesion-strengthening process [41-43], which includes co-receptor binding, conformational changes of viral proteins, and multivalent binding due to receptor diffusion with the "host" bilayer. With X31 virus, the HA proteins do not significantly change conformation upon binding [60] or under the neutral pH conditions used here. Adhesion strengthening is thus most likely caused by multivalent binding of the virus to the

tightly-packed, mobile SA receptors on the SLB. In support of this, the estimated number of glycolipids per cross section area is ~270, assuming a virus diameter is 150 nm and lipid molecules occupy 0.65 nm^2 of the SLB [61]. Furthermore, the glycolipid mobility was confirmed by fluorescence recovery after photobleaching (FRAP) experiments (Supporting Materials 2.2).

A competing interpretation of our unbinding curves is that k_{off} spans a wide range of values due to a wide distribution of virus sizes and thus degree of multivalent binding. To make an empirical model under this interpretation, one would sum many exponential functions for 1:1 binding model that are multiplied by a weight function that reflection the virus size distribution. This approach would also assume multivalent bonds effectively act as a single bond with a stronger binding force. However, the virus distribution is narrow and morphology is uniform according to particle size and EM studies [47]. Additionally, AFM studies showed complex unbinding process [65] that would be inconsistent with the idea that multivalent bonds can be treated as a single bond. Overall, the interpretation that k_{off} varies with t_{res} because of adhesion-strengthening via multivalent binding is more likely to agree with the biology involved in this study.

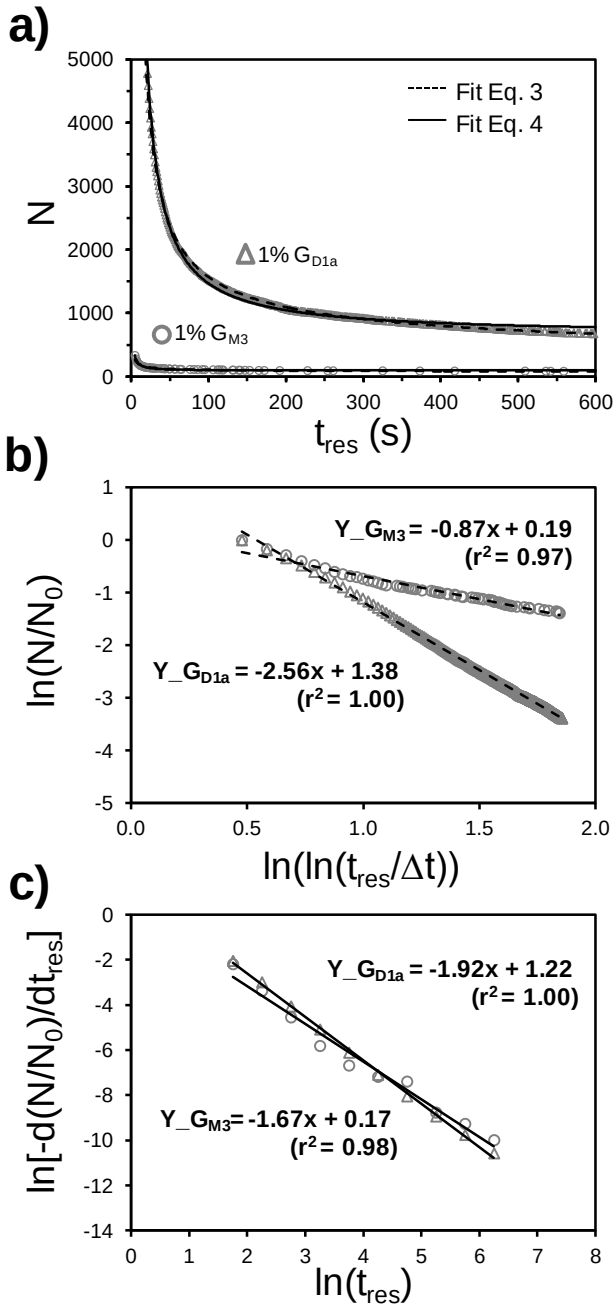

Figure 9 Representative X31 binding survival curves and empirical fits. a) The number of virus bound, N, is plotted against the residence time, t_{res}, to yield a survival curve for binding. The Eq. 3 fit parameter for G_{M3} is [A = 0.87, B = 0.19] and G_{D1a} is [A = 2.56, B = 1.38]. The Eq. 4 fit parameters for G_{M3} is [A = 2.14, B = 1.63] and G_{D1a} is [A = 2.06, B = 1.72]. Note that the Eq. 4 fit parameters differ from those found from the related log plots in panel c. The binning of the binding data in the log plots causes an approximation error. b) Our option to redrawn the survival curve redrawn as log plots. c) Another log plot option based on the fit proposed by Bally et al.[1] (the data has been binned).

The remaining question is why does k_{off} approach infinity if we allow t_{res} to approach 0? Theoretically, this is because as t_{res} goes to 0, an elastic collision between virus and

membrane will count as a binding event, and thus k_{off} will be substantially high to reflect a lack of binding force.

Bridging SPT and SPR data analysis

Since protein-ligand binding are currently often studied via ensemble assays such as SPR (Surface Plasmon Resonance) and QCM (Quartz Crystal Microbalance), we explain how to fit ensemble data using our empirical model from SPT data. Ensemble assays collect data on the net adsorbed mass on a surface over time, which would be similar to the N vs t data from our SPT assay. However, unlike SPT assays, ensemble assays require two experimental procedures to decouple binding and unbinding kinetics, noted as the "association" and "dissociation" phases. The virus must be loaded during the association phase to observe both binding and unbinding, and then a virus-free buffer is loaded during the dissociation phase to observe mainly unbinding. The procedure often requires the virus to be subjected to a gentle hydrodynamic flow that could shear off very weakly bound viruses and affect the final data. Also, rebinding events that occur during that dissociation phase are difficult to completely filter out and could lead to disagreements between expected and actual unbinding curves [66].

With SPT, we can extract association and dissociation curves using stagnant conditions and without conducting a separate dissociation phase procedure, simply by filtering binding events that occur during the "dissociation phase" that is set at the image processing stage. To make SPR-like curves, we plot N vs t, but with few differences. N is now set to start at 0 at t = 0 by removing binding events that occurred at or before the first frame, and a dissociation phase session is defined to start after time t_{diss} = ½ t_{movie}, in which binding events that occurred after that are ignored (Figure 10).

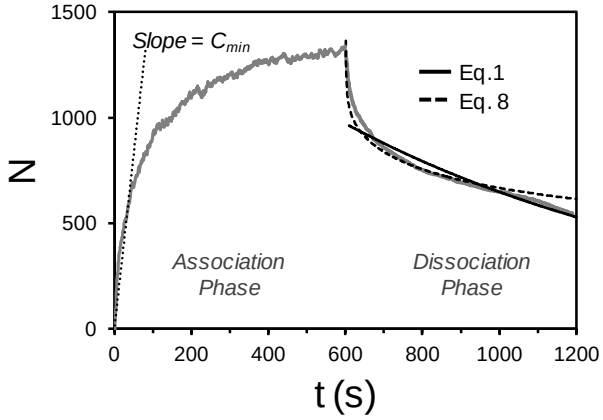

Figure 10 SPR-like curve assemble generated from SPT data for the purpose of comparing and contrasting the approaches. The fit parameters for Eq. 8 are A = 2.0, C = 47 (which is greater than C_{min} = 16.4). The fit parameters for Eq. 1 are N_0 = 971 and k_{off} = 0.001 s^{-1}).

The unbinding curve can be fitted using a modified form of Eq. 3, which the residence time t_{res} is converted into normal time t as shown in Eq. 7. Eq. 7 simply states that number of binding events remaining at $t > t_{diss}$ is the sum of the binding events that occurred at $t < t_{diss}$ and lasted until time t.

Eq. 7

$$N_{diss}(t) = \sum_{t'=0}^{t'=t_{diss}-\Delta t} \Delta t R_{on}(t') \exp(B) \left[\ln \frac{t-t'}{\Delta t} \right]^{-A} \quad \text{for } t \geq t_{diss}$$

Since ensemble assays do not yield $R_{on}(t)$ directly, an simplifying assumption must be made. We approximate $\Delta t R_{on}(t)$ as a constant, C, based on the N_+ vs t plots showing a fairly linear relation and constant slope R_{on} (Figure 6) This yields the fit Eq. 8, which would be used if one were given SPR-like data without knowing exactly what $R_{on}(t)$ is.

Eq. 8

$$N_{diss}(t) = \sum_{t'=0}^{t'=t_{diss}-\Delta t} C\left[\ln\frac{t-t'}{\Delta t}\right]^{-A} \quad \text{for } t \geq t_{diss}$$

C is the number of binding events that occur on average within a time increment Δt. One could instead use a time-varying *C* fit parameter, *C*(*t*), but it may lead to over-fitting issues. A lower bound value of *C* can be set based on the initial slope of the *N* vs *t* curve during the association phase, denoted as C_{min}. Optimal fit parameters can be determined via iterative search strategies. An example of how our adhesion-strengthening model Eq. 8 performs against the standard 1:1 binding model Eq. 1 is shown in Figure 10. The exponential fit model failed to fit the steep drop in unbinding immediately after the dissociation phase start, whereas our empirical model fitted main features of the curve.

CONCLUSIONS

We assessed of the SPT binding assay platform, image restoration, and data analysis for use in virus-membrane binding studies. We developed an image restoration algorithm called STAWASP to enhance dim particle signal and improve SPT binding data quality. STAWASP restored particles that had a SNR as low as 1.1, and preserved appearance/disappearance time of particles with an SNR as low as 2.2. The image restoration enabled the SPT software to extract accurate binding residence curves when tracking particles lasting at least 5 frames.

We explained data analysis strategies for X31 binding to various glycolipids, and showed X31 weakly binds to G_{M3} and to G_{D1a} ~30 times more frequently than to G_{M3}, despite both containing terminal sialic acid that is known to promote receptor binding [38]. On the other hand, ensemble assays and cell infectivity assays had mixed results about whether or not the

virus can bind to G_{M3} [7, 40]. The accessibility of SA appears highly restricted by the close proximity of it to the SLB lipid core.

The binding residence distribution curves show an interesting time-dependent k_{off}, which is unusual in the field of unbinding kinetics that often observe k_{off} to be constant. The empirical model agrees with the interpretation that viruses increase their binding force to host membrane with longer contact time via an adhesion-strengthening process. For this study with X31 virus, adhesion-strengthening most likely occurs via multivalent bonds that form when mobile receptors in the SLBs are recruited to the virus. We provide a general strategy to apply our empirical model to fit ensemble assay unbinding data (Eq. 8) that feature a sharp decline in the dissociation curve, followed by a slow logarithmic decay.

The combined image restoration and analysis tools developed here is easily extendible to other studies that involve imaging low-fluorescence particles binding stochastically with surfaces. We have recently applied these tools for tracking parvovirus binding to transferrin receptors [44], in which both were labeled with limited fluorophores and were difficult to observe without image restoration. Another example where this approach could be useful is for studying viruses that undergo membrane fusion upon receptor binding (such as parainfluenza). In such case, viruses are usually labeled with a quenched membrane dye and would be difficult to track until membrane fusion and dye-dequenching occurs.

ACKNOWLEDGEMENT

We thank Dr. Peter Frazier, Divya Singhvi, and Somya Singhvi for discussions on survival curve analysis. We thank Dr. Gary Whittaker and Dr. Jean Millet for reviewing the manuscript. DWL acknowledges financial support of the National Science Foundation (NSF)

GK12 programs, award number DGE-1045513 to Cornell's Grass Roots program and award number DGE 0841291 to Cornell's Learning Initiative for Medicine and Bioengineering (CLIMB) program. KBB acknowledges support from the Engineering Learning Initiative fund, with donations from Genentech and Proctor & Gamble. We thank the NSF (grant CBET-1263701) for financial support for the project. This work was performed in part at the Cornell NanoScale Facility, a member of the National Nanotechnology Infrastructure Network supported by the NSF (grant ECCS-0335765).

SUPPORTING MATERIALS

1.1 Logic behind STAWASP image restoration

We explain the mechanism behind STAWASP noise removal process. We first define the intensity of a pixel (I) as the summation of the signal (S) and noise (N).

$$I(r,c,t) = S(r,c,t) + N(r,c,t)$$

where r is the row location, c is the column location, and t is the time or frame number of the pixel. We can break up the noise into spatial and temporal components.

$$I(r,c,t) = S(r,c,t) + N_m(r,c) + N_t(t)$$

where, N_m = mean noise that varies only in space (N_m is a positive number), and N_t = fluctuation intensity around the mean noise (N_t can be negative or positive).

The spatial noise can be removed using a background subtraction whereas the temporal noise can be removed using a temporal averaging scheme. As the time span of averaging goes to infinity, $N_t(t)$ approaches 0. However, this works only when there is no particle signal. If there is a particle signal then temporal averaging must be done carefully in segments. The STAWASP algorithm creates these segments based on where and when synced pixels are found. Ideally, synced pixels should only be found when particles appear, disappear, or move. However, noise can generate synced pixels by coincidence. We can estimate the percentage of falsely synced pixels using a binomial distribution.

$$P_{sync} = \frac{Q!}{M!(Q-M)!} p^M (1-p)^{N-M}$$

P_{sync} : probability a cluster of pixels are in sync due to random shot noise

Q : Number of pixels in the neighbor mask for determining a synced cluster

M : Number of pixels within the neighbor mask that actually must be in sync

p : Probability intensity increases or decreases between adjacent frames ($p \approx 0.50$)

Our default setting generates a 5-pixel diameter circular neighbor mask consisting of 15 pixels ($Q = 13$), in which 80% of the pixels must be in sync ($M = 10$). The probability random noise causes synced pixels is roughly 0.0349. The lower the P_{sync} value the stronger the noise reduction scheme. However, Q and M are capped by the smallest size of the particles' airy rings in the videos. To reduce the number of falsely synced pixels, one could impose more stringent rules about what to consider as a pixel intensity change. For example, a rule can be imposed specifying that the intensity of a pixel must change by at least a minimum value between adjacent frames to be counted as an increase or decrease in intensity for the STAWASP algorithm.

1.2 STAWASP GUI usage [Code: stawaspGUI.m or stawaspGUI.exe]

Installation:

Option 1) The standalone STAWASP.exe file requires the MATLAB Runtime Compiler to be installed prior to running the stawasGUI.exe. The MRC installer can be found in the MathWorks website, and the required version is for MATLAB R2015a (8.5).

Option 2) The stawasp GUI can be installed using the STAWASP_WebInstall.exe file instead, which will automatically download the necessary MRC file required to run the program.

Option 3) If MATLAB is installed, the source code can be used directly. Save the source code files into a folder. Open MATLAB, set the folder path to the saved folder, and then run "stawaspGUI" in the command line. Note that the Image Processing Toolbox is required.

Basic Usage:

1) Open STAWASP.exe for the stand-alone version or run stawaspGUI.m in the MATLAB console.

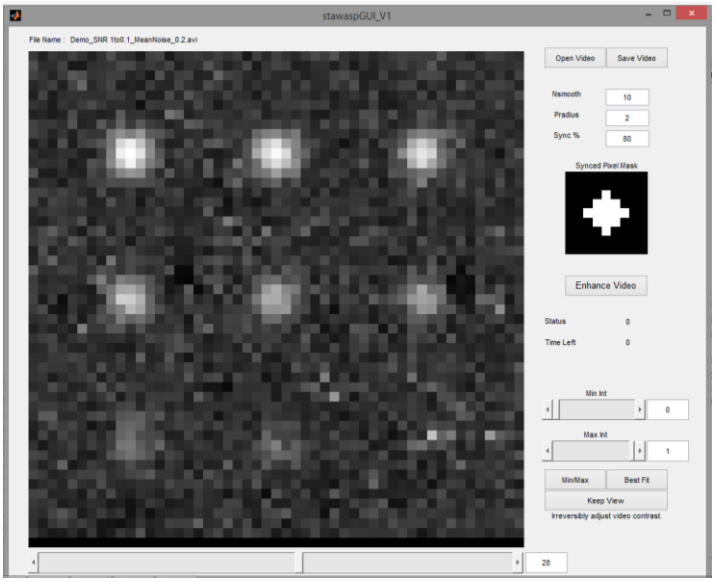

Figure S1 Graphical User Interface for STAWASP Image Restoration

2) Open the video to be processed. Note: limited video file types are supported, and we recommend processing videos with the uncompressed AVI format.

3) Configure the STAWASP algorithm parameters.

   Nsmooth: Maximum number of frames that can be averaged together. Generally, a larger Nsmooth will get rid of noise better.

   Pradius: The radius, in pixels, of the neighborhood mask. Ideally, this will be slightly larger than a pixel, and smaller than the particle of interest. EX: If particles have radius of 3, Pradius should be set between 1 and 2.

SyncPerc: The percentage of the pixels inside the neighborhood mask that actually need to be synced. Generally, a higher SyncPerc will remove noise better.

4) Once the parameters are set, click “Enhance Video” to begin the STAWASP image restoration process. Note that this can take a few minutes depending on the video size and computer. A video of size 512x512 pixels and 1200 frames takes 250 sec to process with a single core CPU 1.8 GHz and 6 GB ram.
5) Optional: Adjust the image brightness to the desired setting and push “Keep View” to make the intensity changes permanent.
6) Save video. The output will be an uncompressed, AVI file.

1.3 Generation of simulated videos

Simulated videos are helpful for testing the performance of image restoration and particle tracking software. We highlight the main steps and codes used to generate these videos.

Step 1: Generate particle information [Code: GenerateParticles.m]

The particles’ locations, intensities, and appearance/disappearance times were created using random number generators or manually, depending on the type of video to be generated. Particle data was stored in MATLAB structure variable called “tracker”. Inside the tracker structure is a field called “History”, which contains a 5-column matrix storing the following data per particle: Col 1) video frame numbers in which the particle exists, Col 2) the particle image pixel row locations, Col 3) the particle image pixel column location, Col 4) particle intensity, and Col 5) particle area.

Step 2: Create a video without noise [Code: CreatePureVideo.m]

Particles were drawn onto the blank video (which is an HxWxZ matrix) according to the particle data stored in the "tracker" variable. We made the particle intensities follow a Gaussian shape with a sigma width of 1.5 pixels around each particle's centroid location.

Step 3: Add shot noise to the simulated video [Code: CreateNoiseVideo.m]

Noise was added to the video made in Step 2. We first studied the background noise of real SPT videos and then chose an appropriate noise model. The background noise is consistent with shot noise that follows a Poisson distribution (Figure S2).

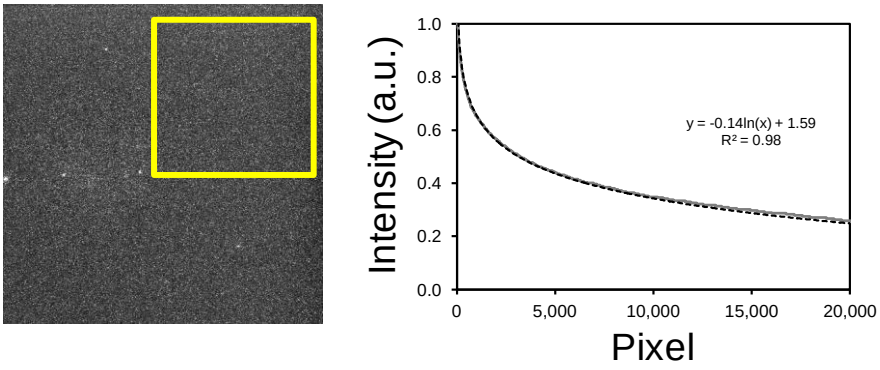

Figure S2 Background noise intensity distribution from real SPT video. The pixel intensities in the image background area (yellow box) were sorted and plotted as an intensity distribution, which reflects that of shot noise. Therefore we used the logarithmic model to mimic shot noise in simulated videos next.

Noise intensities were added to simulated videos using on the following equation: Noise = -MeanNoise*log(R), where R is a uniform random number from 0 to 1and MeanNoise is a user-set constant number between 0 and 1. Noise was added to every pixel in the video, and pixels with an intensity greater than 1 were capped at an intensity of 1 (Figure S3).

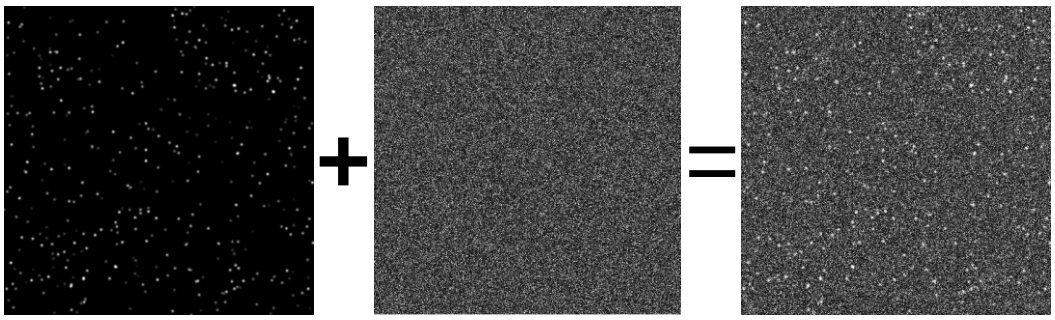

A) Pure Image **B)** Noise Image **C)** Pure + Noise Image

Figure S3 Generating movie of particle binding. A) Image of just the particles, without noise, is created using particle data. B) A pure noise image is generated. C) The noise is added to the pure image to create the final image for testing purposes.

1.4 Particle Detection [Code: ParticleFilter_V5.m]

There are many particle detection algorithms in existence to choose from. Since we deal with particles in high densities, we avoided using Gaussian fitting methods for particle detection that are computationally expensive. To detect particles, we find regions that lack local intensity minima clusters, which normally correspond to a particle region. A particle is then found by searching for the local intensity maxima that reside in these regions lacking a high cluster of local intensity minima. In the last step, particles that do not fit the user-defined intensity and particle size threshold values are removed. The step-by-step particle detection process is portrayed in Figure S4 and Figure S5.

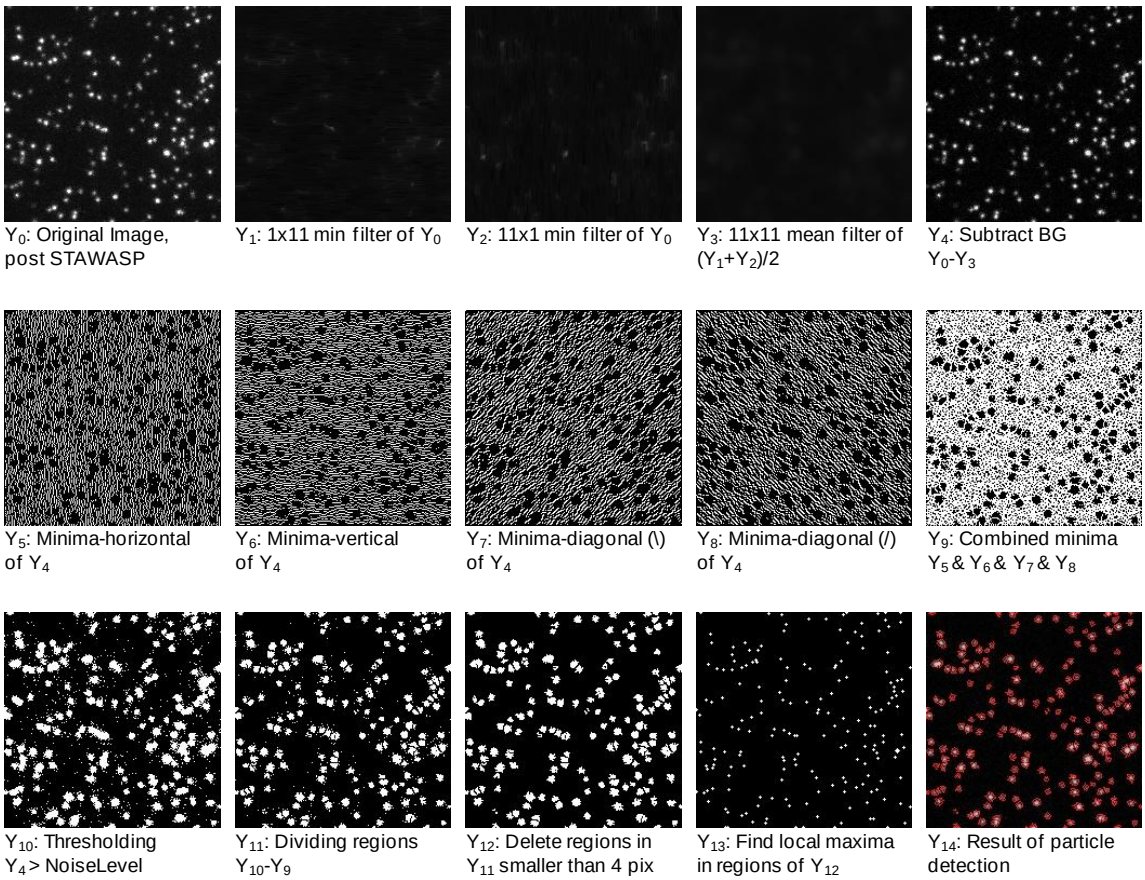

Figure S4 Flow chart of particle detection process. The "Minima" treatment finds the local minimal amongst 3 adjacent pixels in the direction specified after the dash. Note that for Y_{12}, the area of the particle that will be excluded can be adjusted by the user (here, it is set to 4).

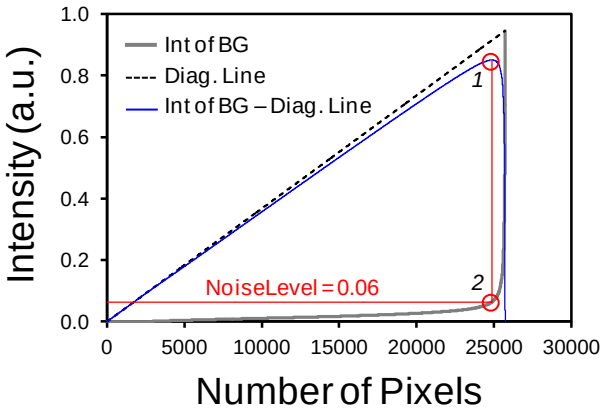

Figure S5 Automatic determination of Noise Level based on the intensity values of Y_4 that overlaps Y_9. Pixel intensities are first sorted and then are plotted (Int of BG). A diagonal line is drawn next (Diag.. Line). The two lines are then subtracted to yield the difference (Int of BG – Diag. Line), and the maximum point of line is used to determine the NoiseLevel.

1.5 Particle linking

After finding the location of the particles in each frame, each particle's trajectory must be linked through time. For this task, we use a simple nearest-distance particle linking algorithm due to the rapid speed and computational simplicity. Particles that are roughly in the same place (within a cutoff radius or 3 pixels = 480 nm) in adjacent images are tracked as a single particle. If a particle in one frame is not found in the next frame, then this particle's trajectory is ended. The particle trajectories can sometimes be ended prematurely due to the failed detection of the particle. This is usually caused by extreme shot noise or blinking particles. Intermittent detection error of stationary particles generates multiple trajectories that overlap the same spot but at different times. We automatically link these trajectories into one because the probability that 3 or more trajectories overlapping the same spot is rare, unless it's the same stationary particle that was intermittently detected. Also, the binding kinetics is more tolerable to accepting 1 long incorrect binding event as opposed to M number of short incorrect binding events. In the final step, any remaining errors in tracking results are manually corrected.

1.6 Testing particle detection and linking performance

In order to confirm that the image enhancement, particle detection, and tracking algorithm are working properly, we calibrated the software on a simulated video containing 1000 particles of known locations and unbinding/binding times. The binding residence time distribution of all events was set to follow a single exponential decay function $N = N_0 \exp(-0.10\ F)$, where F is the image frame number (1 frame = 1 sec). The particle intensity was set to 0.44 and noise with a mean intensity and standard deviation of 0.2 was added to the video. The final video has a particle signal-to-noise ratio of 2.2. The particle detection method described above was used to detect particles before and after image restoration. We chose to focus on STAWASP and the 10-frame moving average method due to their similar temporal filtering processes. Particle detection results show how image restoration affects the particle detection performance (Figure S6).

Compared to detecting particles without any image restoration, the STAWASP-restored video reduced the false particles to 41% and missed particles to 5% while the moving-average-restored movie reduced the false particles to 45% and missed particles to 19%. False particles are difficult to remove using only particle detection algorithms since false particles caused by bright noise pixels look fairly similar to particles. Fortunately, false particles do not persist for long durations and can be removed during the particle linking step by setting a minimum tracking time duration.

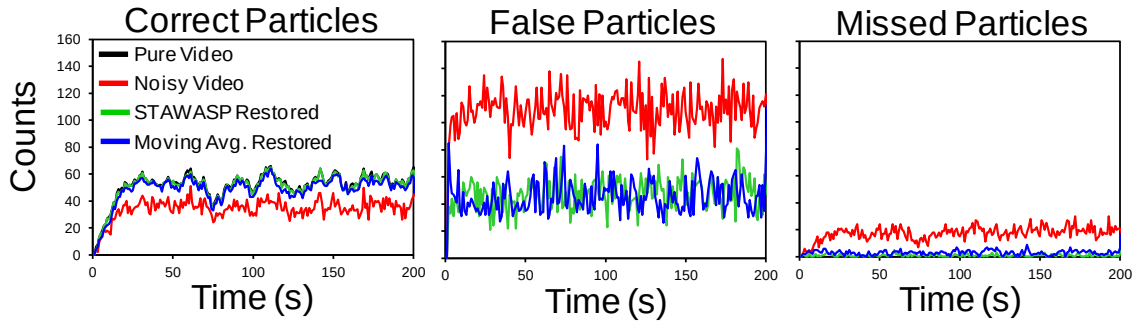

Figure S6 Particle detection results of the simulated particle binding video before or after image restoration. Settings for the STAWASP-restored video are Nsmooth = 10, Pradius = 2, and SyncPerc = 80%. The Moving Avg-restored video uses a 10-frame moving average. The particle detection was set to filter out particles with area less than 6 pixels.

Particle linking was performed to generate particle trajectories and obtain binding on and off times. Biased binding events were filtered according to the procedure explained in manuscript methods, which will discard roughly half of the particle binding events. The resulting survival curves are shown in Figure S7. Without any image restoration, the particle detection and linking processes yield inaccurate binding kinetic data. Using only the 10-frame averaging image restoration, the particle tracking results yields kinetic data that is horizontally shifted. The STAWASP image restoration allows the particle detection and linking process to yield accurate data, but only when t_{res} > 5 frames or seconds. The high error rate before 5 frames is caused by the false particles. We therefore filter binding events shorter than t_{cutoff} = 5 frames to reduce the number of false particle detection errors that must be corrected manually. The close match across the data extracted from the test case movie and the actual data shows that the tracking algorithm functions sufficiently well to extract unbinding kinetic parameters. This also means that the logarithmic decay function of the influenza unbinding kinetics is not likely to be an artifact of the tracking software or the method at which we filter out biased data points.

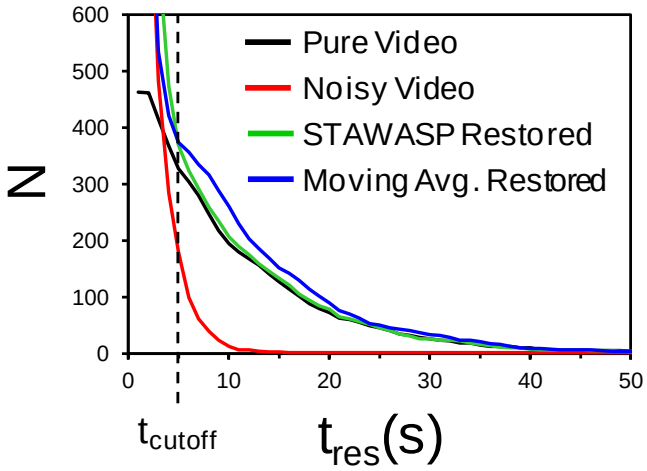

Figure S7 Comparison of binding survival curves from the SPT software before and after image restorations. Settings for the STAWASP-restored video are Nsmooth = 10, Pradius = 2, and SyncPerc = 80%. The Moving Avg-restored video uses a 10-frame moving average.

2.1 Derivation of fit equations

We will first define Eq. 0 as the 1st-order dissociation equation

$$\frac{dN}{dt} = -k_{off} N \quad \text{Eq. 0}$$

The derivation of Eq. 3 and 5.

1) $\ln(N / N_0) = -A \ln\left(\ln \frac{t_{res}}{\Delta t} \right) + B$ from Figure 9b log plots

2) $N / N_0 = \exp\left(-A \ln\left(\ln \frac{t_{res}}{\Delta t} \right) + B \right)$

3) $N = N_0 \exp(B) \left(\ln \frac{t_{res}}{\Delta t} \right)^{-A}$ [Eq. 3]

4) $\frac{dN}{dt} = \frac{-AN_0 \exp(B) \left(\ln \frac{t_{res}}{\Delta t} \right)^{-A-1}}{t_{res}}$

5) $\frac{dN}{dt} = -k_{off} N = -k_{off}\left[N_0 \exp(B)\left(\ln \frac{t_{res}}{\Delta t} \right)^{-A} \right]$ [Eq. 0, using N from Eq. 3]

6) $-k_{off} N_0 \exp(B)\left(\ln \frac{t_{res}}{\Delta t} \right)^{-A} = \frac{-AN_0 \exp(B)\left(\ln \frac{t_{res}}{\Delta t} \right)^{-A-1}}{t_{res}}$

7) $k_{off}(t_{res}) = \frac{A}{t_{res} \ln \frac{t_{res}}{\Delta t}}$ [Eq. 5]

The derivation of Eq. 4 and 6.

1) $\ln\left(\frac{d(-N/N_0)}{dt_{res}} \right) = -A\ln(t_{res}) + B$ from Figure 9c log plots

2) $\frac{d(-N/N_0)}{dt_{res}} = \exp(B) t_{res}^{-A}$

3) $\int_{N_0}^{N} d(-N/N_0) = \exp(B) \int_{t_0}^{t_{res}} t_{res}^{-A} dt_{res}$

4) $N = N_0\left[1 - \frac{\exp(B)}{1-A}\left(t_{res}^{1-A} - t_0^{1-A} \right) \right]$ if A ≠ 1 [Eq. 4]

$N = N_0\left[1 - \exp(B) \ln \frac{t_{res}}{t_0} \right]$ if A = 1

5) $\frac{dN}{dt} = -k_{off} N = -k_{off} N_0\left[1 - \frac{\exp(B)}{1-A}\left(t_{res}^{1-A} - t_0^{1-A} \right) \right]$ if A ≠ 1 [Eq. 0, using N from Eq. 4]

$\frac{dN}{dt} = -k_{off} N = -k_{off} N_0\left[1 - \exp(B) \ln \frac{t_{res}}{t_0} \right]$ if A = 1

6) $$k_{off}(t_{res}) = \frac{\exp(B) t_{res}^{-A}}{1 - \frac{\exp(B)}{1-A}\left(t_{res}^{1-A} - t_0^{1-A}\right)}$$ if A ≠ 1 [Eq. 6]

$$k_{off}(t_{res}) = \frac{\exp(B)}{t_{res}\left(1 - \exp(B)\ln\frac{t_{res}}{t_0}\right)}$$ if A = 1

2.2 Confirming lipid mobility using Fluorescence Recovery after Photobleaching (FRAP)

To ensure that lipids (and glycolipids) in the SLBs are completely mobile and can thus promote multivalent binding, we conducted FRAP tests. A solution containing 0.1 mg/mL of R18 was flown into the channels containing SLBs for 4 hours. Excess R18 was rinsed away using MES buffer. A 561 nm laser with a diameter of 12 μm was focused at the bilayer to photobleach the R18 in the bilayer. The average intensity of the bleached spot was measured over 10 min, along with a reference spot located far enough away from the photobleached spot (sample FRAP images are provided elsewhere[15]). The recovery curve was normalized using the following equation:

$$f_k(t) = \frac{\left[F_k(t) - F_c(t)\right] - \left[F_k(0) - F_c(0)\right]}{\left[F_{k,PB} - F_{c,PB}\right] - \left[F_k(0) - F_c(0)\right]}$$

where $F_k(t)$ and $F_c(t)$ respectively are the average fluorescence intensities of the bleached and reference spots. $F_{k,PB}$ and $F_{c,PB}$ are the fluorescence intensities of the spots before bleaching. The bleaching of fluorophores is completed at t = 0. The normalized recovery curve was then fitted using the equation derived by Axelrod et al.[67], which has two fit parameters: M_f (mobile fraction) and τ_d (characteristic time of diffusion). The full equation along with associated terms are provided below.

$$f_{k,fit}(t) = M_f \left[\frac{F_{k,fit} - F_{k,fit}(0)}{F_{k,fit}(\infty) - F_{k,fit}(0)} \right]$$

$$F_{k,fit}(t) = vK^{-v}\Gamma(v)\chi(2K,2v)$$

$$v = (1 + 2t/\tau_d)^{-1}$$

K is the solution for $F_k(0) = F_{k,BP}K^{-1}(1 - \exp(-K))$

$\Gamma(v)$ is the gamma distribution

$\chi(2K,2v)$ chi-square probability distribution with $2K$ degrees of freedom at $2v$.

The diffusion coefficient can be solved for according to $D = R^2/4\tau_d$, where R is roughly 6 μm in our setup and corresponds to the laser radius at e^{-2} height. Example FRAP images are provided elsewhere[15]. A sample FRAP recovery curve is shown in Figures S8, and the diffusion coefficient (D) and fraction of lipids that are mobile (or mobile fraction, M_f) are shown in Table S1. Note that the mobile fractions and diffusion coefficients are reported for the R18 dye, not the glycolipids themselves. However, the mobility of R18 in lipids is a good indicator for the mobility of lipids and glycolipids. Dye-labeled G_{M1} has already been shown to be mobile with a diffusivity of 0.77 $\mu m^2/s$ [68]. These results also suggest stationary viruses seen in our SPT videos are more likely to be held in place due to multivalent binding as opposed to binding to immobile glycolipids.

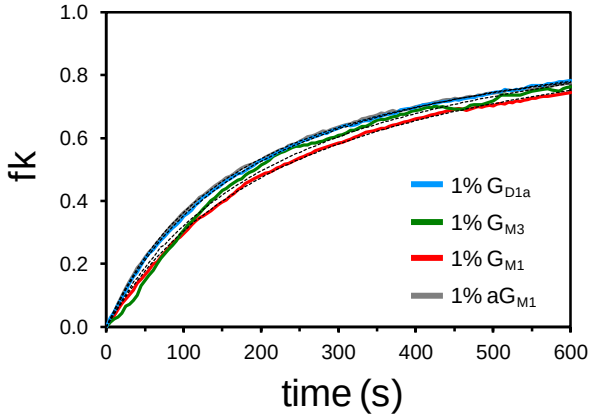

Figure S8 Example set of FRAP recovery curves. Black dotted lines are the fits for the recovery curve.

Table S1 Diffusion coefficient and mobile fractions of bilayers. R18 = octadecyl rhodamine B. Alexa-G_{M1} is a G_{M1} molecule with a fluorescent Alexa 594 probe conjugated to the sugar groups.

Bilayer			Fluorescent Probe	Diff. Coef. ($\mu m^2/s$)	Mobile Fraction
1% aG_{M1}	2% POPG	97% POPC	R18	0.40±0.12	0.97±0.06
1% G_{M1}	1% POPG	98% POPC	R18	0.31±0.06	1.04±0.03
1% G_{M3}	1% POPG	98% POPC	R18	0.28±0.01	1.07±0.04
1% G_{D1a}	0% POPG	99% POPC	R18	0.36±0.03	1.04±0.02
†1% G_{M1}	70%POPC	29% Other Lipids	Alexa594-G_{M1}	0.77	N/A

†Data from Supplemental Materials of work by L. Chao and S. Daniel[68].

REFERENCES

1. Bally, M., A. Gunnarsson, L. Svensson, G. Larson, V.P. Zhdanov, and F. Höök, *Interaction of single viruslike particles with vesicles containing glycosphingolipids.* Physical Review Letters, 2011. **107**(18): p. 188103.
2. Bally, M., K. Dimitrievski, G. Larson, V.P. Zhdanov, and F. Höök, *Interaction of virions with membrane glycolipids.* PHYSICAL BIOLOGY, 2012. **9**(2): p. 026011.
3. Bally, M., M. Graule, F. Parra, G. Larson, and F. Höök, *A virus biosensor with single virus-particle sensitivity based on fluorescent vesicle labels and equilibrium fluctuation analysis.* Biointerphases, 2013. **8**(1): p. 4.
4. Kukura, P., H. Ewers, C. Muller, A. Renn, A. Helenius, and V. Sandoghdar, *High-speed nanoscopic tracking of the position and orientation of a single virus.* Nat Meth, 2009. **6**(12): p. 923-927.
5. Szklarczyk, O.M., N. González-Segredo, P. Kukura, A. Oppenheim, D. Choquet, V. Sandoghdar, A. Helenius, I.F. Sbalzarini, and H. Ewers, *Receptor concentration and diffusivity control multivalent binding of Sv40 to membrane bilayers.* PLOS COMPUTATIONAL BIOLOGY, 2013. **9**(11): p. e1003310.
6. Hayden, O., R. Bindeus, C. Haderspöck, K.-J. Mann, B. Wirl, and F.L. Dickert, *Mass-sensitive detection of cells, viruses and enzymes with artificial receptors.* Sensors and Actuators B: Chemical, 2003. **91**(1): p. 316-319.

7. Hidari, K., S. Shimada, Y. Suzuki, and T. Suzuki, *Binding kinetics of influenza viruses to sialic acid-containing carbohydrates.* Glycoconjugate Journal, 2007. **24**(9): p. 583-590.
8. Floyd, D.L., J.R. Ragains, J.J. Skehel, S.C. Harrison, and A.M. van Oijen, *Single-particle kinetics of influenza virus membrane fusion.* Proceedings of the National Academy of Sciences, 2008. **105**(40): p. 15382-15387.
9. Castellana, E.T. and P.S. Cremer, *Solid supported lipid bilayers: From biophysical studies to sensor design.* Surface Science Reports, 2006. **61**(10): p. 429-444.
10. Wagner, M.L. and L.K. Tamm, *Tethered Polymer-Supported Planar Lipid Bilayers for Reconstitution of Integral Membrane Proteins: Silane-Polyethyleneglycol-Lipid as a Cushion and Covalent Linker.* Biophysical Journal, 2000. **79**(3): p. 1400-1414.
11. Richards, M.J., C.-Y. Hsia, R.R. Singh, S.H. Haider, J.M. Kumpf, T. Kawate, and S. Daniel, *Membrane protein mobility and orientation preserved in supported bilayers created directly from cell plasma membrane blebs.* Langmuir, 2016.
12. Ivanovic, T., J.L. Choi, S.P. Whelan, A.M. van Oijen, and S.C. Harrison, *Influenza-virus membrane fusion by cooperative fold-back of stochastically induced hemagglutinin intermediates.* eLife, 2013. **2**: p. e00333.
13. Wessels, L., M.W. Elting, D. Scimeca, and K. Weninger, *Rapid Membrane Fusion of Individual Virus Particles with Supported Lipid Bilayers.* Biophysical Journal, 2007. **93**(2): p. 526-538.
14. Costello, D.A., D.W. Lee, J. Drewes, K.A. Vasquez, K. Kisler, U. Wiesner, L. Pollack, G.R. Whittaker, and S. Daniel, *Influenza virus-membrane fusion triggered by proton uncaging for single particle studies of fusion kinetics.* Analytical Chemistry, 2012. **84**(20): p. 8480-8489.
15. Lee, D., V. Thapar, P. Clancy, and S. Daniel, *Stochastic fusion simulations and experiments suggest passive and active roles of hemagglutinin during membrane fusion.* BIOPHYSICAL JOURNAL, 2014. **106**(4): p. 843-854.
16. Endesfelder, U. and M. Heilemann, *Art and artifacts in single-molecule localization microscopy: Beyond attractive images.* NATURE METHODS, 2014. **11**(3): p. 235-238.
17. Rowland, D.J. and J.S. Biteen, *Top-Hat and Asymmetric Gaussian-Based Fitting Functions for Quantifying Directional Single-Molecule Motion.* CHEMPHYSCHEM, 2014. **15**(4): p. 712-720.
18. Cheezum, M.K., W.F. Walker, and W.H. Guilford, *Quantitative Comparison of Algorithms for Tracking Single Fluorescent Particles.* BIOPHYSICAL JOURNAL, 2001. **81**(4): p. 2378-2388.
19. Small, A. and S. Stahlheber, *Fluorophore localization algorithms for super-resolution microscopy.* Nat Meth, 2014. **11**(3): p. 267-279.
20. Mortensen, K.I., L.S. Churchman, J.A. Spudich, and H. Flyvbjerg, *Optimized localization analysis for single-molecule tracking and super-resolution microscopy.* Nature Methods, 2010. **7**(5): p. 377-381.
21. Sbalzarini, I.F. and P. Koumoutsakos, *Feature point tracking and trajectory analysis for video imaging in cell biology.* Journal of Structural Biology, 2005. **151**(2): p. 182-195.
22. Rolfe, D., C. McLachlan, M. Hirsch, S. Needham, C. Tynan, S.D. Webb, M. Martin-Fernandez, and M. Hobson, *Automated multidimensional single molecule fluorescence microscopy feature detection and tracking.* European Biophysics Journal, 2011. **40**(10): p. 1167-1186.
23. Smith, Matthew B., E. Karatekin, A. Gohlke, H. Mizuno, N. Watanabe, and D. Vavylonis, *Interactive, Computer-Assisted Tracking of Speckle Trajectories in Fluorescence Microscopy: Application to Actin Polymerization and Membrane Fusion.* Biophysical Journal, 2011. **101**(7): p. 1794-1804.
24. Jaqaman, K. and G. Danuser, *Computational Image Analysis of Cellular Dynamics: A Case Study Based on Particle Tracking.* Cold Spring Harbor Protocols, 2009. **2009**(12): p. pdb.top65.

25. Jaqaman, K., D. Loerke, M. Mettlen, H. Kuwata, S. Grinstein, S.L. Schmid, and G. Danuser, *Robust single-particle tracking in live-cell time-lapse sequences.* NATURE METHODS, 2008. **5**(8): p. 695-702.
26. Bonneau, S., M. Dahan, and L.D. Cohen, *Single quantum dot tracking based on perceptual Grouping using minimal paths in a spatiotemporal volume.* IEEE Transactions on Image Processing, 2005. **14**(9): p. 1384-1395.
27. Dupont, A., K. Stirnnagel, D. Lindemann, and D. Lamb, *Tracking image correlation: Combining single-particle tracking and image correlation.* Biophysical Journal, 2013. **104**(11): p. 2373-2382.
28. Woll, D., C. Kolbl, B. Stempfle, and A. Karrenbauer, *A novel method for automatic single molecule tracking of blinking molecules at low intensities.* Physical Chemistry Chemical Physics, 2013. **15**(17): p. 6196-6205.
29. Sage, D., F.R. Neumann, F. Hediger, S.M. Gasser, and M. Unser, *Automatic tracking of individual fluorescence particles: application to the study of chromosome dynamics.* IEEE Transactions on Image Processing, 2005. **14**(9): p. 1372-1383.
30. Balasubramanian, S., S. Kalishwaran, R. Muthuraj, D. Ebenezer, and V. Jayaraj. *An efficient non-linear cascade filtering algorithm for removal of high density salt and pepper noise in image and video sequence*. in *International Conference on Control, Automation, Communication and Energy Conservation, INCACEC 2009.* 2009.
31. Xu, Y., J.B. Weaver, D.M. Healy, Jr., and J. Lu, *Wavelet transform domain filters: a spatially selective noise filtration technique.* IEEE Transactions on Image Processing, 1994. **3**(6): p. 747-758.
32. Esakkirajan, S., T. Veerakumar, A.N. Subramanyam, and C.H. PremChand, *Removal of High Density Salt and Pepper Noise Through Modified Decision Based Unsymmetric Trimmed Median Filter.* IEEE Signal Processing Letters, 2011. **18**(5): p. 287-290.
33. Rudin, L.I., S. Osher, and E. Fatemi, *Nonlinear total variation based noise removal algorithms.* Physica D: Nonlinear Phenomena, 1992. **60**(1–4): p. 259-268.
34. Costello, D.A., C.-Y. Hsia, J.K. Millet, T. Porri, and S. Daniel, *Membrane Fusion-Competent Virus-Like Proteoliposomes and Proteinaceous Supported Bilayers Made Directly from Cell Plasma Membranes.* LANGMUIR, 2013. **29**(21): p. 6409-6419.
35. Otterstrom, J. and A.M. van Oijen, *Visualization of membrane fusion, one particle at a time.* BIOCHEMISTRY, 2013. **52**(10): p. 1654-1668.
36. Ruigrok, R.W.H., P.J. Andree, R.A.M. Hooft Van Huysduynen, and J.E. Mellema, *Characterization of three highly purified influenza virus strains by electron microscopy.* Journal of General Virology, 1984. **65**(4): p. 799-802.
37. Rogers, G.N., T.J. Pritchett, J.L. Lane, and J.C. Paulson, *Differential sensitivity of human, avian, and equine influenza a viruses to a glycoprotein inhibitor of infection: Selection of receptor specific variants.* Virology, 1983. **131**(2): p. 394-408.
38. Suzuki, Y., M. Matsunaga, Y. Nagao, T. Taki, Y. Hirabayashi, and M. Matsumoto, *Ganglioside GM1b as an influenza virus receptor.* Vaccine, 1985. **3**(3): p. 201-203.
39. Suzuki, Y., T. Nakao, T. Ito, N. Watanabe, Y. Toda, X. Guiyun, T. Suzuki, T. Kobayashi, Y. Kimura, A. Yamada, K. Sugawara, H. Nishimura, F. Kitame, K. Nakamura, E. Deya, M. Kiso, and A. Hasegawa, *Structural determination of gangliosides that bind to influenza A, B, and C viruses by an improved binding assay: Strain-specific receptor epitopes in sialo-sugar chains.* Virology, 1992. **189**(1): p. 121-131.
40. Suzuki, Y., Y. Nagao, H. Kato, M. Matsumoto, K. Nerome, K. Nakajima, and E. Nobusawa, *Human influenza A virus hemagglutinin distinguishes sialyloligosaccharides in membrane-*

associated gangliosides as its receptor which mediates the adsorption and fusion processes of virus infection. Specificity for oligosaccharides and sialic acids and the sequence to which sialic acid is attached. Journal of Biological Chemistry, 1986. **261**(36): p. 17057-17061.

41. Haywood, A.M., *Virus receptors: binding, adhesion strengthening, and changes in viral structure.* Journal of Virology, 1994. **68**(1): p. 1-5.
42. Barton, E.S., J.L. Connolly, J.C. Forrest, J.D. Chappell, and T.S. Dermody, *Utilization of sialic acid as a coreceptor enhances reovirus attachment by multistep adhesion strengthening.* Journal of Biological Chemistry, 2001. **276**(3): p. 2200-2211.
43. Stettner, E., M.H. Dietrich, K. Reiss, T.S. Dermody, and T. Stehle, *Structure of serotype 1 reovirus attachment protein σ1 in complex with junctional adhesion molecule A reveals a conserved serotype-independent binding epitope.* Journal of Virology, 2015. **89**(11): p. 6136-6140.
44. Lee, D.W., A.B. Allison, K.B. Bacon, C.R. Parrish, and S. Daniel, *Single-Particle Tracking Shows that a Point Mutation in the Carnivore Parvovirus Capsid Switches Binding between Host-Specific Transferrin Receptors.* Journal of Virology, 2016. **90**(9): p. doi:10.1128/JVI.03204-15.
45. Brian, A.A. and H.M. McConnell, *Allogeneic stimulation of cytotoxic T cells by supported planar membranes.* Proceedings of the National Academy of Sciences, 1984. **81**(19): p. 6159-6163.
46. Greiff, D., H. Blumenthal, M. Chiga, and H. Pinkerton, *The Effects on Biological Materials of Freezing and Drying by Vacuum Sublimation: II. Effect on Influenza Virus.* The Journal of Experimental Medicine, 1954. **100**(1): p. 89-101.
47. Costello, D.A., G.R. Whittaker, and S. Daniel, *Variations in pH sensitivity, acid stability, and fusogenicity of three influenza virus H3 subtypes.* Journal of Virology, 2015. **89**(1): p. 350-360.
48. Lakadamyali, M., M.J. Rust, H.P. Babcock, and X. Zhuang, *Visualizing infection of individual influenza viruses.* Proceedings of the National Academy of Sciences, 2003. **100**(16): p. 9280-9285.
49. Brandenburg, B. and X. Zhuang, *Virus trafficking–learning from single-virus tracking.* Nature Reviews Microbiology, 2007. **5**(3): p. 197-208.
50. Jerri, A.J., *The Shannon sampling theorem and its various extensions and applications: A tutorial review.* Proceedings of the IEEE, 1977. **65**(11): p. 1565-1596.
51. Rust, M.J., M. Lakadamyali, F. Zhang, and X. Zhuang, *Assembly of endocytic machinery around individual influenza viruses during viral entry.* Nature Structural +ACY- Molecular Biology, 2004. **11**(6): p. 567-573.
52. Cureton, D.K., C.E. Harbison, E. Cocucci, C.R. Parrish, and T. Kirchhausen, *Limited transferrin receptor clustering allows rapid diffusion of canine parvovirus into clathrin endocytic structures.* Journal of Virology, 2012. **86**(9): p. 5330-5340.
53. Kirchhausen, T., *Clathrin.* Annual Review of Biochemistry, 2000. **69**(1): p. 699-727.
54. Karatekin, E. and J.E. Rothman, *Fusion of single proteoliposomes with planar, cushioned bilayers in microfluidic flow cells.* Nat. Protocols, 2012. **7**(5): p. 903-920.
55. Cremer, P.S. and S.G. Boxer, *Formation and Spreading of Lipid Bilayers on Planar Glass Supports.* The Journal of Physical Chemistry B, 1999. **103**(13): p. 2554-2559.
56. Richter, R.P. and A.R. Brisson, *Following the Formation of Supported Lipid Bilayers on Mica: A Study Combining AFM, QCM-D, and Ellipsometry.* Biophysical Journal, 2005. **88**(5): p. 3422-3433.

57. Seu, K.J., A.P. Pandey, F. Haque, E.A. Proctor, A.E. Ribbe, and J.S. Hovis, *Effect of Surface Treatment on Diffusion and Domain Formation in Supported Lipid Bilayers.* Biophysical Journal, 2007. **92**(7): p. 2445-2450.
58. Greenwood, R. and K. Kendall, *Selection of Suitable Dispersants for Aqueous Suspensions of Zirconia and Titania Powders using Acoustophoresis.* Journal of the European Ceramic Society, 1999. **19**(4): p. 479-488.
59. Huertas, A. and G. Medioni, *Detection of intensity changes with subpixel accuracy using Laplacian-Gaussian masks.* IEEE Transactions on Pattern Analysis and Machine Intelligence, 1986(5): p. 651-664.
60. Sauter, N.K., J.E. Hanson, G.D. Glick, J.H. Brown, R.L. Crowther, S.J. Park, J.J. Skehel, and D.C. Wiley, *Binding of influenza virus hemagglutinin to analogs of its cell-surface receptor, sialic acid: analysis by proton nuclear magnetic resonance spectroscopy and x-ray crystallography.* Biochemistry, 1992. **31**(40): p. 9609-9621.
61. Böckmann, R.A., A. Hac, T. Heimburg, and H. Grubmüller, *Effect of sodium chloride on a lipid bilayer.* BIOPHYSICAL JOURNAL, 2003. **85**(3): p. 1647-1655.
62. Takemoto, D.K., J.J. Skehel, and D.C. Wiley, *A Surface Plasmon Resonance Assay for the Binding of Influenza Virus Hemagglutinin to Its Sialic Acid Receptor.* Virology, 1996. **217**(2): p. 452-458.
63. Takahashi, T., S. Kawagishi, M. Masuda, and T. Suzuki, *Binding kinetics of sulfatide with influenza A virus hemagglutinin.* Glycoconjugate Journal, 2013. **30**(7): p. 709-716.
64. Hu, J., R. Lipowsky, and T.R. Weikl, *Binding constants of membrane-anchored receptors and ligands depend strongly on the nanoscale roughness of membranes.* Proceedings of the National Academy of Sciences, 2013. **110**(38): p. 15283-15288.
65. Sieben, C., C. Kappel, R. Zhu, A. Wozniak, C. Rankl, P. Hinterdorfer, H. Grubmüller, and A. Herrmann, *Influenza virus binds its host cell using multiple dynamic interactions.* Proceedings of the National Academy of Sciences, 2012.
66. Nieba, L., A. Krebber, and A. Plückthun, *Competition BIAcore for Measuring True Affinities: Large Differences from Values Determined from Binding Kinetics.* Analytical Biochemistry, 1996. **234**(2): p. 155-165.
67. Axelrod, D., D.E. Koppel, J. Schlessinger, E. Elson, and W.W. Webb, *Mobility measurement by analysis of fluorescence photobleaching recovery kinetics.* Biophysical Journal, 1976. **16**(9): p. 1055-1069.
68. Chao, L. and S. Daniel, *Measuring the Partitioning Kinetics of Membrane Biomolecules Using Patterned Two-Phase Coexistant Lipid Bilayers.* Journal of the American Chemical Society, 2011. **133**(39): p. 15635-15643.

CHAPTER 2: Single-particle tracking shows a point mutation in the carnivore parvovirus capsid switches binding between host-specific transferrin receptors

Donald W. Lee[a]†, Andrew B. Allison[b]†, Kaitlyn B. Bacon, Colin R. Parrish[b]*, and Susan Daniel[a]*

[a]School of Chemical and Biomolecular Engineering, Cornell University, Ithaca, New York

[b]Baker Institute for Animal Health, Department of Microbiology and Immunology, College of Veterinary Medicine, Cornell University, Ithaca, New York, USA

†Both authors contributed equally to this work.
*Corresponding authors

Reprinted with permission from Journal of Virology, Vol 90, Issue 9, Pg 4849-4853.

Received SPOTLIGHT recognition from Journal of Virology.

ABSTRACT

Determining how viruses infect new hosts via receptor-binding mechanisms is important for understanding virus emergence. We studied the binding kinetics of canine parvovirus (CPV) variants isolated from raccoons – a newly recognized CPV host – to different carnivore transferrin receptors (TfRs) using single-particle tracking. Our data suggests CPV may utilize adhesion-strengthening mechanisms during TfR binding, and that a single mutation in the viral capsid at VP2 position 300 can profoundly alter receptor binding and infectivity.

INTRODUCTION

Canine parvovirus (CPV) is a pathogen of dogs that emerged and caused a pandemic of disease in the 1970s, and is >99% identical in nucleotide sequence to feline panleukopenia virus (FPV), a parvovirus that infects cats and other carnivore hosts but not dogs [1-3].

Although the emergence of CPV has been presumed to be the result of a direct transfer of FPV or a similar virus from domestic cats to dogs, we recently demonstrated that CPV exists endemically in sylvatic cycles in North America involving a number of wild carnivore hosts, most notably raccoons [4-5]. These recent findings, along with the lack of isolation or detection of intermediate viruses between FPV and CPV from domestic animals, suggests that parvoviruses transfer frequently between domestic and wild carnivores, and that the events preceding the pandemic emergence of CPV were more complex than previously believed [6].

Although raccoons have long been known to be susceptible to FPV infection [7], they have only recently been identified as an important host for viruses that are closely related to CPV [4, 8]. While CPVs from dogs, wolves, and coyotes all contain a Gly at capsid (VP2) position 300, CPVs from raccoons contain an Asp at that position, suggesting that this mutation is important for the adaptation of CPV to raccoons and possibly other wild carnivore hosts [4, 6]. Additionally, VP2 position 300 is the most variable residue in the capsid [9-11]. Since FPV and CPV capsids can bind to the transferrin receptor type 1 (TfR), in part by involving the structural region surrounding VP2 position 300 [12], the variations observed at this position appear to be selected by the unique TfR structures of individual carnivore hosts. To examine this phenomenon and to better understand the receptor-binding mechanisms involved, we used single-particle tracking (SPT) techniques to characterize the binding of raccoon-derived CPVs, containing either a 300-Asp or 300-Gly VP2 residue, to dog and raccoon TfRs.

METHODS

Preparation of Rac118-300G and Rac118-300D viruses

The virus studied here was the prototype CPV isolated from raccoons (CPV/Raccoon/VA/118-A/07, GenBank JN867610), which contains an Asp at VP2 position 300 and cannot be propagated in dog cells [4, 6]. We refer to this virus as Rac118-300D. However, a single point mutation of the VP2 300-Asp (codon GAT) to a Gly (codon GGT) results in efficient dog cell infection, demonstrating that this capsid residue is important for determining host range [6]. The virus that contains a Gly at VP2 position 300 is referred to as Rac118-300G. For the SPT studies, both the Rac118-300G and -300D viruses were propagated and purified using methods described previously [13]. Infectious virions were extracted from a sucrose gradient, dialyzed in phosphate-buffered saline (PBS), and concentrated using a 100-kD Amicon Ultra-15 centrifugal filter unit (EMD Millipore). The viral genomes were sequenced to confirm that no additional VP1/VP2 capsid mutations had occurred during propagation. The purified particles were labeled with Alexa Fluor 594 succinimidyl ester (Invitrogen) according to manufacturer's instructions, and unbound Alexa dye was removed using Sephadex G-25 PD-10 columns (GE Healthcare Life Sciences). The Alexa dye labeling does not appear to affect the ability of the virus to bind and enter cells based on previous studies [13], and the Asp and Gly residues do not contain free reactive amine groups for dye conjugation.

Preparation of raccoon and dog TfRs

The raccoon and dog TfR ectodomains were expressed as previously described [13-14]. Briefly, the cDNA sequence of each TfR ectodomain was cloned into a pFastBac construct containing an N-terminal hexa-histidine (6 × His) tag and an enhanced green

fluorescent protein (eGFP) fused to its C-terminus. The pFastBac TfR-eGFP constructs were expressed in High Five cells (Life Technologies) using the Bac-to-Bac Baculovirus Expression System (Invitrogen). TfRs were purified by binding to Ni-nitrilotriacetic acid (Ni-NTA) Superflow resin (Qiagen) and eluted with 100 mM imidazole using an ÄTKA fast-performance liquid chromatography system (GE Healthcare Life Sciences). TfRs were dialyzed overnight in PBS, and concentrated using a 10-kD Amicon Ultra-15 centrifugal filter unit (EMD Millipore).

SLB formulation and SPT binding assay setup

Purified TfR-eGFP was loaded on top of a supported lipid bilayer (SLB), formed inside a microfluidic device as described elsewhere [15-16]. A detailed schematic view of the SPT experimental setup is shown in Figure 1. Lipid vesicles that are needed to form SLBs were produced by mixing 1% 1,2-dioleoyl-sn-glycero-3-[(N-(5-amino-1-carboxypentyl)iminodiacetic acid)succinyl] nickel salt (DGS-NTA) and 99% 1-palmitoyl-2-oleoyl-sn-glycero-3-phosphocholine (POPC) (Avanti Polar Lipids) in chloroform, drying them in vacuum, and rehydrating them in MES buffer (1mM 2-(N-morpholino)ethanesulfonic acid, 150 mM NaCl, pH 7.00) such that the final vesicle concentration was 1 mg/ml. Lipids were extruded using 50-nm pore filters (Whatman) to create ~100-nm diameter vesicles. The vesicles were loaded into the microfluidic channel to spontaneously form supported lipid bilayers (SLBs) via the vesicle-rupture method [17]. After 4 h, excess vesicles were rinsed away with MES buffer. Subsequent SPT experiments were performed at 25°C.

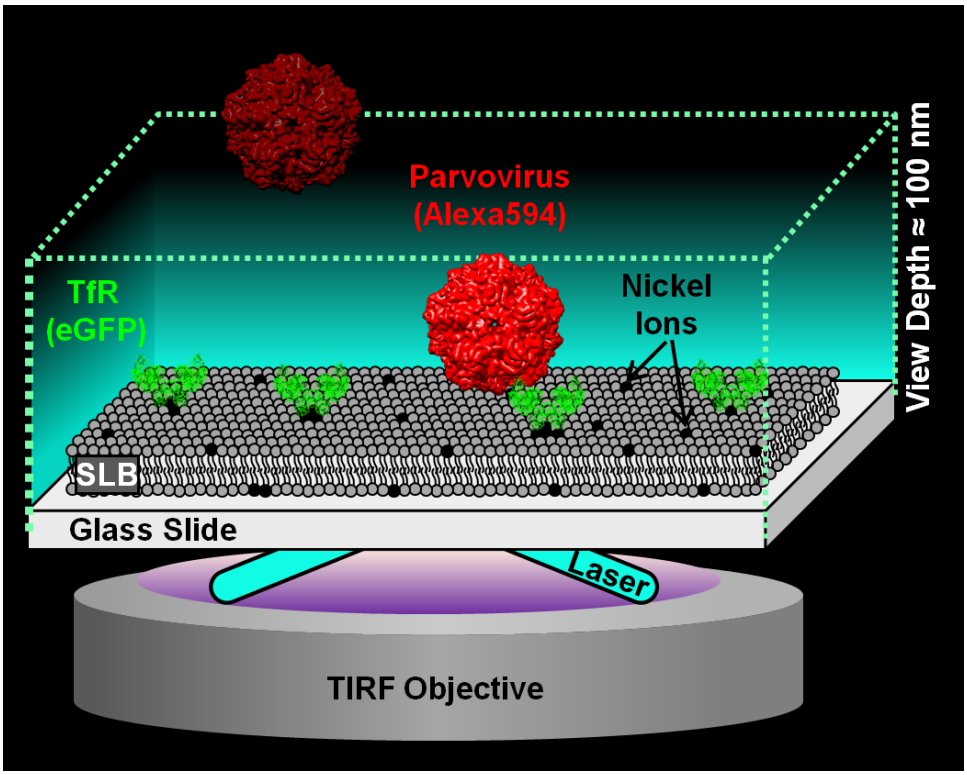

Figure 1 Schematic of the single particle tracking (SPT) binding assay. The device was set up on a 100×, 1.46 numerical aperture, oil-immersion objective in a total internal reflection fluorescence (TIRF) microscope (Carl Zeiss, Model Axio Observer Z1). The TIRF microscope used here produces an evanescent wave that illuminates only a 100-nm deep region away from the glass surface, which is where the virus-TfR binding interaction occurs, thus ignoring virus particles floating in the bulk solution. The eGFP-labeled TfRs are tethered to the supported lipid bilayer (SLB) via nickel-His interactions. The Alexa 594-labeled virus is detected with a 561-nm laser, whereas the eGFP-labeled TfR is detected using a 488-nm laser. The CPV structure is from VIPERdB based on PDB ID: 1P5W. The TfR structure is from PDB ID: 1CX8. Note the CPV and TfR structures are only used for illustrative purposes and deviate from the virus capsid and receptor structures used in this work.

SPT binding experiment procedure

The relative concentrations of Rac118-300D and -300G were determined by nonspecifically adsorbing them directly onto a glass surface for 30 min. Images of the glass-adsorbed viruses were taken when the virus density, V_{glass}, remained fairly constant (Figure 2A). In a separate microfluidic channel containing only the SLBs, viruses were loaded to check for nonspecific binding levels, which was negligible (Figure 2B). Unbound viruses were rinsed away and His-tagged dog or raccoon TfRs were loaded into the channels to bind to the DGS-NTA lipids containing nickel ions. Unbound TfRs were rinsed away and images were taken to determine the TfR location and density, R_{TfR} (Figure 2C). Without changing the

field of view, either Rac118-300D or -300G virus was loaded onto the SLB. As soon as the flow stopped, images were acquired at 500 ms intervals for 10 min (Figure 2D). Using a custom image processing software made in MATLAB (Mathworks), the binding on and off times of the viruses were tracked throughout the movie.

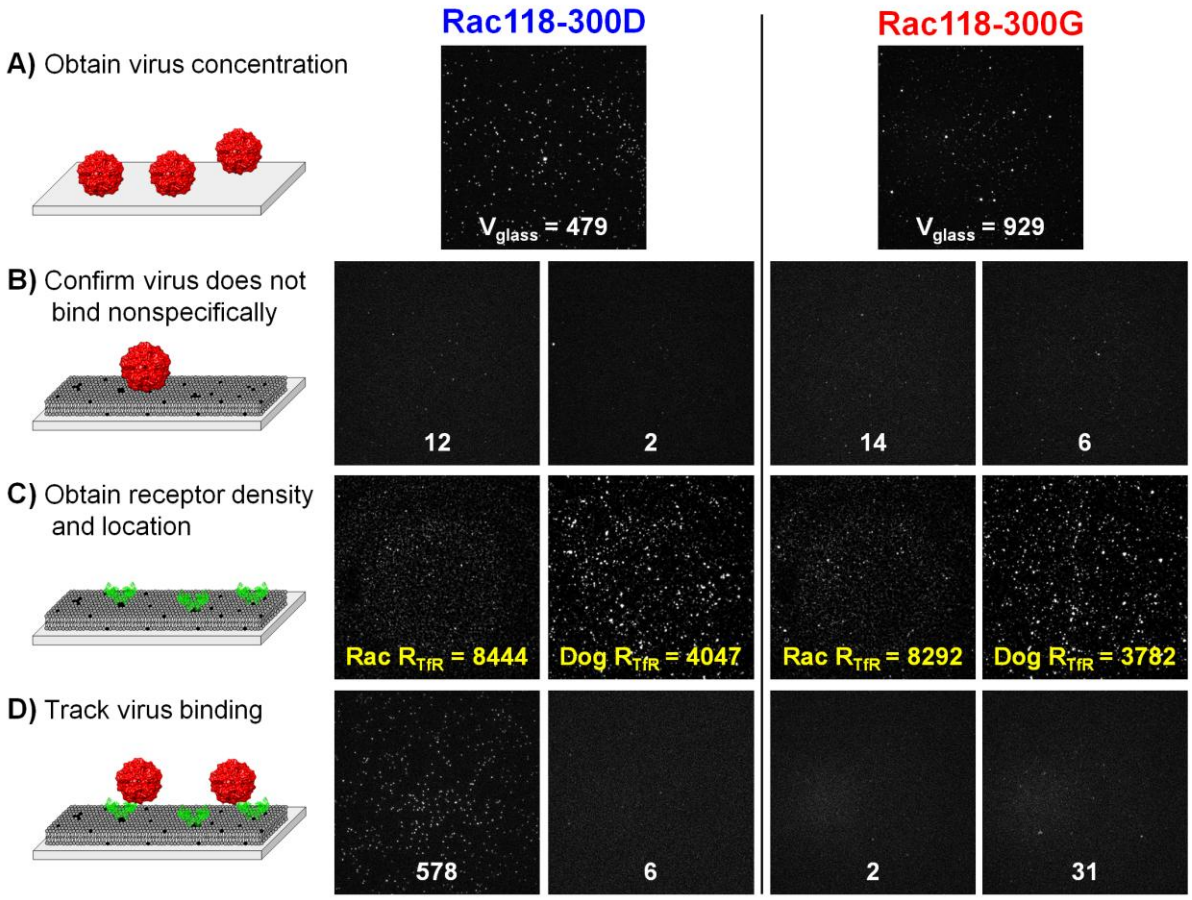

Figure 2 Images of the TfR-parvovirus binding experiments at different stages. (A) Images of the Alexa 594-labeled virus adsorbing to glass after 30 min of incubation. White numbers are the particle counts, P_{count}. In this panel, $P_{count} = V_{glass}$, which is used to quantify the relative virus concentrations between virus batches. P_{count} is shown instead of N or N_+ because P_{count} is insensitive to the binding event criteria. (B) Images of SLBs incubated with virus after a 10 min waiting period. Negligible binding events here indicate the viruses do not readily bind to the SLBs and the SLBs have no defects exposing the glass surface. (C) Images of the eGFP-labeled TfR attached to the SLBs, prior to loading the virus. Yellow numbers are the TfR particle counts, R_{TfR}. (D) Images of parvovirus binding to TfR-loaded SLBs after 10 min. [Image details: Each image portrays an 82 x 82 μm^2 physical space in 512 x 512 pixels. Uneven backgrounds were subtracted out and all image intensities were linearly scaled, which preserves particle features.]

Determination of binding events from SPT videos

Since binding events are extracted via visual cues from the video, we next filtered out ambiguous binding events, such as floating virions or false particles (bright pixels from shot

noise that resemble particles), by setting several criteria. Based on a manual inspection of final particle tracking results, a majority of ambiguous binding events lasted at most 5 frames; hence to remove these from the analysis, we impose a criterion that binding events must last longer than the cutoff time of 5 frames (or 2.5 s). The cutoff time is much shorter than the lifetime of a clathrin-coated pit (~2 min) that the virus is endocytosed into after receptor binding [13]; thus, binding events that are relevant for infection are still captured. Note that changing the cutoff time or camera rate will ultimately affect the number of binding events observed and binding data, and therefore it was important that we kept those settings the same across all trials. Additionally, only immobile particles that were colocalized with a TfR particle were tracked because the TfRs were also immobile (likely due to multiple His residues binding to DGS-NTA lipids), and immobility served as a strong visual cue for authentic virus-TfR contacts. In the cell membrane however, the TfR is not static and this mobility could affect viral binding avidity via the formation of multiple TfR contacts [13]. The immobile TFRs in our SPT setup enable us to directly study 1:1 binding that would otherwise be challenging to do with cell membranes, which helps in understanding how relevant binding avidity is for infection.

RESULTS

Explanation of variables and normalization of binding data

Before describing the kinetic data, we introduce several variables: (i) N is the number of binding events, (ii) N_+ (or N_-) is the accumulated number of binding (or unbinding) events, and (iii) P_{count} is the number of particles in an image. Note that P_{count} is not the same as N because some particles do not last long enough to meet the criteria for a binding event, hence $N \leq P_{count}$. We also have two time variables: (i) t for time, and (ii) t_{res} for binding residence

time of virus to receptors. Lastly, both N and N_+ were normalized by dividing them by virus density (V_{glass}) and TfR density (R_{TfR}), which enables a fair comparison of kinetic data across the different samples. Instead of using V_{glass} as a normalization factor, using the actual concentration of visible virus in the bulk solution, V_{bulk}, would also suffice. However, V_{bulk} is difficult to obtain directly. A calibration curve between V_{glass} and dilutions of V_{bulk} shows a linear relation (Figure 3A); hence V_{bulk} can be substituted by V_{glass} for normalization purposes.

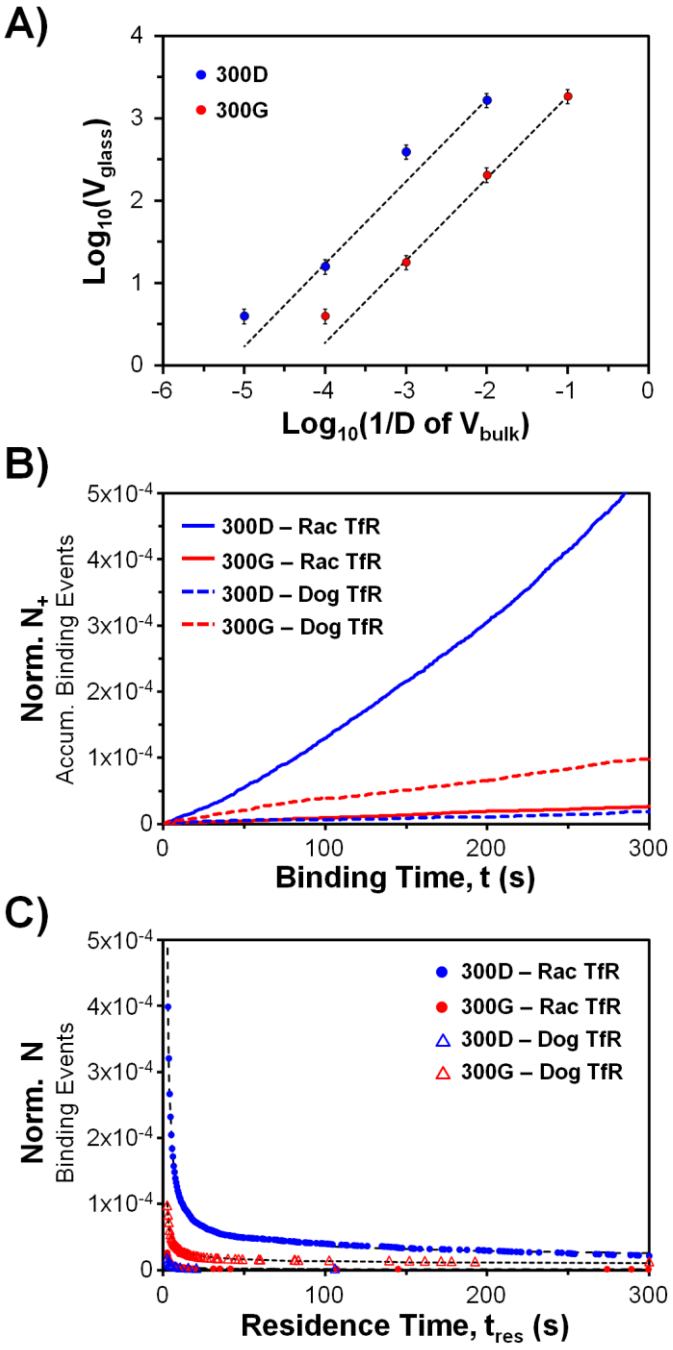

Figure 3 Kinetics of virus binding to raccoon or domestic dog TfR-loaded SLBs. A) Calibration curve to show the linear relationship between V_{glass} and V_{bulk}. We measured V_{glass} at several dilutions factors, D, of V_{bulk} for the Rac118-300D and -300G stock viruses. The dotted fit lines ($y = mx$) have R^2 values greater than 0.98. The m parameters for 300D and 300G virus are 169250 and 18660, respectively. (B) Normalized binding rate data. $R_{on,norm}$ is calculated using the linear fit of the data (Norm $N_+ = R_{on,norm}t$). $R_{on,norm}$, in the order of the legend, are (1.6±0.2) x 10^{-6} s^{-1}, (9.1±1.3) x 10^{-8} s^{-1}, (5.9±0.9) x 10^{-8} s^{-1}, and (3.4±0.5) x 10^{-7} s^{-1}. The R^2 values for linear fits are >0.98 for all cases. The error ranges were calculated via propagation of worst-case 10% errors in each V_{glass} and R_{TfR} due to particle detection software limitations. The true error is expected to be less since errors are corrected manually. (C) Normalized binding residence time distributions. The plot shows how many binding events, N, last longer than a certain residence time, t_{res}. The data are fitted according to EQN 2 (dotted lines), but in normalized form. The fit parameters (with 95% confidence intervals) and the number of binding events included in each distribution (N_{be}), in the order of the legend, are [A = 1.66±0.01, B = 7.52±0.01, N_{be} = 2151], [A = 1.91±0.07, B = 5.20±0.03, N_{be} = 203], [A = 1.57±0.19, B = 3.39±0.07, N_{be} = 36], and [A = 1.27±0.03, B = 5.77±0.02, N_{be} = 345]. The R^2 values for EQN 2 fits are >0.97 for all cases.

Analysis of parvovirus binding rates

The binding frequency rate data are shown in Figure 3B, with the normalized N_+ on the Y-axis, and the time (t) on the X-axis. The slope of the plots is referred to as normalized binding frequency rate, $R_{on,norm}$ (EQN 1). Rac118-300D binds ~18 times more frequently than Rac118-300G to the raccoon TfR. Conversely, Rac118-300G binds ~5.7 times more frequently than Rac118-300D to the dog TfR. However, the binding rate of Rac118-300G with the dog TfR is ~80% lower than that of Rac118-300D with the raccoon TfR. This is not an unexpected result as previous studies have shown that a number of different CPV variants bind to very low levels to the dog TfR relative to the TfRs of other carnivore hosts [4, 14], possibly owing to unique protein structure and/or glycosylation profile of the dog TfR [11].

EQN 1 $$R_{on,norm} = \frac{R_{on}}{V_{glass} R_{TfR}} = \frac{1}{V_{glass} R_{TfR}} \frac{dN_+}{dt}$$

Analysis of parvovirus binding residence time distributions

We next analyzed the binding residence time distribution, which reflects the binding strength of the parvovirus capsid to the TfR. Biased binding events were removed using a criteria as described elsewhere [18]. Briefly, binding events that started since the 1st frame of the movie and those that started after halfway through the movie were discarded due to the inability to determine actual binding times and oversampling of short binding events, respectively. Hence, t_{res} can only be plotted up to half the movie time. The residence time distribution was plotted as N vs t_{res} (Figure 3C), which shows how many binding events last longer than a certain t_{res} time. The unbinding curves do not fit to the standard 1:1 binding model, suggesting a more complex interaction is involved. A different empirical fit equation (EQN 2) was determined by testing various log-log plots. Relating EQN 2 to the standard

dissociation equation $dN/dt_{res} = -k_{off}N$ yields EQN 3 for k_{off}, which is not a constant and varies with t_{res}.

EQN 2 $$N(t_{res}) = \exp(B)\left(\ln\frac{t_{res}}{1s}\right)^{-A}$$ where $t_{res} \geq$ binding event cutoff time (2.5 s).

EQN 3 $$k_{off}(t_{res}) = \frac{A}{t_{res}\ln\frac{t_{res}}{1s}}$$ where $t_{res} \geq$ binding event cutoff time (2.5 s).

The decreasing value of k_{off} with respect to t_{res} (EQN 3) would imply a mechanism for the virus to increase its binding strength to the receptor with longer contact times, a phenomenon generally referred to as adhesion-strengthening [19-21]. Adhesion-strengthening can occur either via multivalent binding, co-receptor binding, or conformation changes occurring to the viral protein upon ligand binding. Multivalent binding is unlikely to occur in our SPT setup because (i) TfRs are spaced greater than 1 camera pixel (160 nm) apart, whereas the virus is only 26 nm in diameter, (ii) the TfRs are immobile and do not diffuse laterally to create multiple bonds, (iii) the planar SLB geometry restricts binding of TfR to one side of the virus, and (iv) TfRs may sterically hinder each other's access to the same virus. Whether the multivalent binding that may occur *in vivo* is a prerequisite for infection is unknown, but rather it may be a byproduct of mobile TfRs clustering around a virus that is already strongly bound to a single TfR. However, CPV does not seem to undergo significant multivalent binding, as it appears the engagement of the virus with TfR may potentially prevent additional binding events from occurring, although the mechanism involved is unknown [12].

A more plausible explanation for the increasing binding strength over time is that there is a complex mechanism of binding of parvovirus to the TfR [12], such that upon receptor binding, the virus capsid and/or TfR changes conformation that results in tighter binding. Our mathematical fit model and raw data agrees with, but does not definitively confirm, adhesion-strengthening via conformation changes that may occur when a virus binds to single TfR. Additional work is needed to confirm and potentially identify the changes to the parvovirus or TfR structure that occur as a direct result of receptor binding.

Comparison of SPT data with cell infection data

To determine if the SPT results agree with cell infection data, relative infectivity studies using raccoon uterine (Pl1Ut; ATCC CCL-74) and domestic dog (A72; ATCC CRL-1542) tumor cells were performed using similar procedures as described elsewhere [6, 11]. Briefly, cells were seeded at a density of ~1 x 10^5 cells/ml in a 1.9-cm^2-well format, and inoculated with a multiplicity of infection of 0.4 50% tissue culture infective dose ($TCID_{50}$) per cell of either Rac118-300D or -300G. At 72 h post-infection, cells were fixed in 10% formalin, triple-washed with PBS, and incubated with a polyclonal rabbit anti-CPV VP1/VP2 antibody in permeabilization buffer (1X PBS, 0.5% bovine serum albumin, 0.5% Triton X-100) for 1 h. The wash step was repeated and cells were incubated with a secondary Alexa Fluor 488-goat anti-rabbit IgG (H+L) antibody (Life Technologies) for 1 h, followed by a final wash in PBS. Immunofluorescence was detected using a Nikon Eclipse TE300 inverted fluorescence microscope equipped with a Hamamatsu OrcaER digital camera (Nikon Corporation). As shown in Figure 4, there was substantial reduction in the number of infected raccoon cells with Rac118-300G when compared to Rac118-300D, whereas a reverse trend was observed with dog cells, as there was a >95% decrease in the number of infected cells with Rac118-

300D in comparison to Rac118-300G. Thus, both the SPT and infectivity data confirm that although the Asp-to-Gly change at VP2 position 300 enabled the prototype raccoon-derived CPV to bind to the dog TfR and to also efficiently infect dog cells when that virus previously could not, the process of dog adaptation also reduced the virus' ability to bind to the raccoon TfR and to infect raccoon cells. These results not only further demonstrate the importance of this single capsid residue in host switching [11], but show that in this particular case, viral adaptation to a new host (dog) simultaneously led to the loss in the ability to efficiently infect the previous host of isolation (raccoon). Additionally, the unbinding kinetic data suggests these parvoviruses may increase their binding strength during prolonged contact with their receptors, which may alter infectivity, and preliminary studies using biolayer interferometry approaches have also shown similar dissociation kinetics (unpublished data).

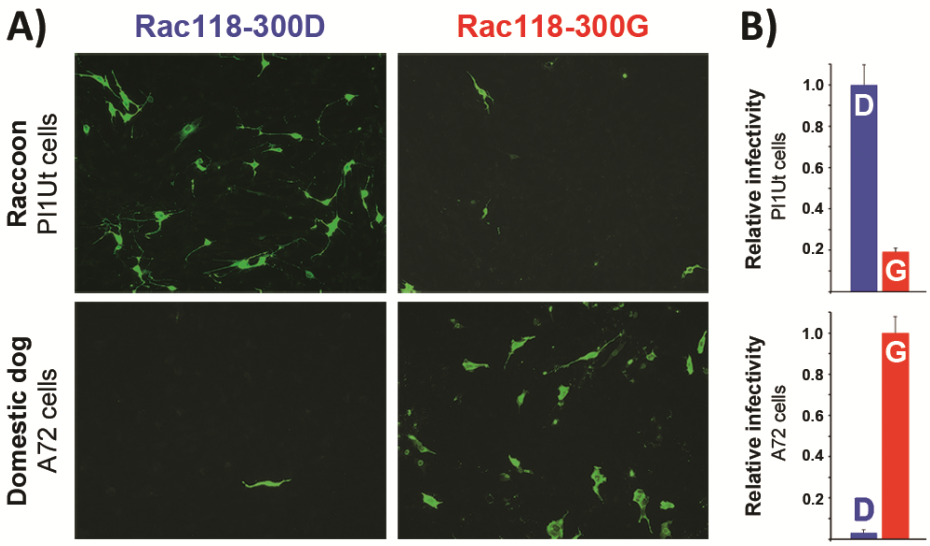

Figure 4 Relative infectivity of domestic dog and raccoon cells to Rac118-300D and -300G. (A). Dog (A72) and raccoon (Pl1Ut) cells were infected with equivalent amounts of Rac118-300D or -300G and fixed, stained, and analyzed by immunofluorescence at 72 h post-infection using a polyclonal rabbit anti-CPV VP1/VP2 antibody and a goat anti-rabbit Alexa Fluor 488 secondary. (B) For relative infectivity estimates, Alexa Fluor 488-positive cells were visually counted and the number of infected cells seen with the normal VP2 position 300 mutation associated with each host (i.e., Asp in raccoons, Gly in dogs) was set to 1.0. Error bars indicate standard deviations for duplicate experiments.

CONCLUSION

As the platform of the SPT binding assay illustrated here allows for the examination of a variety of TfR–parvovirus combinations along with their complex receptor-binding behaviors, future work will be aimed at applying this binding model to examine the virus unbinding kinetic data obtained from other assays, and determining how single or multiple capsid or receptor mutations affect binding to the TfRs from other carnivore hosts. Such studies will give a better understanding of how viruses successfully cross species barriers to infect novel hosts.

ACKNOWLEDGEMENTS

This work was performed in part at the Cornell NanoScale Facility, a member of the National Nanotechnology Infrastructure Network supported by the National Science Foundation (NSF) (grant ECCS-0335765).

FUNDING

Research was funded by NSF grant CBET-1263701 to SD and National Institutes of Health (NIH) grants RO1 GM8496821 and RO1 AI092571 to CRP. ABA is supported by a NRSA post-doctoral fellowship from the National Institute of Allergy and Infectious Diseases, NIH (F32AI100545). DWL acknowledges financial support from NSF GK12 programs, award number DGE-1045513 to Cornell's Grass Roots program and award number DGE-0841291 to Cornell's Learning Initiative for Medicine and Bioengineering (CLIMB) program. KBB acknowledges the funding from Cornell Engineering Learning Initiative (ELI), with donations from Genentech and Proctor & Gamble. All funders had no roles in the

study design, data collection and interpretation, and decision to submit the work for publication.

REFERENCES

1. Parrish, C.R., P.H. O'Connell, J.F. Evermann, and L.E. Carmichael, *Natural variation of canine parvovirus.* SCIENCE, 1985. **230**(4729): p. 1046-1048.
2. Parrish, C.R., P. Have, W.J. Foreyt, J.F. Evermann, M. Senda, and L.E. Carmichael, *The global spread and replacement of canine parvovirus strains.* J. Gen. Virol, 1988. **69**(Pt 5): p. 1111-1116.
3. Chang, S., J. Sgro, and C. Parrish, *Multiple amino acids in the capsid structure of canine parvovirus coordinately determine the canine host range and specific antigenic and hemagglutination properties.* Journal of Virology, 1992. **66**(12): p. 6858-6867.
4. Allison, A.B., C.E. Harbison, I. Pagan, K.M. Stucker, J.T. Kaelber, J.D. Brown, M.G. Ruder, M.K. Keel, E.J. Dubovi, and E.C. Holmes, *Role of multiple hosts in the cross-species transmission and emergence of a pandemic parvovirus.* JOURNAL OF VIROLOGY, 2012. **86**(2): p. 865-872.
5. Allison, A.B., D.J. Kohler, K.A. Fox, J.D. Brown, R.W. Gerhold, V.I. Shearn-Bochsler, E.J. Dubovi, C.R. Parrish, and E.C. Holmes, *Frequent cross-species transmission of parvoviruses among diverse carnivore hosts.* JOURNAL OF VIROLOGY, 2013. **87**(4): p. 2342-2347.
6. Allison, A.B., D.J. Kohler, A. Ortega, E.A. Hoover, D.M. Grove, E.C. Holmes, and C.R. Parrish, *Host-specific parvovirus evolution in nature is recapitulated by in vitro adaptation to different carnivore species.* PLOS PATHOGENS, 2014. **10**(11): p. e1004475.
7. Barker, I.K. and C.R. Parrish, *Parvovirus infections.* Infectious Diseases of Wild Mammals, Third Edition, 2001: p. 131-146.
8. Kapil, S., G. Rezabek, B. Germany, and L. Johnston, *Isolation of a virus related to canine parvovirus type 2 from a raccoon (Procyon lotor).* VETERINARY RECORD, 2010. **166**(1): p. 24-25.
9. Qin, Q., I.K. Loeffler, M. Li, K. Tian, and F. Wei, *Sequence analysis of a canine parvovirus isolated from a red panda (Ailurus fulgens) in China.* VIRUS GENES, 2007. **34**(3): p. 299-302.
10. Xiao-Ying, C., X. Zhi-Jing, Z. Zhong-Peng, J. Shi-Jin, Z. Hong-Kun, Z. Yan-Li, and Z. Xing-Xiao, *Genetic diversity of parvovirus isolates from dogs and wild animals in China.* JOURNAL OF WILDLIFE DISEASES, 2011. **47**(4): p. 1036-1039.
11. Allison, A.B., L. Organtini, S. Zhang, S.L. Hafenstein, E.C. Holmes, and C.R. Parrish, *Single mutations in the VP2 300 loop region of the three-fold spike of the carnivore parvovirus capsid can determine host range.* JOURNAL OF VIROLOGY, 2015. **JVI.02636-15**.
12. Hafenstein, S., L.M. Palermo, V.A. Kostyuchenko, C. Xiao, M.C. Morais, C.D.S. Nelson, V.D. Bowman, A.J. Battisti, P.R. Chipman, C.R. Parrish, and M.G. Rossmann, *Asymmetric binding of transferrin receptor to parvovirus capsids.* Proceedings of the National Academy of Sciences of the United States of America, 2007. **104**(16): p. 6585-6589.
13. Cureton, D.K., C.E. Harbison, E. Cocucci, C.R. Parrish, and T. Kirchhausen, *Limited transferrin receptor clustering allows rapid diffusion of canine parvovirus into clathrin endocytic structures.* Journal of Virology, 2012. **86**(9): p. 5330-5340.
14. Palermo, L.M., S.L. Hafenstein, and C.R. Parrish, *Purified feline and canine transferrin receptors reveal complex interactions with the capsids of canine and feline parvoviruses that correspond to their host ranges.* Journal of Virology, 2006. **80**(17): p. 8482-8492.

15. Lee, D., V. Thapar, P. Clancy, and S. Daniel, *Stochastic fusion simulations and experiments suggest passive and active roles of hemagglutinin during membrane fusion.* BIOPHYSICAL JOURNAL, 2014. **106**(4): p. 843-854.
16. Costello, D.A., D.W. Lee, J. Drewes, K.A. Vasquez, K. Kisler, U. Wiesner, L. Pollack, G.R. Whittaker, and S. Daniel, *Influenza virus-membrane fusion triggered by proton uncaging for single particle studies of fusion kinetics.* Analytical Chemistry, 2012. **84**(20): p. 8480-8489.
17. Castellana, E.T. and P.S. Cremer, *Solid supported lipid bilayers: From biophysical studies to sensor design.* Surface Science Reports, 2006. **61**(10): p. 429-444.
18. Bally, M., A. Gunnarsson, L. Svensson, G. Larson, V.P. Zhdanov, and F. Höök, *Interaction of single viruslike particles with vesicles containing glycosphingolipids.* Physical Review Letters, 2011. **107**(18): p. 188103.
19. Haywood, A.M., *Virus receptors: binding, adhesion strengthening, and changes in viral structure.* Journal of Virology, 1994. **68**(1): p. 1-5.
20. Barton, E.S., J.L. Connolly, J.C. Forrest, J.D. Chappell, and T.S. Dermody, *Utilization of sialic acid as a coreceptor enhances reovirus attachment by multistep adhesion strengthening.* Journal of Biological Chemistry, 2001. **276**(3): p. 2200-2211.
21. Stettner, E., M.H. Dietrich, K. Reiss, T.S. Dermody, and T. Stehle, *Structure of serotype 1 reovirus attachment protein σ1 in complex with junctional adhesion molecule A reveals a conserved serotype-independent binding epitope.* Journal of Virology, 2015. **89**(11): p. 6136-6140.

CHAPTER 3: Stochastic fusion simulations and experiments suggest passive and active roles of hemagglutinin during membrane fusion

Donald W Lee, Vikram Thapar, Paulette Clancy, and Susan Daniel*
Chemical and Biomolecular Engineering, Cornell University, Ithaca, NY, USA, 14853
Reprinted with permission from Biophysical Journal, Vol 106, Issue 4, Pg 843-854, 2014.

ABSTRACT

Influenza enters the host cell cytoplasm by fusing the viral and host membrane together. Fusion is mediated by hemagglutinin (HA) trimers that undergo conformational change when acidified in the endosome. It is currently debated how many HA trimers, *w*, and how many conformationally-changed HA trimers, *q*, are miniFmally required for fusion. Conclusions vary because there are several different approaches for determining *w* and *q* from fusion data. One approach correlates the fusion rate with the fraction of fusogenic HA trimers and leads to the conclusion that one HA trimer is required for fusion. A second approach correlates the fusion rate with the total concentration of fusogenic HA trimers and yields that more than one HA trimer is required. A third approach applies statistical models to fusion rate data obtained at a single HA density to establish *w* or *q* and points to more than one HA trimer being required. In this work, all three approaches are investigated through stochastic fusion simulations and experiments to elucidate the roles of HA and its ability to bend the target membrane during fusion. We find that the apparent discrepancies among the results from the various approaches may be resolved if non-fusogenic HA participates in fusion through interactions with a fusogenic HA. Our results, based on H3 and H1 serotypes, suggest that

three adjacent HA trimers and one conformationally-changed HA trimer are minimally required to induce membrane fusion ($w = 3$ and $q = 1$).

INTRODUCTION

Membrane fusion is an important process that enveloped viruses such as influenza use to enter host cells. The surface of the influenza viruses contains hemagglutinin (HA) proteins that govern both the attachment of the virus to sialic acid receptors on host cells and the fusion of the viral envelope with the host membrane. The HA protein is a trimer of three monomers; this protein unit will be referred to as an HA trimer. Below a pH of 5.8 [1], HA trimers can undergo conformational changes that insert hydrophobic fusion peptides into the target membrane to initiate membrane fusion [2]. Despite extensive research on the fusion mechanism, the minimum number of HA trimers that are needed for fusion is still a matter of debate. In this work, we use simulations and experiments to resolve the possible roles of hemagglutinin in fusion.

Adopting the notation used by Bentz [3], we refer to the *minimum* number of HA trimers that are required for fusion as w, and the *minimum* number of HA trimers within the subset of w that must undergo conformational change as q. A direct way of determining w and q would be to observe distinct HA trimers inducing fusion in real time, but this is not currently possible. Therefore, w and q are extracted indirectly through the analysis of the kinetics of HA-induced membrane fusion, combined with electron micrograph (EM) images [4-7] and crystallographic data [8-10] of intermediate states of membrane fusion. The general techniques used to study membrane fusion kinetics are discussed in the following references [11-12]. The kinetic data are often collected as a distribution of lag times between the

acidification of HA trimers and the membrane fusion event, which is normally detected through the dequenching of membrane fluorophores. In past studies, different values for *w* and *q* were proposed depending on the experimental systems used to obtain the lag time distributions and the statistical models used to interpret the data. Additionally, many past studies did not assume that *w* and *q* can have different values. Generally, values of *w* or *q* greater than 1 suggest that multiple HA trimers act cooperatively to induce fusion, whereas a value of 1 suggests HA trimers do not act cooperatively to induce fusion. Past studies have provided evidence for both cooperative *and* non-cooperative behavior of HA trimers to induce fusion, which appears to be contradictory. Through simulations and analysis of prior and new kinetic data, we propose that cooperative and non-cooperative observations can be reconciled if conformationally-changed HA trimers play an active role in fusion while unchanged HA trimers play a passive role.

Variations in Approaches that have led to Different Conclusions for w and q

There are three common approaches for determining *w* and *q* using kinetic data from fusion experiments. One approach is to monitor how the fusion lag times change as the ratio between the number of fusogenic HA trimers ($HA_{1,2}$) and non-fusogenic HA trimers (HA_0) is varied, while the total HA density is kept constant. This method is referred to as the Variable F approach by Imai et al. [13] because the fusion (F) capacity of virions (or virosomes) is being varied and not their binding (B) capacity. The fusion rate, *V*, can then be extracted from the slope of the cumulative lag time distribution. Considering the fusion event as a "reaction", an n^{th}-order reaction equation such as $V = k[HA_{1,2}]^n$ could be used to correlate *V* with the number of cooperating HA trimers, *n*. Note that many past studies did not consider *w* and *q* as separate values, hence, *n* is considered as being either *w* or *q* (*n* = *w* or *q*). Most

kinetic data from the Variable F approach [13-16] support that HA trimers do not act cooperatively to induce fusion (n = 1).

Another approach is to find the correlation between fusion rate and the total concentration of HA trimers, all of which are fusogenic ($HA_{1,2}$). This method is referred to as the Variable FB approach [13] since both the fusion (F) and binding (B) capacities of virions (or virosomes) are varied. Most results from past studies that used this approach [3, 13, 17-19] show that the fusion rate scales nonlinearly with fusogenic HA density, which indicates that HA trimers act cooperatively to induce fusion (n > 1).

A third approach deduces n by analyzing the shape of the lag time distribution obtained at a constant fusogenic HA density. This method is referred to as the Constant FB approach since the fusion and binding capacities of the virions (or virosomes) are not varied, though environmental conditions such as the pH to trigger fusion can be varied. Often, statistical models with n as the fitting parameter are used to fit the expected lag time distribution to the actual distribution, which usually concludes that n is greater than 1 [3, 19-25]. Table S1 in Supporting Material provides an extended summary of related works, along with their concluded values of w or q.

The work by Imai et al. [13] demonstrates that fusion kinetics are sensitive to different approaches, despite the fact that the experimental system is otherwise the same. Imai el al.'s Variable F result suggests n is 1 while the Variable FB result suggests n is greater than 1. Since the authors did not consider that w and q can have different values, one value for n had to be chosen amongst the Variable F and FB results. They decided n = 1 according to the Variable F approach. However, we show that both of their results are consistent with each

other if we allow w and q to take different values ($w \neq q$). The interpretation that w and q are not equal is that fusion proceeds through the involvement of both conformationally-changed and unchanged HA trimers.

We present a mechanistic model and simulation strategy that can generate kinetic data showing both cooperative and non-cooperative behaviors of HA trimers in inducing fusion when w is 3 and q is 1.The results for w and q were validated using kinetic data from both Imai et al.'s and our fusion experiments, which studied the membrane fusion behavior of the H1 and H3 serotypes of HA trimers, respectively. We note here that the obtained values for w and q may not extend across other experimental systems that use different HA serotypes or fusion conditions. In addition to extracting w and q from kinetic data, our model is able to capture the dependence of fusion lag times on target membrane properties, as shown by other works [26-28]. Our model is notably different from other simulation models [19, 24-25], which do not generate kinetic data that agree with the data from all three approaches and do not explicitly consider how target membrane properties affect fusion.

METHODS: EXPERIMENT

Influenza Virus Labeling

To label the viral envelope with a fluorescent fluorophore, 5 μL of X31 A/Aichi/68 H3N2 [Charles River, Wilmington, MA] at a concentration of 2 mg/mL, 0.1 μL of 1.8 mM octadecyl rhodamine B chloride (R18) [Invitrogen, Carlsbad, CA] in ethanol, and 250 μL of MES buffer (1 mM 2-*(N*-morpholino*)*ethanesulfonic acid, 150 mM NaCl, pH 7) were mixed in a vial for 1 hour at room temperature using a water sonicator bath. Unincorporated R18 fluorophores were removed from solution using a G25 Sephadex spin column [GE Healthcare

Biosciences, Pittsburg, PA]. The filtered virus solution was diluted in MES buffer by 10-fold before use.

Target Bilayer Compositions

1,2-dioleoyl-sn-glycero-3-phosphocholine (DOPC), 1-palmitoyl-2-oleoyl-sn-glycero-3-phosphocholine (POPC), 1-stearoyl-2-hydroxy-sn-glycero-3-phosphocholine (LPC), and cholesterol [Avanti Polar Lipids, Alabaster, AL] were individually dissolved in chloroform. The sialic acid receptor, G_{D1a} [Sigma-Aldrich, St. Louis, MO], was dissolved in a 2:1 chloroform to methanol solution. Oregon Green DHPE [Invitrogen, Carlsbad, CA], an acid-sensitive membrane fluorophore, was dissolved in ethanol. Two different lipid compositions were prepared, labeled as composition A and B. Composition A was prepared by mixing lipid components at a molar ratio of 4:4:2:0.1:0.001 DOPC/POPC/Cholesterol/G_{D1a}/Oregon Green DHPE, and composition B was prepared similarly, but POPC was replaced with LPC. The lipid solutions were dried under vacuum for 3 hours and rehydrated in MES buffer to a concentration of 0.5 mg/mL. Lipids were extruded 10 times through a 50 nm pore size cellulose membrane filter [GE Healthcare Life Science, Pittsburgh, PA] to form vesicles that were ~100 nm in diameter, determined by dynamic light scattering [Malvern Instruments, Worcestershire, UK].

Fusion Assay

Fusion experiments were performed inside microfluidic devices. The device assembly procedure is provided in the Supporting Material. The outlet tubes of the microfluidic device were attached to a syringe pump while the inlet tubes were placed in a vial containing a loading solution. The first loading solution contained the lipid vesicles, which were drawn

into the microfluidic device to form a supported lipid bilayer (SLB) over the course of 20 minutes. This SLB acts as the target membrane for the virus, and the SLB can either consist of composition A (SLB A) or B (SLB B). Excess vesicles were rinsed away by flowing MES buffer through the device channels. Virions were loaded into the channels and then allowed to bind to the G_{D1a} in the bilayer. Unbound virions were rinsed away with MES buffer. Fusion was triggered by flowing in a citric acid buffer (1 mM citric acid, 150 mM NaCl) at prescribed pH values at a flow rate of 500 μL/min for 30 sec (Figure S1).

Hemifusion Lag Time Data from Experiments

The R18-labeled virus was observed through total internal reflection fluorescence microscopy (TIRFM) using an inverted microscope [Carl Zeiss, Oberkochen, Germany] and a 100x oil-immersion objective. 561 nm and 488 nm lasers illuminated the labeled virus and the Oregon Green in the bilayer. When the acid reached the bilayer, the Oregon Green fluorophores quenched in the target bilayer and R18 fluorophores in the virus dequenched upon lipid mixing. The time between these events is the lag time for hemifusion. In this work, we use the term “fusion” and “hemifusion” interchangeably to describe the merging of two outer leaflets of the viral and target membrane. Figure S1 shows how the fusion lag time is determined; additional details about fusion lag time acquisition can be found elsewhere [21, 23, 29].

Target Membrane Quality and Lipid Diffusivity

The diffusion coefficients of R18 fluorophores in the supported lipid bilayers at various pH conditions were determined using the fluorescence recovery after photobleaching (FRAP). FRAP was performed to check the bilayer quality and detect changes in membrane

properties. FRAP experiments and analyses are described in the Supporting Material and in Figure S2.

METHODS: SIMULATION

Defining the Spatial Domain with a 2D Hexagonal Lattice

The spatial domain of the simulation is defined as a 2D plane representing the overlapped projection of the viral and target membrane, similar to the setup used by Schreiber et al. [19]. To capture some 3D aspects of fusion, such as the curvature of the viral membrane, we define two regions in the spatial domain: the contact area and the surrounding area. In the contact area, the viral and host membrane are located at an optimal distance from each other to allow HA trimers to mediate receptor binding and membrane fusion. In the surrounding area, the HA trimers are too far away from the target membrane to interact with the receptor. Note that due to the 2D spatial system, fusion intermediate structures, such as the hemifusion stalk and membrane dimples, cannot be shown visually, but their formation can still be described kinetically by associating these structures with distinct species that occupy space within the simulation spatial domain.

The spatial domain was discretized into a lattice array as a coarse-graining strategy to reduce simulation time at the cost of losing spatial resolution. We used a hexagonal lattice, instead of a square lattice, because tightly-packed HA trimers tend to adopt a triangular arrangement [30-31]. To simulate HA positions more realistically, a continuous spatial domain could be deployed using an off-lattice system. However, such a simulation method would be considerably more computationally expensive. If HA trimers must be close together to cooperatively induce fusion, then the hexagonal lattice suffices in capturing this arrangement of HA trimers.

The circumdiameter of one hexagonal unit was set at 6 nm to match the diameter of an HA trimer [7, 10]; this lattice element size ensures that HA trimers will not physically overlap. The total simulation space size was set at 25x25 grid elements (14625 nm^2), or roughly half the surface area of a spherical virus with a diameter of 100 nm. A larger spatial domain could be used, though this may be unnecessary as fusion occurs at a smaller contact area. The contact area was approximated as a 10x10 lattice domain (2338 nm^2) positioned in the center of the entire simulation space. The influenza strains we are studying are generally spherical and span a range of diameters between 85 to 170 nm [32-33]. To determine whether the contact area size has an impact on the values obtained for *w* and *q*, we also considered other contact area sizes. In short, *w* and *q* were not sensitive to contact area size (see Supporting Material and Figure S6).

Defining the Simulation Species

The total number of receptors, *R*, was set arbitrarily to 65, while the number of HA trimers was varied depending on the approach being used. All species were placed randomly across the entire spatial domain. The maximum number of HA trimers used in our simulation was 200 to be consistent with the HA density of a typical 100 nm-diameter virion that contains roughly400 HA trimers [34]. This maximum HA number density is referred to as $\boldsymbol{\rho}_{\mathrm{HA,200}}$. Note that Imai et al. [13] report the unit of HA density as a weight ratio of HA-to-lipid. Our $\boldsymbol{\rho}_{\mathrm{HA,200}}$ corresponds to their maximum HA density and a 3.4 HA-to-lipid mass ratio.

There are two types of HA trimers in our model, HA_0 and $HA_{1,2}$. Both can bind to receptor *R*, but only $HA_{1,2}$ can undergo conformational change to become an $HA_{1,2}^*$ species. An *HA* species can move laterally to an adjacent free grid element that has no *HA* in it, and a

similar rule applies for *R* as well. An *HA* and an *R* can overlap the same grid element since *HA* and *R* exist in two different membranes. An $HA_{1,2}^{*}$ inside the contact area is interpreted as an HA trimer that has inserted its fusion peptide into the target bilayer, and this is then treated as an immobile species. Here, fusion peptide insertion can occur without receptor binding [1, 35-36], which is also consistent with several reports showing that receptor binding is not required for fusion [22, 37-41]. Table S2 summarizes the species involved in our simulation and their permitted locations in the simulation space.

The positions of HA trimers are important when defining a "*fusible unit*" species. A *fusible unit* is defined by an arrangement of *HA* (HA_0 or $HA_{1,2}$) and $HA_{1,2}^{*}$ species in adjacent grid elements that is characterized by *w* and *q*. An example of a $w = 3$ and $q = 1$ criterion for forming a *fusible unit* is shown in Figure 1; examples of other arrangements that were tested are provided in Supporting Material, Figure S4. Note that the actual number of conformationally-changed HA trimers inside the fusible unit arrangement can exceed *q* and follow a distribution; however, *q* itself cannot follow a distribution because *q* represents the *minimum* number of conformationally-changed HA trimers that are required for fusion.

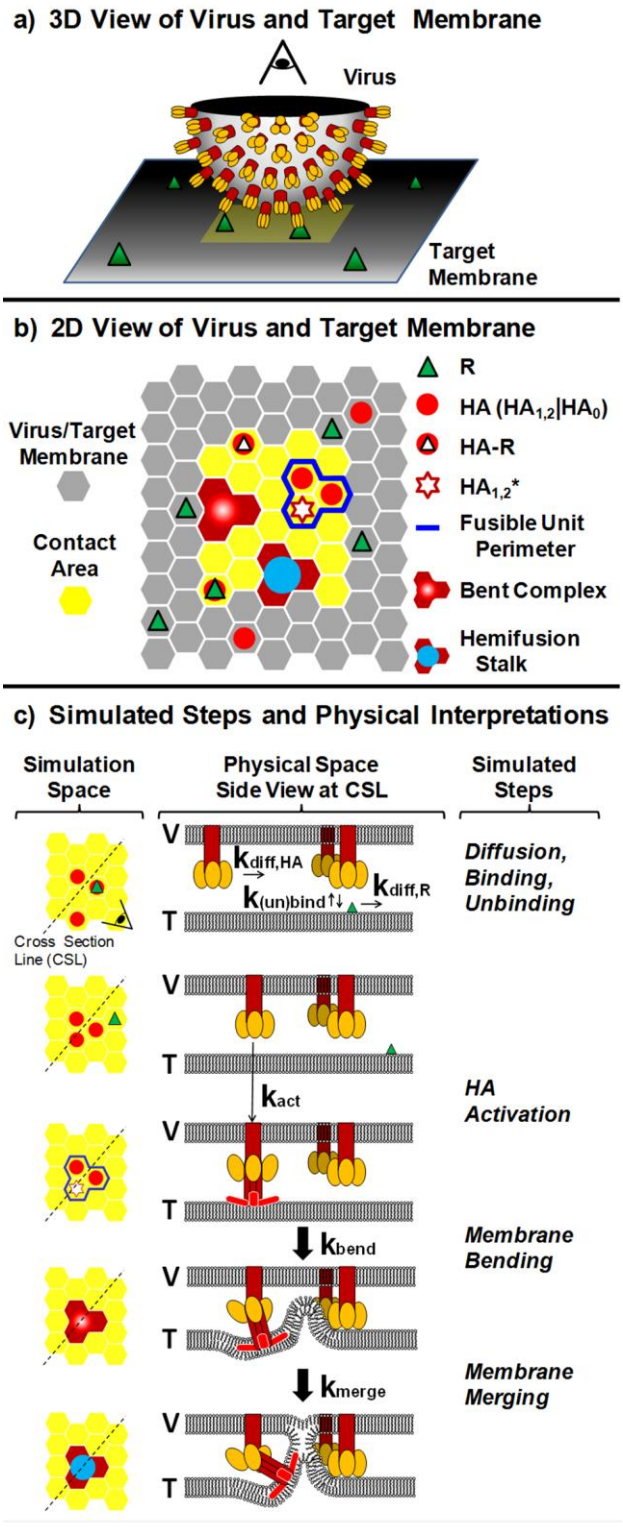

Figure 1 Virus-cell interaction represented in the simulation space. (a) A close-up 3D view of half of the virus bound to the host membrane. (b) 2D representation of the 3D picture. The simulation space represents the viral membrane overlapping the target membrane. The *HA* and *R* species move within a hexagonal lattice domain. Any interaction between the virus and host membrane occurs within the contact area (yellow). An example of using a $w = 3$, $q = 1$ criterion for forming a fusible unit is outlined by the blue perimeter. (c) Catalog of simulated events in the fusion model. The simulation species are shown on the left-hand side as a top-down view; the corresponding physical interpretations of the species are shown in the middle through cross-sectional side views. The viral and target membranes are labeled "V" and "T", respectively, the yellow ovals are the HA_1 binding domain, and the red objects are the HA_2 fusion domain of an $HA_{1,2}$ trimer. The brighter red portions of the HA_2 domain represent the hydrophobic fusion peptides that inserts into the target membrane.

An unresolved issue remains whether or not the *fusible unit* consists of an irreversible aggregation of HA trimers. Based on the EM picture provided by Kanaseki et al. [6], aggregated HA trimers are not apparent before or after fusion. Aggregation has been theorized mainly due to the "rosette" seen after the acidification of HA trimers [4]. The *fusible unit* in our model is not an aggregated HA trimer complex, but rather it is a transient configuration in the contact area where HA trimers can "pinch" the target bilayer into a dimple. Once a *fusible unit* is identified within the contact area, it is treated as a distinct simulation species that can transition into a "*bent complex*" intermediate, which is analogous to the fusion dimple observed in EM studies of influenza membrane fusion [5-6]. The bent complex can then proceed to a merged state of the outer leaflets of the two membranes, defined as a "*hemifusion stalk*." The time when the first *hemifusion stalk* appears dictates the fusion lag time in both the fusion simulations and experiments. Figure 1 shows the simulated reaction/diffusion events and Table 1 summarizes the rate parameter values used in this work [17, 19, 42-43].

Table 1 List of simulated reaction events and their associated symbols and values. "HA" refers to either HA_0 or $HA_{1,2}$. The bracketed rate parameter values were used only when matching Imai et al.'s data.

Reaction Event	Rate Symbol	Rate Value (s^{-1})
Diffusion of HA and R		
HA($\mathbf{r}_1$) → HA($\mathbf{r}_2$)	$k_{diff,HA}$	740[17]
R($\mathbf{r}_1$) → R($\mathbf{r}_2$)	$k_{diff,R}$(Glycoprotein) $k_{diff,R}(G_{D1a})$	[74][19, 42] 2000*
Actions of HA and R		
HA + R → HA-R	k_{bind}	0.20[19]
HA-R → HA + R	k_{unbind}	0.15[19]
$HA_{1,2}$ → $HA_{1,2}$*	k_{act}(pH = 5.2) k_{act}(pH < 4.9)	[0.067]† 5.78[43]
Membrane Events		
[Fusible Unit] → [Bent Complex]	k_{bend}	Fitted parameter
[Bent Complex] → [Hemifusion Stalk]	k_{merge}	0.10

* Capped value. See text and Supporting Material for more details.
† k_{act} values for the H1 serotype of HA in Imai's virosomes are unknown. Values of 0.01 s^{-1} and 0.067 s^{-1} were tested. More details are provided in the Supporting Material.

Defining the Reaction Rate Parameters

The hopping rate of *HA* or *R* from one grid element to an adjacent element is defined as $k_{diff,HA}$ and $k_{diff,R}$, respectively. These parameters were calculated from their corresponding diffusion coefficients as described in the Supporting Material. The binding and unbinding rates between an HA trimer and receptor, defined as k_{bind} and k_{unbind}, respectively, were adopted from Schreiber et al.'s work [19]. Note that Imai et al. [13] used glycoprotein on red blood cells as the viral receptor, whereas we used G_{D1A} glycolipid instead. Hence, the $k_{diff,R}$ value for glycoprotein (i.e., 74 s^{-1}) was used to simulate Imai et al.'s data, whereas the $k_{diff,R}$ value for G_{D1A} (capped at 2000 s^{-1}) was used when simulating our own data.

The activation rate, k_{act}, of an HA trimer as a function of pH has been determined experimentally by Krumbiegel et al. [43] for the X31 virus (H3N2) that we are using. They report a k_{act} value of 5.78 s^{-1} for pH conditions below 4.9. Since Imai et al. performed

experiments at a higher pH value of 5.2 and with a different HA serotype (H1), a different k_{act} value had to be used to simulate their data. But, to our knowledge, k_{act} is unknown for the H1 serotype of HA trimer, therefore as a starting point, we used the k_{act} value (0.067 s^{-1}) for the H3 serotype at a pH value of 5.2 that was found by Krumbiegel et al. [43]. We then tested another arbitrary k_{act} value of 0.010 s^{-1} to see how this affects our conclusion for w and q. Results for these tests are provided in the Supplemental Material and in Figure S7; in short, our conclusions on w and q did not depend on k_{act} within the tested range.

A lumped rate parameter that describes how fast a *fusible unit* can bend the target membrane is defined as k_{bend}. Parameter k_{bend} depends on both the HA trimer's ability to bend the membrane as well as the properties of the target membrane that dictate its ability to bend. The value for k_{bend} is unknown and k_{bend} is an important fitting parameter in our model. An approximate value for $k_{bend,}$ which we denote as $k_{bend,approx}$, is found by adjusting k_{bend} until the simulated distribution is not statistically different from the actual distribution according to a KS test, as described below. When a more precise value of k_{bend} is necessary to make conclusions about membrane bending rates, which is the case when studying k_{bend} as a function of pH or membrane properties, k_{bend} is refined using a bootstrap method [44]. This refinement method is described in Supporting Material. The k_{bend} values reported in Figure 5 and 6 have been refined.

The frequency rate at which a highly bent target membrane transitions into a hemifusion stalk, k_{merge}, is expected to be similar in magnitude to that for vesicle-vesicle fusion. Lee and Lentz [45] provided a comprehensive review on the similarities between PEG-induced and HA-induced fusion. The half-life for PEG-induced fusion is around 10 sec [45-46] which if

fitted to the equation $k_{merge} = - \ln(1/2) / t_{1/2}$, the associated rate constant is 0.07 s^{-1}. To find a value for k_{merge} that is most representative of an influenza virus fusing with a host membrane, we look to existing fusion data in the pH range where HA conformational change is not limited by proton availability. Floyd et al. [21] showed that at pH 3, the fusion lag time distribution reflects a single rate-limiting step with a rate constant of 0.1 s^{-1}. If the rate-limiting step is the merging of the membrane at this low pH, then the rate constant value of 0.1 s^{-1} is in good agreement with that estimated from PEG-induced vesicle fusion studies. We therefore assigned k_{merge} to be 0.1 s^{-1} in our simulation model.

Technique for Simulating Hemifusion Lag Time

Our simulation uses the Stochastic Simulation Algorithm (SSA) developed by Gillespie [47] to predict the lag time for a virus hemifusion event. Any changes to a simulation species or its position are treated as a "reaction event." The probability of a reaction event occurring within a small time increment, [t, $t + dt$], is defined as a "propensity." The propensity of a reaction event is calculated from both the rate parameters and the number of species involved for each reaction event. At a simulated time of t = 0, the system is considered to be acidified and fusogenic HA trimers are allowed to change conformation and participate in forming a *hemifusion stalk*. Using random numbers and an iterative loop, all reaction events can be simulated based on their propensities. The formation of the first *hemifusion stalk* species dictates the fusion lag time and ends the simulation. Simulations are repeated 1000 times to collect a distribution of lag times. More details on the simulation algorithm are provided in the Supporting Material.

Matching Simulated and Actual Fusion Lag Time Distributions

To determine if the simulated lag time distribution is an acceptable fit for the experimental data, the two-population Kolmogorov-Smirnov (KS) test [48-49] was used. The null hypothesis for the KS test is that two distributions are statistically the same. If the KS statistic (D_{test}), defined as the greatest vertical distance between two normalized cumulative lag time distributions, is greater than the critical KS statistic (D_{crit}) for a 5% significance level, then the null hypothesis is rejected. The critical KS statistic is calculated using the equation below, where $c(\alpha) = 1.36$ for the 5% significance level, n_{exp} = number of data points from experiment, n_{sim} = number of data points from simulation.

$$D_{crit} = c(\alpha)\sqrt{\frac{n_{sim} + n_{\exp}}{n_{sim} n_{\exp}}}$$

If $D_{test} \geq D_{crit}$, simulation results are rejected

If $D_{test} < D_{crit}$, simulation results are accepted

The criteria for accepting a simulation result is that D_{test} must be less than D_{crit}, which means the simulated distribution is *not* statistically different from the experimental distribution within the 95% confidence interval. Values for D_{test} and D_{crit} are provided in the legends of the figures that show the lag time distributions (Figure 2, 5, and 6).

Determining Rate Limiting Steps using Sensitivity Analysis

To determine the rate-limiting steps (RLSs) for fusion, the common strategy of comparing the magnitude of rate parameters could not be used because this neglects the fact that multiple HA trimers can act in parallel to induce fusion. Another way to determine the RLSs is to make use of the fact that the fusion lag time output will be most sensitive to the RLSs; hence, a sensitivity analysis was performed for each rate parameter. To perform the sensitivity

analysis, the rate parameter being evaluated was adjusted by 10% and 20% from the current value while other parameters were fixed, and simulations were run to extract the new, altered lag time distributions. A sensitivity index, S_a, is calculated for each rate parameter using the formula below [25, 50]:

$$S_a = \frac{\partial Y}{\partial p} = \frac{\left|Y_{alt} - Y_{ref}\right|}{\left|p_{alt} - p_{ref}\right|}$$

where Y_{alt} is the mean lag time obtained at the altered parameter value p_{alt}, and Y_{ref} is the mean lag time obtained at the original value of the parameter p_{ref}. The RLSs are associated with the rate parameters with the highest, relative sensitivity index values.

RESULTS

Overview of the Strategy for Determining w and q

The unknown parameters in our model are w, q, and k_{bend}. We begin by using the Constant FB approach to find multiple valid combinations of w, q, and k_{bend} that allow the simulated lag time distributions to match that of Imai et al. when the $HA_{1,2}$ density is $\boldsymbol{\rho}_{\mathrm{HA,200}}$ (Figure 2, black line). The rate parameters that were used for this step are listed in Table 1 for Imai et al.'s experimental system, which involves virosomes with HA trimer (H1 serotype) binding to glycoprotein receptors and fusing with a cell membrane at a pH of 5.2. We then use the Variable F and FB approach to find a unique solution for w, q, and k_{bend} by matching the simulated trends in fusion rates versus HA densities with Imai et al.'s trends. After a unique solution of w, q, and k_{bend} is determined, we retain the w and q values and perform a model validation procedure to see if the model can predict the fusion kinetics of the H3N2 (X31) influenza virus.

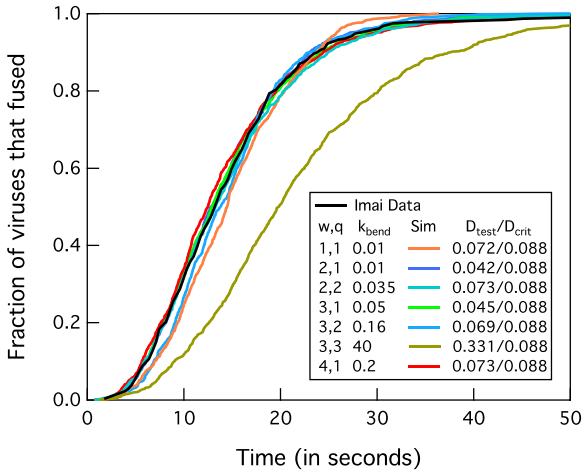

Figure 2 Determining possible solutions for w, q, and k_{bend} using Constant FB approach on Imai et al.'s fusion data at $\boldsymbol{\rho}_{HA,200}$ and using rate values in Table 1 for pH 5.2. The ratio D_{test}/D_{crit} is used to determine if simulations match with Imai et al.'s data. If D_{test}/D_{crit} is less than 1, simulations are accepted. An example of an invalid solution is shown when $w = 3$ and $q = 3$ (olive green line), as noted by D_{test}/D_{crit} being greater than 1.

The model is validated if simulated lag time distributions match with those from X31 fusion experiments performed at different pH conditions and membrane compositions. Since the HA densities were not varied, this process is categorized under the Constant FB approach. The rate parameters that were used are listed in Table 1 for our experimental system, which involves the H3N2 virus binding to G_{D1A} receptors and fusing with a supported lipid bilayer at a pH between 3 and 4.5. We assumed w and q are constant across the H3 and H1 serotypes of HA trimers and for the experimental conditions used here. Parameter k_{bend} was left as the sole fitting parameter while all other parameters were held constant. If the simulations cannot match the lag time distributions found from fusion experiments through the adjustment of k_{bend}, then the model assumptions are invalid and need to be revised. If simulations can match with experiments, then the model assumptions are validated and the resulting solution for w and q is accepted. The above simulation strategy is summarized in a flow chart provided in Fig S5.

Finding potential solutions for w, q, k_{bend} using Constant FB

The Constant FB approach was used to simulated Imai et al.'s lag time distribution when the $HA_{1,2}$ density is $\boldsymbol{\rho}_{HA,200}$ and the pH is 5.2. The rate parameters, besides k_{bend}, that were used are shown in Table 1 for Imai et al.'s experimental system, which were held constant. Figure 2 shows the matched cumulative fusion lag time distributions for many combinations of w, q, and k_{bend}. Note that this also shows that the Constant FB approach cannot be used alone to find a unique solution for w and q. Variable F and FB approaches are needed to reduce the number of solutions.

Eliminating w, q, k_{bend} solutions using Variable F

For each possible solution of w, q, and k_{bend} found above, simulations were run to mimic Imai et al.'s Variable F approach [13] to see which set of values could recapitulate results from their experimental data set. In the simulation, the number of $HA_{1,2}$ trimers was incrementally decreased from 200 to 10 while the number of HA_0 trimers was incrementally added so that the total number of HA trimers in the simulation space remained constant at 200. The cumulative lag time distributions for each concentration of $HA_{1,2}$ were then plotted and the maximum slope, V_{max}, was determined for each distribution for each $HA_{1,2}$ density. Imai et al.'s slope value for a plot of log V_{max} vs. log [$HA_{1,2}$] from the Variable F approach is 0.85 (95% Confidence Interval, CI, between 0.63 and 1.08). Simulation yields a slope value within Imai et al.'s 95% CI when q is 1 (Figure 3a and 4) and w is 2 or 3. The slope value increased with higher q values (Figure 3a and 4), and therefore values of q greater than 3 did not need to be tested as this would cause simulation results to diverge further from Imai et al.'s results.

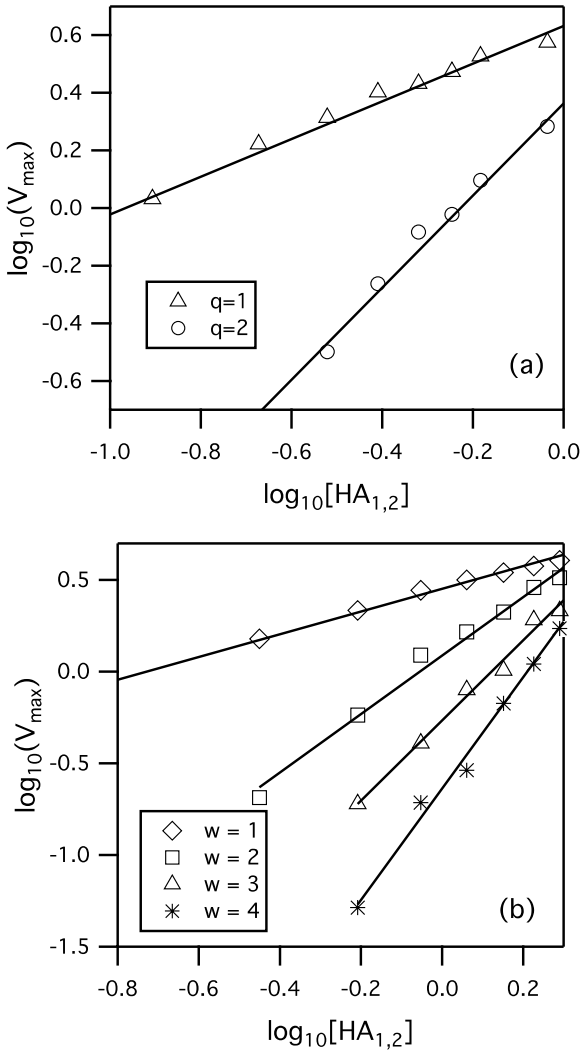

Figure 3 Sample simulation log-log plot of V_{max} versus $HA_{1,2}$ density for (a) Variable F approach for the condition that w = 3 while q is varied. The slopes of the best-fit lines are 0.65 and 1.6 for q = 1 and 2, respectively. (b) Variable FB approach for q = 1 while w is varied. The slopes of the best-fit lines are 0.62, 1.59, 2.19, and 3.03 for w values of 1, 2, 3, and 4, respectively. The r^2 values for all regression lines are at least 0.99. The unit of HA density, [$HA_{1,2}$], has been converted to its corresponding mass ratio of HA to lipid to be consistent with the results of Imai et al.

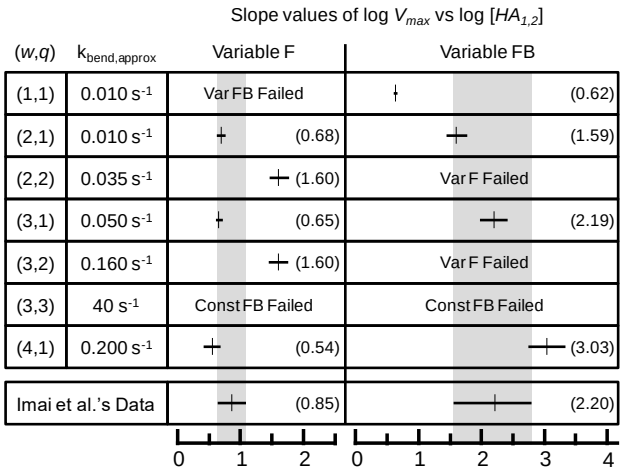

Figure 4 Slope values of log V_{max} vs. log [$HA_{1,2}$] for various combinations of w and q values. Some simulations were unnecessary due to the inability to yield results that are consistent with Imai et al.'s fusion data. The gray bar represents the 95% confidence interval of Imai et al.'s data. The numerical values of the slopes are provided in parentheses.

Eliminating w, q, k_{bend} solutions using Variable FB

For each possible solution of w, q, and k_{bend}, simulations were also run to mimic Imai et al.'s Variable FB approach [13]. Here, the number of $HA_{1,2}$ trimers was incrementally decreased from 200 to 10 and no HA_0 trimers were present. Imai et al.'s slope value from the plot of log V_{max} vs log [$HA_{1,2}$] for the Variable FB approach is 2.2 (95% CI between 1.55 and 2.79). The simulation slope value falls within Imai et al.'s 95% CI when w is 2 or 3 and q is 1 (Figure 3b and 4). The slope value increased with higher values of w; therefore values of w greater than 4 did not need to be tested as this would cause simulation results to diverge further from Imai et al.'s results.

The combinations of w and q that agree with both of Imai et al.'s Variable F and FB results are either $w = 3$ and $q = 1$, or $w = 2$ and $q = 1$. Other combinations of w and q failed to match at least one of Imai et al.'s data set. We concluded that w is more likely to be 3 instead of 2 because for the Variable FB results, the 95% CI for simulation slope values falls completely inside that of Imai et al.'s 95% CI only when $w = 3$. But regardless of whether the

value of w is 2 or 3, any value of w greater than 1 suggests HA trimers act cooperatively to induce fusion.

Validating Simulation Model using Constant FB at Varying pH Conditions

Fusion experiments were performed with the X31 (H3N2) virus and SLB A at several pH conditions, and corresponding simulations were run to validate the model against this data. By adjusting only k_{bend}, while holding w and q constant and using the appropriate rate parameter values in Table 1 for our experimental system, the simulation model was able to replicate the kinetic data (Figure 5a) from fusion experiments. Note that $k_{diff,R}$ is now 2000 s^{-1} since we used G_{D1A} as the receptor, and k_{act} is 5.78 s^{-1} since experiments were done at a pH less than 4.9. The good agreement between simulations and experiments validates our model and assumption that w and q do not change over the range of pH's tested and across the HA protein serotypes of H1 and H3.

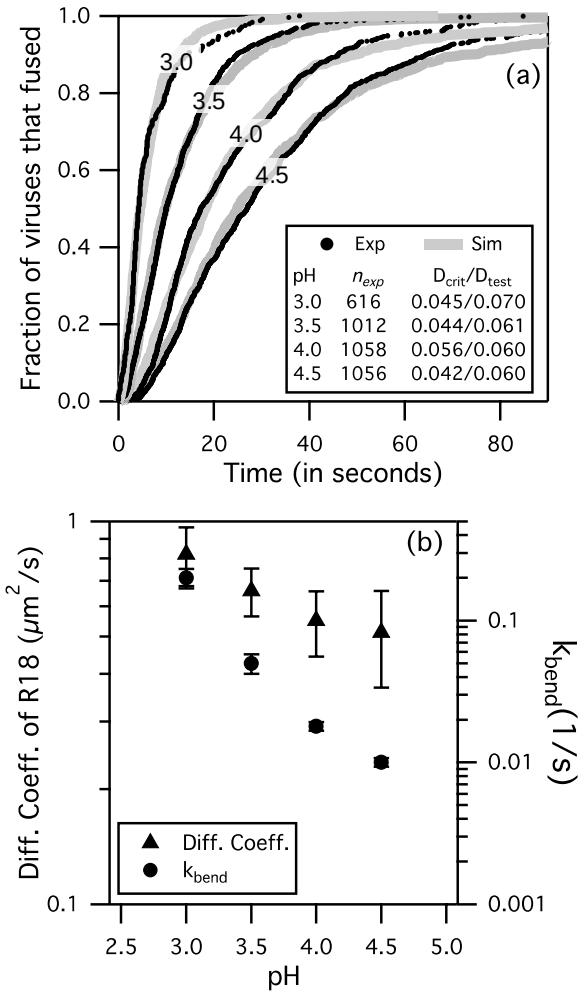

Figure 5 X31 fusion results at various pH conditions for SLB A at $\boldsymbol{\rho}_{HA,200}$. (a) Simulations are able to fit experimental data by adjusting only k_{bend} while keeping $w = 3$ and $q = 1$. (b, right axis and red circles) The mean k_{bend} values for pH 3.0, 3.5, 4.0, and 4.5 are 0.2 s^{-1}, 0.05 s^{-1}, 0.018 s^{-1}, and 0.01s^{-1}, respectively, with standard deviation shown in error bars. (b, left axis and black circles) The mean R18 diffusivity values for pH 3.0, 3.5, 4.0, and 4.5 are 0.82, 0.66, 0.55, and 0.51 $\mu m^2/s$, respectively, with standard deviation shown in error bars. Mobile fractions of R18 were close to 1 for all cases. Both R18 diffusivity and k_{bend} decrease with increasing pH over this range.

A closer look at the simulation results shows that the k_{bend} values for pH 4.0 and 4.5 are considerably smaller than those for pH 3.5 and 3.0, but k_{bend} is still a non-zero number (Figure 5b). Recall that k_{bend} represents both the HA trimer's ability to bend the target membrane and the deformability of the membrane itself. One interpretation of a smaller k_{bend} value is that the HA trimers are having more difficulty bending the target membrane. Another possible explanation is that the target membrane itself is harder to bend due to changes in membrane

properties, as suggested by the decreasing diffusion coefficient of R18 membrane fluorophores at higher pH conditions (Figure 5b). We note that diffusion coefficient itself is not a measure of membrane flexibility but is merely used here as an indicator to show that the target membrane has changed in some way. This change could be embodied as a change in lipid packing due to different pH conditions or ionic strengths [51-52].

Validating Simulation Model using Constant FB at two Target Membrane Compositions

To further confirm that fusion is affected by target membrane properties, we changed the composition of the target membrane by replacing POPC with LPC lipid (SLB B). LPC lipid has been shown to impede fusion [27] by hindering the bending of membranes. Indeed, fusion experiments at pH 4.0 show that viruses fused much slower with SLB B than with SLB A (Figure 6). In addition, simulations were able to match both SLB A and SLB B fusion lag time data by adjusting only k_{bend}. Parameters w and q did not have to be altered to fit the data, suggesting that they are not sensitive to changes in membrane properties between SLB A and SLB B. The strong dependence of k_{bend} on target membrane properties agrees well with Chernomordik et al.'s findings [28] that fusion is sensitive to target membrane properties at a step after HA activation, but before membrane merging.

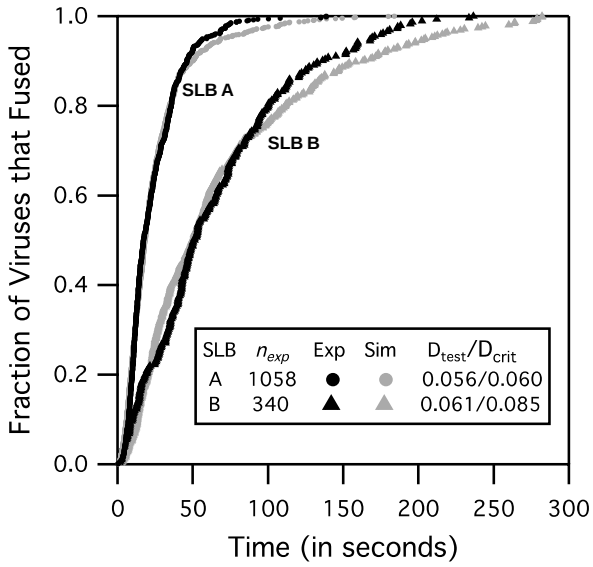

Figure 6 X31 fusion results at pH 4.0 using SLB A and SLB B. Simulations were able to match experimental data for two different target membranes membrane compositions by adjusting k_{bend} only. The values of k_{bend} from the fits are 0.018 (± 0.001) s^{-1} for SLB A and 0.0035 (± 0.0002) s^{-1} for SLB B.

Note that for the same bilayer composition, higher lipid mobility is indicative of a more fluid membrane, which should be easier to bend. However, comparisons of membrane mobility across different SLB compositions in order to rank membrane flexibility is not appropriate because other factors such as lipid shape, bilayer elasticity, and bilayer thickness can also affect the membrane flexibility. We emphasize that the work here focuses on fluid-like membrane compositions; we have not simulated or examined other membrane types, e.g. raft-like membranes, which could cause the assumptions made earlier about the model to become invalid. Hence, we restrict our model results to apply under similar experimental conditions and fluid target membrane compositions used in this and Imai et al.'s work.

Sensitivity Analysis Result

A sensitivity analysis was performed on the simulation model to determine how sensitive the lag time distribution is to slight perturbations to the rate parameters. In this case, the rate parameters that lead to the greatest change in fusion lag time output when perturbed must also

be associated with the rate-limiting steps of fusion, as described above in Simulation Methods section. Sensitivity analysis was done for X31 fusion simulations at pH 3 and 4.5 conditions for when SLB A is the target membrane. The sensitivity index values for each simulation rate parameters (Figure 7) were calculated according to the method described in the Simulation Methods section.

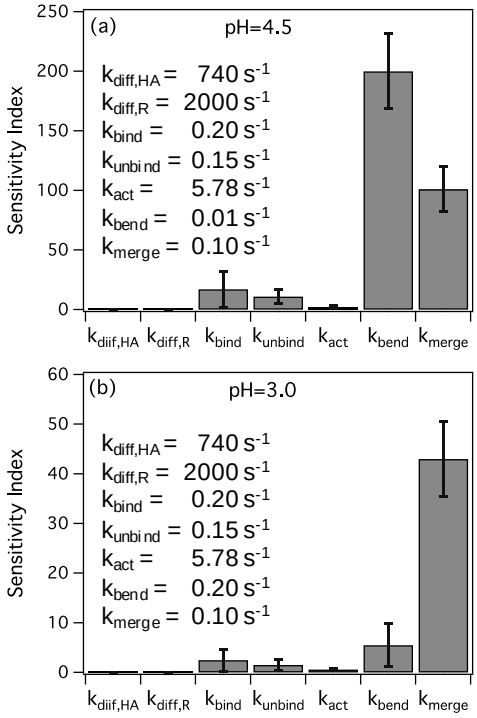

Figure 7 Sensitivity index values for rate parameters at (a) pH 4.5. Both k_{bend} and k_{merge} have large sensitivity index values relative to other parameters. (b) pH 3.0. Here, k_{merge} is the most sensitive parameter. The parameter values are provided in the legend of each plot.

At pH 4.5, both k_{bend} and k_{merge} are sensitive parameters relative to the other parameters, suggesting that two steps, membrane bending and merging, are dominating all the others and are rate-limiting. However, at pH 3.0, k_{merge} is the most sensitive parameter relative to other parameters, suggesting one step, membrane bending, is rate limiting. To confirm these results, we compared them to the number of rate-limiting steps predicted by the gamma distribution fitting strategy [21, 53] . The gamma distribution fits resolve parameter N and k

that represents the number of significant rate-limiting steps and the observed rate constant for each step, respectively. At pH 4.5, a gamma fit yields $N = 2.04 \pm 0.02$ and $k = 0.07 \pm 0.01$ s^{-1}, agreeing with our sensitivity analysis that shows two rate-limiting steps. At pH 3.0, a gamma distribution fit yields $N = 1.12 \pm 0.06$ and $k = 0.15 \pm 0.01$ s^{-1}, agreeing with the sensitivity analysis showing one rate-limiting step. Note that when N is close to 1, the gamma fit k of 0.15 s^{-1} is similar in value to that for k_{merge} of 0.1 s^{-1}. Recall that k_{merge} was estimated from the gamma fit of Floyd et al.'s data at pH 3, in which $N = 1$ and $k = 0.1$ s^{-1}.

The remaining rate parameters, besides k_{merge} and k_{bend}, appear to be insensitive parameters that do not affect fusion lag times much for the X31 virus at pH conditions 4.5 or lower, as shown in Figure 7. There are several explanations for these observations. The tight-packing of HA trimers and immobilization of HA trimers at the contact area due to receptor binding and membrane insertion may render HA diffusion negligible at the contact area. Fusion lag times are weakly sensitive to receptor binding and unbinding since HA trimers were allowed to participate in fusion regardless of receptor binding, to be consistent with prior work that showed that binding is not necessary for fusion [22, 37-41]. Lastly, HA activation rate does not contribute significantly to the fusion lag time because we are studying X31 fusion kinetics at a pH value below 4.9 where the conformational change is fast [43] and is not expected to be rate-limiting.

DISCUSSION

Due to some similarities between ours and Schreiber et al.'s simulation model [19], we provide a more detailed comparison between the two. The main similarities are that both used the SSA algorithm [47] to simulate fusion kinetics and the spatial domain was setup up

similarly. The differences are many. First, our spatial domain distinguishes between a contact area and the surrounding area whereas Schreiber et al.'s spatial domain represents only the contact area. Second, their model considers that all HA trimers have undergone conformational change a t = 0 whereas we simulate the conformational change through rate parameter k_{act}. Third, contrary to Schreiber et al.'s model, we do not assume $w = q$ and we allowed fusion to occur without receptor binding [22, 37-41]. Fourth, Schreiber et al.'s model does not simulate the rate of membrane bending. Our model simulates membrane bending by including the transition rate of a *fusible unit* to a *bent complex*, granting us the ability to capture the dependence of fusion rate on target membrane properties [26-28].

According to our results, the minimum number of HA trimers required for fusion is three, but at least one HA trimer has to undergo conformational change ($w = 3$, $q = 1$). These results have not yet been tested against HA serotypes beyond H1 and H3, and for other experimental systems that do not involve virions or virosomes fusing to a fluid target membrane. Additionally, the results are valid only under the assumptions made when building the model. Whether or not this w and q pair applies for the other systems would be an interesting future study.

The practicality of q being 1 is reasonable when one considers the energy required to form a hemifusion stalk [54-57]. The energy released by the conformational change of an HA trimer has been estimated to be around 125 k_bT [58], which is more than enough energy to form a hemifusion stalk that requires around 40 k_bT of energy [57].

The roles of the neighboring HA trimers that do not change conformation during membrane fusion, referred to as HA_{adj}, are unknown. We hypothesize that HA_{adj} trimers act as

support structures that the conformationally-changed $HA_{1,2}^{*}$ trimer exploits to bend the target membrane into a sharp dimple that promotes fusion, as depicted in Figure 1. To confirm this hypothesis, one possible experiment is to make virosomes containing inactive and active HA trimers, and observe them fusing to a target at various stages through electron microscopy. These inactive HA proteins could either be the uncleaved HA_0 trimers, mutated HA trimers with the fusion peptides removed, or HA trimers that are deactivated with anti-fusogenic antibodies. A visual confirmation that a fusion dimple exists between active and inactive HA trimers would support the idea that adjacent, unchanged HA trimers could act passively to induce fusion.

To postulate why different approaches result in different conclusions about the HA-induced fusion mechanism, we summarize the insight provided by each approach. Fusion experiments at varying number of fusogenic HA trimers at a constant total HA trimer density (Variable F) yield information about the level of cooperativity between only conformationally- changed HA trimers. Fusion experiments at varying total densities of fusogenic HA trimers (Variable FB) reveal the number of HA trimers in a fusion complex. Lastly, fitting fusion lag time distributions, obtained at a single HA density, to statistical distributions (Constant FB) yields quantitative information about the sequential and parallel steps leading to fusion. The information obtained from all three approaches must be processed together to resolve the fusion mechanism from kinetic data.

CONCLUSION

The simulation model presented here demonstrates the importance of considering the differences between the three approaches to studying membrane fusion kinetics. The

mechanistic insight this model provides is that some fraction of HA trimers could potentially act passively to assist in membrane fusion, which would explain why some experiments show that HA act cooperatively to induce fusion while others do not. This simulation model is the first that we know of to explicitly capture the role of the host membrane into the model through the inclusion of rate parameter k_{bend}. Although we chose to focus on the influenza virus because of the plethora of data available to validate the model, the simulation and modeling approach is general enough that it could be extended to study other viruses. Whether the model is able to accurately recapitulate the fusion behaviors of other viruses will be an interesting future study.

ACKNOWLEDGEMENTS

D.W.L. is a recipient of a National Science Foundation GK-12 Fellowship in Biomedical Engineering. V.T. was funded by the Semiconductor Research Corporation, contract no. 2012-VJ-2272. P.C. thanks Intel Corporation for provision of computing support. We thank Dr. Radhendushka Srivastava for helpful discussions on statistical analysis. We thank Professor Manfred Lindau for his insightful comments.

SUPPLEMENTAL NOTES

Overview

This supporting material provides additional details on prior literature, microfluidic preparation, fusion assay setup, fluorescence recovery after photobleaching (FRAP) experiments, extents of fusion, a list of species used in simulation, calculation of "hopping rate" for species diffusion in the simulation, refining the k_{bend} values, the fusible unit species tested by simulation, our simulation algorithm, flow chart of simulation strategy, and a sensitivity analysis of slopes of log V_{max} vs log [$HA_{1,2}$] plots.

Summary of literature work

The minimal number of HA trimers necessary for membrane fusion, *w*, and the minimal number of activated HA trimers required, *q*, have been debated for more than two decades. Table S1 is a summary of past work related to this topic, together with the authors' original hypothesis or conclusions for suitable values of *w* and *q*. Each work has been classified according to the experimental approach used to determine *w* and *q*, as described in the table caption. Note that many previous studies did not consider *w* and *q* as separate parameters, which is why *w* and *q* often appear as the same value.

Table S1 Chronological list of experiments related to determining *w* or *q*. Variable F (var F) varies the fraction of fusogenic HA trimers at a constant total HA density. Variable FB (var FB) varies the total density of fusogenic HA trimers. Constant FB (const FB) does not vary HA density and extracts *w* or *q* by fitting fusion lag time data to statistical models. The reported *w* and *q* values from other studies were interpreted from the original references and not obtained through simulations performed in this work.

Year	Authors	Approach	*w*	*q*	Fitting Method	Source of HA trimer	Fusion Exp. or Simulation
1986	Gibson et al.	Var F	1	1	Multiple-Hit-Multiple-Target Model	A/PR/8/34 (H1N1)	Virus-Vesicle
1987	Bundo-Morita et al.	Var F	1	1	Multiple-Hit-Multiple-Target Model	A/PR/8/34 (H1N1)	Virus-Vesicle
1990	Ellens et al.	Var FB	2-5	2-5	N/A	A/Japan/305/57 (H2N2)	Cell-Vesicle
1990	Stegmann et al.	Const. FB	> 1	> 1	N/A	X-31 A/Aichi/68 (H3N2)	Virus-Vesicle
1996	Danieli et al.	Var FB	3-4	3-4	Hill Equation	A/Japan/305/57 (H2N2)	Cell-Cell
1996	Blumenthal et al.	Const FB	6	6	Power Law	A/Japan/305/57 (H2N2)	Cell-Cell
2000	Günther-Ausborn et al.	Var F	1	1	$V_{initial} = k[HA_{1,2}]^q$	A/Shangdong (H3N2) X-47 (H3N2)	Virosome-Cell
2000	Bentz	Var FB + Const FB	> 8	2-3	Mass Action Kinetic Model	A/Japan/305/57 (H2N2)	Cell-Cell
2001	Schreiber et al.	Var FB + Const FB	3	3	Simulation	A/Japan/305/57 (H2N2)	Cell-Cell
2006	Imai et al.	Var F Var FB	1 > 1	1 > 1	$V_{max} = k[HA_{1,2}]^q$	A/PR/8/1934 (H1N1)	Virosome-Cell
2008	Floyd et al.	Const FB	3	3	Gamma Distribution	X-31 A/Aichi/68 (H3N2)	Virus-SLB
2011	Dobay et al.	Const FB	6	3	Simulation	A/PR/8/1934 (H1N1) X-31 A/Aichi/68 (H3N2)	Virus-SLB
2012	Costello et al.	Const FB	≤ 2	≤ 2	Gamma Distribution	X-31 A/Aichi/68 (H3N2)	Virus-SLB
2013	Ivanovic et al.	Const FB	3-4	3-4	Gamma Distribution & Simulation	A/Udorn/62 (H3N2) X-31 A/Aichi/68 (H3N2)	Virus-SLB
2013	Lee et al. (this work)	Var F + Var FB + Const FB	3	1	Simulation	A/PR/8/1934 (H1N1) X-31 A/Aichi/68 (H3N2)	Virosome-Cell Virus-SLB

Microfluidic preparation

The microfluidic devices used for fusion experiments were prepared according to the following procedure. Glass coverslip slides (No. 1.5 thickness) [VWR, Radner, PA] were cleaned for 10 min using a piranha solution consisting of 45 mL of 50% hydrogen peroxide [Sigma-Aldrich, St. Louis, MO] and 105 mL of sulfuric acid [VWR, Radner, PA]. Cleaned glass slides were rinsed and stored in deionized water. A polydimethylsiloxane (PDMS) [Dow Corning, Midland, MI] mold of microfluidic channels was prepared using a patterned silica wafer made through photolithography. The microfluidic channel dimensions are 135 μm wide, 75 μm deep, and 1.5 cm long. A glass slide and PDMS mold were annealed together after a 30-second oxygen plasma cleaning step. Tygon tubes (0.02”ID x 0.06”OD) [Saint-Gobain Performance Plastic, Worcester, MA] were attached to the microfluidic device to facilitate the loading of various solutions into the channels. The microfluidic device is shown in Figure S1.

Images of fusion assay and sample hemifusion event

Figure S1 shows a picture of the microfluidic device and schematic drawing of the fusion assay setup. A sample image sequence of a virus is also shown. The intensity traces of the membrane dye (R18) in the viruses and the acid-sensitive membrane dye (Oregon Green) in the target membrane are used to determine the hemifusion lag time for individual virions.

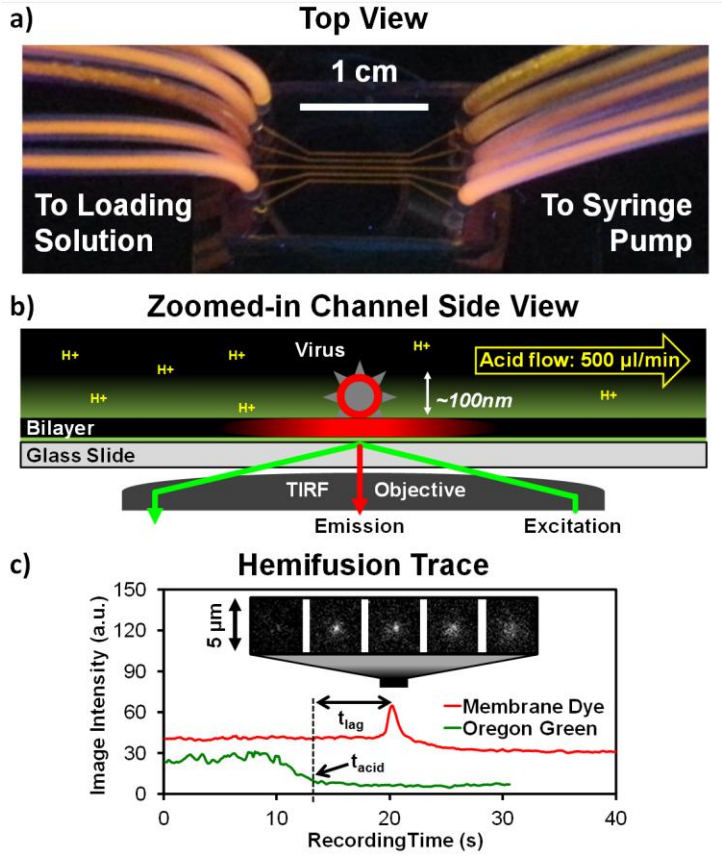

Figure S1 Virus fusion assay setup and sample hemifusion trace. (a) Photo of a typical microfluidic device. Channels were filled with fluorescent dye for visualization purposes. (b) Schematic diagram of a microfluidic channel used in experiments. A dye-labeled virus is shown fusing to a supported lipid bilayer (SLB) upon an acid trigger, inside a channel. Total internal reflection fluorescence (TIRF) microscopy is used to observe the fusion events. (c) Sample virus fusion images and hemifusion trace showing how the hemifusion lag time, t_{lag}, is determined.

Fluorescence recovery after photobleaching (FRAP) experiments

The mobility of the target membranes were determined using FRAP. The target membranes were labeled with R18 membrane fluorophores by adding 0.5 µL of 1.8 mM R18 in ethanol solution to 500 µL of lipid A or lipid B vesicle solutions. The solutions were sonicated for 30 min before loading them into microfluidic channels to form supported lipid bilayers (SLBs), which were allowed to form over the course of 20 min. Channels with SLBs were rinsed with citric acid buffer set at pH 3.0, 3.5, 4.0, or 4.5. The bilayer was illuminated with a 561 nm wavelength light source. A 16 µm-diameter circular area in the bilayer was photobleached with a 5 mW, 561 nm wavelength Gaussian laser for 3 seconds. Video images

of the bilayer were recorded before and after photobleaching, and the mean intensity of the bleached spot over time was measured. Another area that has not been photobleached, the reference spot (see Figure S2), was monitored to correct for global photobleaching caused by the microscope light source. The normalized mean intensity of the photobleached region, $f_k(t)$, was determined according to the following equation:

$$f_k(t) = \frac{[F_k(t) - F_c(t)] - [F_k(0) - F_c(0)]}{[F_k(-\infty) - F_c(-\infty)] - [F_k(0) - F_c(0)]}$$

where $F_k(t)$ and $F_c(t)$ are the fluorescence intensities at time t of the bleached and reference spot, respectively. The time immediately after photobleaching is $t = 0$, and the time before photobleaching is $t = -\infty$. The methods of Axelrod et al. [59] were used to fit the fluorescence recovery data and extract the characteristic time for diffusion, t_d, for a bleach spot made from a Gaussian laser. The diffusion coefficient was calculated as $D = r^2/(4t_d)$, where r is the radius of the laser beam at e^{-2} laser intensity height. D values for R18 fluorophores in SLB A are shown in Figure 7b of the main report.

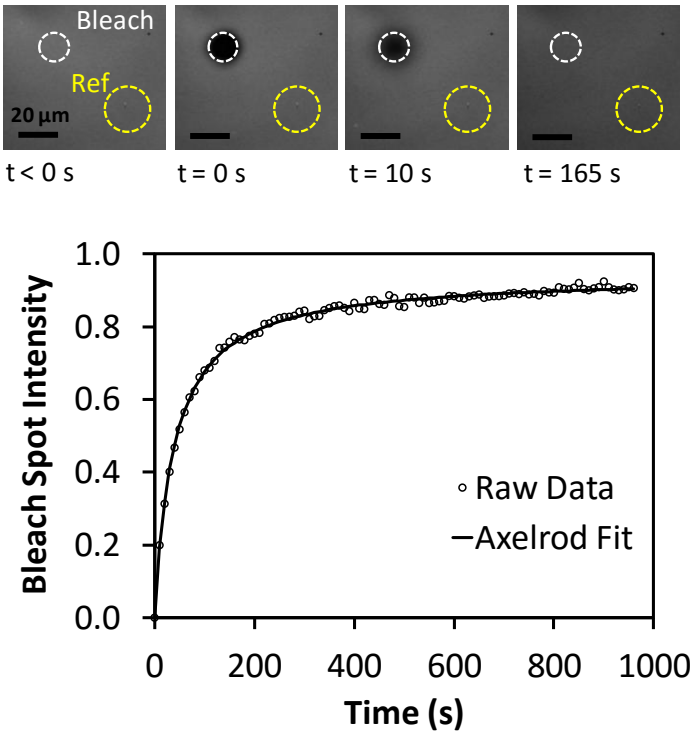

Figure S2 A representative FRAP recovery curve used to determine diffusion coefficient in supported bilayers. (Top) Image sequence of a R18-labeled supported lipid bilayer with LPC lipid (SLB B) at pH 4.5. The mean intensity of the photobleached circular region (white dotted circle) is tracked and compared with a reference region (yellow dotted circle) that has not been photobleached. (Bottom) the normalized intensity of the bleached spot is plotted with time and fitted to the diffusion equation derived by Axelrod et al. [59] to extract the characteristic time for diffusion, t_d. For this example, the bleach spot radius, r, is 8.13 µm and t_d is 36 s. The calculated D is 0.46 µm^2/s.

Extents of fusion of experimental data

The fraction of bound viruses that fused was tracked to verify that protein denaturation and subsequent loss of function due to acidification is negligible in the range of pH employed in these studies. An in-house particle counting program was developed in MATLAB to detect and count fluorescently-labeled virus particles by identifying high-intensity spots that have a circular morphology. Extent of fusion is defined as the number of viruses that fused divided by the total number of viruses observed. Figure S3 show the resulting extents of fusion at various pH conditions for triggering fusion. The consistent fusion extents across the tested pH range suggest that the virions were similarly functional across the experiments, and also that acid-induced denaturation of HA trimers is not occurring across the pH range. This result is

also in agreement with studies by Doms et al. in 1985 [1], who investigated acid-induced denaturation of HA trimers.

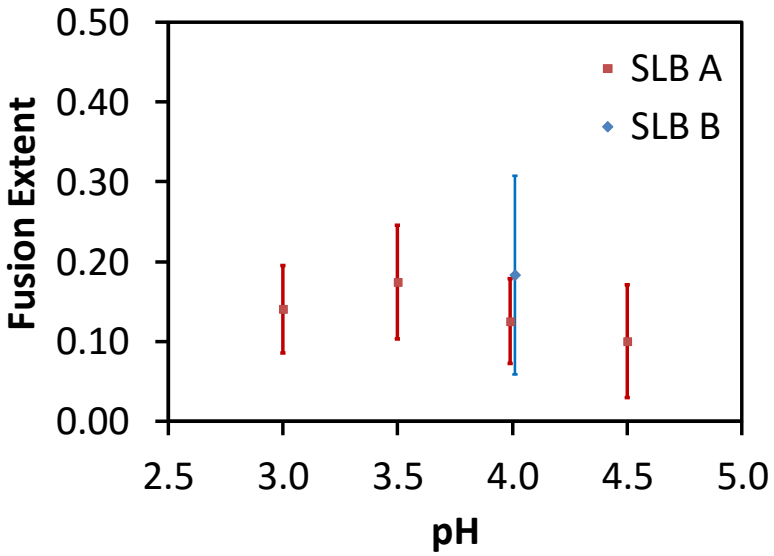

Figure S3 Extent of fusion for the X31 virus as the pH is varied in the range 3.0-4.5. The extent of fusion in this range is essentially the same within the uncertainty in the data.

List of species used in simulation

Table S2 provides a list of all species used in the simulation, with their description and allowable locations in the simulation space. Species that are physically associated with both the viral and host membrane are only allowed in the contact area region.

Outside the contact area, only HA_0, $HA_{1,2}$, $HA_{1,2}^*$, and *R* are mobile species. Inside the contact area, any HA trimers that are physically interacting with the target membrane or receptor are treated as immobile species. Unbound HA_0 and unbound *R* remain mobile inside the contact area. Table S2 summarizes the mobility of species.

Table S2 Summary of the species involved in the simulations.

Symbol	Description	Allowed Location	Mobility
R	Sialic acid receptor	Anywhere	Mobile
$HA_{1,2}$	Fusogenic $HA_{1,2}$ trimer	Anywhere	Mobile
HA_0	Non-fusogenic HA_0 trimer	Anywhere	Mobile
$HA_{1,2}$-*R* HA_0-*R* $HA_{1,2}$*-*R*	An HA trimer that is bound to R	Contact Area	Immobile
$HA_{1,2}$*	Conformationally changed $HA_{1,2}$	Anywhere	Immobile inside contact area. Mobile elsewhere.
Fusible Unit	An arrangement of HA trimers that can bend the target bilayer.	Contact Area	N/A
Bent Complex	A bent state of the target bilayer, which precedes hemifusion.	Contact Area	Immobile
Hemifusion Stalk	A merged state of the virus and target bilayer.	Contact Area	Immobile

Calculation of "hopping rate" for species diffusion in the simulation

The only diffusive species in our simulation are receptors, *R*, and HA trimers, HA_0, $HA_{1,2'}$, or $HA_{1,2}^*$. A diffusion event is defined as the migration of a molecule from one grid element to a neighboring grid element. This is modeled as a unimolecular reaction [60], where the hopping rate parameter is related to the macroscopic diffusion coefficient *D* through the relation $k_{diff} = nD/h^2$, where *h* is the center to center distance between two adjacent grid elements, and *n* is 2/3 for a hexagonal lattice system [61-62]. The diffusion coefficients for HA and glycoprotein receptor were estimated from existing FRAP experiments by Danieli et al. [17] and Sheetz [42], respectively. The hopping rate for HA, $k_{diff,HA}$, was calculated as 740 s^{-1}, while that for the glycoprotein is 74 s^{-1}. We assumed that the viruses studied by Imai et al. were attached to the glyocoprotein on the ghost red blood cell membranes. As for our own experiments, the viruses were bound to a different receptor called GD_{1a}, a glycolipid with sialic acid groups. The diffusion coefficient for $GD_{1a}$was estimated at 1 $\mu m^2/s$ based on the

diffusion coefficient of the lipid fluorophore, R18. However, the calculated hopping rate for GD_{1a}, $k_{diff,R}$,is 24,700 s^{-1}, which is many orders of magnitude greater than other rate parameters in the simulation. The simulation algorithm (discussed in detail below) will simulate each reaction event according to their reaction propensities, and therefore GD_{1a} diffusion would dominate the most of the simulation processing power. To prevent this from happening, we have capped $k_{diff,R}$ for GD_{1a} at 2000 s^{-1}.

Refining k_{bend} values

To refine the k_{bend} values starting with $k_{bend,approx}$, the bootstrap method [44] is used. In this method, the k_{bend} parameter is varied at 10 evenly spaced values in the interval [$0.8k_{bend,approx}$, $1.2k_{bend,approx}$] in which 3000 simulations are performed for each k_{bend} value. In one iteration of refinement, 500 random lag times from each distribution for each k_{bend} value are compared to the actual lag time distribution through a KS test. The simulated distribution with the smallest KS statistic (D_{test}) is determined, and the k_{bend} value for that distribution is stored. This iteration is performed for a total of 6 times to find the mean and standard deviation of these stored k_{bend} values. In the main text, any k_{bend} values with their error bars reported have been refined using this procedure.

Fusible unit species tested by simulation

A fusible unit is defined by an arrangement of HA trimers in adjacent grid elements. At least q number of HA trimers must be pH-activated and the relative locations of the pH-activated and un-activated HA trimers do not matter within the fusible unit perimeter, highlighted by a thick blue line in Figure S4. Other configurations of fusible units for different combinations of w and q are shown below in Figure S4.

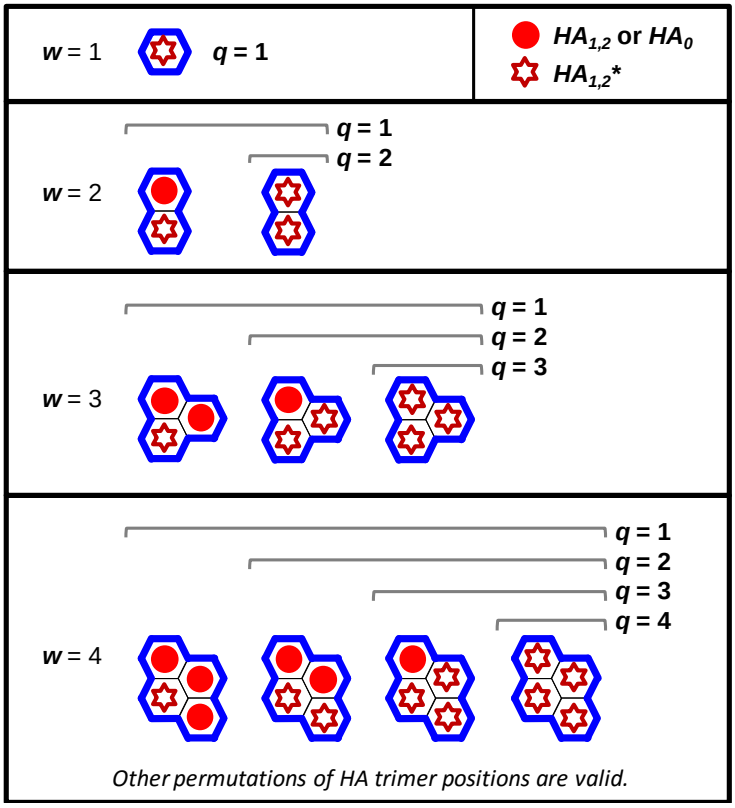

Figure S4 Fusible unit species studied in this simulation. A fusible unit is defined as a localized group of hexagonal lattice grid elements that contain *w* HA trimers, regardless of conformational state, and at least *q* activated HA trimers. Permutations of the positions of HA trimers within the blue fusible unit perimeter do not matter when defining a fusible unit species.

Simulation algorithm

Stochastic fusion simulations are performed using the following iterative procedure.

1) Initialize the system at time $t = 0$, which corresponds to the time at which the system is acidified.

2) Calculate the propensity, $a(t)$, of all molecular events using the relation $a_i(t) = k_i G_i(t)$, where k_i is the rate parameter of event i and $G_i(t)$ is the number of species involved, which here would be the number hexagonal lattice grid elements (or groups of elements) containing those species.

3) Select a random molecular event *j* by finding the minimum *j* value that satisfies $\frac{\sum_{j'=1}^{j} a_{j'}(t)}{a_0(t)} \geq r_1$, where $a_0(t)$ is the total propensity of all events and r_1 is a uniform random number in an interval [0,1].

4) Calculate time step, τ, using the relation $\tau = \frac{1}{a_0} \ln\left(\frac{1}{r_2}\right)$, where r_2 is a uniform random number in an interval [0,1].

5) Advance the simulated time, *t*, by τ and update the population/location of species in the simulation based on the chosen event.

6) Repeat steps 2 through 5 until a terminating event occurs. Our termination events were the formation of a hemifusion stalk species or a simulated time of t = 5 min.

Flow chart of simulation strategy

The flow chart in Figure S5 summarizes the strategy used to determine the unknown parameters (w, q, and k_{bend}) and also to validate the model. More details are provided in the Main Text in the section titled "Strategy Overview for Determining *w* and q.*"*

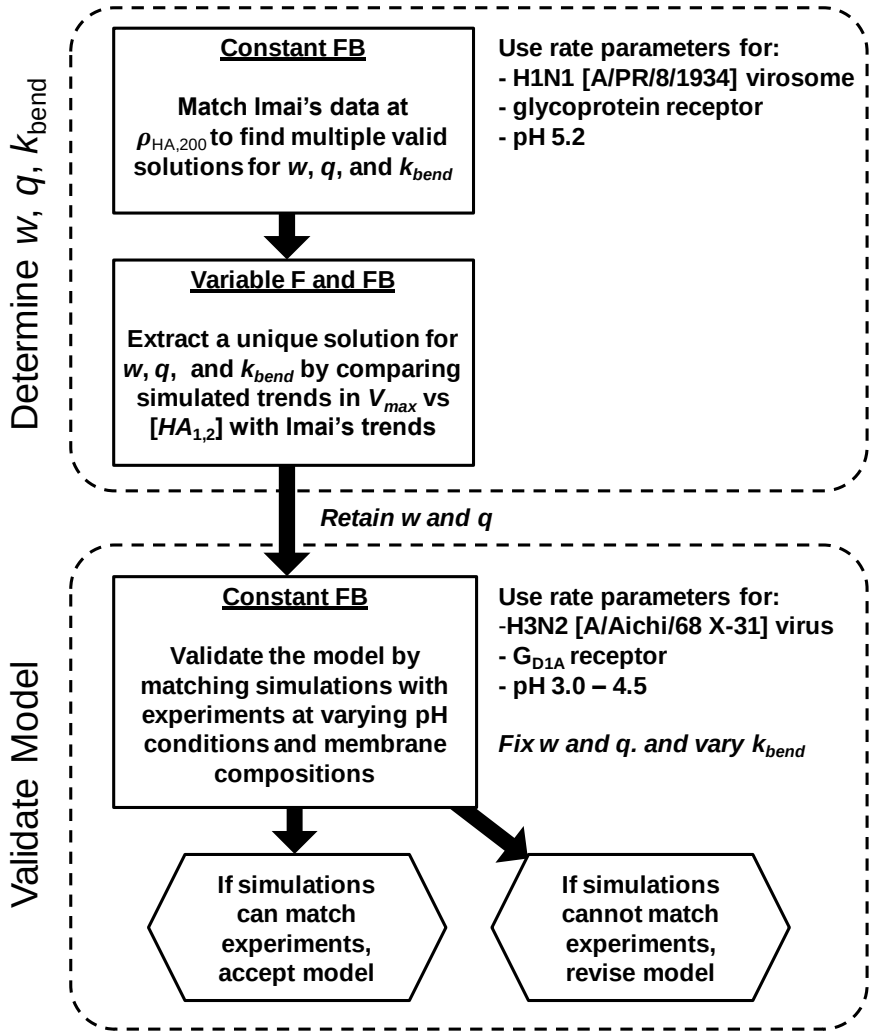

Figure S5 Flow diagram of the simulation process used to determine values for k_{bend}, w, and q.

Sensitivity analysis of slopes of log V_{max} vs log [$HA_{1,2}$] plots

We performed two types of sensitivity analysis to illustrate the robustness of our model in determining w and q. In the first analysis, we repeated the Variable F and FB simulations at two other contact areas to ensure that w and q values were dependent on our original choice of contact area size. The slopes of plots of log V_{max} vs log [$HA_{1,2}$] for both Variable F and FB simulations did not change significantly for 8×8, 10×10, and 14×14 grid sizes for the contact area. Thus, our conclusions regarding optimal w and q values are not affected by the choice of contact area size (Figure S6). We note that the choice of contact area size does alter the

k_{bend} values obtained by matching with Imai et al.'s distribution at $\boldsymbol{\rho}_{HA,200}$. A larger contact area increases the rate of fusion, which is compensated by a lower k_{bend} value in order to match experimental data. We thus emphasize that our numerical rate value reported for k_{bend} is based on the contact area being 2338 nm^2 (which is equivalent to 10x10 hexagonal grid elements), and that it scales directly with contact area size.

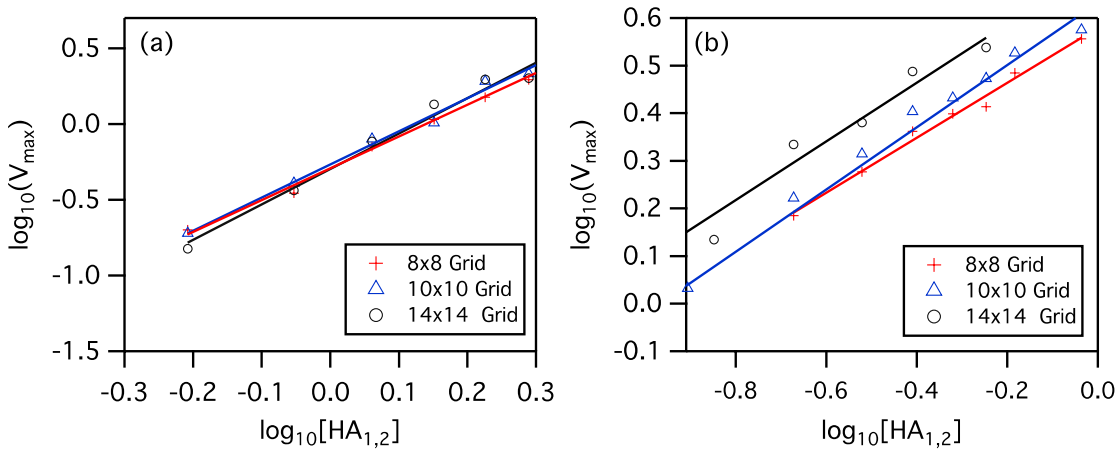

Figure S6 Insensitivity of slopes of log Vmax vs log [HA1,2] to choice of contact area size, for w =3, q = 1, and kact = 0.067 s-1. (a) Results from Variable FB simulations. The slopes of the best-fit lines are 2.09 (r2 = 0.99), 2.19 (r2 = 0.99) and 2.34 (r2 = 0.99) for contact area sizes of 8×8, 10×10, and 14×14 grid elements, respectively. (b) Results from Variable F simulations. The slopes of the best-fit lines are 0.58 (r2 = 0.98), 0.65 (r2 = 0.99) and 0.62 (r2 = 0.97) for contact area sizes of 8×8, 10×10, and 14×14 grid elements, respectively. The HA density, [HA1,2], has been converted to its corresponding mass ratio of HA to lipid in this plot to be consistent with Imai et al.'s studies [13]. The kbend, approx values determined from the fits are 0.078 s-1, 0.05 s-1, and 0.0255 s-1 for the 8x8, 10x10, and 14x14 contact area sizes, respectively.

In the second analysis, we repeated the Variable F and FB simulations at another k_{act} value to ensure that this parameter did not change our choice of values for *w* and *q*. We performed this analysis because we do not know the rate of conformational change for the HA trimers in the H1N1 influenza virus used by Imai et al. [13]. We began by using a value for k_{act} of 0.067 s^{-1}, which is the HA activation rate for X31 virus (H3N2) at pH 5.2, the pH value used by Imai et al. For a second value, we chose an arbitrary k_{act} value of 0.01 s^{-1}. Variable F and FB simulations were run for both cases of k_{act} using the same procedure described in the main manuscript. Despite an almost order of magnitude difference in k_{act}, the slopes of the log V_{max}

vs log [$HA_{1,2}$] plots did not change, as shown in Figure S6. In the main manuscript, we also showed that using a k_{act} value of 5.2 s^{-1} did not require us to change w and q when studying fusion kinetics at pH values below 4.5 and with different membrane compositions. Taken together, these results suggest that w and q is insensitive to the choice of k_{act} value, at least within the range of 0.01 and 0.067 s^{-1} studied here.

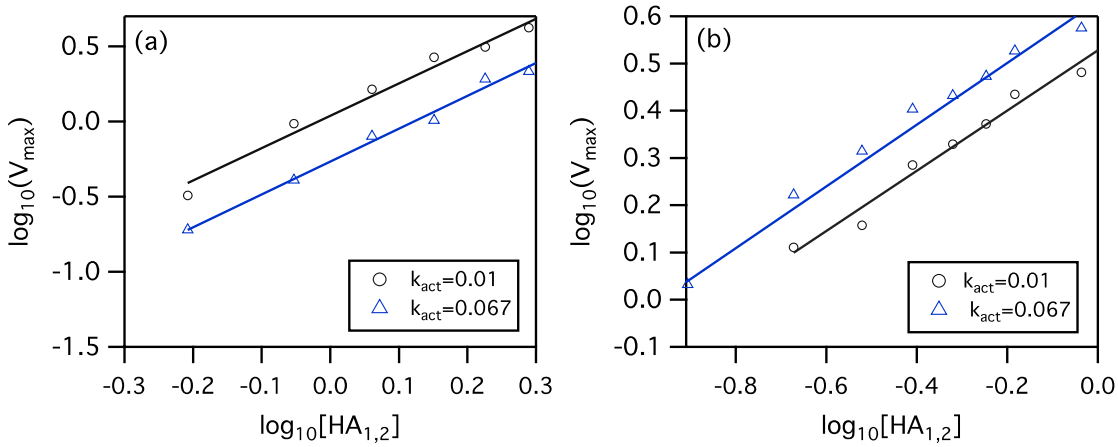

Figure S7 Insensitivity of slopes of log Vmax vs log [HA1,2] to the choice of kact, for w = 3, q = 1, and contact area = 10x10 grid size (2338 nm2). a) Results from Variable FB simulations. The slopes of the best-fit lines are 2.19 (r2 = 0.99) and 2.23 (r2 = 0.98) when kact is 0.067 and 0.01 s-1, respectively. b) Results from Variable F simulations. The slopes of the best-fit lines are 0.65 (r2 = 0.99) and 0.62 (r2 = 0.98) when kact is 0.067 and 0.01 s-1 respectively. The HA density, [HA1,2], has been converted to its corresponding mass ratio of HA to lipid in this plot to be consistent with Imai et al. [13]. The kbend, approx values from the fits are 0.28 and 0.05 s-1for kact values of 0.01 and 0.067 s-1, respectively.

REFERENCES

1. Doms, R.W., A. Helenius, and J. White, *Membrane fusion activity of the influenza virus hemagglutinin. The low pH-induced conformational change.* Journal of Biological Chemistry, 1985. **260**(5): p. 2973-2981.
2. Skehel, J.J. and D.C. Wiley, *Receptor binding and membrane fusion in virus entry: the influenza hemagglutinin.* Annual Review of Biochemistry, 2000. **69**(1): p. 531-569.
3. Bentz, J., *Minimal aggregate size and minimal fusion unit for the first fusion pore of influenza hemagglutinin-mediated membrane fusion.* Biophysical Journal, 2000. **78**(1): p. 227-245.
4. Doms, R.W. and A. Helenius, *Quaternary structure of influenza virus hemagglutinin after acid treatment.* Journal of Virology, 1986. **60**(3): p. 833-839.
5. Lee, K.K., *Architecture of a nascent viral fusion pore.* EMBO J, 2010. **29**(7): p. 1299-1311.
6. Kanaseki, T., K. Kawasaki, M. Murata, Y. Ikeuchi, and S. Ohnishi, *Structural features of membrane fusion between influenza virus and liposome as revealed by quick-freezing electron microscopy.* The Journal of Cell Biology, 1997. **137**(5): p. 1041-1056.

7. Böttcher, C., K. Ludwig, A. Herrmann, M. van Heel, and H. Stark, *Structure of influenza haemagglutinin at neutral and at fusogenic pH by electron cryo-microscopy.* FEBS Letters, 1999. **463**(3): p. 255-259.
8. Bullough, P.A., F.M. Hughson, J.J. Skehel, and D.C. Wiley, *Structure of influenza haemagglutinin at the pH of membrane fusion.* Nature, 1994. **371**(6492): p. 37-43.
9. Wiley, D.C. and J.J. Skehel, *The structure and function of the hemagglutinin membrane glycoprotein of influenza virus.* ANNUAL REVIEW OF BIOCHEMISTRY, 1987. **56**(1): p. 365-394.
10. Wilson, I.A., J.J. Skehel, and D.C. Wiley, *Structure of the haemagglutinin membrane glycoprotein of influenza virus at 3 [angst] resolution.* Nature, 1981. **289**(5796): p. 366-373.
11. Struck, D.K., D. Hoekstra, and R.E. Pagano, *Use of resonance energy transfer to monitor membrane fusion.* BIOCHEMISTRY, 1981. **20**(14): p. 4093-4099.
12. Otterstrom, J. and A.M. van Oijen, *Visualization of membrane fusion, one particle at a time.* BIOCHEMISTRY, 2013. **52**(10): p. 1654-1668.
13. Imai, M., T. Mizuno, and K. Kawasaki, *Membrane fusion by single influenza hemagglutinin trimers.* Journal of Biological Chemistry, 2006. **281**(18): p. 12729-12735.
14. Bundo-Morita, K., S. Gibson, and J. Lenard, *Estimation by radiation inactivation of the size of functional units governing Sendai and influenza virus fusion.* Biochemistry, 1987. **26**(19): p. 6223-6227.
15. Gibson, S., C.Y. Jung, M. Takahashi, and J. Lenard, *Radiation inactivation analysis of influenza virus reveals different target sizes for fusion, leakage, and neuraminidase activities.* Biochemistry, 1986. **25**(20): p. 6264-6268.
16. Günther-Ausborn, S., P. Schoen, I. Bartoldus, J. Wilschut, and T. Stegmann, *Role of hemagglutinin surface density in the initial stages of influenza virus fusion: Lack of evidence for cooperativity.* Journal of Virology, 2000. **74**(6): p. 2714-2720.
17. Danieli, T., S.L. Pelletier, Y.I. Henis, and J.M. White, *Membrane fusion mediated by the influenza virus hemagglutinin requires the concerted action of at least three hemagglutinin trimers.* The Journal of Cell Biology, 1996. **133**(3): p. 559-569.
18. Ellens, H., J. Bentz, D. Mason, F. Zhang, and J.M. White, *Fusion of influenza hemagglutinin-expressing fibroblasts with glycophorin-bearing liposomes: role of hemagglutinin surface density.* Biochemistry, 1990. **29**(41): p. 9697-9707.
19. Schreiber, S., K. Ludwig, A. Herrmann, and H.G. Holzhütter, *Stochastic Simulation of Hemagglutinin-Mediated Fusion Pore Formation.* Biophysical Journal, 2001. **81**(3): p. 1360-1372.
20. Blumenthal, R., D.P. Sarkar, S. Durell, D.E. Howard, and S.J. Morris, *Dilation of the influenza hemagglutinin fusion pore revealed by the kinetics of individual cell-cell fusion events.* The Journal of Cell Biology, 1996. **135**(1): p. 63-71.
21. Floyd, D.L., J.R. Ragains, J.J. Skehel, S.C. Harrison, and A.M. van Oijen, *Single-particle kinetics of influenza virus membrane fusion.* Proceedings of the National Academy of Sciences, 2008. **105**(40): p. 15382-15387.
22. Stegmann, T., J.M. White, and A. Helenius, *Intermediates in influenza induced membrane fusion.* EMBO J, 1990. **9**(13): p. 4231-4241.
23. Costello, D.A., D.W. Lee, J. Drewes, K.A. Vasquez, K. Kisler, U. Wiesner, L. Pollack, G.R. Whittaker, and S. Daniel, *Influenza virus-membrane fusion triggered by proton uncaging for single particle studies of fusion kinetics.* Analytical Chemistry, 2012. **84**(20): p. 8480-8489.
24. Ivanovic, T., J.L. Choi, S.P. Whelan, A.M. van Oijen, and S.C. Harrison, *Influenza-virus membrane fusion by cooperative fold-back of stochastically induced hemagglutinin intermediates.* eLife, 2013. **2**: p. e00333.

25. Dobay, M.P., A. Dobay, J. Bantang, and E. Mendoza, *How many trimers? Modeling influenza virus fusion yields a minimum aggregate size of six trimers, three of which are fusogenic.* Molecular BioSystems, 2011. **7**(10): p. 2741-2749.
26. Razinkov, V.I., G.B. Melikyan, R.M. Epand, R.F. Epand, and F.S. Cohen, *Effects of spontaneous bilayer curvature on influenza virus–mediated fusion pores.* The Journal of General Physiology, 1998. **112**(4): p. 409-422.
27. Chernomordik, L., A. Chanturiya, J. Green, and J. Zimmerberg, *The hemifusion intermediate and its conversion to complete fusion: regulation by membrane composition.* Biophysical Journal, 1995. **69**(3): p. 922-929.
28. Chernomordik, L.V., E. Leikina, V. Frolov, P. Bronk, and J. Zimmerberg, *An early stage of membrane fusion mediated by the low pH conformation of influenza hemagglutinin depends upon membrane lipids.* The Journal of Cell Biology, 1997. **136**(1): p. 81-93.
29. Wessels, L., M.W. Elting, D. Scimeca, and K. Weninger, *Rapid membrane fusion of individual virus particles with supported lipid bilayers.* Biophysical Journal, 2007. **93**(2): p. 526-538.
30. Wrigley, N.G., *Electron microscopy of influenza virus.* BRITISH MEDICAL BULLETIN, 1979. **35**(1): p. 35-38.
31. Hess, S.T., M. Kumar, A. Verma, J. Farrington, A. Kenworthy, and J. Zimmerberg, *Quantitative electron microscopy and fluorescence spectroscopy of the membrane distribution of influenza hemagglutinin.* The Journal of Cell Biology, 2005. **169**(6): p. 965-976.
32. Vijayakrishnan, S., C. Loney, D. Jackson, W. Suphamungmee, F.J. Rixon, and D. Bhella, *Cryotomography of budding Influenza A virus reveals filaments with diverse morphologies that mostly do not bear a genome at their distal end.* PLOS PATHOGENS, 2013. **9**(6): p. e1003413.
33. Harris, A., G. Cardone, D.C. Winkler, J.B. Heymann, M. Brecher, J.M. White, and A.C. Steven, *Influenza virus pleiomorphy characterized by cryoelectron tomography.* Proceedings of the National Academy of Sciences, 2006. **103**(50): p. 19123-19127.
34. Ruigrok, R.W.H., P.J. Andree, R.A.M. Hooft Van Huysduynen, and J.E. Mellema, *Characterization of three highly purified influenza virus strains by electron microscopy.* Journal of General Virology, 1984. **65**(4): p. 799-802.
35. Skehel, J.J., P.M. Bayley, E.B. Brown, S.R. Martin, M.D. Waterfield, J.M. White, I.A. Wilson, and D.C. Wiley, *Changes in the conformation of influenza virus hemagglutinin at the pH optimum of virus-mediated membrane fusion.* Proceedings of the National Academy of Sciences, 1982. **79**(4): p. 968-972.
36. Gething, M.J., R.W. Doms, D. York, and J. White, *Studies on the mechanism of membrane fusion: site-specific mutagenesis of the hemagglutinin of influenza virus.* The Journal of Cell Biology, 1986. **102**(1): p. 11-23.
37. Schoen, P., L. Leserman, and J. Wilschut, *Fusion of reconstituted influenza virus envelopes with liposomes mediated by streptavidin/biotin interactions.* FEBS LETTERS, 1996. **390**(3): p. 315-318.
38. Stegmann, T., I. Bartoldus, and J. Zumbrunn, *Influenza hemagglutinin-mediated membrane fusion: Influence of receptor binding on the lag phase preceding fusion.* Biochemistry, 1995. **34**(6): p. 1825-1832.
39. White, J., J. Kartenbeck, and A. Helenius, *Membrane fusion activity of influenza virus.* EMBO Journal, 1982. **1**(2): p. 217-222.
40. Niles, W.D. and F.S. Cohen, *Single event recording shows that docking onto receptor alters the kinetics of membrane fusion mediated by influenza hemagglutinin.* Biophysical Journal, 1993. **65**(1): p. 171-176.

41. Wharton, S.A., J.J. Skehel, and D.C. Wiley, *Studies of influenza haemagglutinin-mediated membrane fusion.* VIROLOGY, 1986. **149**(1): p. 27-35.
42. Sheetz, M.P., *Membrane skeletal dynamics: role in modulation of red cell deformability, mobility of transmembrane proteins, and shape.* SEMINARS IN HEMATOLOGY, 1983. **20**(3): p. 175-188.
43. Krumbiegel, M., A. Herrmann, and R. Blumenthal, *Kinetics of the low pH-induced conformational changes and fusogenic activity of influenza hemagglutinin.* Biophysical Journal, 1994. **67**(6): p. 2355-2360.
44. Efron, B. and R. Tibshirani, *An introduction to the bootstrap*. Vol. 57. 1993: CRC press.
45. Lentz, B. and J. Lee, *Poly(ethylene glycol) (PEG)-mediated fusion between pure lipid bilayers: a mechanism in common with viral fusion and secretory vesicle release? (Review).* MOLECULAR MEMBRANE BIOLOGY, 1999. **16**(4): p. 279-296.
46. Lee, J. and B.R. Lentz, *Evolution of lipidic structures during model membrane fusion and the relation of this process to cell membrane fusion.* BIOCHEMISTRY, 1997. **36**(21): p. 6251-6259.
47. Gillespie, D.T., *General Method for Numerically Simulating Stochastic Time Evolution of Coupled Chemical Reactions.* Journal of Computational Physics, 1976. **22**(4): p. 403-434.
48. Massey, F.J., *The Kolmogorov-Smirnov test for goodness of fit.* JOURNAL OF THE AMERICAN STATISTICAL ASSOCIATION, 1951. **46**(253): p. 68-78.
49. Smirnov, N., *Table for estimating the goodness of fit of empirical distributions.* The Annals of Mathematical Statistics, 1948. **19**(2): p. 279-281.
50. Bar Massada, A. and Y. Carmel, *Incorporating output variance in local sensitivity analysis for stochastic models.* Ecological Modelling, 2008. **213**(3–4): p. 463-467.
51. Böckmann, R.A., A. Hac, T. Heimburg, and H. Grubmüller, *Effect of sodium chloride on a lipid bilayer.* BIOPHYSICAL JOURNAL, 2003. **85**(3): p. 1647-1655.
52. Pabst, G., A. Hodzic, J. Štrancar, S. Danner, M. Rappolt, and P. Laggner, *Rigidification of neutral lipid bilayers in the presence of salts.* BIOPHYSICAL JOURNAL, 2007. **93**(8): p. 2688-2696.
53. Floyd, D.L., S.C. Harrison, and A.M. Van Oijen, *Analysis of kinetic intermediates in single-particle dwell-time distributions.* BIOPHYSICAL JOURNAL, 2010. **99**(2): p. 360-366.
54. Cohen, F.S. and G.B. Melikyan, *The energetics of membrane fusion from binding, through hemifusion, pore formation, and pore enlargement.* Journal of Membrane Biology, 2004. **199**(1): p. 1-14.
55. Kuzmin, P.I., J. Zimmerberg, Y.A. Chizmadzhev, and F.S. Cohen, *A quantitative model for membrane fusion based on low-energy intermediates.* Proceedings of the National Academy of Sciences, 2001. **98**(13): p. 7235-7240.
56. Chizmadzhev, Y.A., *The mechanisms of lipid-protein rearrangements during viral infection.* Bioelectrochemistry, 2004. **63**(1-2): p. 129-136.
57. Kozlovsky, Y. and M.M. Kozlov, *Stalk Model of Membrane Fusion: Solution of Energy Crisis.* Biophysical Journal, 2002. **82**(2): p. 882-895.
58. Huang, Q., R.P. Sivaramakrishna, K. Ludwig, T. Korte, C. Böttcher, and A. Herrmann, *Early steps of the conformational change of influenza virus hemagglutinin to a fusion active state: Stability and energetics of the hemagglutinin.* Biochimica et Biophysica Acta-Reviews on Biomembranes, 2003. **1614**(1): p. 3-13.
59. Axelrod, D., D.E. Koppel, J. Schlessinger, E. Elson, and W.W. Webb, *Mobility measurement by analysis of fluorescence photobleaching recovery kinetics.* Biophysical Journal, 1976. **16**(9): p. 1055-1069.

60. Bernstein, D., *Simulating mesoscopic reaction-diffusion systems using the Gillespie algorithm.* Physical Review E, 2005. **71**(4): p. 041103.
61. Arjunan, S. and M. Tomita, *A new multicompartmental reaction-diffusion modeling method links transient membrane attachment of E. coli MinE to E-ring formation.* Systems and Synthetic Biology, 2010. **4**(1): p. 35-53.
62. Klein, A.M., V. Nikolaidou-Neokosmidou, D.P. Doupé, P.H. Jones, and B.D. Simons, *Patterning as a signature of human epidermal stem cell regulation.* JOURNAL OF THE ROYAL SOCIETY INTERFACE, 2011. **8**(65): p. 1815-1824.

CHAPTER 4: Influenza Virus-Membrane Fusion triggered by Proton Uncaging for Single-Particle Studies of Fusion Kinetics

Deirdre A. Costello[†], Donald W. Lee[†], Jennifer Drewes[‡], Kevin A. Vasquez[†], Kassandra Kisler[§], Ulrich Wiesner[‡], Lois Pollack[§], Gary R. Whittaker[⊥], and Susan Daniel[†*]

†School of Chemical and Biomolecular Engineering, Cornell University, Ithaca, New York, United States
‡Department of Materials Science and Engineering, Cornell University, Ithaca, New York, United States
§School of Applied and Engineering Physics, Cornell University, Ithaca, New York, United States
⊥Department of Microbiology and Immunology, Cornell University, Ithaca, New York, United States

Reprinted with permission from Analytical Chemistry, Vol 84, Issue 20, Pg 8480-8489, 2012.

ABSTRACT

We report a method for studying membrane fusion, focusing on influenza virus fusion to lipid bilayers, which provides high temporal resolution through the rapid and coordinated initiation of individual virus fusion events. Each fusion event proceeds through a series of steps, much like multistep chemical reaction. Fusion is initiated by a rapid decrease in pH that accompanies the "uncaging" of an effector molecule from o-nitrobenzaldehyde, a photoisomerizable compound that releases a proton to the surrounding solution within microseconds of long-wave ultraviolet irradiation. In order to quantify pH values upon UV irradiation and uncaging, we introduce a simple silica nanoparticle pH sensor, useful for reporting the pH in homogeneous nanoliter volumes under conditions where traditional organic dye-type pH probes fail. Subsequent single-virion fusion events are monitored using total internal reflection fluorescence microscopy. Statistical analysis of these stochastic events

uncovers kinetic information about the fusion reaction. This approach reveals that the kinetic parameters obtained from the data are sensitive to the rate at which protons are delivered to the bound viruses. Higher resolution measurements can enhance fundamental fusion studies and aid antiviral antifusogenic drug development.

INTRODUCTION

Fusion of cell membranes is a ubiquitous biological process involved in vesicle fusion to membrane synapses, fertilization between sperm and egg cells, the merging of intracellular lysosomes, and membrane-enveloped virus fusion to endosomes[1]. The fusion step is critical to the delivery of material across membranes. For example, in virus infection, membrane-enveloped viruses, such as influenza, infect cells via the endocytotic pathway, which necessitates the merging of the viral membrane with the endosomal membrane to pass viral genetic material into the cytosol. For many enveloped viruses, a drop in endosomal pH triggers conformational changes in the viral coat proteins required to initiate fusion between the viral and endosomal membranes[2]. Characterization of virus fusion kinetics is important for a number of reasons beyond understanding fundamental fusion processes, such as classification of viral strain virulence and in the development of antifusogenic drugs[3]. Yet, directly studying fusion in vivo is difficult because it occurs inside intracellular compartments that are cumbersome to control and assay. Therefore, much of what is known about virus fusion has been determined using bulk or ensemble in vitro fusion assays that report on the collective fusion behavior of many viruses to model membranes[4-14].

In bulk fusion assays, virus fusion is typically reported by a collective change in intensity resulting from fluorescence dequenching upon fusion of an ensemble of fluorescently labeled

viruses to model membranes[4-14]. Fusion is initiated by acidification of the bulk solution. From the resulting temporal change in the fluorescence signal, some information about the kinetics of virus fusion can be obtained. Many studies of virus fusion to date have been conducted using this type of assay[4-14], but there are significant limitations with this approach. First, because individual events cannot be observed in this assay, viral binding and fusion cannot be distinguished from each other; this constraint impedes the separation of transport limitations from the fusion kinetics. Second, as the output signal is an aggregate of fluorescence changes resulting from many stochastic fusion events, only averaged information can be obtained from these assays; this drawback can obscure processes that occur at shorter time scales. Third, temporal limitations in uniformly acidifying the solution can spread initiation times of individual events, impacting signal response and its analysis. This limitation can reduce the temporal resolution of the measurements and obscure the sensitivity of initiating pH on kinetics[15].

Direct observation of individual virus fusion events circumvents many of the drawbacks of ensemble methods. Single particle virus fusion methods were first developed around the early 1990s[16-18] and have improved significantly since then with modern electronics and optics capable of single molecule fluorescence detection, microfluidic approaches for fluid handling, and new strategies for creating robust membranes. More recent work has provided information on the kinetics of intermediate steps of the fusion mechanism by employing total internal reflection fluorescence microscopy (TIRF)[19] to detect individual virus fusion events to solid-supported lipid bilayers (SLBs) adsorbed to the walls of microfluidic devices[20-21]. Although today's single particle virus fusion studies are easier to implement and can provide more insight into virus fusion than previously possible, two significant

limitations of this approach remain: the rate at which acidification can be achieved in the confined space of the microfluidic device via acidic buffer exchange and the subsequent shearing that is imposed in the channel due to the flow.

Here, we describe a method to achieve rapid acidification under quiescent conditions by integrating a photoisomerizable compound, o-nitrobenzaldehyde (o-NBA), into our single particle fusion assay. o-NBA donates a proton to the surrounding solution when illuminated with a 355 nm longwave ultraviolet laser[22] with release times on the order of microseconds[23]. This acidification method will hereafter be referred to as "proton uncaging". The photolysis of o-NBA to create a pH jump has been used in the investigation of the mechanisms of biological systems because it offers very high time resolution for kinetic measurements. In a review by McCray et al. [22], applications for uncaging are highlighted that include the study of active transport of proteins in muscle fibers, mechanistic studies of ion channels, and time-resolved responses of bacterial flagella motors to rapid changes in extracellular pH. Abbruzzetti et al. [24] used it to examine the dissociation kinetics of histidines in Gu HCl-unfolded Fe(III) cytochrome C to increase the temporal resolution of data acquisition and allow for investigation over a wider temperature range. Saxena et al.[25] studied the kinetics of proton transfer in green fluorescent protein (GFP) using o-NBA, as a model system for characterizing the correlation between dynamics and function of proteins in general. Each of these examples illustrates the advantages of using a rapid pH jump to study pH-dependent kinetic processes. To the best of our knowledge, however, uncaging has not yet been employed for the study of pH-dependent fusion kinetics of enveloped viruses to host membranes.

There are several advantages of an uncaging strategy that are particularly beneficial for kinetic studies of viral fusion. First, the rate of release of the effector molecule (a proton) is much faster than rapid exchange of solution. Second, the effector molecule can be released close to the target, i.e., the fusion protein. Increasing the certainty of when the acidification occurs and ensuring the coordinated initiation of fusion events improves the resolution of fusion kinetics. Uncaging times are much faster than the protein conformational change for influenza hemagglutinin (HA) X:31 at the optimum triggering pH of ~5.0 [26] . A third advantage is that the environment in which the dynamics are studied is unperturbed by external forces resulting from hydrodynamic flow. The quiescent surroundings more closely mimic the endosomal environment and eliminate the possibility of hydrodynamic deformation of protein structures, which could (slightly) change the conformation of the protein− receptor complex and impact fusion kinetics. Fourth, the absence of flow makes it possible to follow multiple processes (e.g., binding, hemifusion, pore formation) within an individual virion without it leaving the field of view.

By adjusting the concentration of o-NBA, the triggering pH immediately following uncaging can be tuned to achieve pH values within the range of physiological fusion pH for influenza. The characterization of the pH change in nanoliter volumes is a challenge, however, as the UV irradiation triggering proton uncaging also typically bleaches pH sensing reporter dyes. In order to be able to quantify pH, a more UV resistant sensor probe thus had to be developed.

METHODS

Supported Lipid Bilayers

The following lipids were used in these experiments: 1,2-dioleoyl-sn-glycero-3-phosphocholine (DOPC), 1-palmitoyl-2-oleoyl-sn-glycero-3-phosphocholine (POPC), cholesterol, and total ganglioside extract (bovine, brain). Lipid vesicles were prepared using a molar ratio of 4:4:2:0.5 of DOPC, POPC, cholesterol, and total ganglioside extract. For acidic flow experiments, 0.01 mol % Oregon green DHPE lipid was added to the bilayer formulation to signal the pH drop. A detailed procedure for making liposomes used to form the supported bilayers and characterization can be found in the Supporting Information.

Virus Labeling

Influenza X:31 (H3N2) with a hemagglutinin (HA) concentration of 2 mg/mL (as determined by Charles River Laboratories) was used in all experiments. Virus membranes were labeled with lipophilic fluorophores, octadecylrhodamine B chloride (R18), a red-emitting fluorophore, or Rhodamine 110 octadecyl ester (R110C18), a green-emitting fluorophore, at sufficient concentrations to (semi-) quench fluorescence, following slight modifications to standard procedures[4, 27] as described in the Supporting Information. Virus internal contents were labeled with Sulforhodamine B (SRB), a red-emitting fluorophore, as described in the Supporting Information.

C Dot pH Sensor Synthesis and Characterization

Fluorescent core−shell silica nanoparticle (Cornell or C dots) sensors were synthesized via a modified Stöber synthesis[28-29]. In contrast to earlier ratiometric two-color sensor particles[30-31], here, only single-color C dot sensors were required as pH sensing was performed in environments homogeneous on the length scale of the optical microscope

resolution. To that end, first, Oregon green maleimide was conjugated with MPTMS at a molar ratio of 1:50 (dye/MPTMS) in dimethyl sulfoxide under nitrogen for 12 h. The dye conjugate solution was then added to an ethanolic solution of 0.02 M ammonia and 4.275 M deionized water at a final concentration of $1.7 \times 10{-}5$ M dye conjugate. To this, a pure silica precursor, tetraethylorthosilicate, TEOS, was added at a concentration of 0.05 M. After reacting for 12 h, the cores were coated with a shell of additional TEOS (0.140 M) added in 31 equal aliquots at 10 min intervals. The C dots were allowed to react for 12 h after the shell addition and were then dialyzed to deionized water. The particles in water were then densified by heating at 120 °C in a tightly sealed reaction vial for 48 h. This postsynthesis densification step provided improved UV stability of the encapsulated dye (data not shown). The final size of the single- color C dots sensor was determined by dynamic light scattering using a Malvern Zetasizer Nano, indicating an average diameter of 28 nm.

TIRF Microscope Configuration

Fusion assays were carried out using total internal reflection fluorescence microscopy using an inverted Zeiss Axio Observer.Z1 with a α Plan-Apochromat 100× oil objective with a numerical aperture (NA) of 1.46. Index-matching liquid (Carl Zeiss, Inc.) was used to couple the glass coverslip of the flow cell device to the objective. In this setup, two lasers can be used simultaneously to excite different color fluorophores; we used 561 and 488 nm excitation wavelengths from solid-state lasers. These were coupled into the optical pathway of the microscope using a Laser TIRF 3 slider (Carl Zeiss, Inc.), which controlled the angles of incidence. Exceeding the critical angle (~62°) ensured total internal reflection of the lasers and created evanescent waves about 100 nm thick. The evanescent waves excited fluorescently labeled virus bound to sialic acid groups of the ganglioside lipids comprising

the lipid bilayers, which was positioned within several nanometers of the glass−water interface. The excitation laser light was band-pass filtered through a Semrock 74 HE GFP/mRFP filter cube and then combined with a dichroic mirror before being focused on the outer edge of the back aperture of the objective. The fluorescence emission signal was filtered through a 525/31 and 616/57 nm dual band-pass emission filter and then sent to an electron multiplying CCD camera (Hamamatsu ImageEM C9100-13, Bridgewater, NJ). For acid flow and dual labeling experiments, the emission was passed through a splitter (Photometrics DV2) to divide and focus green and red channels onto separate regions of the EMCCD camera.

Execution of the o-Nitrobenzaldehyde Proton Uncaging Assay

Supported lipid bilayers were formed in the flow cell via vesicle fusion[32-34] by drawing a 10% dilution of liposomes into each channel at a flow rate of 100 μL/min for 1 min using a syringe pump (PHD 2000 Infuse/Withdraw, Harvard apparatus, Holliston, MA). After 1 min, the flow rate was reduced to 10 μL/min for 10 more minutes and then stopped to allow the channel to incubate for an additional 10 min. After this incubation, a fresh solution of liposomes was drawn into the channels and incubated for an additional 5 min to ensure a defect-free bilayer and complete coverage of the channel walls. The channels were then rinsed with buffer A (150 mM NaCl, 1.5 mM MES, 5 mM citric acid) for 2 min at 100 μL/min to remove unfused liposomes. Labeled virus was then pumped into the channels at 30 μL/min and allowed to incubate for 20 min. After the first incubation, additional virus was pumped into the channels, incubated for 10 min, and repeated until the desired surface density was reached. After the final incubation, o-NBA solution (for buffer B, see Supporting Information for preparation) was drawn into the channels at 100 μL/min for 3 min. We note

that no fusion was observed during the flow steps in any assay at any condition we used. The o-NBA solution was then incubated in the channel for 20 min to reduce any residual convection in the channel after pumping ceased.

The pH drop was initiated by irradiating a 100 μm diameter section of the channel with a 4 mW UV laser for 200 ms. The beam diameter was measured to be approximately 100 μm; thus, when the beam was centered in the field of view of the microscope, it actually covered an area greater than the field of view. We ensured that the uncaging was uniform by mapping out the fusion events across the field of view in time, as shown in Figure S1 in Supporting Information. The alignment of the laser is critical to ensuring that the uncaging is not biased; this can be achieved using a fluorescently labeled bilayer in an extra channel to map out the precise alignment prior to uncaging in virus-filled channels. Using this method, the time of the pH drop is known precisely, as the cleavage of protons from the o- NBA molecules occurs on the order of microseconds[23]. The lag between the closing of the UV shutter and the opening of the camera shutter was 200 ms. The UV flash time was 200 ms. Because of the accurate time control of this technique, it removed the requirement for a pH sensitive fluorescent probe to be present in the lipid bilayers to mark when the change in pH occurred. These probes can potentially interfere with the fusion and increase background noise in the images. Hemifusion lag times are defined as the time elapsed between acidification of the field-of-view and fluorescence dequenching for individual virus particles. Pore formation lag times are defined as the time between the start of the hemifusion step and the start of the release of the internal viral fluorophore.

The deprotonation of o-NBA resulted in a pH decrease from 7.0 to 5.4, 4.9, or 4.6, depending on the amount of o-NBA added to the buffer (see Supporting Information for exact formulations of the buffers). Fluorescence images of the viral fusion events were collected at 50 ms intervals for 2 min. In a few cases, images were taken for longer times to ensure all fusion events were captured within the typical 2 min acquisition time.

Execution of the Acidic Buffer Flow Exchange Assay

In this experiment, the formation of bilayers, virus binding, and rinsing steps were conducted as described above. Here, instead of initiating hemifusion using the proton uncaging method, hemifusion was initiated by flowing buffer A (150 mM NaCl, 1.5 mM MES, 5 mM citric acid) precalibrated over a range of low pH values into the flow-cell at a flow rate of 100 μL/min for 2 min. The time at which acidification of the flow cell occurred was marked by a decrease in fluorescence of Oregon green DHPE present in the supported bilayer for this purpose. Images were collected at an interval of 100 ms for 3 or 4 min.

RESULTS

Individual Virion Fusion Assay

We monitored individual influenza X:31 (H3N2) virus fusion events occurring inside a microfluidic device that had its walls coated with supported lipid bilayers to mimic the endosomal membrane. Supported lipid bilayers have served as excellent cell membrane mimics in numerous applications since their introduction in the 1980s[32] because they are chemically tunable and preserve the twodimensional fluidity of constituents. This fluidity is key, as influenza is capable of multivalent binding to sialic acid receptors present in the bilayer. In this application, we employed a bilayer containing a mix of sialic receptors for virus binding. Once the bilayer formed in the device, fluorescently labeled virus was

introduced into the channel and bound to the supported bilayer as described in Materials and Methods.

The microfluidic device was coupled to a total internal reflection fluorescence microscope, as illustrated in Figure 1A, and used to image the individual virus fusion events. After fusion initiation by acidification, fluorescence dequenching of a green fluorophore in the viral membrane signals the onset of the merging of the opposing leaflets of the virus and the supported bilayer, called "hemifusion." The fluorescent "spike" and "cloud" features are easily monitored with TIRF[20-21] because TIRF is a surface-specific technique that effectively eliminates any fluorescent signal from the bulk that might obscure single fusion events. Pore formation is marked by radial diffusion of a red fluorophore originating from inside the virus, colocalized with the green fluorophore. A sequence of images showing these features is given in Figure 2A and is described in more detail in the Supporting Information. A movie of virus fusion is also provided in the Supporting Information.

The fusion process is hypothesized to occur in several steps[12-14, 35-36]. First, the viral fusion protein, HA, undergoes a conformational change from a prefusion folded state to an extended state, exposing hydrophobic fusion peptides which insert into the host membrane. This intermediate undergoes an additional conformational change which brings the two distal leaflets of each membrane close to each other, causing them to merge. Merging of the outer leaflets results in the creation of a hemifusion stalk, aided by the concerted action of several HA trimer units. We will hereafter refer to this coordinated unit as a "fusogenic complex." Eventually, this structure transforms into a fusion pore through which the viral RNA escapes the endosome and enters the cytosol of the cell. Each step and conformational intermediate

has a characteristic lifetime; here, we focus on measuring the kinetic rate constant leading up to the hemifusion step and the lag time for pore formation following hemifusion. In this work, we compare the fusion of fluorescently labeled influenza virus to solid-supported lipid bilayers inside microfluidic channels initiated by the traditional acidification method (acidic buffer exchange by flow) and the proton uncaging method (Figure 1).

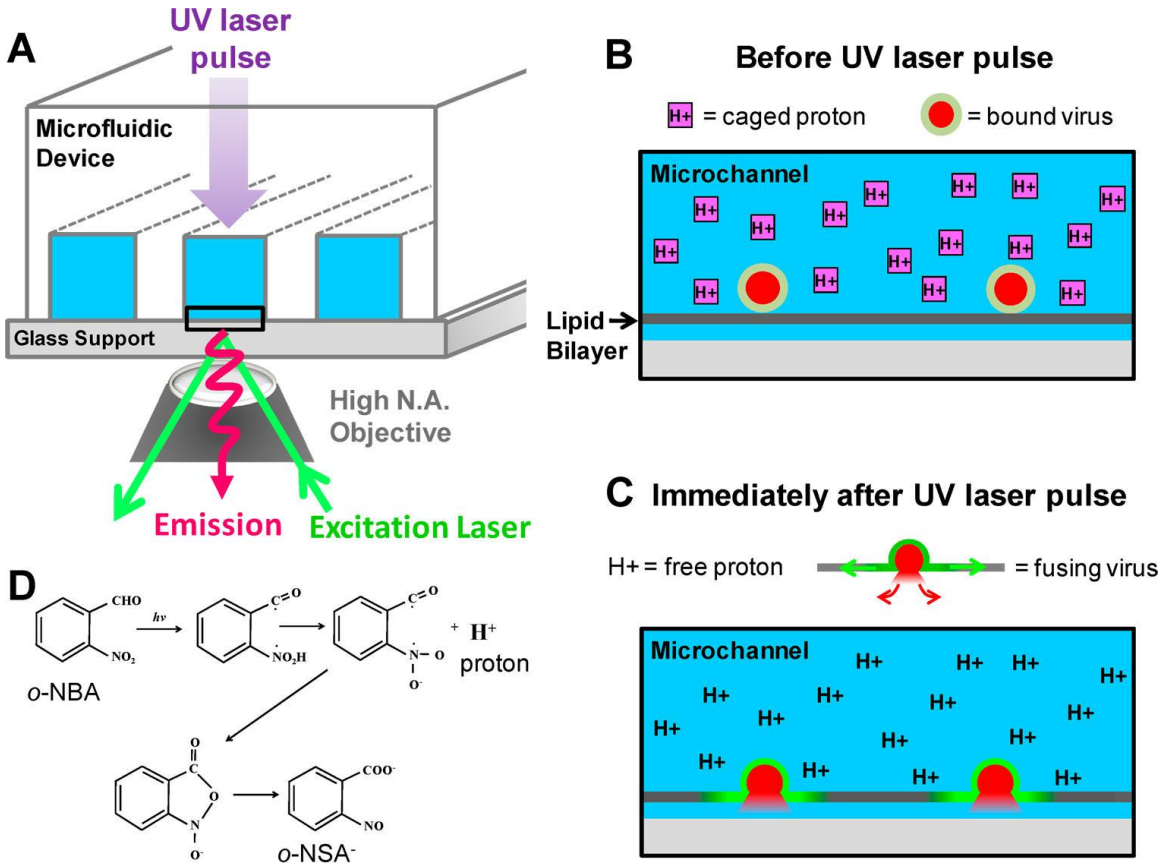

Figure 1 (A) An illustration of the microfluidic device coupled to a TIRF microscope for imaging individual virion fusion events. The purple arrow entering the top of the device represents a UV laser that is aligned directly with the microscope objective beneath the device. Note that thedimensions of this drawing are not to scale. The actual channel is about 130 μm wide by 70 μm high, and the diameter of the UV laser beam is about100 μm. (B) An inset of the region within the field of view of the camera, drawn as the black rectangle in (A), prior to UV irradiation at a neutral pH. This illustration shows that the glass surface comprising the fourth wall of the microchannel is coated with a solid supported lipid bilayer (gray).Virus labeled with a quenching concentration of fluorophore is colored light green with a red interior. The dark pink boxes represent proton cages(o-NBA) that release protons when illuminated with 355 nm light. Note that this drawing is also not to scale; influenza virus is typically 100 nm in diameter, and the bilayer is ~4 nm thick. (C) Immediately following UV irradiation, the caged protons are released (denoted as free H+ in the diagram), acidifying the surrounding solution. Fusing viruses are now colored bright green to denote the dequenching of green fluorophores and the escape of the internal red dye upon pore formation. (D) The photochemistry of uncaging: the conversion of o-nitrobenzaldehyde to o-nitrosobenzoicacid and a proton upon irradiation with UV light. Adapted from ref [37]. Copyright 1980 American Chemical Society.

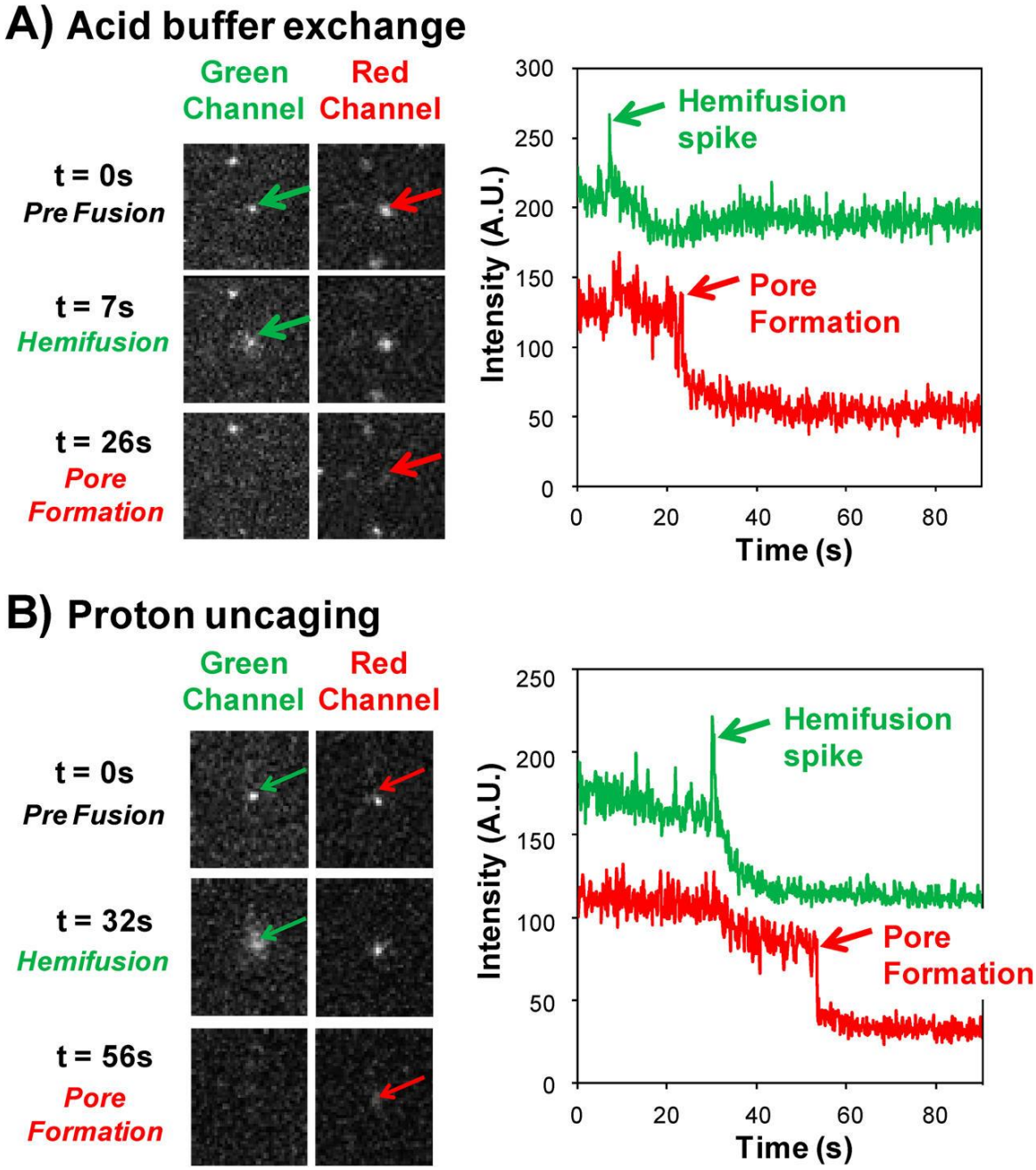

Figure 2 (A) Virus fusion initiated by acidic buffer flow exchange. Green and red fluorescence images of a single fusing virus, marked by the arrows. After acidification, the green channel shows the hemifusion of the membranes; the spike in fluorescence is observed in the plot to the right. The red channel shows the radial diffusion of the internal red fluorophore after pore formation. The drop in red signal can be observed in the plot to the right; here, it takes ~20 s between hemifusion and pore formation. (B) Virus fusion initiated by proton uncaging. Here, it takes ~15 s between hemifusion and pore formation.

Single Particle Fusion Assay Using Acidic Buffer Flow Exchange to Initiate Virus Fusion

As both a validation of our assay setup and a control case, we initiated virus fusion by acidic buffer exchange, i.e., by flowing an acidic buffer through the microfluidic channel, not by uncaging. Initially, virus was introduced into the microfluidic device at pH 7.0 and allowed to bind. Unbound virus was gently rinsed from the channel with buffer at pH 7.0. Subsequently, citric acid buffer at various pHs was sent through the channels at a rate of 100 μL/min. We chose this specific flow rate for several reasons. First, we wanted to match conditions as closely as possible with previously published reports[20]. Second, we selected this moderate flow rate as a compromise between fast flow (for rapid delivery of protons) and slow flow (to minimize shear rates). The rate of buffer exchange must be low enough to minimize tearing viruses off the receptors and/or stretching of the protein conformations which could cause non-native fusion protein− proton interactions and impact kinetics. Balancing these constraints, the 100 μL/min flow rate leads to acidification times for the field of view at 100× magnification of several seconds, as measured by the drop in fluorescence of a pHsensitive fluorophore (Oregon green DHPE) doped into the supported bilayer. Images of the field of view were acquired just before and during acidification at 100 ms intervals. All fusion events within the field of view were recorded and cataloged by the time point at which the dequenching spike occurred immediately following acidification. A representative set of data for the frequency of events as a function of time after acidification using acid buffer exchange is shown in Figure 3A (open black circles). These data were fit with a cumulative gamma distribution as described in the Supporting Information. Hemifusion kinetic parameters were determined from the best fits of the data for various initiating pHs, as shown in Figure 4 (black circles). The good agreement with previously reported values[20], using

the same experimental conditions, validates our assay and provides a point of comparison for the uncaging acidification strategy examined later.

The lag time between the hemifusion step and pore formation was also monitored. Previous work under similar experimental conditions has shown that pore formation lags hemifusion on the order of tens of seconds[20] and that this step is independent of pH[13, 20]. A histogram for the pore formation lag time for one set of data taken at pH 4.5 is shown in Figure 4B (top) and agrees with previous work. We note that, in our case, however, a polymer cushion was not used to support the bilayer as employed in previous work[20]. Despite this, our results are quite similar indicating that the polymer cushion may not be necessary for this assay. Eliminating this cushion preparation step can reduce the assay preparation time greatly.

To compare these results to the proton uncaging acidification strategy, it is imperative to know the pH following the uncaging event, but to our knowledge, there is no published characterization of the postirradiated pH following uncaging, most likely because no reporter probe existed that could withstand the high energy irradiation of UV without significant photobleaching. Therefore, we first report results obtained from a simple pHsensing probe we developed to calibrate the pH in nanoliter volumes that can withstand the UV irradiation conditions in our experiment. pH-sensing single-color C dots are composed of Oregon green fluorophore encapsulated in a silica core and surrounded by a pure silica shell. As described in the Materials and Methods section, these C dots sensors were densified in a postsynthesis heating step. Our rational for this dyeencapsulation approach was based on the fact that (i) silica is known to absorb (and therefore shield from) UV radiation and (ii) the C dot

architecture is known to improve photobleaching behavior of organic chromophores through its rigid silica matrix[38]. Such particles may also find uses as pH sensors in small volumes in other microfluidic or in vivo applications (e.g., endosomal pH monitoring) or as novel UV sensors beyond the application presented in this work.

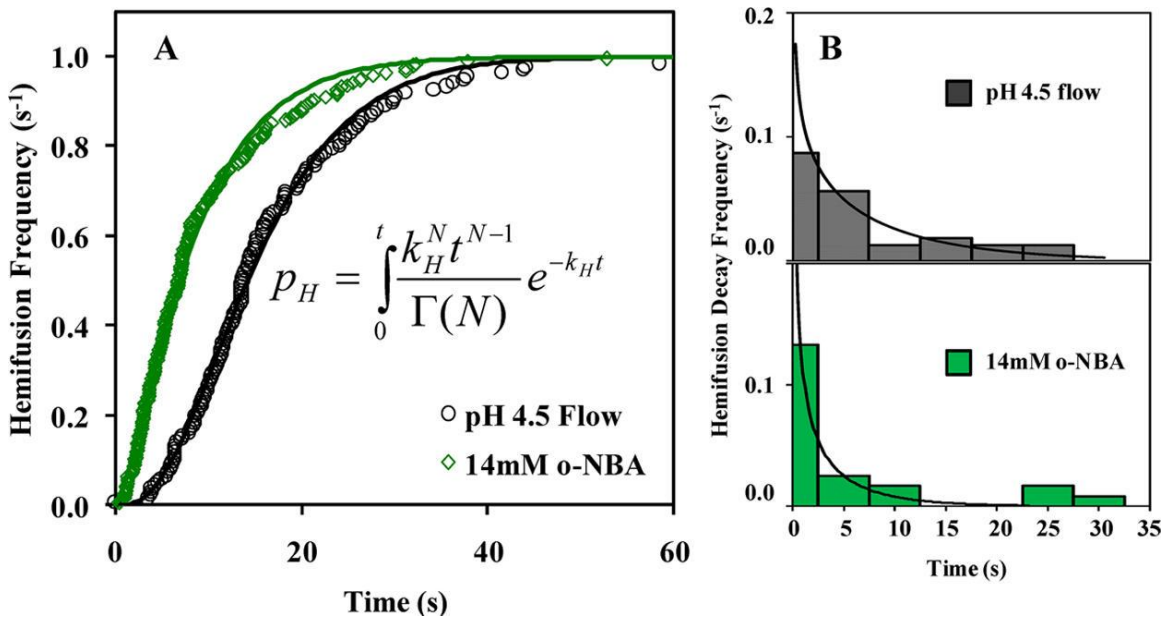

Figure 3 (A) Frequency of hemifusion events plotted as a function of time for initiation pH 4.5 obtained either by acidic buffer exchange (open black circles) or by proton uncaging using 14 mM o-NBA (open green diamonds). The lines are the best fits to gamma function equation shown in the inset and are described in detail in the Supporting Information. The rate of hemifusion, kH, was 0.20 ± 0.01 s−1 and 0.17 ± 0.01 s−1 for acidic buffer exchange and proton uncaging, respectively. N values for acid exchange and uncaging are 3.2 ± 0.1 s−1 and 1.51 ± 0.05 s−1, respectively. (B) Histograms of lag times between the onset of hemifusion and the onset of pore formation. (Top) Acidic buffer exchange; (Bottom) proton uncaging. The rate of transition from hemifusion to pore formation (kH→P) using the acid flow and uncaging methods was found to be 0.08 ± 0.02 s−1 and 0.09 ± 0.05 s−1, respectively. N was less than 1 in both cases (0.7 ± 0.1 for acid flow and 0.5 ± 0.1 for uncaging), which agrees with previous findings that there is a single step transition between hemifusion and pore formation.

Comparison of pH-Sensing Sensitivity between Free Oregon Green and Silica-Encapsulated Oregon Green after UV irradiation

Release of protons from o-NBA occurs within microseconds[23] when illuminated with 355 nm wavelength light. A pulsed diode pumped solid state laser by Teem Photonics (Model # SNV-04P-000, Lafayette, CO) was used to initiate proton uncaging in the microfluidic device. Uniformity of laser illumination was confirmed by mapping the virus fusion event location in the field of view and noting that the events were random (Supporting

Information). The pH in the microfluidic channel after the 200 ms UV pulse was measured using the pH sensitive C dot sensors encapsulating Oregon green. We note here that free Oregon green (devoid of a silica shell) suffered significant photobleaching from the UV pulse and thus could not be used as a pH sensor in this application. Other pH-sensitive fluorophores we tried also failed due to significant photobleaching. Figure 5A compares the level of photobleaching of free Oregon green and the silica-encapsulated Oregon green. This figure clearly shows that the silica capsule protects the Oregon green from photobleaching and that the level of photobleaching is not dependent on the pH of the solution.

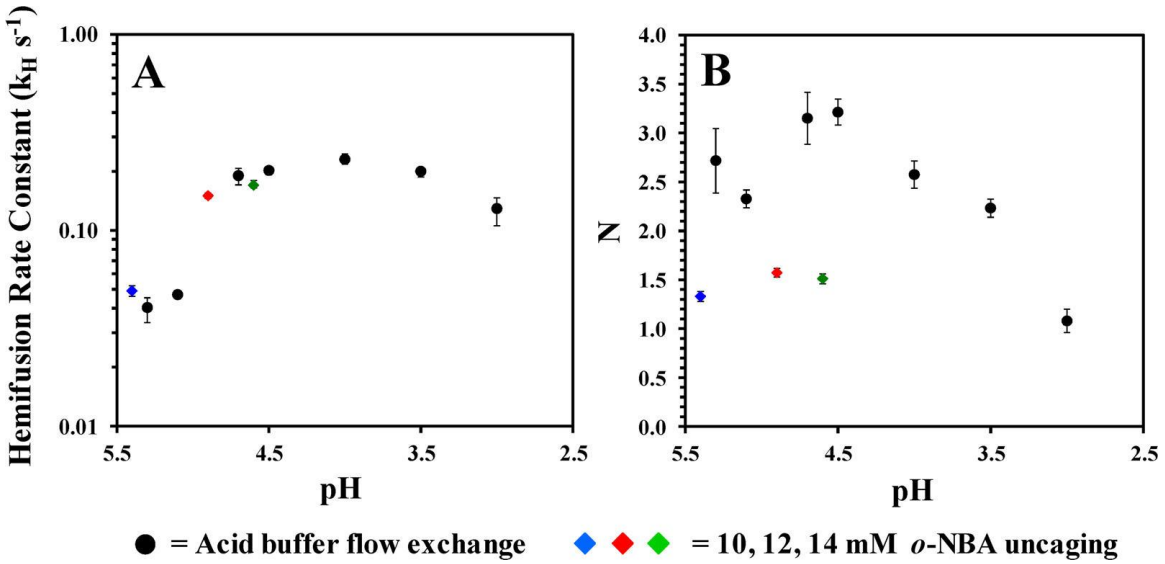

Figure 4 (A) Hemifusion rate constants, k_H, and (B) N parameters for a range of fusion initiation pH values.

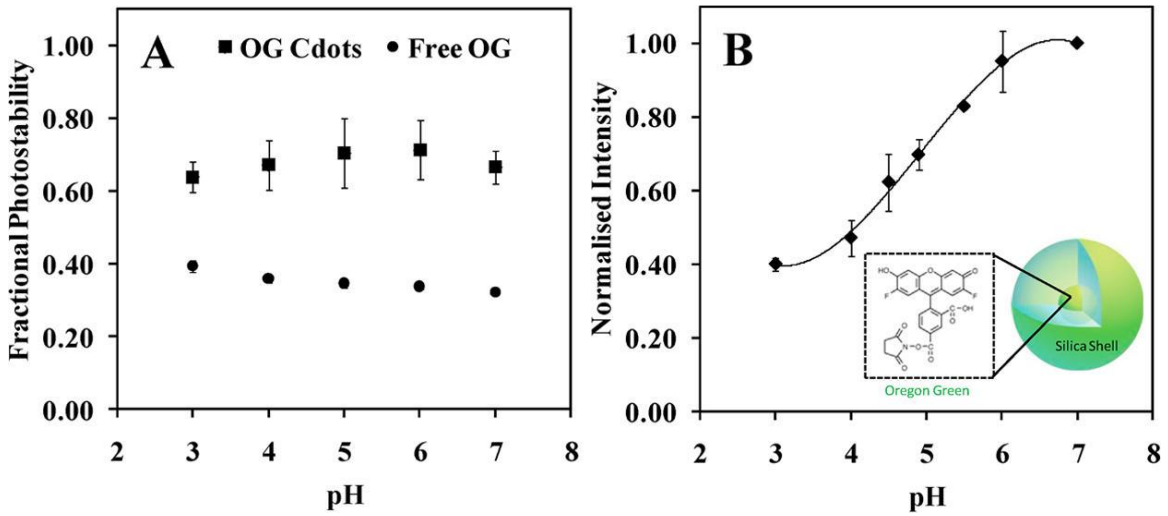

Figure 5 (A) Comparison of photobleaching between Oregon green C dots sensor and free Oregon green after exposure to UV light for 200 ms. Note that the error bars in the free OG case are within the data point. All values are normalized to the intensity value before the 200 ms UV bleach to obtain a fractional photostability at each pH. (B) Calibration curve for Oregon green C dot sensor fluorescence intensity at various pH values. All data were normalized to the pH 7.0 value so that intensities post-UV irradiation could be compared directly. Note that these data were taken after irradiating the samples with UV light to account for photobleaching in the uncaging runs. (Inset) Structure of the Oregon green C dot.

Calibration of the Final pH after Irradiation of o- Nitrobenzaldehyde Buffer with UV Light Using C Dots

Solutions of single-color C-dot sensors were prepared in buffer C (1.25 mM MES, ranging from pH 3 to 7). These solutions were loaded into microfluidic channels and imaged under quiescent conditions. Each channel containing a different pH solution was exposed to a 200 ms UV pulse, and images were acquired at an exposure time of 100 ms for 1 min. A calibration curve matching fluorescence intensity to pH (Figure 5B) was generated by normalizing the post-UV bleach intensity value of each solution to the post-UV bleach intensity at pH 7 according to the following equation

$$I_{calibration} = \frac{I_{bleach}^{pHX} - I_{background}}{I_{bleach}^{pH7} - I_{background}}$$

where pHX is the pH of the calibration solution or the 10, 12, or 14 mM solution of o-NBA in buffer C. The pH post-UV pulse was then determined by matching the normalized intensity for each o-NBA concentration to the corresponding pH on the calibration curve. Note that this calibration curve matches well to the published Oregon green pH response curve[39] and indicates that as expected the presence of the silica shell does not impede the pH sensing ability of the Oregon green molecule.

It should be noted that the pH reported in Table 1 is the pH approximately 200−300 ms after the UV pulse, as there is a lag time between the laser shutter closing and the detector turning on. This delay may contribute to the variation in the measurements, as it is possible that the exact pH in the irradiated zone just after the laser hits is slightly lower than what we report here due to the diffusion of any unbound protons along the length of the channel. Because the entire channel is not irradiated with the UV light, the pH in the irradiated zone will recover (see Supporting Information for details on recovery characteristics in this device). Previous work has shown, however, that the steps following the initial conformational change of the protein induced by low pH do not require a low pH environment themselves[13-14]; therefore, recovery postfusion initiation should not impact the kinetics obtained. Our work corroborates this previous work, as will be discussed later. All experiments were conducted at ambient temperature (~23 °C).

Table 1 Post-UV pH Calibration Table for Various Cage Solutions

Concentration of o-NBA in buffer	**10 mM**	**12 mM**	**14 mM**
Intensity Value	0.83 ± 0.12	0.69 ± 0.06	0.63 ± 0.01
pH from Calibration Curve	5.4 ± 0.5	4.9 ± 0.2	4.6 ± 0.1

Single Particle Fusion Assay Using Proton Uncaging to Initiate Virus Fusion.

In this set of experiments, acidification was achieved by proton uncaging. The chemical reaction upon UV excitation of o-NBA is shown in Figure 1D: o-NBA undergoes an intramolecular proton transfer reaction and is converted to a nitronate ion and a proton. The nitronate ion is then converted to an o-nitrosobenzoic anion[40].

In these experiments, virus was introduced into the microfluidic device at pH 7.0 and allowed to bind, as previously described. Buffer at pH 7.0 containing a precalibrated amount of o-NBA was used to rinse out the unbound virus. Next, a small region of the channel, prealigned with and encompassing the field of view of the microscope objective, was irradiated for 200 ms with 355 nm light from a solid state UV laser to "uncage" the proton of the o-NBA, as shown in Figure 1A,B. Immediately preceding and following irradiation, images were recorded at 50 ms intervals. Fusion events were detected and cataloged using the same procedure described previously for the acidic buffer exchange. A typical set of images of virus fusion initiated by proton uncaging acidification is shown in Figure 2B. Values for kH and N obtained from best fits of the data at various initiating pHs for buffer exchange (flow) acidification and uncaging are reported in Figure 4.

Comparing the results from the two experiments, there are important similarities and differences depending on the acidification method used (Figure 4). Interestingly, kH stays about the same, regardless of the acidification method; however, N is reduced. N is often interpreted to be the number of protein trimers that must act concertedly to initiate fusion[20, 41]. Several previous studies report a value of around three for hemifusion to occur[20, 42-

43], although prior literature includes the possibility that it could be as low as one[44] or as high as six[45-46].

There are several possibilities that could impact fusion kinetics and explain the lowering of N in the uncaging experiment relative to the acidic buffer exchange method. These include: (1) changes in the virus fusion machinery caused by UV irradiation, (2) interactions of the o-NBA or the reaction product, o-NSA−, with the fusion protein, (3) a significant change (drop) in the overall number of particles fusing per experiment (extent of fusion) that affects kinetic analysis, and (4) changes in the delivery rate of protons to the fusion proteins (leading to better coordination of initiation of events, more certainty of when the pH dropped, and elimination of shear effects). To identify the cause of the change, we ran a series of control experiments. A brief summary of the results is presented here only; the details and results of these control experiments are provided in the Supporting Information.

Impact of UV Irradiation on Kinetics

To ensure that UV irradiation itself does not trigger hemifusion or enhance fusion kinetics, a flow cell was prepared under the same experimental conditions as described previously for the proton uncaging experiment, except that it did not contain o-NBA. The flow cell was irradiated with the UV laser for 200 ms, and then, images were acquired at a rate of 200 ms post-UV irradiation. No fusion events were detected. Following this data acquisition, fusion was induced by flowing acidic buffer at pH 5.1 into the channel. In this part of the experiment, hemifusion occurred as previously reported in the acidic buffer exchange experiments, indicating that prior exposure to long wave UV radiation did not affect the

ability of the prebound viruses to fuse, in accordance with prior literature[47]. kH obtained for these conditions was 0.07 ± 0.003 s−1 with N value of 2.2 ± 0.10.

Impact of o-NBA or o-NSA− on Fusion Kinetics

To ensure that the presence of o-NBA or o-NSA− did not alter the fusion kinetics, we conducted fusion experiments in exactly the same way as described previously for acidic flow experiments, except the virus was incubated with either o-NBA or o-NSA− (both at pH 7.0) for 30 min prior to acidic buffer flow exchange. Upon acidification by acidic buffer exchange, the kinetic parameters obtained were nearly the same as in the absence of these compounds. The respective values of kH and N obtained for each case were 0.17 ± 0.006 and 2.1 ± 0.07 and 0.21 ± 0.01 and 2.9 ± 0.14. Thus, we confirmed that the presence of o-NBA or o-NSA− did not lead to significant changes in kinetic parameters compared to the acidic flow case devoid of these compounds and that only during uncaging were differences in N observed.

Assessment of Changes in the Extent of Fusion

To ensure that there was no artifact in the kinetic analysis resulting from a reduction in extent of fusion by the proton uncaging method, we compared the extents of fusion between the acidic buffer exchange experiments and the uncaging method. We found that the overall number of virions fusing in a given experiment at a given pH were similar (Table 2). This result shows that the uncaging process has enough power to initiate the fusion of any virus present in the UV beam during the short pulse duration. We corroborated this result by irradiating the same area with a second UV pulse and found that no more fusion was initiated within a given region. Even though the UV pulse is short-lived, we obtain the same extent of

fusion and hemifusion rate constants with uncaging as we obtain with the buffer exchange method; only N differs. Previous studies of influenza X:31 fusion after neutralization immediately following acidification show that, once the fusion protein is "activated," the rest of the process does not necessarily require a low pH environment[13-14]. Therefore, the similarity of the fusion extents and hemifusion rate constants we obtain by these different acidification methods also corroborates these reports in the literature that the intermediate fusion steps are not strongly pH dependent.

Table 2 Extent of Virus Fusion Obtained with Various Fusion Initiation Methods

Fusion Initiation Method	Extent of Fusion (%)
14 mM o-NBA uncaging	27 ± 5
pH 4.5 acid flow exchange	17±6
pH 4.7 acid flow exchange	25 ± 7

Impact of the Method and Rate of Proton Delivery to the Fusion Proteins on Kinetics

The final possibility that could explain the lower value of N is the immediate availability of protons to fusion proteins upon uncaging compared to the acidic flow experiments. As N is in the exponent of the gamma fitting equation, it will be quite sensitive to initiation time. In the case of uncaging, the acidification to the target pH is rapid: the drop is complete after the 200 ms UV pulse. In contrast, the time to drop the pH by the acidic buffer flow exchange is significantly longer (order of seconds) due to the no slip boundary condition at the bilayer surface. The impact of faster proton delivery on kinetics could be manifested in several ways. First, immediate availability of protons at the fusion protein ensures the coordination of initiation of fusion events at a specific pH value; second, faster acidification means better precision in knowing the time when acidification actually occurred (time = 0) for more certainty in determining lag times used in kinetic analysis.

To speed up the delivery of protons by acidic buffer exchange to better coordinate events, we carried out experiments at higher flow rates (500 μL/min) to ascertain the difference in the data and fits, as shown in Figure 6. With faster flow rate, we do observe a shift in the data toward the uncaging trend and a decrease in N; however, the effect is small with only a 5-fold change in flow rate. We are precluded from increasing the flow rate much more in an attempt to match the uncaging value because the increased hydrodynamic shear on the bound virions starts to disrupt their attachment to the bilayer and significant shear may also lead to changes in kinetics as the HA may stretch and alter the binding pocket for the proton.

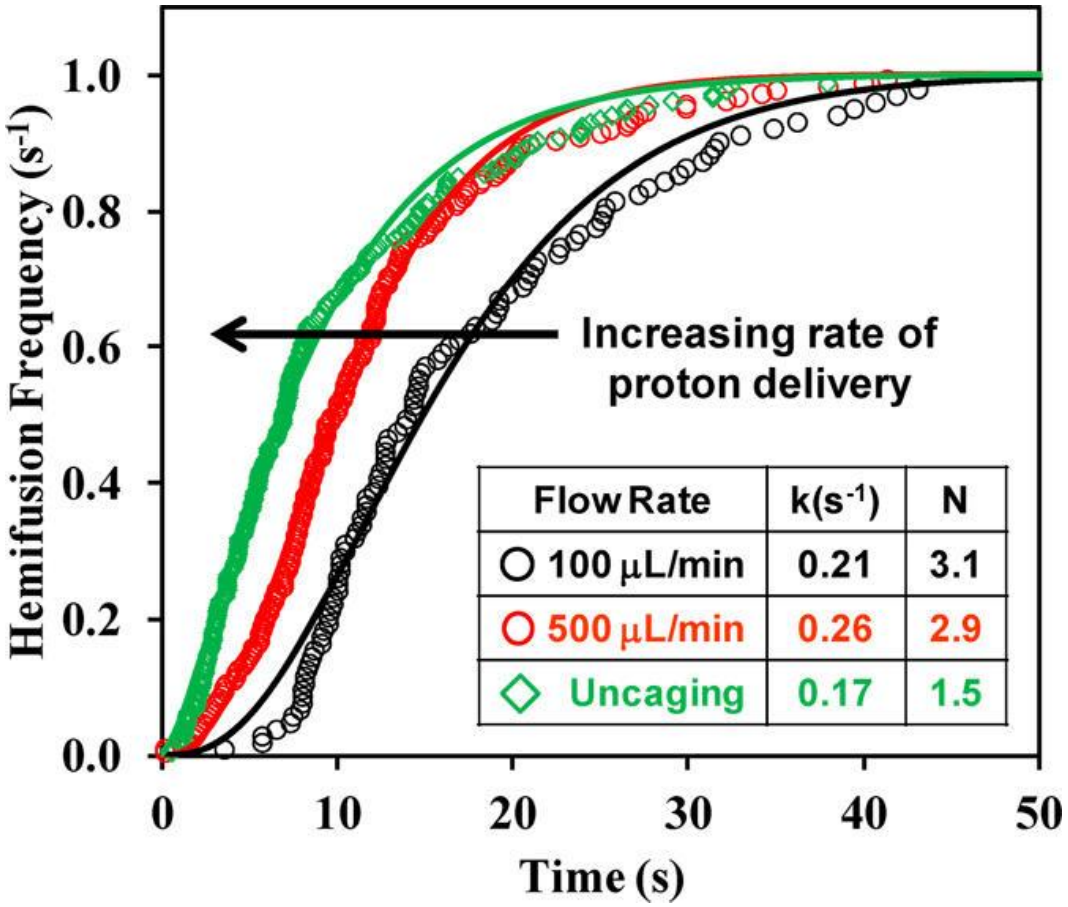

Figure 6 Fusion data at an initiation pH of 4.7. As the flow rate increases, the data trends shift closer to the uncaging data.

CONCLUSIONS

The dynamics of the HA protein conformational changes measured by variations in intrinsic tryptophan fluorescence are known to be on the millisecond time scale near pH 5.0[26]. While at the "optimal" pH (4.9), the protein conformational change is not thought to be the rate-limiting step in the fusion process; at "suboptimal" pHs (5.1 and above), a slower transition to the fusogenic conformational form of HA could explain slower fusion kinetics[26]. To eliminate proton transport effects on the measurement of the fusion kinetic parameters at "suboptimal" fusion pHs greater than 5.0, we used a proton uncaging strategy. The immediate availability of protons not only reduces or eliminates proton transport limitations but also synchronizes individual initiation times, increasing the resolution of the measurements obtained from analysis of the hemifusion data. Our data are consistent with the prevailing mechanism for influenza fusion mediated by HA, and the main finding here is that the number of trimers required for fusion is closer to two rather than three.

The commercially available o-NBA compound employed in this work is limited by its solubility in aqueous solutions to yielding a maximum change in pH from 7.0 to ~4.5; thus, we did not examine fusion below pH 4.5. We note that, under physiological conditions, influenza fusion occurs within this pH range in the endosome. However, other more soluble proton caged compounds can be synthesized[48-49] and used to study fusion at lower pH values using the uncaging method, which may be advantageous for studying other virus strains. Additionally, this approach is adaptable to studies of other membrane fusion processes (e.g., SNARE-mediated fusion) by changing the effector molecule to calcium[50-51], for example.

The impact of this work from a practical standpoint is that obtaining higher temporal resolution measurements of kinetic parameters between different virus strains aids in characterizing mutations that lead to enhanced fusion and viral infection. Furthermore, the fusion step, and in particular the HA protein, has become a target for antiviral drug development. Antifusogenic drugs, such as tert-butyl hydroquinone have been shown to strongly interact with the HA binding pocket to stabilize the neutral pH structure, which then presumably inhibits the conformational changes required for membrane fusion[3]; and more recently, antibodies have been developed that target the stem region of the HA and are expected to disrupt fusion activity[52-53]. With the method described here, the inhibition of viral fusion using these compounds could be tested directly and at a level of detail not available to date. This information will further refine antiviral drug design and characterization. SM Materials and suppliers, buffer preparations, surface preparation, microfluidic device fabrication, supported bilayer preparation and characterization, virus labeling and purification, fluorescence dequenching, and image processing. This material is available free of charge via the Internet at http://pubs.acs.org.

ACKNOWLEDGEMENTS

We thank the NIAID Centers of Excellence for Influenza Research and Surveillance (CEIRS) and, in particular, the New York Influenza Center of Excellence (NYICE) pilot program at the University of Rochester (grant 414529-G to S.D. and L.P.), the Nanobiotechnology Center at Cornell University (to L.P., G.R.W., and S.D.), the National Institutes of Health (grant R01 AI48678 to G.R.W.), and start-up funds from Cornell University (to S.D.) for supporting this work.

SUPPLEMENTAL NOTE (UNPUBLISHED)

Overview

The following materials are other contributions I made to this project. The first task was to formulate an appropriate buffer solution for uncaging. An issue is that since UV uncaging occurs in a small area within the microfluidic channels. The pH can suddenly drop and recover to neutral pH over time. Hence, I developed a micro-well system to remove the surrounding fluid issue. I also discuss how we arrived at the solution we used in the paper. The addition of both MES and citric acid was critical to ensure the pH range after uncaging does not always reach the pKa of oNBA. My duties entailed synthesizing the R110C18 dye via optimizing the procedure outlined by Floyd [20].

Developing appropriate buffer for UV uncaging

Since the pKa of oNBA is 2.7, the acidification can reach levels that are highly non-physiological. In order to address this issue, we must develop a buffer capable of buffering a wide pH range. Unlike acid-flow experiments where different buffers can be used to maintain pH of the solution (ie citric acid buffer for low pH and MES buffer for neutral pH), uncaging experiments requires a single buffer capable of maintaining all pH ranges. We combined MES and CA at 1mM concentration each and built a pH titration curve (Figure S1). We found that it has a very wide pH stability range, suitable for oNBA studies, and we were able to determine the amount of oNBA required in the solution to obtain a pH range suitable for virus fusion studies.

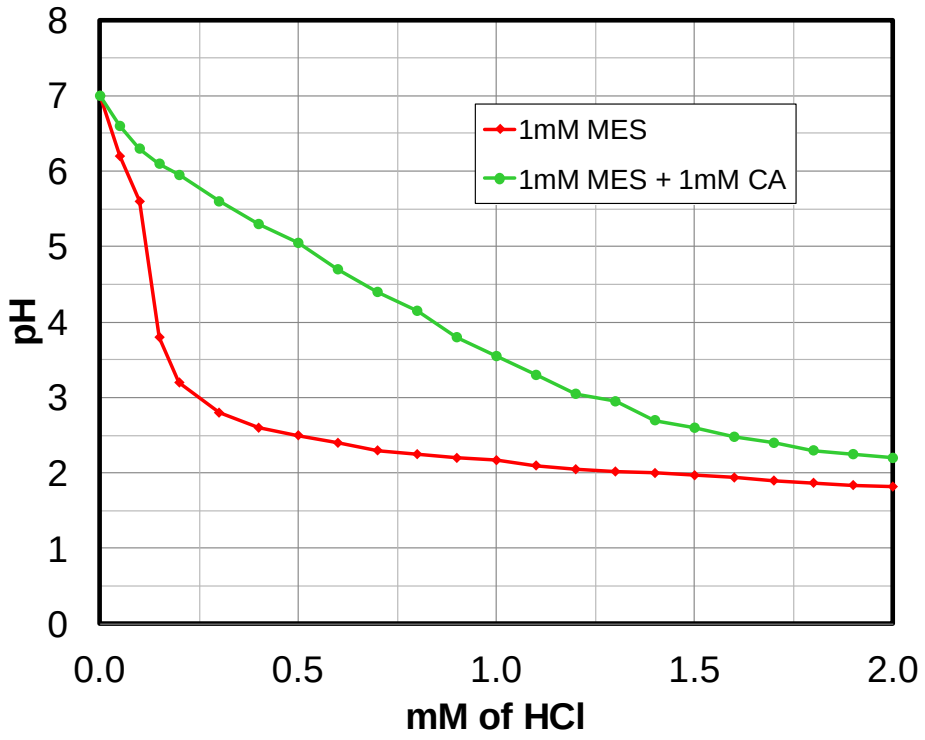

Figure S1 Titration curve for the uncaging buffer. Buffer with 1 mM citric acid (CA) and 1 mM (MES) enables a smooth transition of pH as acid is added.

Microwell assay for preventing pH recovery after rapid acidification (Unpublished)

A problem associated with using microfluidic channels for these studies is that not all of the solution in the channel can be shined with a concentrated UV laser that is required to uncage the oNBA compounds. Hence, the pH of the solution drops and then recovers over time due to the mixing of the surrounding solution at neutral pH. For influenza virus, this recovery of pH is not a critical issue since HA conformation is irreversible for the H3 serotype once acidified[54-56]. However, in cases when the protein of interest can reversibly change conformation with pH (such as VSV G proteins [57-59]), developing strategies to maintaining a low pH after oNBA uncaging becomes important. To address this issue, we developed a different platform using microwells (Figure S2), which allow for the uncaging of an entire small chamber of sample without issues of pH recovery.

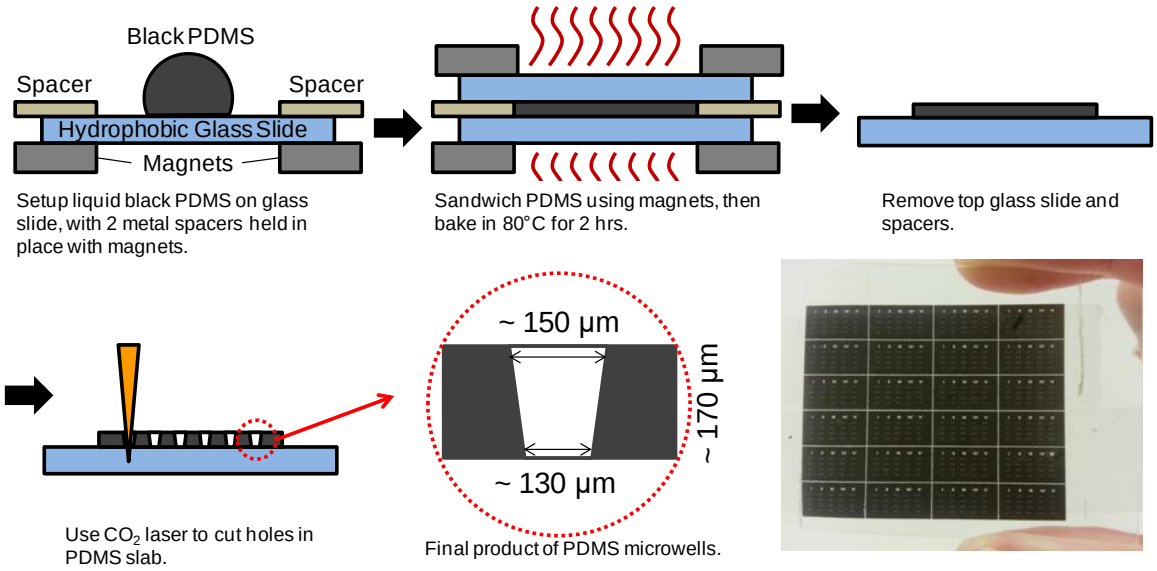

Figure S2 Procedure for making PDMS microwell slab.

To make these microwells, black PDMS solution was sandwiched in between two fluoro-silane treated glass slides spaced 300 µm apart (Figure S2). The PDMS was baked in the 80 C oven, and one side of the slide was removed carefully while leaving the PDMS slab attached to the other glass slide. Using a CO_2 laser cutter, 130 µm diameter microwells were burned into the PDMS slab, and the slab were cut into smaller rectangular slabs.

To setup the device, a small PDMS slab was placed on top of a plastic rolling pin and plasma cleaned along with a cleaned glass slide at 700 µmHg oxygen pressure (Figure S3). The slab was then "rolled" onto the glass slide, and the setup was plasma cleaned again to make the PDMS slab hydrophilic enough for the solution to fill the microwells. A drop of 1 mg/ml vesicle solution was placed on top of the device to form SLBs inside the wells. Excess vesicles were rinsed away using a squirt bottle containing MES buffer. Virus was added to the oNBA solution, and the oNBA solution drop was placed on top of the wells to allow for virus attachment to the SLBs. After 20 minutes of binding, a clear PDMS slab was placed on

top of the microwell to seal them and prevent them from drying out. The device was decontaminated with ethanol prior to placing them on the TIRF microscope for view. From here on, the experiment procedure proceed the same as described in the manuscript.

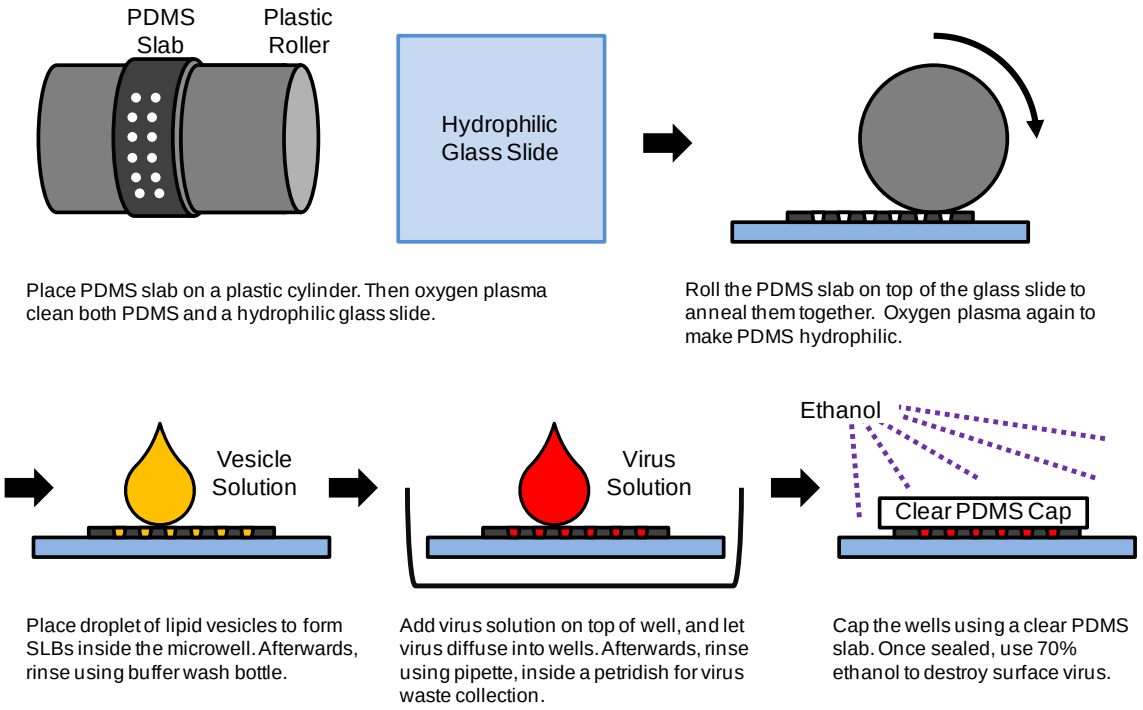

Figure S3 Procedure for assembling microwell for virus membrane fusion triggered via oNBA uncaging method.

REFERENCES

1. Wilschut, J. and D. Hoekstra, *Membrane Fusion*. 1991.
2. Skehel, J.J. and D.C. Wiley, *Receptor binding and membrane fusion in virus entry: the influenza hemagglutinin.* Annual Review of Biochemistry, 2000. **69**(1): p. 531-569.
3. Russell, R.J., P.S. Kerry, D.J. Stevens, D.A. Steinhauer, S.R. Martin, S.J. Gamblin, and J.J. Skehel, *Structure of influenza hemagglutinin in complex with an inhibitor of membrane fusion.* Proceedings of the National Academy of Sciences, 2008. **105**(46): p. 17736-17741.
4. Hoekstra, D., T. De Boer, K. Klappe, and J. Wilschut, *Fluorescence method for measuring the kinetics of fusion between biological membranes.* BIOCHEMISTRY, 1984. **23**(24): p. 5675-5681.
5. Hoekstra, D. and K. Klappe, *Fluorescence assays to monitor fusion of enveloped viruses.* METHODS IN ENZYMOLOGY, 1993. **220**: p. 261-276.
6. Chernomordik, L.V., E. Leikina, V. Frolov, P. Bronk, and J. Zimmerberg, *An early stage of membrane fusion mediated by the low pH conformation of influenza hemagglutinin depends upon membrane lipids.* The Journal of Cell Biology, 1997. **136**(1): p. 81-93.

7. Polozov, I.V., L. Bezrukov, K. Gawrisch, and J. Zimmerberg, *Progressive ordering with decreasing temperature of the phospholipids of influenza virus.* NATURE CHEMICAL BIOLOGY, 2008. **4**(4): p. 248-255.
8. Ramalho-Santos, J., S. Nir, N. Duzgunes, A. Pato de Carvalho, and M.d.C. Pedroso de Lima, *A common mechanism for influenza virus fusion activity and inactivation.* BIOCHEMISTRY, 1993. **32**(11): p. 2771-2779.
9. Clague, M.J., C. Schoch, and R. Blumenthal, *Delay time for influenza virus hemagglutinin-induced membrane fusion depends on hemagglutinin surface density.* Journal of Virology, 1991. **65**(5): p. 2402-2407.
10. Stegmann, T., D. Hoekstra, G. Scherphof, and J. Wilschut, *Kinetics of pH-dependent fusion between influenza virus and liposomes.* Biochemistry, 1985. **24**(13): p. 3107-3113.
11. Korte, T., K. Ludwig, Q. Huang, P.S. Rachakonda, and A. Herrmann, *Conformational change of influenza virus hemagglutinin is sensitive to ionic concentration.* EUROPEAN BIOPHYSICS JOURNAL, 2007. **36**(4-5): p. 327-335.
12. Bentz, J., *Intermediates and kinetics of membrane fusion.* BIOPHYSICAL JOURNAL, 1992. **63**(2): p. 448.
13. Stegmann, T., J.M. White, and A. Helenius, *Intermediates in influenza induced membrane fusion.* EMBO J, 1990. **9**(13): p. 4231-4241.
14. Blumenthal, R., C. Schoch, A. Puri, and M.J. Clague, *A Dissection of Steps Leading to Viral Envelope Protein-Mediated Membrane Fusion.* ANNALS OF THE NEW YORK ACADEMY OF SCIENCES, 1991. **635**(1): p. 285-296.
15. Niles, W.D. and F.S. Cohen, *Single event recording shows that docking onto receptor alters the kinetics of membrane fusion mediated by influenza hemagglutinin.* Biophysical Journal, 1993. **65**(1): p. 171-176.
16. Georgiou, G.N., I.E. Morrison, and R.J. Cherry, *Digital fluorescence imaging of fusion of influenza virus with erythrocytes.* FEBS LETTERS, 1989. **250**(2): p. 487-492.
17. Niles, W.D. and F.S. Cohen, *Fusion of influenza virions with a planar lipid membrane detected by video fluorescence microscopy.* The Journal of general physiology, 1991. **97**(6): p. 1101-1119.
18. Sarkar, D.P., S.J. Morris, O. Eidelman, J. Zimmerberg, and R. Blumenthal, *Initial stages of influenza hemagglutinin-induced cell fusion monitored simultaneously by two fluorescent events: cytoplasmic continuity and lipid mixing.* The Journal of Cell Biology, 1989. **109**(1): p. 113-122.
19. Axelrod, D., T.P. Burghardt, and N.L. Thompson, *Total internal reflection fluorescence.* ANNUAL REVIEW OF BIOPHYSICS AND BIOENGINEERING, 1984. **13**(1): p. 247-268.
20. Floyd, D.L., J.R. Ragains, J.J. Skehel, S.C. Harrison, and A.M. van Oijen, *Single-particle kinetics of influenza virus membrane fusion.* Proceedings of the National Academy of Sciences, 2008. **105**(40): p. 15382-15387.
21. Wessels, L., M.W. Elting, D. Scimeca, and K. Weninger, *Rapid Membrane Fusion of Individual Virus Particles with Supported Lipid Bilayers.* Biophysical Journal, 2007. **93**(2): p. 526-538.
22. McCray, J.A. and D.R. Trentham, *Properties and uses of photoreactive caged compounds.* ANNUAL REVIEW OF BIOPHYSICS AND BIOPHYSICAL CHEMISTRY, 1989. **18**(1): p. 239-270.
23. Dantzig, J.A., H. Higuchi, and Y.E. Goldman, *Studies of molecular motors using caged compounds.* METHODS IN ENZYMOLOGY, 1998. **291**: p. 307-348.
24. Abbruzzetti, S., C. Viappiani, J.R. Small, L.J. Libertini, and E.W. Small, *Kinetics of histidine deligation from the heme in GuHCl-unfolded Fe (III) cytochrome c studied by a laser-induced*

pH-jump technique. JOURNAL OF THE AMERICAN CHEMICAL SOCIETY, 2001. **123**(27): p. 6649-6653.
25. Saxena, A.M., J.B. Udgaonkar, and G. Krishnamoorthy, *Protein dynamics control proton transfer from bulk solvent to protein interior: a case study with a green fluorescent protein.* PROTEIN SCIENCE, 2005. **14**(7): p. 1787-1799.
26. Krumbiegel, M., A. Herrmann, and R. Blumenthal, *Kinetics of the low pH-induced conformational changes and fusogenic activity of influenza hemagglutinin.* Biophysical Journal, 1994. **67**(6): p. 2355-2360.
27. Loyter, A., V. Citovsky, and R. Blumenthal, *The use of fluorescence dequenching measurements to follow viral membrane fusion events.* Methods of Biochemical Analysis, Volume 33, 1988: p. 129-164.
28. Stöber, W., A. Fink, and E. Bohn, *Controlled growth of monodisperse silica spheres in the micron size range.* JOURNAL OF COLLOID AND INTERFACE SCIENCE, 1968. **26**(1): p. 62-69.
29. Ow, H., D.R. Larson, M. Srivastava, B.A. Baird, W.W. Webb, and U. Wiesner, *Bright and stable core-shell fluorescent silica nanoparticles.* NANO LETTERS, 2005. **5**(1): p. 113-117.
30. Burns, A., P. Sengupta, T. Zedayko, B. Baird, and U. Wiesner, *Core/Shell Fluorescent Silica Nanoparticles for Chemical Sensing: Towards Single-Particle Laboratories.* SMALL, 2006. **2**(6): p. 723-726.
31. Hidalgo, G., A. Burns, E. Herz, A.G. Hay, P.L. Houston, U. Wiesner, and L.W. Lion, *Functional tomographic fluorescence imaging of pH microenvironments in microbial biofilms by use of silica nanoparticle sensors.* APPLIED AND ENVIRONMENTAL MICROBIOLOGY, 2009. **75**(23): p. 7426-7435.
32. Brian, A.A. and H.M. McConnell, *Allogeneic stimulation of cytotoxic T cells by supported planar membranes.* Proceedings of the National Academy of Sciences, 1984. **81**(19): p. 6159-6163.
33. Mao, H., T. Yang, and P.S. Cremer, *Design and characterization of immobilized enzymes in microfluidic systems.* ANALYTICAL CHEMISTRY, 2002. **74**(2): p. 379-385.
34. Yang, T., S.-y. Jung, H. Mao, and P.S. Cremer, *Fabrication of phospholipid bilayer-coated microchannels for on-chip immunoassays.* ANALYTICAL CHEMISTRY, 2001. **73**(2): p. 165-169.
35. Harrison, S.C., *Viral membrane fusion.* Nat Struct Mol Biol, 2008. **15**(7): p. 690-698.
36. Tamm, L.K., *Hypothesis: spring-loaded boomerang mechanism of influenza hemagglutinin-mediated membrane fusion.* BIOCHIMICA ET BIOPHYSICA ACTA-BIOMEMBRANES, 2003. **1614**(1): p. 14-23.
37. George, M. and J. Scaiano, *Photochemistry of o-nitrobenzaldehyde and related studies.* The Journal of Physical Chemistry, 1980. **84**(5): p. 492-495.
38. Larson, D.R., H. Ow, H.D. Vishwasrao, A.A. Heikal, U. Wiesner, and W.W. Webb, *Silica nanoparticle architecture determines radiative properties of encapsulated fluorophores.* CHEMISTRY OF MATERIALS, 2008. **20**(8): p. 2677-2684.
39. Haughland, R., *The Handbook: A guide to fluorescent probes and labelling techniques.* USA: Invitrogen Corporation, 2005.
40. Choi, J., N. Hirota, and M. Terazima, *A pH-jump reaction studied by the transient grating method: photodissociation of o-nitrobenzaldehyde.* The Journal of Physical Chemistry A, 2001. **105**(1): p. 12-18.
41. Markovic, I., E. Leikina, M. Zhukovsky, J. Zimmerberg, and L.V. Chernomordik, *Synchronized activation and refolding of influenza hemagglutinin in multimeric fusion machines.* The Journal of Cell Biology, 2001. **155**(5): p. 833-844.

42. Ramalho-Santos, J. and M.C.P. de Lima, *The influenza virus hemagglutinin: a model protein in the study of membrane fusion.* Biochimica et Biophysica Acta (BBA)-Reviews on Biomembranes, 1998. **1376**(1): p. 147-154.
43. Danieli, T., S.L. Pelletier, Y.I. Henis, and J.M. White, *Membrane fusion mediated by the influenza virus hemagglutinin requires the concerted action of at least three hemagglutinin trimers.* The Journal of Cell Biology, 1996. **133**(3): p. 559-569.
44. Imai, M., T. Mizuno, and K. Kawasaki, *Membrane fusion by single influenza hemagglutinin trimers.* Journal of Biological Chemistry, 2006. **281**(18): p. 12729-12735.
45. Blumenthal, R., D.P. Sarkar, S. Durell, D.E. Howard, and S.J. Morris, *Dilation of the influenza hemagglutinin fusion pore revealed by the kinetics of individual cell-cell fusion events.* The Journal of Cell Biology, 1996. **135**(1): p. 63-71.
46. Dobay, M.P., A. Dobay, J. Bantang, and E. Mendoza, *How many trimers? Modeling influenza virus fusion yields a minimum aggregate size of six trimers, three of which are fusogenic.* Molecular BioSystems, 2011. **7**(10): p. 2741-2749.
47. Redfield, D.C., D. Richman, M. Oxman, and L. Kronenberg, *Psoralen inactivation of influenza and herpes simplex viruses and of virus-infected cells.* INFECTION AND IMMUNITY, 1981. **32**(3): p. 1216-1226.
48. Janko, K. and J. Reichert, *Proton concentration jumps and generation of transmembrane pH-gradients by photolysis of 4-formyl-6-methoxy-3-nitrophenoxyacetic acid.* Biochimica et Biophysica Acta (BBA)-Biomembranes, 1987. **905**(2): p. 409-416.
49. Barth, A. and J.E. Corrie, *Characterization of a new caged proton capable of inducing large pH jumps.* BIOPHYSICAL JOURNAL, 2002. **83**(5): p. 2864-2871.
50. Brown, E.B., J.B. Shear, S.R. Adams, R.Y. Tsien, and W.W. Webb, *Photolysis of caged calcium in femtoliter volumes using two-photon excitation.* BIOPHYSICAL JOURNAL, 1999. **76**(1): p. 489-499.
51. Burgalossi, A., S. Jung, G. Meyer, W.J. Jockusch, O. Jahn, H. Taschenberger, V.M. O'Connor, T.-i. Nishiki, M. Takahashi, and N. Brose, *SNARE protein recycling by αSNAP and βSNAP supports synaptic vesicle priming.* NEURON, 2010. **68**(3): p. 473-487.
52. Corti, D., J. Voss, S.J. Gamblin, G. Codoni, A. Macagno, D. Jarrossay, S.G. Vachieri, D. Pinna, A. Minola, and F. Vanzetta, *A neutralizing antibody selected from plasma cells that binds to group 1 and group 2 influenza A hemagglutinins.* SCIENCE, 2011. **333**(6044): p. 850-856.
53. Ekiert, D.C., R.H.E. Friesen, G. Bhabha, T. Kwaks, M. Jongeneelen, W. Yu, C. Ophorst, F. Cox, H.J.W.M. Korse, B. Brandenburg, R. Vogels, J.P.J. Brakenhoff, R. Kompier, M.H. Koldijk, L.A.H.M. Cornelissen, L.L.M. Poon, M. Peiris, W. Koudstaal, I.A. Wilson, and J. Goudsmit, *A Highly Conserved Neutralizing Epitope on Group 2 Influenza A Viruses.* SCIENCE, 2011. **333**(6044): p. 843-850.
54. Skehel, J.J., P.M. Bayley, E.B. Brown, S.R. Martin, M.D. Waterfield, J.M. White, I.A. Wilson, and D.C. Wiley, *Changes in the conformation of influenza virus hemagglutinin at the pH optimum of virus-mediated membrane fusion.* Proceedings of the National Academy of Sciences, 1982. **79**(4): p. 968-972.
55. Doms, R.W., A. Helenius, and J. White, *Membrane fusion activity of the influenza virus hemagglutinin. The low pH-induced conformational change.* Journal of Biological Chemistry, 1985. **260**(5): p. 2973-2981.
56. Wiley, D.C. and J.J. Skehel, *The structure and function of the hemagglutinin membrane glycoprotein of influenza virus.* ANNUAL REVIEW OF BIOCHEMISTRY, 1987. **56**(1): p. 365-394.

57. Eidelman, O., R. Schlegel, T.S. Tralka, and R. Blumenthal, *pH-dependent fusion induced by vesicular stomatitis virus glycoprotein reconstituted into phospholipid vesicles.* Journal of Biological Chemistry, 1984. **259**(7): p. 4622-4628.
58. Gaudin, Y., R.W. Ruigrok, M. Knossow, and A. Flamand, *Low-pH conformational changes of rabies virus glycoprotein and their role in membrane fusion.* J. Virol., 1993. **67**(3): p. 1365-1372.
59. Gaudin, Y., *Reversibility in Fusion Protein Conformational Changes The Intriguing Case of Rhabdovirus-Induced Membrane Fusion*. 2002. p. 379-408.

CHAPTER 5: Feline coronaviruses associated with feline infectious peritonitis have modifications to spike protein activation sites at two discrete positions

Beth N. Licitra[1], Kelly L. Sams[1], Donald W. Lee[2], and Gary R. Whittaker[1*]

[1]Dept. of Microbiology & Immunology, College of Veterinary Medicine, Cornell University, Ithaca, NY, USA

[2]School of Chemical & Biomolecular Engineering, Cornell University, Ithaca, NY, USA

Published in Cornell arXiv. Available at http://arxiv.org/abs/1412.4034

ABSTRACT

Abstract. Feline infectious peritonitis (FIP) is associated with mutations in the feline coronavirus (FCoV) genome that are thought to convert the subclinical feline enteric coronavirus (FECV) into the lethal feline infectious peritonitis virus (FIPV). A key feature of FIPV, not shared with FECV, is the productive infection of macrophages. Therefore mutations in proteins that govern cell tropism, such as the spike glycoprotein, may play an important role in FIP progression. In a prior study, involving a limited number of samples, we have shown an association of FIP with mutations in the protease cleavage-activation site located between the receptor-binding and fusion domains of the FCoV spike (S1/S2). Here, we extend these studies to investigate a larger sample set and to obtain a more refined analysis of the mutations at this S1/S2 site. Our larger data set more clearly shows that the mutations acquired by FIPV at S1/S2 are also accompanied by additional mutations at a second protease cleavage-activation site located in the fusion domain (S2'), adjacent to the viral fusion peptide. Overall, our data indicate a pattern of mutations across the two protease recognition sites that results in substitutions, and/or altered recognition, of critical basic/polar amino acid residues needed for virus activation in the enteric tract. Typically, FIPVs have

substitutions of non-polar, aliphatic or aromatic residues in the protease recognition sites. These changes likely modulate the proteolytic activation of the virus and its ability to productively infect macrophages in vivo.

INTRODUCTION

Feline infectious peritonitis (FIP) is a fatal infection of cats caused by a feline coronavirus (FCoV) [1]. FCoV infections are common, especially in high-density housing situations such as animal shelters and breeding facilities. There are two biotypes of FCoV, classified as either feline enteric coronavirus (FECV) or feline infectious peritonitis virus (FIPV). The biotypes differ based on the severity of infection in cats. Typically, the FECV biotype of FCoV transmits readily via the fecal-oral route, infects enterocytes in the gastrointestinal tract of cats, and causes only a mild infection. If the viral infection worsens and becomes systemic and lethal, then the virus is classified as the FIPV biotype. Symptoms associated with the FIPV biotype infection are granulomatous lesions, vascular leakage, and/or pleural and peritoneal effusion. The current understanding is that FIPV arises during in vivo infection due to genetic mutations of FECV [2-5]. In approximately 1-5% of enteric infections, such spontaneous “internal mutation(s)” extend FCoV tropism to include blood monocytes and tissue macrophages [3]. The resulting productive infection of these cells, a hallmark of FIP, enables systemic spread and results in macrophage activation, with concomitant immune-mediated events leading ultimately to death. To date, the precise mutation(s) that account for a shift in the FCoV biotype have not been identified and there is no definitive diagnostic test for FIP, except through post-mortem histopathological analysis by immunocytochemistry. In addition to the two different biotypes (FECV and FIPV), two FCoV serotypes have been identified. Serotype 1 FCoVs are highly prevalent clinically [6-8], but do not propagate in

cell culture and are therefore studied less often than serotype 2 FCoVs, which are easily propagated in vitro but not as clinically prevalent. In this study, we chose to study FECV and FIPV from serotype I FCoV. The FCoV genome is approximately 29 kB with 11 open reading frames encoding replication, structural, and accessory proteins [9]. Like other RNA viruses, coronavirus replication is error prone, with an estimated mutation rate of approximately 4×10-4 nucleotide substitutions/site/year [10-11]. It has been suggested that mutations in the spike protein (S), 3c, and/or 7b genes are associated with the transition of FECV to FIPV [3, 12-18]. Since the FCoV spike protein mediates receptor binding (through the S1 subunit) and fusion (through the S2 subunit), and mutations in the S gene allowed FCoV to infect macrophages [19], we focused on correlating mutations in this S gene with the biotype switch and changes in cellular tropism. The coronavirus spike protein (S) is a class I fusion protein, which typically requires activation by cellular proteases to be able to mediate cell entry. Mutation of the proteolytic cleavage sites can have profound implications for disease progression [20-21], and therefore we sought to determine whether mutations at protease cleavage sites are evident in the FIPV biotype. Proteases cleave their substrates though recognition of specific amino acid motifs within the relative position designation P6-…-P1 | P1'-…-P6', where cleavage occurs at the P1 position, adjacent to the P1' position [22]. In this paper, we will denote the cleavage site between P1 and P1' using the vertical bar "|" symbol. For a typical serine protease like trypsin, there is a strong requirement for a basic amino acid (Arg or Lys) at the P1 cleavage position. Substrate residues flanking P1 can also have major impacts on the rate and specificity of cleavage for a given protease; in the case of influenza, the addition of arginine/lysine residues upstream of the P1 residue (the polybasic region) of the viral HA can allow an alternate protease called furin to cleave HA and increase

the virulence of this virus [4]. Until recently, FCoVs were thought to use uncleaved S proteins to enter cells. However, a functional furin cleavage site has been identified in two examples of serotype 1 FECVs, located at the boundary of the S1 and S2 subunits [23]. Furin is a ubiquitous proprotein convertase (PC) enriched in the trans-Golgi network and is well conserved among mammals [24]. Furin cleaves a wide range of protein precursors into biologically active products at a consensus motif that is often defined as R-X-K/R-R, where R is the basic arginine residue, X is any residue, and K is the basic lysine residue [25]. The minimum requirement for furin cleavage is for a P1 and P4 arginine. In addition to the P1-P4 arginines, these residues are often flanked by serine residues, and promoted by the presence of a basic residue at P2. The general cleavage requirement for a PC enzyme is defined as cleavage at paired basic residues (B-X_{2n}-B), where the intermediate residues (-X_{2n}-) consist of 0, 2, or 4 amino acids [24]. For many enveloped viruses, protease cleavage occurs adjacent to the fusion peptide site, which is located at the boundary of the receptor-binding and fusion domains of the envelope protein. For coronaviruses the fusion peptide is located within the fusion domains, in close proximity to second processing site denoted as S2'. The actual proteases that cleave at this site are currently unknown, but may include members of the cathepsin family that function in endosomes and lysosomes. Mutations at the S2' cleavage site could be important and therefore we have chosen to study this site in addition to the S1/S2 cleavage site. In this work, we used an approach to studying FIP that complements and extends previous work. We focused on sequence analysis of the two cleavage-activation sites of the spike gene (S1/S2 and S2'), which are functionally relevant regions for virus entry and infection. To obtain FECV gene samples, fecal material from healthy cats that carried FCoV was sequenced for the S gene. These gene samples were operationally defined as being from

the FECV biotype, and 56 FECV samples were obtained in this study. To obtain FIPV samples, tissue and body fluid samples were collected from cats that were diagnosed with FIP. For tissue samples, cats were typically euthanized based on a clinical diagnosis of FIP, and samples were collected post-euthanasia. In many cases, a diagnosis of FIP was reconfirmed by immunohistochemistry (IHC) of tissue from the euthanized cats, but not all samples were examined by IHC for logistical reasons. Viral gene sequences obtained from FIP cats were operationally defined as being from the FIPV biotype. In this study, 84 FIPV samples were sequenced from 39 cats and various organs and tissues. Samples from our previous study [26] were also included to provide as complete a data set as possible, and we compared our data to those of a separate study by Chang et al. [14]. Our studies were consistent with the hypothesis that mutations in both the S1/S2 and S2' protease cleavage sites were present in FIPV samples.

METHODS

FCoV sample acquisition and sequence analysis

Fecal samples from subclinically infected cats and tissue samples from cats with a clinical diagnosis of FIP were solicited from shelters, breeders and veterinarians throughout the United States. To initially confirm samples were FCoV-positive, RNA was extracted using QIAamp Viral RNA Mini (Qiagen, Valencia, CA) and FCoV primers that detect most circulating strains were used to screen all fecal samples using the procedure outlined by Herrewegh and coworkers [27]. RNA extracted from the FIPV-TN406/Black lab-adapted strain was used as positive control. Fresh tissue samples from FIP-diagnosed cats were harvested and RNA samples were extracted using MagMAX Express (Life Technologies, Grand Island, NY). For all samples that were FCoV-positive, 50 μL RT-PCR reactions were

performed with One-Step RT-PCR (Qiagen, Valencia, CA) using gene-specific S primers, encompassing S1/S2 and S2': S1/S2 primer pair 5'-GCACAAGCAGCTGTGATTA-3' and 5'-GTAATAGAATTGTGGCAT-3'; S2' primer pair 5'- GATATGATCACAGTATCAGATCG -3' and 5'-ATAATC ATCATCAACAGTGCC-3'. PCR conditions were: 30 min at 50°C, 15 min at 95°C, and 39 or 35 cycles of: 1 min at 94°C, 1 min at 55°C, 1 or 1.5 min at 72°C, 10 min at 72°C. PCR products were purified using Qiaquick Gel Extraction (Qiagen, Valencia, CA). Sanger-based dideoxy sequencing was performed at the Life Sciences Core Laboratories (Cornell University). DNA sequences were translated into protein sequences and alignments were performed using Geneious 5.4 (http://www.geneious.com).

Visual Representation of Mutation Data

To visualize the biochemical changes in the protease cleavage sites of the S protein, we developed a specialized scatter plot through MATLAB [MathWorks, Natick, MA]. A separate plot was made for each residue position being evaluated, and the Van der Waals (VdW) volume of amino acids [28] was plotted against their hydropathy index (HPI) [29]. In general, amino acids with lower HPI are more hydrophilic whereas those with higher HPI are more hydrophobic. Each data point corresponds to an amino acid that was found at the residue position being evaluated, and the size of the data point scales with the frequency of occurrence of that amino acid within a data set. We caution here that the data point size does not denote an error range in VdW volume or HPI. Other important properties of the amino acids were portrayed by color-coding the data points as such: polar positive (blue: H,K,R), polar negative (red: D,E), polar neutral (green: S,T,N,Q), nonpolar aliphatic (gray: A,V,L,I,M), nonpolar aromatic (magenta: F,W,Y), unique (brown: P,G), and disulfide bond-forming (cyan: C).

RESULTS

FECV sequence from healthy cats

The amino acid sequence motifs for the S1/S2 and S2' regions are shown in Table 1. For the S1/S2 site, the previously recognized motif -R-R-S/A-R-R-S- [26] was again found to be highly conserved. There was a limited variability in the P5 position, with Arg substituted for: Gly (1 cat) and Lys (1 cat). The functional relevance of this variation is unclear, though the P5 position is not generally considered to be highly important for furin cleavage. There was also a single case with a change in the P3 position with Ser/Ala substituted for Val (1 cat). As with P5, the type of amino acid residue at the P3 position is not functionally critical for furin cleavage. Based on the expanded dataset available from this study, we also noted a high degree of conservation at the P6 cleavage position (which can be highly important for furin cleavage). All samples contained a polar uncharged residue (S, T or Q) at the P6 position. Overall, the expanded data set reinforces the notion that the S1/S2 motif is cleaved by furin. Based on the data from this study, we consider to following as an "FECV" motif at the S1/S2 position: -S/T/Q-R-R-S/A-R-R-S-.

At the S2' site, the conserved nature of the FCoV fusion peptide (SAVEDLLF) was readily apparent, along with the expected conserved arginine residue in the P1 cleavage position (Table 1). All FECV samples tested contained a P2 lysine, with the high level of conservation implicating this as a functionally critical residue. The P1' residue (S) was also 100% conserved, consistent with a role in protease cleavage, as well as in fusion peptide function. Overall, we found an invariant motif -K-R-S- at the S2' position of FECV, and the dibasic nature of this site is consistent with cleavage by a range of proteases, including non-furin PCs and cathepsin B.

FIPV sequence from FIP cats

The amino acid sequence motifs for the S1/S2 and S2' regions in the FCoV spike gene amplified from various tissues and body fluid samples are shown in Table 2. For S1/S2, the FECV motif -S/T/Q-R-R-S/A-R-R-S- was disrupted in the vast majority of samples. In addition, the S2' FECV -K-R-S- motif was disrupted in many samples. Fecal material from FIP cats is shown in Table 3, with sequences very similar to FECV samples.

For S1/S2, we focused our analysis on the "core" residues for furin cleavage, i.e. the P1', P1, P2 and P4 residues. The most frequent substitution was at the P1 position, where 11 cats displayed a change of Arg for Gly (4 cats), Met (4 cats), Trp (2 cats), Thr (1 cat) and Ser (1 cat). The next most frequent substitution was at the P2 position, where 10 cats displayed a change of Arg for Leu (6 cats), Pro (3 cats), Ser (1 cat) and His (1 cat). Five cats had a substitution at the P4 position, which displayed a change of Arg for Thr (2 cats) Gly (1 cat), Ser (1 cat), and Met (1 cat). Four cats had a substitution at the P1' position, which displayed a change of Ser for Ala (2 cats) Pro (1 cat), Gly (1 cat), and Leu (1 cat). All of these changes in the core residues would be expected to be highly functionally significant for furin cleavage.

At the S2', the conserved nature of the fusion peptide (SAVEDLLF) was again readily apparent, along with an invariant Ser at the P1' position (Table 2). While most FIPV cats contained a P1 arginine, three cats had substitutions for Ser. This change would be expected to be highly functionally significant for protease cleavage. There were more substitutions in the P2 residue, with five cats displaying a change of Lys for Met (3 cats) and Glu (2 cats). These changes would also be expected to be highly functionally significant for protease

cleavage. The overall switch in the dibasic nature of the S2' site in some cats is consistent with a change in the protease(s) cleaving at this position.

For the core residues at S1/S2 and S2'. 31 out of 39 FIP cats (77%) had samples that were modified from the FECV consensus (-S/T/Q--R-R-S/A-R-R-S-). Healthy cats showed no deviation from the core motif The P6, P5 and P3 residues within the S1/S2 site (- S/T/Q--R-R-S/A-R-R-S-) were defined as "non-core" residues as these are likely to be less functionally relevant for furin cleavage. Of these residues, P6 likely impacts furin cleavage the most. For the P6 position, five cats displayed a change of Ser/Thr/Gln for Pro (2 cats), Phe (1 cats), Ala (1 cat) and Leu (1 cat). All of these changes would be expected to be functionally significant for furin cleavage.

Including S1/S2 P6 as a core residue revealed that 33 out of 39 FIP cats (85%) had samples that were modified from the FECV consensus (-S/T/Q-R-R-S/A-RR-S-). Healthy cats showed no deviation from a core motif including P6. For the non-core S1/S2 P5 position, nine cats displayed a change of Arg for Lys (8 cats), as seen for FECV. For the non-core S1/S2 P3 position, two cats displayed a change of Ser/Ala for Met (1 cats) and Thr (1 cat). The significance of these changes is uncertain. The S2' noncore P1' residue showed no deviation in either FIP or healthy cats. Including both core and non-core residues at S1/S2 and S2', we found that 37/39 FIP cats (95%) had mutations compared to healthy cats. 9% of healthy cats showed a mutation within the non-core residues.

It is noteworthy that many cats had multiple changes across the two proteolytic cleavage sites and while there was a wide variety of different substitutions present in different cats, sampling of multiple tissues within an individual cat (e.g. cat#197) revealed relatively limited

variation. It is also noteworthy that most of our samples would be expected to be comprised of “end-stage” viruses, where cats have more obvious clinical signs of FIP. It will be interesting to track cats that might be in an “early”, possibly subclinical, phase of FIP. These cats may harbor viruses that have different mutations to end-stage viruses sampled here, in particular in the “non-core” residues.

While a prediction of the proteases coming into play for FIPV is quite uncertain, the trend in our data is for the replacement of critical basic residues and serine with more hydrophobic residues, a pattern consistent with cleavage by an alternative protease(s). Such proteases may include cathepsins [30], or matrix metalloproteases (MMPs) [31]. MMPs are known to be highly expressed on macrophages [32] and to our knowledge, MMP-mediated cleavage of a viral envelope protein would be unique situation for a virus entry pathway. Both MMPs and cathepsin demonstrate relatively broad substrate specificity, in line with the range of mutations seen in the cleavage site(s) of FIPVs.

Comparison to a separate study (Chang et. al. 2012) and to database sequences

The data generated during the course of our study was compared to that generated by a separate study, Chang et al. 2012 [33], as well as to additional database sequences (Table 4). For S1/S2, of the ten FECV sequences in Chang et al., the -Q/R/S-R-R-S/A-R-R-Smotif was preserved with one exception, where one cat had a P6 Pro residue. All core residues were identical to our study. A P6 Pro was also found in one other database sequence. The pattern of residues in FIPV samples followed the same general pattern as described for our study; i.e. introduction of non-polar, aliphatic or aromatic residues in the protease recognition sites. Of the eleven FIP cats samples in Chang et al. 2012, four had P1 substitutions (G, W and S), two

had P1’ substitutions (L and P), two had P4 substitutions (G and S), and three had P6 substitutions (L and P). Of seven database samples, three had P1 substitutions (G, W and S), two had P1’ substitutions (P), one had P4 substitutions (Q), and five had P6 substitutions (A and P).

At S2’, Chang et al. 2012 show some limited changes of the invariant KRS motif for FECV, with different P2 residues in four cats, substituted with Arg (3 cats) and Thr (1 cat). Cats with FIP showed an introduction of a hydrophobic reside at P2 in five cases, with Lys being substituted for Met (4 cats) and Val (1 cat). A similar trend was present in database samples, with introduction of Val, Ala and Gln in three individual cases. Overall, we consider that the data from Chang et al. 2012, as well as other database sequences, are in strong agreement with the data from this study. 10/11 (91%) of samples from Chang et al 2012. and 4/4 (100%) of database samples had functionally significant mutations in the spike cleavage sites.

Visual representation of sequences in the protease activation sites of FECV and FIPV spike proteins

Finding a mutation pattern that could explain the transformation of FECV to FIPV is challenging because amino acids have multiple properties that are similar or dissimilar with each other, such as molecular size, hydrophobicity, and charge [34]. In order to simultaneously visualize changes to multiple biochemical properties, we developed a specialized scatter plot through MATLAB that shows the Van der Waals volume (Y-axis), hydropathy index (X-axis), frequency of occurrence (data point size), and unique property (color code) of amino acids found at the cleavage site positions. The resulting plots are shown

in Figure 1 for the residues at the S1/S2 and S2' cleavage sites for both the FECV and FIPV samples.

Compared to FECV, FIPV contains the following changes in the S1/S2 cleavage site: P6 and P1' mutates from polar neutral residues to nonpolar residues, P4 and P2 mutates from arginine to smaller and more hydrophobic residues, and P1 mutates from arginine to more hydrophobic residues. At the S2' cleavage site, FIPV contains the following mutations: P2 mutates from positively charged lysine to either negatively charged glutamate or uncharged methionine, and P1 mutates from positively charged arginine to polar neutral serine that is half the volume of arginine. In summary, the visualization of biochemical changes at the cleavage sites using our plotting method can greatly aid with the identification of mutation patterns associated with FIP.

Potential use of this study for diagnosis of FIP in cats

We believe that our study will be of benefit in the diagnosis of FIP in cats by detecting mutations in S protein cleavage site that mimic those found in FIPV. However, the pattern of variant viruses seen in FIP cats is complex. We consider that the tracking of the ten amino acids that comprise the cleavage sites of FCoV spike (-S/T/Q-R-R-S/A-R-R-S- from S1/S2 and -K-R-S from S2') with respect to the biochemical parameters of size, hydrophobicity, and charge can be used to predict the likelihood of FIP in cats. To simplify the detection of FIPV-like mutations, one could potentially use the changes in these biochemical parameters in conjunction with a ranking of the core and non-core residues to arrive at a "FIP diagnostic score." Such a scoring system could help clinicians identify which cats are likely to develop FIP without the need to functionally investigate every mutation found. The use of this scoring

metric for samples that clinicians can easily access (e.g. blood) would be helpful for diagnosing FIP early and quickly. While our current study only utilized a limited number of blood samples, mutations consistent with a FIPV biotype were seen in all positive samples. However, it is known that FCoV can be present in the blood monocytes of healthy cats without necessarily leading to FIP [18, 27, 35]. Further investigation into the spike protein cleavage site changes in blood samples of both healthy and FIP cats will form a future focus of this study.

We considered that fecal samples from FIP cats were likely to be contaminated with an ongoing infection with FECV, and so not discriminatory for FIP. This was confirmed, as the FIP cats tested in this study continued to shed FECV-like viruses, based on the highly limited sequence variation observed at the spike cleavage sites (Table 3).

FIP exists in two clinical manifestations (wet and dry) [17]. As in our previous study [26], we found no correlation between sequence alterations at the spike cleavage sites between "wet" and "dry" FIP cats. These differences in clinical presentation are likely to be due to immunological factors in individual cats, rather than differences in the cleavage-activation of the viruses infecting these cats.

The use of the techniques reported here for serotype I FCoVs may also be applied to serotype II FCoVs; however, these viruses lack an equivalent S1/S2 motif. Investigation of predictive changes in the S2' region of serotype II FCoVs is currently ongoing.

ACKNOWLEDGMENTS

We thank Jean Millet, Lisa Bolin and members of the Whittaker laboratory, Ruth Collins, Dante Lepore and members of Collins laboratory, and Susan Daniel and members of Daniel laboratory for advice and discussion during the course of this study. The authors also thank Drs. Meredith Brown, Stephen O'Brien, Sean McDonough, Edward Dubovi and Gerald Duhamel for providing some of the clinical samples used in this study, Andrew Regan and Kirsten Elfers for initial work on this project, and Nadia Chapman, Vera Rinaldi, Misty Pocwiercz, Valerie Marcano, Rod Getchell and Wendy Wingate for technical assistance. This work was funded in part by a sponsored project from Antech Diagnostics. B.L. was supported by funds from the Cornell University College of Veterinary Medicine DVM/PhD program. Work in the author's lab is also supported by grants from the Cornell Feline Health Center, the Winn Feline Health Foundation and the Morris Animal Foundation. The sponsors had no influence in the study design, the collection, analysis and interpretation of data, the writing of the manuscript, or in the decision to submit the manuscript for publication. All work with animals was approved by the Institutional Animal Use and Care Committee at Cornell University (Ithaca NY)

Table 1 Amino acid sequences in the S1/S2 and S2' regions of the FCoV spike obtained from fecal samples from heathly cats. The ten amino acids comprising the predicted proteolytic cleavage sites are in bold, with modifications to these residues colored (green = modification to non-core residue).

CatID	Sample	S1/S2	S2'
150	Feces	TSSRRSRRSTTE	HSIG**KRS**AVED
106	Feces	TQSRRSRRSYPD	PTIG**KRS**AVED
110	Feces	TQTRRSRRSTSE	PRIG**KRS**AVED
111	Feces	THSRRARRSTVE	PRIG**KRS**AVED
125	Feces	TQSRRARRSTVE	PTIG**KRS**AVED
126	Feces	TQSRRSRRSASS	PTIG**KRS**AVED
128	Feces	THSRRARRSTVE	PTIG**KRS**AVED
129	Feces	TQSRRSRRSTSD	PTIG**KRS**AVED
131	Feces	TQSRRSRRSASN	PTIG**KRS**AVED
132	Feces	TQSRRSRRSAPE	PRIG**KRS**AVED
135	Feces	TQSRRARRSLPA	PRIG**KRS**AVED
136	Feces	TQSRRSRRSVVE	PQIG**KRS**AVED
137	Feces	TSSRRSRRSTPE	HSIG**KRS**AVED
138	Feces	TQSRRSRRSVAE	PTIG**KRS**AVED
140	Feces	TQSRRSRRSVVE	PTIG**KRS**AVED
141	Feces	TQSRRSRRSVVE	PQIG**KRS**AVED
142	Feces	THSRRARRSTVE	PTIG**KRS**AVED
143	Feces	TSSRRARRSSVE	PTIG**KRS**AVED
144	Feces	TQSRRSRRSASM	PTIG**KRS**AVED
146	Feces	THSRRARRSTVE	PKIGKRSAVED
149	Feces	TSSRRSRRSTPE	HSIG**KRS**AVED
150	Feces	TSSRRSRRSTTE	HSIG**KRS**AVED
152	Feces	THSRRSRRSNSD	PRIG**KRS**AVED
153	Feces	PHSRRSRRSTNY	PTIG**KRS**AVED
155	Feces	TQSGRSRRSASD	n/a
160	Feces	THSKRSRRSTSN	PTIG**KRS**AVED
167	Feces	THSKRSRRSTSN	PTIG**KRS**AVED
234.1	Feces	THTRRSRRSAPV	PTIG**KRS**AVED
246	Feces	TQSKRSRRSAPH	PKIG**KRS**AVED
304	Feces	THTRRSRRSAPV	PTIG**KRS**AVED
307	Feces	THTRRSRRSAPV	PTIG**KRS**AVED
308	Feces	THTRRSRRSAPI	PKIG**KRS**AVED
308	Feces	THTRRSRRSAPI	PTIG**KRS**AVED
310	Feces	THTRRSRRSAPA	PTIG**KRS**AVED

313	Feces	ARTRRSRRSAPV	PKIG**KRS**AVED
349	Feces	TQSRRARRSASD	PQIG**KRS**AVED
352	Feces	TQSRRARRSASD	PQIG**KRS**AVED
277.2	Feces	TQSRRSRRSTSD	PTIG**KRS**AVED
278	Feces	TQSRRVRRSVQE	PTIG**KRS**AIED
BL1	Feces	THTRRSRRSAPA	PTIG**KRS**AVED
BL10	Feces	THTRRSRRSAPV	PTIG**KRS**AVED
BL11	Feces	THTRRSRRSAPV	PTIG**KRS**AVED
BL12	Feces	THTRRSRRSAPV	PTIG**KRS**AVED
BL13	Feces	THTRRSRRSAPV	PTIG**KRS**AVED
BL2	Feces	THTRRSRRSAPA	PTIG**KRS**AVED
BL3	Feces	THTRRSRRSAPA	PTIG**KRS**AVED
BL4	Feces	THTRRSRRSAPA	PTIG**KR**SAVED
BL5	Feces	THTRRSRRSAPV	PTIG**KR**SAVED
BL6	Feces	THTRRSRRSAPI	PTIG**KR**SAVED
BL7	Feces	THTRRSRRSAPI	PTIG**KR**SAVED
BL8	Feces	THTRRSRRSAPI	PTIG**KR**SAVED
BL9	Feces	THTRRSRRSAPA	PTIG**KR**SAVED
FECV-4582	Feces	TQQRRSRRSTSD	PTIG**KR**SAVED
FECV-4594	Feces	TQQRRSRRSTSD	PTIG**KR**SAVED
FECV-FCA4597	Feces	TQQRRSRRSTSD	PTIG**KR**SAVED
FECV-FCA4606	Feces	TQQRRSRRSTSD	PTIG**KR**SAVED

Table 2 Amino acid sequences in the S1/S2 and S2' regions of the FCoV spike obtained from tissue and body fluid samples from cats diagnosed with FIP. The ten amino acids comprising the predicted proteolytic cleavage sites are in bold, with modification to these residues colored (red and blue = modification to core residue, green and violet = modification to non-core residue). ND = not determined.

Cat ID	Tissue	S1/S2	S2'
129308	Mesentery	TSSRRS**PRS**TLD	n/a
	Lower Gut	TSSRRS**LRS**TVR	n/a
147	Blood	TQSRRARSSASD	PRIG**ERS**AVED
148	Ascites	TSSRRSRR**P**TTE	HSIGKRSAVED
151643-08	Heart	TQ**FRRARRS**AVR	n/a
	Spleen	TQ**FRRSRRS**TPG	n/a
	Liver	TQ**FRRSRRS**TVR	n/a
157	Ascites	TQ**PRRARRS**VSE	PSIGKRSAVED
	Liver	TQ**PRRARRS**VSE	PSIGKRSAVED
	Spleen	TQ**PRRARRS**VSE	PSIGKRSAVED
	Spleen	TQ**PRRARRS**VSE	PSIGKRSAVED
159	Ascites	TSSRRSR**MS**TPE	PSIGKRSAVED
162	Ascites	TQSRRSRR**A**TSN	PTTGKRSAVED
	Ascites	TQSRRSRR**A**TSN	PTTGKRSAVED
163	Urinary Discharge	TQSRRSR**MS**TSD	PRVGK**S**SAIED
166	Brain	TH**PRRSRGS**TIE	n/a
170	Ascites.1	TQSRRSRRSTSD	PTIGKRSAVED
	Ascites.2	TQSRRSRRSTSD	PTIGKRSAVED
	Liver	n/a	PTIGKRSAVED
	Lung	TQSRRSRRSTSD	PTIGKRSAVED
179	Ascites	TQSR**GSRRS**TSD	PTIGKRSAVED
181	Chest Fluid	TQSRRSRRSTSD	PTIGKRSAVED
	Liver	TQSRRSRRSTSD	PTIGKRSAVED
	Lung	TQSRRSRRSTSD	PTIGKRSAVED
	Spleen	TQSRRSRRSTSD	PTIGKRSAVED
182	Ascites	TQSR**SSRRS**TPV	PSIGKRSAVED
192	Thoracic Fluid	TQSRRSR**GS**TSD	PTIGKRSAVED
195	Spinal Cord	TQS**KTAPRG**TSD	n/a
		TQS**KTAPRA**TSD	n/a
197	Ascites	THS**KRARWS**TSD	PRIG**MRS**AIED
	Kidney	THSRRS**LRS**APV	n/a
	Liver	THS**KRARWS**TSD	PRIG**MRS**AIED
	Lung.1	THTRRS**LRS**APD	n/a
	Lung.2	THS**KRARWS**TSD	PRIG**MRS**AIED
	Omentum	THS**KRARWS**TSD	PRIG**MRS**AIED

	Small Intestine.1	THSRRSRRSASD	n/a
	Small Intestine.2	THSKRARWSTSD	PRIGMRSAIED
	Spleen	THSKRARWSTSD	PRIGMRSAIED
211	Ascites	THLRRSRRSTPE	RVGKRSAVED
215	Ascites	TQSKSARRSTSD	PRIGKRSAIED
232	Liver	TQSKSARRSTSD	n/a
	Lung	TQSKSARRSTSD	n/a
	Spinal Fluid	TQSKSARRSTSD	PRIGKRSAIED
234	Kidney	THTRRSLRSAPV	n/a
	Lung	THTRRSLRSAPV	PTIGKRSAVED
239	Blood	TQSKTARRSTSD	PRVGKSSAIED
	Brain	TQSKTARRSTSD	PRVGKSSAIED
		TQSKTALRSTSD	n/a
	Cerebellum	TQSKTALRSTSD	PRVGKSSAIED
		TQSKTARRSTSD	n/a
	Cerebrum	TQSKTARRSTSD	PRVGKSSAIED
	Kidney.1	THTRRSLRSAPV	n/a
	Kidney.2	TQSKTARRSTSD	PRVGKSSAIED
	Spleen	TQSKTARRSTSD	PRVGKSSAIED
241	Ascites	THSRRSLSSTPE	PRIGKRSAVED
244	Mesentery	HSRRASTSTSN	n/a
	Mesenteric lymph node	TQSRRASTSTSN	n/a
245	Spinal Fluid	TQSRRSRRSKSN	PTVGKSSAVED
		n/a	TVGKRSAVED
256	Ascites	THSKRARWSTSD	PRIGMRSAIED
259	Brain	TQSKSARRSTSD	KRSAIED
	Lung	TQSKSARRSTSD	n/a
261	Liver	TQSRRMRRSTSN	n/a
	Small Intestine	TRSRRMRRSTSN	n/a
	Spleen	TQSRRMRRSTSN	n/a
350	Kidney	TSARRSRRSASE	PTIGKRSAVED
	Lung	TSARRSRRSASE	PTIGKRSAVED
77	Kidney	THSRRSRMSTQN	n/a
	Cerebellum.1	THSRRSLRSTQN	n/a
	Cerebellum.2	THSRRSRRSTQN	n/a
08-153990	Kidney	TQPRRARMSVPE	n/a
	Cerebrum	TQPRRARMSVPE	PTIGMRSAVED
	Brain stem	TQPRRAPMSVPE	PTIGMRSAVED
	Cerebellum	TQPRRARMSVPE	PTIGMRSAVED
N04-93	Kidney	THLRRSHRSTSE	n/a

	Cerebrum	TLT**G**R**S**H**RS**TSE	n/a
N05-48	Cerebellum	TQSR**S**S**RRS**TSD	n/a
N05-110	Mesenteric lymph node	TQT**K**R**SRRS**TPQ	PTIGKRSAVED
	Cerebellum	TQT**K**R**SRRS**TPA	n/a
N07-95	Cerebrum	THTR**K**T**RRS**IAD	n/a
D04-397	Spleen	TQSRRSRRSTVD	n/a
	Mesentric lymph node	TQSRRSRR**L**TSN	n/a
D06-327	Spleen	THSRRSR**G**SAPN	n/a
	Mesentery	THSRRSR**G**SAPN	n/a
429	Omentum	TSSRSSRRSTSE	SRIG**E**RSAVED
430	Omentum	SQSRRSR**S**STSE	PRVGKRSAVED

Table 3 Amino acid sequences in the S1/S2 and S2' regions of the FCoV spike obtained from fecal samples from cats diagnosed with FIP. The ten animo acids comprising the predicted proteolytic cleavage sites are in bold, with modification to these residues colored (green = modification to non-core residue).

Cat ID	Sample	S1/S2	S2'
107	Feces	TTSRRPRRSDPA	PTIGKRSAVED
108	Feces	QSSRRSRRSTSD	PTIGKRSAVED
145	Feces	THSRRARRSTVE	PKIGKRSAVED
148	Feces	TSSRRSRRSTTE	PKIGKRSAVED
215	Feces	THARRSRRSTPE	PRIGKRSAIED
251	Feces	TQSKRARRSTSD	PRIGKRSAIED
347	Feces	TRSRRSRRSTLEP	PRVGKRSAVED
352	Feces	TQSRRARRSASDS	PQIGKRSAVED

Table 4 Amino acid sequences in the S1/S2 and S2' regions of the FCoV spike obtained from Chang et al. and databases. The ten amino acids comprising the predicted proteolytic cleavage sites are in bold, with modification to these residues colored (red and blue = modifiation to core residue, green = modification to non-core residue). Modifications that are not expected to be functionally relevent are shown in gray. n/a - not applicable/unknown.

FECV			
Name	**Tissue**	**S1/S2**	**S2'**
UU2	feces	SRRSRRS	RRS
UU7	feces	SRRARRS	KRS
UU10	feces	SKRSRRS	KRS
UU11	feces	SKRSRRS	KRS
UU18	feces	PRRSRRS	KRS
UU19	feces	SRRSRRS	TRS
UU20	feces	SRRSRRS	KRS
UU22	feces	SRRSRRS	RRS
UU23	feces	SRRSRRS	RRS
UU31	feces	SRRSRRS	KRS
Database Sequence			
RM	n/a	PRRSRRS	KRS
FIPV			
Name	**Tissue**	**S1/S2**	**S2'**
UU3	n/a	SRRSRRS	MRS
UU4	n/a	SRSARGS	MRS
UU5	n/a	SRRSRGS	KRS
UU8	n/a	SRRSRRS	KRS
UU9	n/a	SRRSRRL	KRS
UU15	n/a	LRRSRRP	KRS
UU16	n/a	PRGSRRS	MRS
UU17	n/a	SRRSRRS	VRS
UU21	n/a	SRRSRWS	MRS
UU24	n/a	SRRSRSS	KRS
UU30	n/a	LRRSRRS	KRS
Database Sequence			
Black/TN406	Liver	AKRSRRP	VRS
FCoV C1Je	Jejunum	PRQSRRS	KRS
Q66951_9ALPC_(KU-2)	n/a	ARRSRSS	KRS
Q8JVL1_9ALPC_(Black/TN406)	n/a	AKRSRRP	ARS
Q8JVL2_9ALPC_(UCD1)	n/a	SRRSRGS	QRS

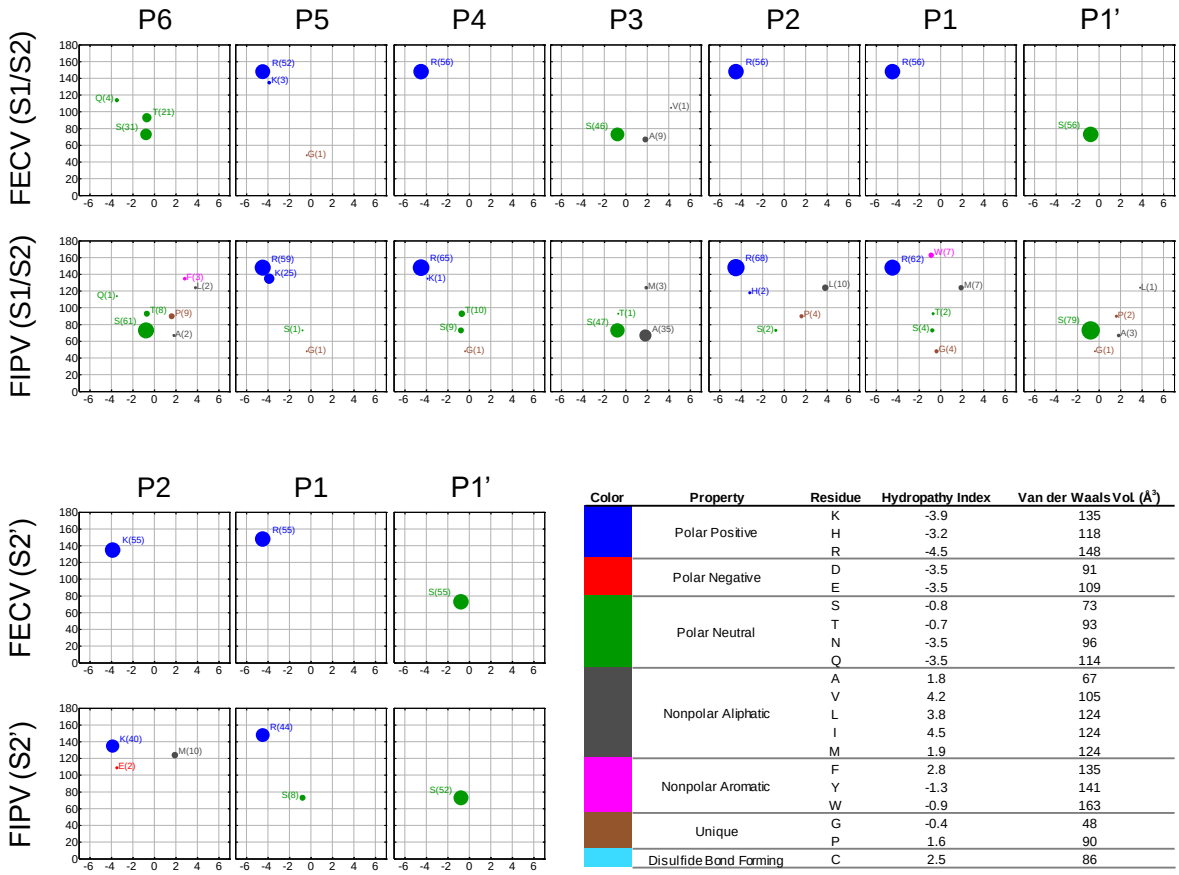

Figure 1 Visual representation of amino acid properties in the S1/S2 and S2' cleavage sites for FECV and FIPV. The Y-axis is the Van der Waals volume (Å3), and the X-axis is the hydropathy index (unitless). The data point size corresponds to the frequency of occurrence. Note that for FIPV, the frequency of occurrence is based on all samples collected and not just the number of FIP cats sampled. The table/legend summarizes all amino acid properties and color code.

REFERENCES

1. Haijema, B.J., P. Rottier, and R.J. de Groot, *Feline coronaviruses: a tale of two-faced types.* Coronaviruses: molecular and cellular biology. Caister Academic Press, Norfolk, United Kingdom, 2007: p. 183-203.
2. Herrewegh, A.A., H. Vennema, M.C. Horzinek, P.J. Rottier, and R.J. de Groot, *The molecular genetics of feline coronaviruses: comparative sequence analysis of the ORF7a/7b transcription unit of different biotypes.* VIROLOGY, 1995. **212**(2): p. 622-631.
3. Pedersen, N.C., H. Liu, K.A. Dodd, and P.A. Pesavento, *Significance of coronavirus mutants in feces and diseased tissues of cats suffering from feline infectious peritonitis.* Viruses, 2009. **1**(2): p. 166-184.
4. Perdue, M.L., *Molecular determinants of pathogenicity for avian influenza viruses.* Avian influenza, 2008: p. 23-41.
5. Vennema, H., A. Poland, J. Foley, and N.C. Pedersen, *Feline infectious peritonitis viruses arise by mutation from endemic feline enteric coronaviruses.* VIROLOGY, 1998. **243**(1): p. 150-157.

6. Benetka, V., A. Kübber-Heiss, J. Kolodziejek, N. Nowotny, M. Hofmann-Parisot, and K. Möstl, *Prevalence of feline coronavirus types I and II in cats with histopathologically verified feline infectious peritonitis.* VETERINARY MICROBIOLOGY, 2004. **99**(1): p. 31-42.
7. Hohdatsu, T., H. Yamada, Y. Ishizuka, and H. Koyama, *Enhancement and neutralization of feline infectious peritonitis virus infection in feline macrophages by neutralizing monoclonal antibodies recognizing different epitopes.* MICROBIOLOGY AND IMMUNOLOGY, 1993. **37**(6): p. 499-504.
8. Shiba, N., K. Maeda, H. Kato, M. Mochizuki, and H. Iwata, *Differentiation of feline coronavirus type I and II infections by virus neutralization test.* VETERINARY MICROBIOLOGY, 2007. **124**(3): p. 348-352.
9. King, A.M., M.J. Adams, and E.J. Lefkowitz, *Virus taxonomy: classification and nomenclature of viruses: Ninth Report of the International Committee on Taxonomy of Viruses*. Vol. 9. 2011: Elsevier.
10. Salemi, M., W.M. Fitch, M. Ciccozzi, M.J. Ruiz-Alvarez, G. Rezza, and M.J. Lewis, *Severe acute respiratory syndrome coronavirus sequence characteristics and evolutionary rate estimate from maximum likelihood analysis.* JOURNAL OF VIROLOGY, 2004. **78**(3): p. 1602-1603.
11. Vijgen, L., E. Keyaerts, E. Moës, I. Thoelen, E. Wollants, P. Lemey, A.-M. Vandamme, and M. Van Ranst, *Complete genomic sequence of human coronavirus OC43: molecular clock analysis suggests a relatively recent zoonotic coronavirus transmission event.* JOURNAL OF VIROLOGY, 2005. **79**(3): p. 1595-1604.
12. Bank-Wolf, B.R., I. Stallkamp, S. Wiese, A. Moritz, G. Tekes, and H.-J. Thiel, *Mutations of 3c and spike protein genes correlate with the occurrence of feline infectious peritonitis.* VETERINARY MICROBIOLOGY, 2014. **173**(3): p. 177-188.
13. Chang, H.-W., R.J. de Groot, H.F. Egberink, and P.J. Rottier, *Feline infectious peritonitis: insights into feline coronavirus pathobiogenesis and epidemiology based on genetic analysis of the viral 3c gene.* JOURNAL OF GENERAL VIROLOGY, 2010. **91**(2): p. 415-420.
14. Chang, H.-W., H.F. Egberink, R. Halpin, D.J. Spiro, and P. Rottier, *Spike protein fusion peptide and feline coronavirus virulence.* EMERGING INFECTIOUS DISEASES, 2012. **18**(7): p. 1089-95.
15. Chang, H.-W., H.F. Egberink, and P. Rottier, *Sequence analysis of feline coronaviruses and the circulating virulent/avirulent theory.* EMERGING INFECTIOUS DISEASES, 2011. **17**(4): p. 744-6.
16. Licitra, B.N., K.L. Sams, D.W. Lee, and G.R. Whittaker, *Feline coronaviruses associated with feline infectious peritonitis have modifications to spike protein activation sites at two discrete positions.* arXiv preprint arXiv:1412.4034, 2014.
17. Pedersen, N.C., *An update on feline infectious peritonitis: virology and immunopathogenesis.* The Veterinary Journal, 2014. **201**(2): p. 123-132.
18. Porter, E., S. Tasker, M.J. Day, R. Harley, A. Kipar, S.G. Siddell, and C.R. Helps, *Amino acid changes in the spike protein of feline coronavirus correlate with systemic spread of virus from the intestine and not with feline infectious peritonitis.* VETERINARY RESEARCH, 2014. **45**(1): p. 49.
19. Rottier, P.J., K. Nakamura, P. Schellen, H. Volders, and B.J. Haijema, *Acquisition of macrophage tropism during the pathogenesis of feline infectious peritonitis is determined by mutations in the feline coronavirus spike protein.* JOURNAL OF VIROLOGY, 2005. **79**(22): p. 14122-14130.
20. Bosch, B.J. and P.J. Rottier, *Nidovirus entry into cells.* 2008.
21. Klenk, H.-D. and W. Garten, *Host cell proteases controlling virus pathogenicity.* TRENDS IN MICROBIOLOGY, 1994. **2**(2): p. 39-43.
22. Polgar, L., *Mechanisms of protease action*. 1989: CRC press.

23. de Haan, C., B. Haijema, P. Schellen, P.W. Schreur, E. Te Lintelo, H. Vennema, and P. Rottier, *Cleavage of group 1 coronavirus spike proteins: how furin cleavage is traded off against heparan sulfate binding upon cell culture adaptation.* JOURNAL OF VIROLOGY, 2008. **82**(12): p. 6078-6083.
24. Seidah, N.G. and A. Prat, *The biology and therapeutic targeting of the proprotein convertases.* NATURE REVIEWS DRUG DISCOVERY, 2012. **11**(5): p. 367-383.
25. Thomas, G., *Furin at the cutting edge: from protein traffic to embryogenesis and disease.* NATURE REVIEWS MOLECULAR CELL BIOLOGY, 2002. **3**(10): p. 753-766.
26. Licitra, B.N., J.K. Millet, A.D. Regan, B.S. Hamilton, V.D. Rinaldi, G.E. Duhamel, and G.R. Whittaker, *Mutation in spike protein cleavage site and pathogenesis of feline coronavirus.* EMERGING INFECTIOUS DISEASES, 2013. **19**(7): p. 1066-73.
27. Herrewegh, A., R. De Groot, A. Cepica, H.F. Egberink, M.C. Horzinek, and P. Rottier, *Detection of feline coronavirus RNA in feces, tissues, and body fluids of naturally infected cats by reverse transcriptase PCR.* JOURNAL OF CLINICAL MICROBIOLOGY, 1995. **33**(3): p. 684-689.
28. Richards, F.M., *The interpretation of protein structures: total volume, group volume distributions and packing density.* JOURNAL OF MOLECULAR BIOLOGY, 1974. **82**(1): p. 1-14.
29. Kyte, J. and R.F. Doolittle, *A simple method for displaying the hydropathic character of a protein.* JOURNAL OF MOLECULAR BIOLOGY, 1982. **157**(1): p. 105-132.
30. Choe, Y., F. Leonetti, D.C. Greenbaum, F. Lecaille, M. Bogyo, D. Brömme, J.A. Ellman, and C.S. Craik, *Substrate profiling of cysteine proteases using a combinatorial peptide library identifies functionally unique specificities.* JOURNAL OF BIOLOGICAL CHEMISTRY, 2006. **281**(18): p. 12824-12832.
31. Kridel, S.J., E. Chen, L.P. Kotra, E.W. Howard, S. Mobashery, and J.W. Smith, *Substrate hydrolysis by matrix metalloproteinase-9*.* JOURNAL OF BIOLOGICAL CHEMISTRY, 2001. **276**(23): p. 20572-20578.
32. Barrett, A.J., J.F. Woessner, and N.D. Rawlings, *Handbook of proteolytic enzymes*. Vol. 1. 2012: Elsevier.
33. Chang, H.-W., H.F. Egberink, R. Halpin, D.J. Spiro, and P.J. Rottier, *Spike protein fusion peptide and feline coronavirus virulence.* EMERGING INFECTIOUS DISEASES, 2012. **18**(7): p. 1089.
34. Taylor, W.R., *The classification of amino acid conservation.* JOURNAL OF THEORETICAL BIOLOGY, 1986. **119**(2): p. 205-218.
35. Gunn-Moore, D.A., T.J. Gruffydd-Jones, and D.A. Harbour, *Detection of feline coronaviruses by culture and reverse transcriptase-polymerase chain reaction of blood samples from healthy cats and cats with clinical feline infectious peritonitis.* VETERINARY MICROBIOLOGY, 1998. **62**(3): p. 193-205.

CHAPTER 6: The binding of alpha synuclein protein to anionic membranes may be a nonspecific interaction (Report)

Donald W. Lee[1], Jun Yan[1], David Eliezer[2], Susan Daniel[1]

[1]School of Chemical & Biomolecular Engineering, Cornell University, Ithaca, NY, USA

[2] Department of Biochemistry, Weill Cornell Medical College, NY, NY, USA

INTRODUCTION

Alpha synuclein is a protein that is associated with the onset of Parkinson's Disease. The roles this protein has in neurons are still unknown. Asyn has been shown to bind to anionononic bilayers [1-2] and sharply-curved lipid structures [1, 3]. These finding suggests that perhaps asyn modulates the synaptic vesicle fusion occurring in the synaptic ends of neural cells. However, there exist some ambiguous results that require a second confirmation through our assay. Specifically, we are uncertain if asyn truly binds via electrostatic interactions with anionic bilayers, or via defects present throughout membranes made of anionic lipids.

METHODS

Forming Anionic Supported Lipid Bilayers

We first developed strategies to form anionic supported lipid bilayers on glass slide, which will be used as the target membrane to bind alpha synuclein (asyn) through electrostatic interactions. Anionic bilayers are typically difficult to form on glass slides because both have highly negatively charged surfaces. By using acidic incubation conditions at pH 3.5, anionic bilayers containing 30% POPS 70% POPC were successfully formed directly on glass

surfaces. We believe the acidity helps by neutralizing the negative charge of POPS, which becomes neutrally charge at around pH 4 (Figure 1).

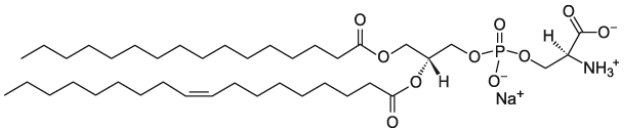

POPS (Phosphatidylserine)

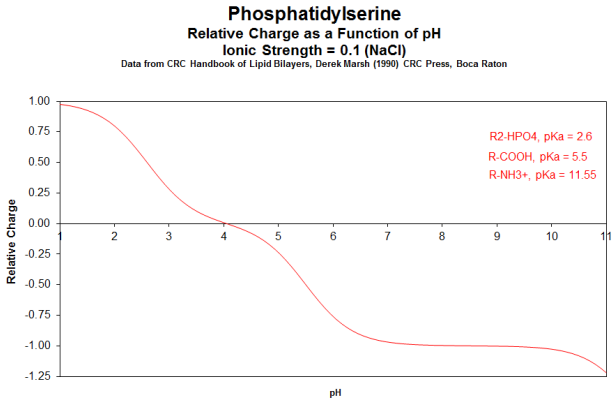

Figure 1 Chemical structure and charge vs pH profile of POPS.

Performing SPT binding studies of asyn to SLBs

After forming the bilayer for 4 hours at pH 3.5, excess vesicles were rinsed away using a 150mM NaCl pH 7 buffer (MES7 buffer), and asyn (labeled with Alexa 488 dye) was added. For control, we used Alexa 488-labeld streptavidin (strept) due to its small size and similar surface charge density as asyn. Strept is only 3 times larger than asyn (Figure 2) and both asyn and strept have surface zeta potentials between -6 and -7 mV at 150 mM NaCl, pH 7 conditions (Figure 3).

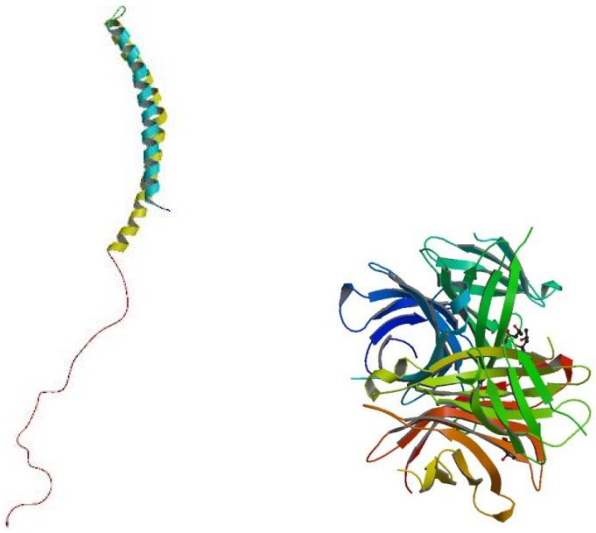

Figure 2 Structure of human alpha-synuclein in membrane-bound form (PDB 1XQ8. 14.476 kDa) and streptavidin protein tetramer (PDB 4BX6. 54.967 kDa)

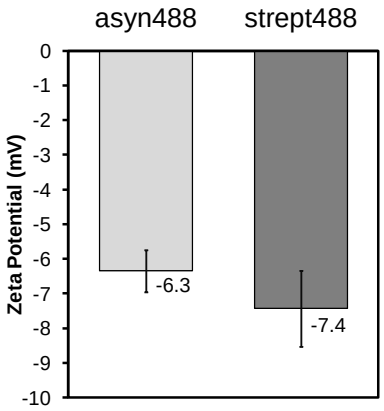

Figure 3 Zeta potential of strept and asyn that are labeled with Alexa 488. Zeta potential measures the surface charge indirectly by looking how fast particles move in solution under an applied voltage drop. The zeta potential is defined as the charge potential at the slipping plane of ions. Dye-labeled asyn and strept respectively have zeta potentials of -6.3 ± 0.6 mV and -7.4 ± 1.1 mV at 150 mM NaCl and pH 7 conditions, confirming that they are both similarly charged and negative.

RESULTS

In our first test, asyn bound to the anionic 30%POPS bilayer (Figure 4, middle), agreeing with literature work [1-4]. However, strept also bound similarly (Figure 4, right). To identify properties of asyn that are unique for asyn, we performed a series of other controls and tests.

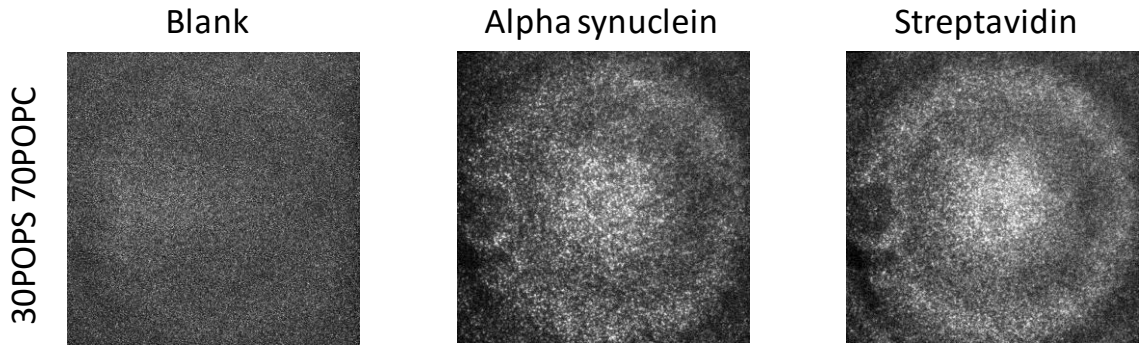

Figure 4 Binding of Asyn and Strept to 30POPS 70POPC bilayers. Left) Image of 30POPS 70POPC without any proteins. Middle) Asyn488 binding to 30% POPS 70% POPC bilayers formed on glass. Right) Strept488 binding to 30% POPS 70% POPC bilayers. Strept binds similar to asyn.

We checked asyn and strept binding to 100% POPC neutral bilayers and confirmed that asyn does not bind to neutral bilayer (Figure 5, Left). Strept also did not bind to POPC bilayers (Figure 5, Right).

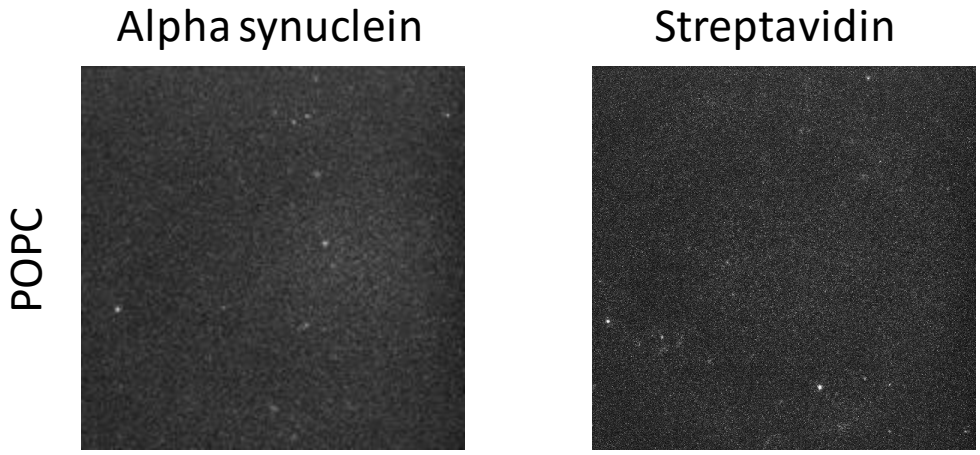

Figure 5 Binding of Asyn to 100% POPC bilayers. Left) Asyn did not bind to 100% POPC bilayers to any significant level. Right) Strept also did not bind.

It may be possible that 30% POPS bilayer contains adhesive micro defects that expose the glass surface or hydrophobic regions of the bilayers. Both proteins bind very well directly to glass in the absence of any membranes (Figure 6).

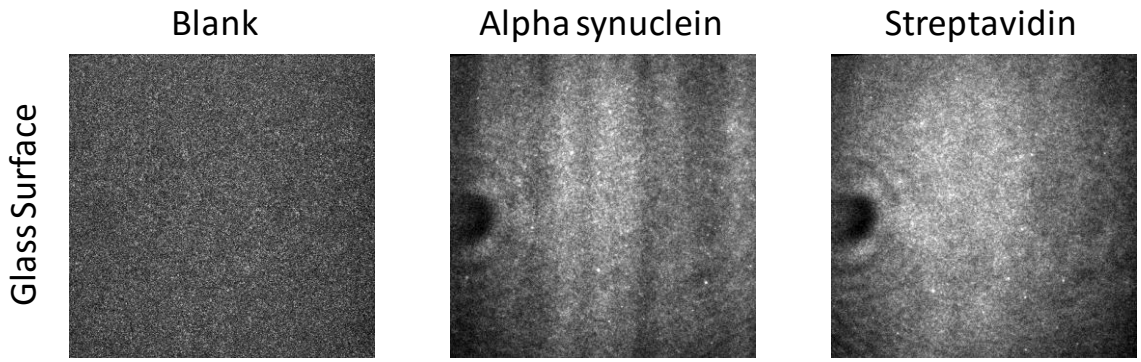

Figure 6 Binding of Asyn and Strept to a glass surface. Left) Empty channel for reference. Middle) Asyn binding to glass. Right) Strept binding to glass.

Another possibility is that a bilayer was not completely formed, though this can be checked using fluorescence recovery after photobleaching (FRAP) tests. For the FRAP test, Texas Red DHPE lipid fluorophores were added to the 30POPS bilayer composition, and fluorophores were bleached using a concentrated 561 nm laser. The recovery rate of fluorescence signal at the bleached spot was recorded and then fitted to diffusion equations derived by Soumpasis *et al.* [5]. FRAP tests shows that the lipids are highly mobile with a mobile fraction = 1 and diffusion coefficient of Texas Red DHPE at 0.24 ± 0.03 $\mu m^2/s$ (Figure 7). Improperly formed bilayers would have a mobile fraction much lower than 1.

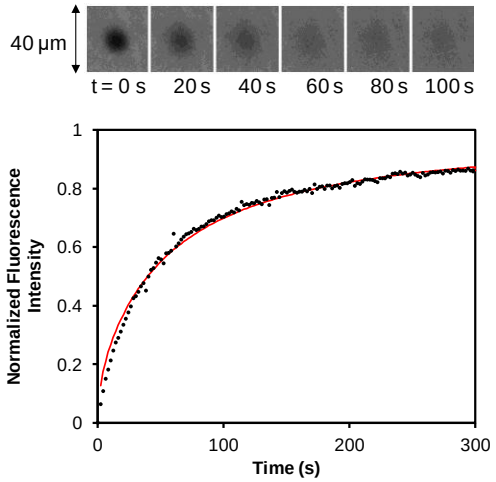

Figure 7 Sample FRAP experiments on 30% POPS 69.9% POPC 0.1% Texas Red (TR) DHPE bilayer. Fluorophores were bleached with high-intensity lasers at t = 0 sec, and the fluorescence intensity of the photobleached region was recorded over time. The bleached spot recovered within 5 minutes due to lipid diffusion. Using fitting equations provided by Soumpasis et al.[5], the diffusion coefficient of lipids is 0.24 ± 0.03 µm2/s and the lipid mobile fraction is 1 (all lipids are mobile). Bilayers that formed improperly would have a mobile fraction lower than 1.

A limitation of FRAP tests is the inability to detect micro defects, and we found that mobile bilayers do not necessarily guarantee that the bilayer is pristine. In an attempt to remove micro defects, presuming they are present, we formed 30POPS bilayer at pH 3.5 and then filled in the defects at pH 7 using 100% POPC vesicles. The idea is that POPC vesicles will "heal" any defects in the bilayer. When loading asyn and strept to these POPC-backfilled 30POPS bilayers, we found that asyn and strept bound very infrequently or not at all (Figure 8). Using BSA to "block" defects also greatly reduced the binding of asyn and strept to 30POPS bilayers (Figure 9). The reduction of asyn and strept binding after procedures to block and heal defects in the bilayers suggests that micro defects may be prevalent in untreated 30POPS bilayers.

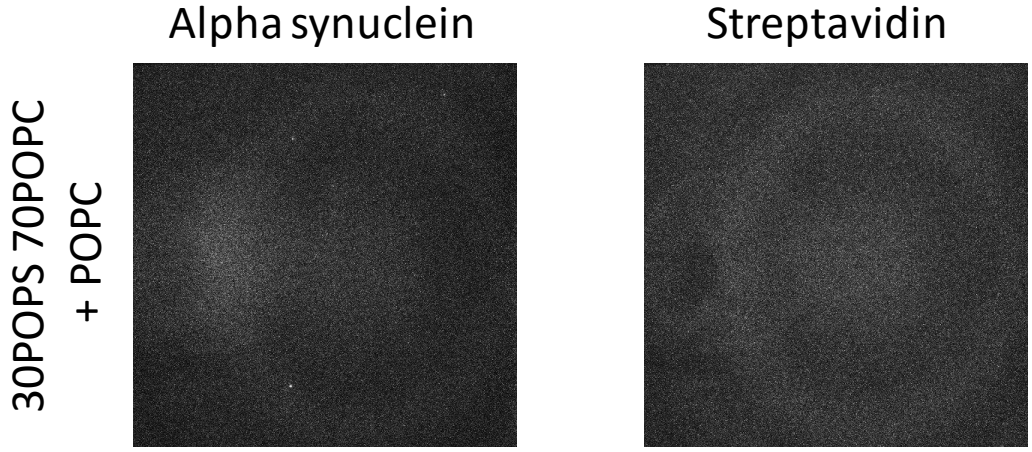

Figure 8 Asyn and strept binding to 30POPS 70POPC bilayers backfilled with POPC vesicles. Asyn did not bind to 30% POPS bilayers after the defects were filled with POPC vesicles. Strept also did not bind to 30% POPS backfilled with POPC vesicles.

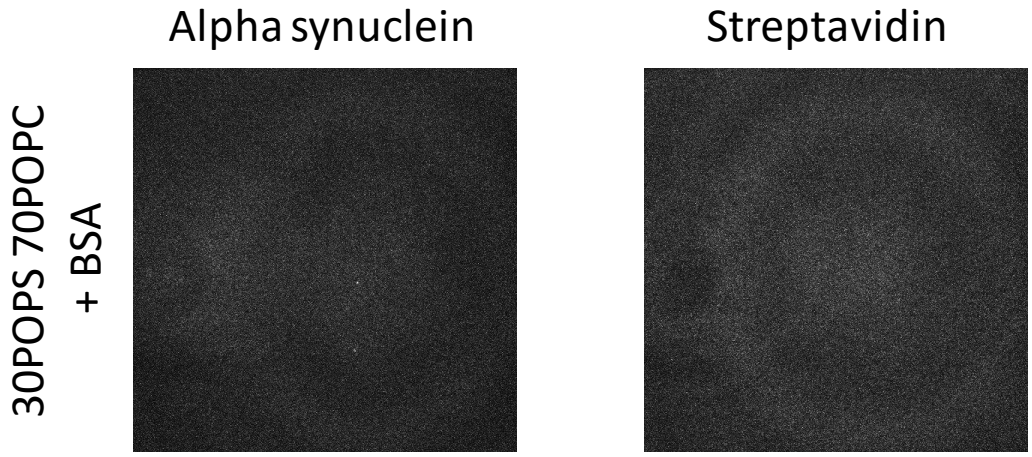

Figure 9 Asyn and strept binding to 30POPS 70POPC bilayers backfilled with BSA. Asyn did not bind to 30% POPS bilayers after the defects were blocked with BSA. Strept also did not bind to 30% POPS blocked with BSA.

Some concerns with healing bilayers with POPC vesicles are that POPC might fill in just the defects to form micro domains and it can displace or dilute POPS. FRAP tests confirm that the bilayer is still 100% mobile, and hence POPC do not form micro domains to any noticeable level. The diffusion coefficient of POPC-backfilled 30POPS bilayers is higher than that without backfilling, but it is lower than that containing only 10% POPS (Figure 10). This suggests that POPC incorporated into the 30POPS bilayer and the POPS content is still somewhere between 10 to 30 mol %. We also probed for the presence of POPS using annexin V protein, which binds to POPS via calcium ions [6]. MES buffer containing 10mM $CaCl_2$ and annexin V labeled with fluorescein was added to the 30POPS bilayer that was backfilled with POPC. For control, annexin V was added to a pure POPC bilayer. After 30 min, excess annexin V was rinse away with MES7 buffer. Results show that annexin V bound to the 30POPS bilayer that was backfilled with POPC, but annexin V did not bind to pure POPC bilayers (Figure 11). This shows that POPS is still present in these POPC-backfilled bilayers.

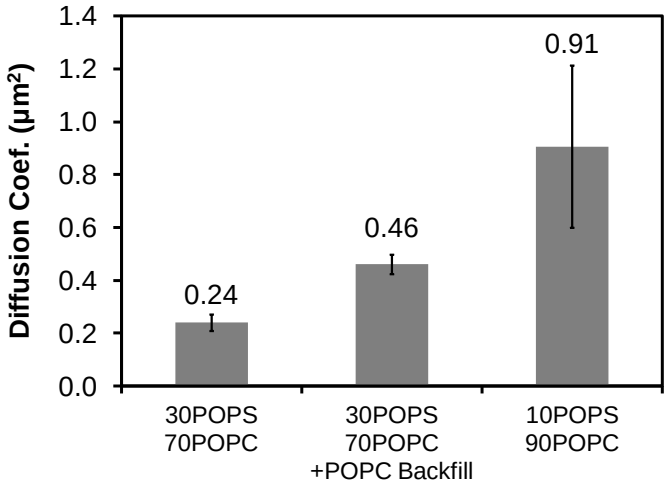

Figure 10 Diffusion coefficients of Texas Red DHPE in various bilayers. The "30POPS 70POPC" bilayer was formed at pH 3.5 and then rinsed with pH 7 buffer. The "30POPS 70POPC" bilayer was formed similarly, but POPC vesicles were flown over the bilayer at pH 7 for 1 hour before rinsing the bilayer. The "10POPS 90POPC" bilayer was formed at pH 7.

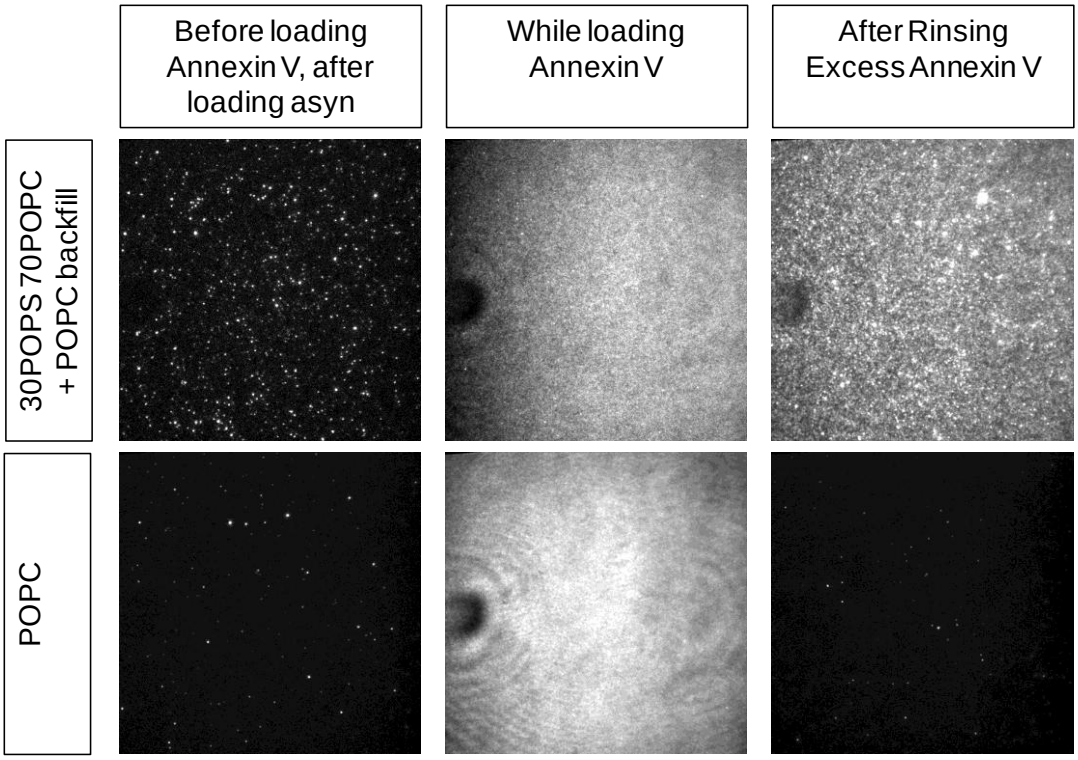

Figure 11 Use of annexin to confirm POPS content. First column shows asyn on the two types of bilayers as specified in the labels. The second column shows how the bilayers looks like while loading annexin V. The third column shows annexin and asyn after rinsing away excess annexin. The image intensities of the 1st and 3rd columns span the same min and max intensity range for fair comparison of intensity changes (no intensity auto adjust for individual images).

In pursuit of a different research direction, we wondered why does asyn stay near synaptic terminals? Asyn appears to bind to highly curved lipid vesicles, hence asyn might interact with synaptic vesicles. Based on the curvature-dependent binding behaviors of asyn, we

suspected that membrane fusion intermediates (which contain highly curved structures) might also promote asyn binding. To test this possibility, we made 100% POPC SLBs (which asyn does not bind to) and then added a mixture of R18 micelles and asyn488. R18 micelles spontaneously fuse to POPC bilayers upon contact. A simple schematic picture of the setup is shown in Figure 12.

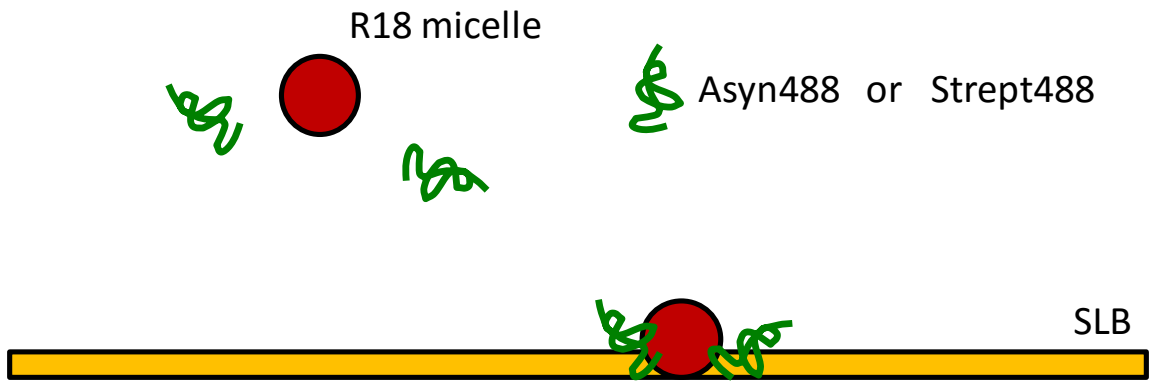

Figure 12 Hypothesis of R18 fusion-induced binding of asyn to membranes.

Results show that R18 micelle fused randomly over the SLB and asyn deposited at the site of fusion (Figure 13 top). However, strept also did the same thing (Figure 13 bot). This suggests that asyn aggregating at fusion sites was not a unique function of asyn. One explanation is that fusion generates hydrophobic structures that can bind nonspecifically to proteins. Another explanation for this is that positively charged R18 micelles are encapsulating the negatively charged asyn and strept proteins, and thus R18 fusion simply brings the proteins to the fusion site (Figure 14). Yet, a careful look does show a very subtle difference. Asyn sometimes dissociate with the membrane after being deposited to the bilayer, whereas strept remained bound (Figure 13). The reversible binding of asyn, though infrequent in our experiments, agrees with literature work that suggests asyn reversibly binds to membranes in a similar fashion as apolipoproteins [7-8]. All these evidences could serve as a clue as to asyn's true function in neurons.

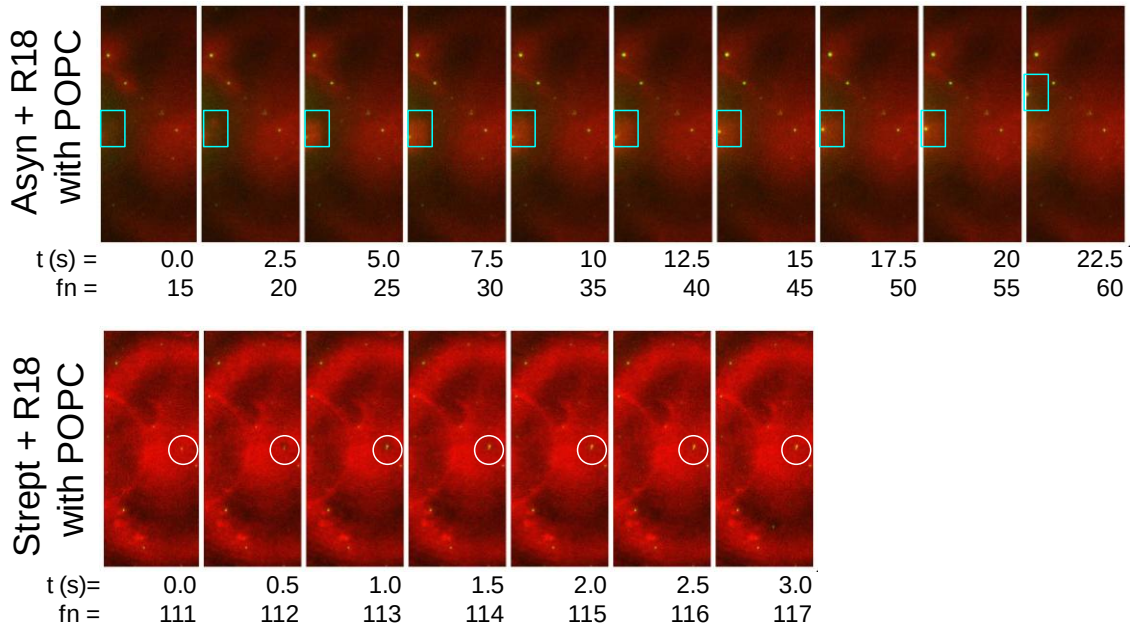

Figure 13 Composite image sequence of R18 micelle fusion in the presence of asyn or strept. Top) Time lapse image of asyn488 binding to the POPC bilayers. The red color shows the R18 dye whereas green color shows asyn. The blue rectangle tracks the appearance of asyn after R18 fuses, and also the dislodging and movement of asyn. See VIDEO 1. Bottom) This shows the same thing as the top image, but for strept488 instead asyn488. The white circle tracks an R18 fusion event (dark dye-quenching clouds) and the appearance of strept488 (bright spot). See VIDEO 2.

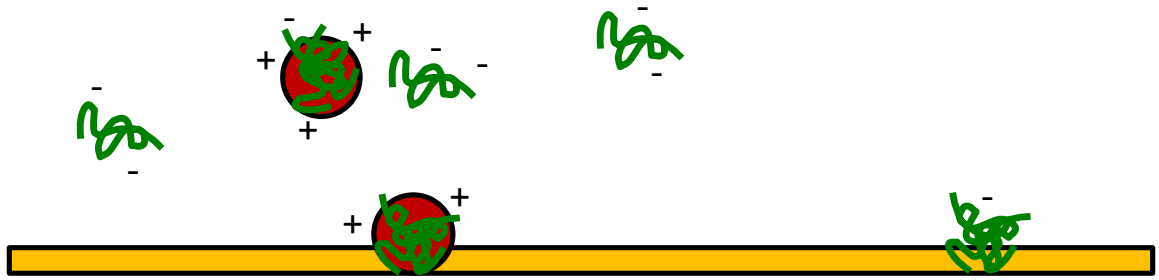

Figure 14 Hypothesis for R18-mediated delivery of asyn and strept to fusion sites. Possible that R18 dye holds onto asyn or strept and drops it off at the R18 fusion site.

Since lipid curvature appears to modulate asyn binding, we did a preliminary test to see if asyn will bind to spherical influenza viruses that were roughly ~100 nm in diameter. Influenza, X31 strain, was labeled with R18 and then loaded on to POPC bilayers that were formed for 4 hours at pH 7 and contained 1% GD1a glycolipid, which serves as the viral receptor. Asyn was then loaded into the channel. Using a dual view microscopy feature, the green asyn and strept proteins were tracked on the left side of the camera view while the red

virus particles were tracked on the right side. Results show that asyn did not bind to the virus at pH 7 (See VIDEO 3, left channel at early time points before acidification). We then acidified the virus to pH 4 to promote viral membrane fusion, shown as fusion clouds on the right side of the videos. Asyn adsorbed onto the SLB at acidic conditions (See VIDEO 3, left channel at later time points after acidification occurred). After rinsing away excess asyn with pH 7 buffer, we can see that asyn bound to the SLB at many other places in addition to where the viruses were bound (Figure 15, Left image and left side). Strept also behaved similarly (Figure 15, Right image and left side.). It may be possible that the acidification of the bilayer changes the headgroup spacing and exposes the adhesive regions that bind strept and asyn. In support of this theory, bilayers with DOPC, which has a larger hydrophobic tail than POPC, promotes asyn binding as shown by Hellstrand *et al*. [2].

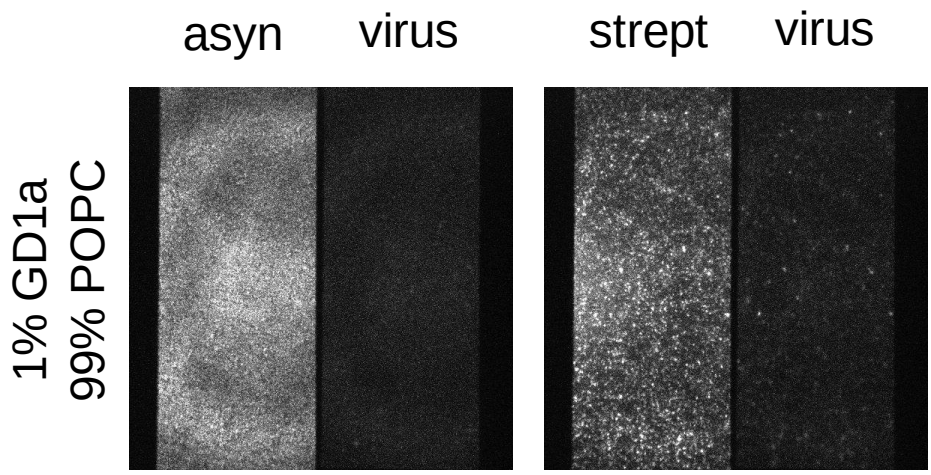

Figure 15 Binding of asyn to highly curved X31 virus membranes. Left) The left channel shows asyn adsorbed ubiquitously to 1% GD1a 99% POPC bilayer after acidifying the bilayer containing X31 influenza virus, and then rinsing with pH 7 buffer. The right channel shows the X31 virus, which is hard to see due to membrane fusion and the spreading of the R18 dye label. See VIDEO 3. Right) This image shows the same thing, but for strept on the left side instead.

We caution that using viruses to test curvature effects of asyn binding may not be appropriate since acidified virus become hydrophobic due to the exposure of HA fusion peptides. What we did learn though, is that asyn and strept did not bind to viruses at pH 7,

despite having highly curved membrane surfaces. This could be due to steric hindrance as viruses contain an abundance of membrane proteins that may limit membrane interactions with asyn and strept. Note that viral membranes are net negatively charted (- 2mV zeta potential for X31 labeled with R18).

CONCLUSIONS

In an attempt to build a platform to asyn's functional role, we were unable to find conditions in which our control protein, streptavidin, behaves differently than asyn when binding to anionic and neutral bilayers. Most literature work did not use control proteins as their control was asyn interacting with neutral bilayers. Alpha synuclein appears to bind to anionic bilayer through sites that are able to be blocked using POPC vesicles or BSA. Electrostatics may not be playing a major role in binding, and anionic bilayer may intrinsically contain many sites for nonspecific adsorption. Binding of asyn and strept to anionic bilayers can be reduced by forming pristine bilayers, healing defects using POPC vesicle, or blocking defects using BSA. Both asyn and strept binds to POPC bilayers when the bilayer is perturbed through R18 micelle fusion events or virus fusion / acidification events. These above findings support the idea that asyn does not bind to bilayers due to purely electrostatic interactions, and that other factors may play a more important role (i.e. curvature and exposure of hydrophobic regions).

Our results do not necessarily mean alpha synuclein's functional role does not involve nonspecific binding to membranes. A possible function for asyn could be in fact to block defects that form at neuron membranes before other proteins nonspecifically bind to them. Asyn can then be degraded via ubiquitin pathways. Fusion appears to generate high levels of membrane defects that can bind to proteins (Figure 15). Since synaptic vesicles fuse

frequently at synaptic terminals and asyn is localized here, asyn might serve to bind near these fusion sites to stabilize membranes and to prevent other proteins from also binding. Unstable membranes could also lead to spontaneous fusion between vesicles and membranes; this could explain why lack of asyn in mice leads to loss of presynaptic vesicles in the reserve pool [9].

REFERENCES

1. Davidson, W.S., A. Jonas, D.F. Clayton, and J.M. George, *Stabilization of α-Synuclein Secondary Structure upon Binding to Synthetic Membranes.* JOURNAL OF BIOLOGICAL CHEMISTRY, 1998. **273**(16): p. 9443-9449.
2. Hellstrand, E., M. Grey, M.-L. Ainalem, J. Ankner, V.T. Forsyth, G. Fragneto, M. Haertlein, M.-T. Dauvergne, H. Nilsson, P. Brundin, S. Linse, T. Nylander, and E. Sparr, *Adsorption of α-Synuclein to Supported Lipid Bilayers: Positioning and Role of Electrostatics.* ACS Chemical Neuroscience, 2013. **4**(10): p. 1339-1351.
3. Middleton, E.R. and E. Rhoades, *Effects of Curvature and Composition on α-Synuclein Binding to Lipid Vesicles.* BIOPHYSICAL JOURNAL, 2010. **99**(7): p. 2279-2288.
4. Pandey, A.P., F. Haque, J.-C. Rochet, and J.S. Hovis, *Clustering of α-Synuclein on Supported Lipid Bilayers: Role of Anionic Lipid, Protein, and Divalent Ion Concentration.* BIOPHYSICAL JOURNAL, 2009. **96**(2): p. 540-551.
5. Soumpasis, D.M., *Theoretical analysis of fluorescence photobleaching recovery experiments.* Biophysical Journal, 1983. **41**(1): p. 95-97.
6. Seaton, B. and J. Dedman, *Annexins.* BIOMETALS, 1998. **11**(4): p. 399-404.
7. Bussell Jr, R. and D. Eliezer, *A Structural and Functional Role for 11-mer Repeats in α-Synuclein and Other Exchangeable Lipid Binding Proteins.* JOURNAL OF MOLECULAR BIOLOGY, 2003. **329**(4): p. 763-778.
8. Segrest, J.P., M.K. Jones, H. De Loof, C.G. Brouillette, Y.V. Venkatachalapathi, and G.M. Anantharamaiah, *The amphipathic helix in the exchangeable apolipoproteins: a review of secondary structure and function.* JOURNAL OF LIPID RESEARCH, 1992. **33**(2): p. 141-66.
9. Cabin, D.E., K. Shimazu, D. Murphy, N.B. Cole, W. Gottschalk, K.L. McIlwain, B. Orrison, A. Chen, C.E. Ellis, and R. Paylor, *Synaptic vesicle depletion correlates with attenuated synaptic responses to prolonged repetitive stimulation in mice lacking α-synuclein.* The Journal of neuroscience, 2002. **22**(20): p. 8797-8807.

FUTURE OUTLOOK

PSEUDOVIRUS BINDING AND FUSION STUDIES

While the virus studied in this thesis are classified as BSL-2 agents, the viruses of current interests, such as Ebola, MERS, and avian flu viruses (eg H5N1), are BSL-3 or 4 agents that cannot be studied easily due to heavy safety restrictions. In order to study these BSL-3+ human pathogens in a safe manner and using the assays developed here, pseudovirus particles can be used that mimic these pathogens but cannot cause infection. The Daniel Lab have recently demonstrated the usage of pseudovirus particles, made with VSV backbone embedded with surface proteins of flu virus and coronavirus, to conduct SPT fusion studies [1]. This setup can be used to study binding of Ebola GP protein to NPC-1 membrane receptors, without the associated health risk of a BLS-4 virus since the pseudovirus lacks a complete genome for viral infection. The assays and image processing tools developed during this work is generalized enough to be used in studies of these pertinent virus-host membrane interactions.

SIMULATION OF OTHER MEMBRANE FUSION SYSTEMS

The kinetic model for influenza virus fusion resolves a large debate on how viral proteins work together and independently to induce membrane fusion [2]. Similar versions of this debate exist for other types of membrane fusion systems. For instance, HIV is believed to use multiple Env fusion proteins to induce fusion[3], but some studies suggest a single Env protein can induce fusion[4]. The same controversy also exists for SNARE-mediate fusion. Work by Mohrmann et al. in 2010 provide evidence of cooperativity of SNARE complexes in fusion [5], whereas in the same year, Bogaart et al. found a lack of cooperativity [6].

According to our model for HA-mediated membrane fusion, we propose that both results could be correct if proteins can act passively to induce membrane fusion. Extending our simulation to study these membrane fusion systems could help to resolve conflicting theories and provide predictions about these system responses to changes in environmental conditions.

BINDING OR PROTEASE-TRIGGERED FUSION OF VIRUSES

The fusion-triggering event for membrane fusion differs amongst the various enveloped viruses. For instance, unlike influenza viruses that undergo membrane binding and fusion as separate events, viruses like HIV[7] and Parainfluenza[8] undergo fusion as triggered by the binding event itself. Furthermore, it is also possible that the fusion triggering event is the protease cleavage activation of the viral proteins. The SPT assay is highly appropriate for studying such binding-triggered, or protease-triggered, fusion events. For these studies, fluorescent labeling will be challenging since the membrane dye must be quenched for fusion experiment, but quenched dyes are not desirable for binding studies. The development of image restoration strategies (STAWASP) will be critical for tracking the binding events of particles with low fluorescence signals, while not disturbing the dye dequenching event. The lag time between binding (or introduction of proteases) and membrane fusion can then be collected fairly accurately. Simulation models similar to the one we developed for HA-mediated membrane fusion could be deployed to interpret the resulting lag time data.

MICROWELL ARRAY ASSAY FOR SPT

A possible future work is to use of the microwell setup as discussed in CHAPTER 4 to conduct a glycan array-like, high-throughput experiments. The current microfluidic device setup used here is not designed for large-scale studies as it can only do five experiments per

device. Scaling up the number of experiment based on the current device design is not ideal as the number of tubing required for the additional experiments will scale by factor of 2 (two tubings are needed per channel). The microwell platform can potentially perform hundreds of experiments on a single glass slide without any additional tubing, though the challenge lies in building an automated machine to load the wells with different components. Assuming this is possible, this will enable SPT assay to quickly search for optimal receptors for binding and optimal membrane compositions for fusion. If the virus requires an acidic condition for fusion to occur, the fusion can be triggered simply by using the rapid-uncaging technique as discussed in CHAPTER 5 [9]. These high-throughput SPT microarray systems could eventually surpass the utility of glycan arrays for virus-receptor and virus-membrane interaction studies.

TESTING ANTIVIRAL COMPOUNDS

Antiviral research often entails the use of an *in vitro* assay to test the efficacy of anti-binding or anti-fusion candidates. Often, these compounds are tested in cell assays during the proof-of-concept stage to ensure viral infection is reduced and the compounds are not cytotoxic. However, cell-based assays do not necessary reveal if the compound is inhibiting binding, fusion, or both. The assay and technique developed here, using SLBs as host membrane mimics, provide a convenient way to measure and visually confirm the inhibition of binding and fusion by antiviral compounds. Eventually, SPT assay could be used for screening antiviral compounds as a standard protocol. To make this option appealing for pharmaceutical companies, a fully automated microscopy and image processing software would be required, and a high-throughput SPT device must be developed.

OVERCOMING THE IMAGE PROCESSING BOTTLENECK

Imaging processing techniques are a very large component of SPT studies. It is impractical to manually track >10,000 particles throughout a microscopy movie, and thus particle detection and tracking algorithms are required. Much research has been devoted to improving these algorithms [10-27], but the fact remains that no algorithm works perfectly [28] due to inherent noise in the images that have similar size and intensity profiles as dim particles. These issues are present even with the super resolution microscopy technique that uses a similar single-molecule tracking technology to obtain high-spatial resolution information about cells (~ 20 nm [29]). Super resolution illuminates fluorophores stochastically (not all at once) in order to obtain images of bright spots, in which the spot centroid location can be determined with sub-pixel accuracy using Gaussian fitting algorithms [14]. However, super-resolution faces similar image processing constraints in that tracking millions of particle is not feasible to do manually. One of the largest barriers for using super resolution microscopy is implementing effective particle detection and tracking algorithms [30]. The image processing algorithms developed here for SPT (see CHAPTER 1) is universally applicable for microscopy images dealing with low fluorescent particles in high static noise images. Coupling our algorithms with machine-learning capabilities [31] and testing it for super resolution imaging would be a logical next step. The work towards finding a "perfect" (or human-like) particle detection and tracking algorithm will always be an active research goal in bioimaging and signal processing fields.

REFERENCES

1. Costello, D.A., C.-Y. Hsia, J.K. Millet, T. Porri, and S. Daniel, *Membrane Fusion-Competent Virus-Like Proteoliposomes and Proteinaceous Supported Bilayers Made Directly from Cell Plasma Membranes.* LANGMUIR, 2013. **29**(21): p. 6409-6419.

2. Lee, D., V. Thapar, P. Clancy, and S. Daniel, *Stochastic fusion simulations and experiments suggest passive and active roles of hemagglutinin during membrane fusion.* BIOPHYSICAL JOURNAL, 2014. **106**(4): p. 843-854.
3. Sougrat, R., A. Bartesaghi, J.D. Lifson, A.E. Bennett, J.W. Bess, D.J. Zabransky, and S. Subramaniam, *Electron Tomography of the Contact between T Cells and SIV/HIV-1: Implications for Viral Entry.* PLoS Pathog, 2007. **3**(5): p. e63.
4. Yang, X., S. Kurteva, X. Ren, S. Lee, and J. Sodroski, *Stoichiometry of Envelope Glycoprotein Trimers in the Entry of Human Immunodeficiency Virus Type 1.* Journal of Virology, 2005. **79**(19): p. 12132-12147.
5. Mohrmann, R., H. de Wit, M. Verhage, E. Neher, and J.B. Sørensen, *Fast Vesicle Fusion in Living Cells Requires at Least Three SNARE Complexes.* SCIENCE, 2010. **330**(6003): p. 502-505.
6. van den Bogaart, G., M.G. Holt, G. Bunt, D. Riedel, F.S. Wouters, and R. Jahn, *One SNARE complex is sufficient for membrane fusion.* NATURE STRUCTURAL +ACY- MOLECULAR BIOLOGY, 2010. **17**(3): p. 358-364.
7. Alkhatib, G., C. Combadiere, C.C. Broder, Y. Feng, P.E. Kennedy, P.M. Murphy, and E.A. Berger, *CC CKR5: a RANTES, MIP-1α, MIP-1β receptor as a fusion cofactor for macrophage-tropic HIV-1.* SCIENCE, 1996. **272**(5270): p. 1955-1958.
8. Bose, S., A. Zokarkar, B.D. Welch, G.P. Leser, T.S. Jardetzky, and R.A. Lamb, *Fusion activation by a headless parainfluenza virus 5 hemagglutinin-neuraminidase stalk suggests a modular mechanism for triggering.* Proceedings of the National Academy of Sciences, 2012. **109**(39): p. E2625–E2634.
9. Costello, D.A., D.W. Lee, J. Drewes, K.A. Vasquez, K. Kisler, U. Wiesner, L. Pollack, G.R. Whittaker, and S. Daniel, *Influenza virus-membrane fusion triggered by proton uncaging for single particle studies of fusion kinetics.* Analytical Chemistry, 2012. **84**(20): p. 8480-8489.
10. Endesfelder, U. and M. Heilemann, *Art and artifacts in single-molecule localization microscopy: Beyond attractive images.* NATURE METHODS, 2014. **11**(3): p. 235-238.
11. Rowland, D.J. and J.S. Biteen, *Top-Hat and Asymmetric Gaussian-Based Fitting Functions for Quantifying Directional Single-Molecule Motion.* CHEMPHYSCHEM, 2014. **15**(4): p. 712-720.
12. Cheezum, M.K., W.F. Walker, and W.H. Guilford, *Quantitative Comparison of Algorithms for Tracking Single Fluorescent Particles.* BIOPHYSICAL JOURNAL, 2001. **81**(4): p. 2378-2388.
13. Small, A. and S. Stahlheber, *Fluorophore localization algorithms for super-resolution microscopy.* Nat Meth, 2014. **11**(3): p. 267-279.
14. Mortensen, K.I., L.S. Churchman, J.A. Spudich, and H. Flyvbjerg, *Optimized localization analysis for single-molecule tracking and super-resolution microscopy.* Nature Methods, 2010. **7**(5): p. 377-381.
15. Sbalzarini, I.F. and P. Koumoutsakos, *Feature point tracking and trajectory analysis for video imaging in cell biology.* Journal of Structural Biology, 2005. **151**(2): p. 182-195.
16. Rolfe, D., C. McLachlan, M. Hirsch, S. Needham, C. Tynan, S.D. Webb, M. Martin-Fernandez, and M. Hobson, *Automated multidimensional single molecule fluorescence microscopy feature detection and tracking.* European Biophysics Journal, 2011. **40**(10): p. 1167-1186.
17. Smith, Matthew B., E. Karatekin, A. Gohlke, H. Mizuno, N. Watanabe, and D. Vavylonis, *Interactive, Computer-Assisted Tracking of Speckle Trajectories in Fluorescence Microscopy: Application to Actin Polymerization and Membrane Fusion.* Biophysical Journal, 2011. **101**(7): p. 1794-1804.
18. Jaqaman, K. and G. Danuser, *Computational Image Analysis of Cellular Dynamics: A Case Study Based on Particle Tracking.* Cold Spring Harbor Protocols, 2009. **2009**(12): p. pdb.top65.

19. Jaqaman, K., D. Loerke, M. Mettlen, H. Kuwata, S. Grinstein, S.L. Schmid, and G. Danuser, *Robust single-particle tracking in live-cell time-lapse sequences.* NATURE METHODS, 2008. **5**(8): p. 695-702.
20. Bonneau, S., M. Dahan, and L.D. Cohen, *Single quantum dot tracking based on perceptual Grouping using minimal paths in a spatiotemporal volume.* IEEE Transactions on Image Processing, 2005. **14**(9): p. 1384-1395.
21. Dupont, A., K. Stirnnagel, D. Lindemann, and D. Lamb, *Tracking image correlation: Combining single-particle tracking and image correlation.* Biophysical Journal, 2013. **104**(11): p. 2373-2382.
22. Woll, D., C. Kolbl, B. Stempfle, and A. Karrenbauer, *A novel method for automatic single molecule tracking of blinking molecules at low intensities.* Physical Chemistry Chemical Physics, 2013. **15**(17): p. 6196-6205.
23. Balasubramanian, S., S. Kalishwaran, R. Muthuraj, D. Ebenezer, and V. Jayaraj. *An efficient non-linear cascade filtering algorithm for removal of high density salt and pepper noise in image and video sequence*. in *International Conference on Control, Automation, Communication and Energy Conservation, INCACEC 2009.* 2009.
24. Xu, Y., J.B. Weaver, D.M. Healy, Jr., and J. Lu, *Wavelet transform domain filters: a spatially selective noise filtration technique.* IEEE Transactions on Image Processing, 1994. **3**(6): p. 747-758.
25. Esakkirajan, S., T. Veerakumar, A.N. Subramanyam, and C.H. PremChand, *Removal of High Density Salt and Pepper Noise Through Modified Decision Based Unsymmetric Trimmed Median Filter.* IEEE Signal Processing Letters, 2011. **18**(5): p. 287-290.
26. Rudin, L.I., S. Osher, and E. Fatemi, *Nonlinear total variation based noise removal algorithms.* Physica D: Nonlinear Phenomena, 1992. **60**(1–4): p. 259-268.
27. Sage, D., F.R. Neumann, F. Hediger, S.M. Gasser, and M. Unser, *Automatic tracking of individual fluorescence particles: application to the study of chromosome dynamics.* IEEE Transactions on Image Processing, 2005. **14**(9): p. 1372-1383.
28. Chenouard, N., I. Smal, F. de Chaumont, M. Maska, I.F. Sbalzarini, Y. Gong, J. Cardinale, C. Carthel, S. Coraluppi, M. Winter, A.R. Cohen, W.J. Godinez, K. Rohr, Y. Kalaidzidis, L. Liang, J. Duncan, H. Shen, Y. Xu, K.E.G. Magnusson, J. Jalden, H.M. Blau, P. Paul-Gilloteaux, P. Roudot, C. Kervrann, F. Waharte, J.-Y. Tinevez, S.L. Shorte, J. Willemse, K. Celler, G.P. van Wezel, H.-W. Dan, Y.-S. Tsai, C.O. de Solorzano, J.-C. Olivo-Marin, and E. Meijering, *Objective comparison of particle tracking methods.* Nat Meth, 2014. **11**(3): p. 281-289.
29. Rust, M.J., M. Bates, and X. Zhuang, *Sub-diffraction-limit imaging by stochastic optical reconstruction microscopy (STORM).* Nature Methods, 2006. **3**(10): p. 793-796.
30. Huang, B., M. Bates, and X. Zhuang, *Super resolution fluorescence microscopy.* Annual Review of Biochemistry, 2009. **78**: p. 993.
31. Smal, I., M. Loog, W. Niessen, and E. Meijering, *Quantitative comparison of spot detection methods in fluorescence microscopy.* Medical Imaging, IEEE Transactions on, 2010. **29**(2): p. 282-301.

APPENDIX 1: Building a working phage virus model (NSF GK-12)

INVOLVEMENT WITH BME NSF GK-12

I was a part of the biomedical engineering GK12 program sponsored by NSF and CLIMB. The goal is teach state-of-the-art science to the community by getting graduate students to teach science at local schools. I had the opportunity to develop a curriculum that teaches students how viruses work, how they targets and infect cells, and how to block virus infection. This activity involves building a model of a phage virus that actually works. The idea came from my involvement with the chemical engineering WOMEN's group, outreach event in May 2011. When I became a NSF GK12 fellow the same year, I was able to develop the curriculum further into what is shown below. I worked with Paula Jones at Homer Higher School, and Ellen Schneider at Marcellus High School to test and refine this activity with their biology classes. Below is the final project.

OBJECTIVE

Students will learn the basics of virology and the infection process by building a working model of the bacteriophage virus. In addition, they will learn about how virus research is conducted and how antiviral strategies work. Student will:

- Learn the anatomy of a bacteriophage virus.
- Learn how viruses target and enter cells.
- Learn how viral proteins functions.
- Learn how viruses are made in cells through self-assembly processes.
- Measure the lag time between virus activation and viral gene delivery.

- Develop antiviral objects that resemble actual antiviral compounds.
- Understand how viruses can be used for other purposes, such as drug delivery agents.

SCIENCE CONTENT FOR THE TEACHER

In order to infect a cell, viruses must bind to a cell and deliver their genome across the cellular membrane. Binding is governed by viral proteins located on the virus surface, which tends to target certain chemical receptors located on the target cell. The specificity between this binding protein and host cell receptor dictates the virus tropism, or the range of host that the virus can infect. This would explain why the avian flu has difficulty infecting humans, because humans and birds have different receptors. However, mutations in the viral protein can allow the avian flu to bind to human receptors.

Depending on what whether or not the virus has a lipid bilayer envelope, the mechanism of delivering genetic material into cell differs. Influenza has an envelope, and therefore the virus must eventually merge its viral membrane with the cell membrane. This event is called membrane fusion and it allows the internal content of the virus to escape inside the cell. On the other hand, common bacteriophage viruses do not have an envelope. Phages deliver its genome across cells in an injection manner much as how a syringe punctures through a skin.

Most viruses have a trigger signal that tells the virus to activate and enter cells. For influenza, membrane fusion is triggered by acidic conditions. Following activation, there is a lag time until the viral genome enters the cells. This lag time is related to the mechanism involved to initiate fusion, and current research on viruses utilizes lag time data to study virus entry behaviors.

The ultimate goal for virus research is to develop cures for viral infection. Vaccination has been a popular "preventive" measure against viruses, but it rarely helps people who are already infected. Developing antiviral medication that can be used post infection is an ongoing challenge today.

VOCABULARY

- Binding Proteins: These are any viral proteins that help with the attachment of the virus to the target receptor molecule. Binding protein and the fusion protein are often the same.

- Enveloped vs non-enveloped Viruses: Enveloped viruses are viruses that contain a lipid bilayer surrounding the viral genome. This bilayer is normally taken from the host cell during the virus assembly process. Non-enveloped viruses lack this lipid bilayer and the viral genome is protected mainly by the nucleocapsid.

- Fusion Inhibitor: Any compound that blocks the virus fusion step. Virus fusion can be inhibited by physically blockings the fusion protein from changing configuration to initiate fusion, or by disabling the activation trigger mechanism.

- Fusion Proteins: Enveloped viruses contain functional surface proteins that help with the merging of the viral and host membrane. These proteins are called fusion proteins. Some examples are the hemagglutinin protein of influenza virus, G protein of rabies viruses, and gp120 protein of HIV.

- Lytic Cycle: A virus replication cycle in which the viral genome is replicated separately from the host cell's genome. This cycle is the main mode of virus replication, which

usually involves the destruction of the host cell as the new viruses emerge from it. This differs from the lysogenic cycle.

- Lysogenic Cycle: A second replication cycle where the viral genome is integrated into the host genome so that when the host genome is replicated due to cell division, the viral genome is also transferred to the new cell. In this cycle, the presence of an intact virus is not necessary to spread to a new cell.

- Nucleocapsid: Proteins that surround and protect the viral genome. The nucleocapsid usually adopts an icosahedral or cylindrical geometry.

- Receptor: This is any molecule that the binding protein of a virus likes to attach to. Common receptors are sialic acid and membrane proteins located on the target cell surface.

- Tropism: Tropism defines the range of cell type or animal species that the virus can infect. For instance, HIV has a cell tropism for CD4 cells and host tropism for humans. The tropism of a virus can change if mutations occur in the binding protein that allows it to attach to a different receptor molecule.

- Vaccine: Usually a cocktail of deactivated viral proteins or non-infectious viruses that is used to stimulate an immune response and antibody production against the actual virus.

- Virus Fusion: In order for an enveloped virus to deliver its genome inside a host cell, the viral envelope must eventually merge with the host cell's membrane. This event is called virus fusion. After virus fusion, the viral genome will be in inner volume space of the cells where virus replication can occur.

PREPARATIONS

Materials

- Scotch tape
- Loading Syringe with blunt needle (Transfer pipettes can be used instead)
- Scalpel/Razor/Scissor
- Water Bucket
- Food Coloring
- Small rubber balloon
- Alka-Seltzer tablet
- Two soft disc/doughnut magnets
- 1mL Plastic Syringe without needle
- >290 Neodymium magnetic beads
- Narrow but sturdy straw (Ex: Capri Sun or air duster straws.)
- 50mL beaker
- Aluminum Foil

Safety

Sharps safety is required due to use of scalpel. Blunt end needle of loading syringe is a poking hazard. Use transfer pipettes for more safety.

Overview

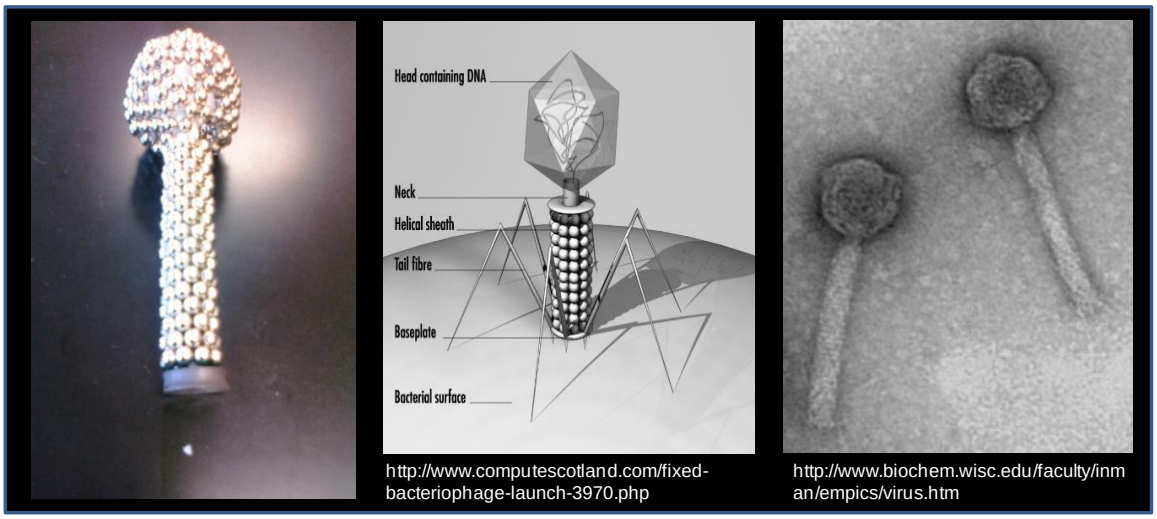

A good way to learn about viruses is to build one that works. Here, we will build the bacteriophage virus model (shown in left), which resembles very closely to the actual phage virus (shown in right). This activity should be initiated as an engineering puzzle. Students will be given a set of tools to which they must design and build a simple device that could 1) bind to a target object and 2) inject a solution into this target object automatically. With some guidance, they should see the resemblance of this device to the bacteriophage virus, or vice versa, they should see that the virus resembles a device with set functions.

Tips for teacher

- If the straws are a little too large to fit inside the syringe tip, then cut the tip a little to widen the diameter of the syringe hole. The straw must be able to fit inside the syringe tip with ease.

- Drill holes into the soft disc magnets so that the plastic syringe tip can lodge into it without falling off. Note: This step can be skipped if doughnut magnets with the right size hole can be purchased.

- The neodymium beads are not necessary to demonstrate how a virus functions, though these would complete the model's outer structure.

CLASSROOM PROCEDURES

Lab Day 1: Building the working phage model (45min)

1) Cut the straw so that it can fit inside the syringe when the piston is pulled back the length of the Alka-Seltzer tablet. Sharpen the straw as well. See below.

2) Pull the balloon over the syringe piston so that the piston is inside the balloon.

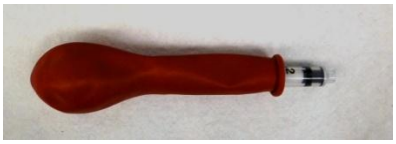

3) Stretch the balloon neck towards the syringe tip. Then twist and tape the balloon neck to hold the balloon in a stretched state. It should be difficult to pull on the piston against the

balloon. Cut away excess parts of the balloon.

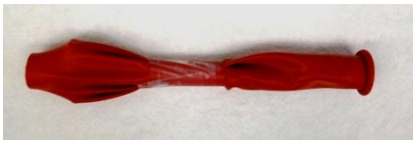


4) With a scalpel, cut a slit across the balloon where the piston is. The slit should be long enough to fit an Alka-Seltzer tablet into it when stretched.

5) Pull the piston out and squeeze the Alka-Seltzer tablet into the slit made in the balloon. The tablet should hold the piston out while the balloon tries to push the piston back in.

6) Load the syringe with food coloring using another syringe with a blunt end needle. LESSON: Dyes are used in real research to track the internal contents of a virus. Here, the dye also serves to represent the viral genome and any internal enzymes.


7) Split into two groups, a large one and a small one. Each person will act like a ribosome making structural viral proteins. Using magnetic beads, the large group should make 9-

bead triangles. At the end, arrange the triangles into the wrench-like shape shown below. *Lesson: The instruction to make these structures is like the viral genome that tells the cells to make viral proteins.*

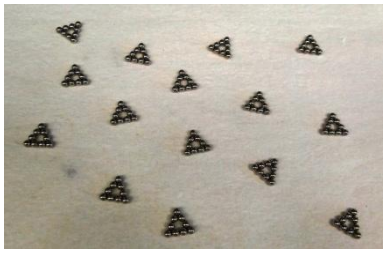

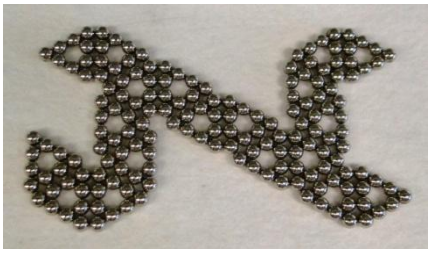

8) Folding the wrench-like shape carefully will yield an icosahedral sphere with 1 missing triangle. LESSON: This shows how large viral structures can be made through the self-assembly of many smaller subunits. The hand acts as helper proteins that aid the proper folding of viral proteins.

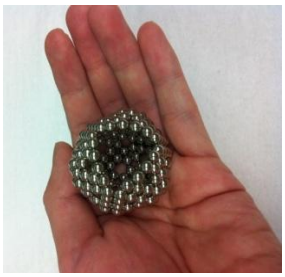

9) The smaller group of students should first start by making a linear strand of magnetic beads. Then have someone wrap the strand into a cylinder that is the length of the syringe tube and barely wider than the syringe tube. *LESSON: Notice how this structure is faster to make and thus less people were needed in this group. If more resource was allocated to make this structure, then the assembly of the icosahedral shape would take much longer.*

In order to conserve resource and time, viruses have a system that causes proteins to be synthesized at the right ratio and speed so that there enough proteins to make a full virus.



10) Place the dissolvable tablet and piston side of the assembled syringe into the icosahedron.

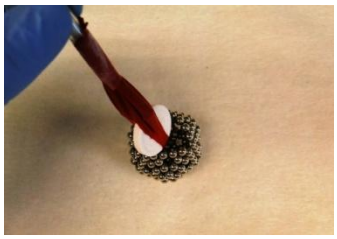


(For aesthetic purposes, the holes in the triangles can be filled with magnetic beads.)

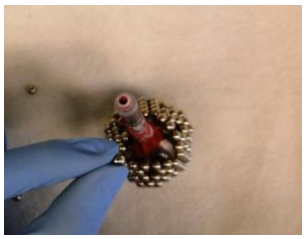


11) Place the syringe body into the helix and then cap the syringe tip with a doughnut magnet. Then place the straw inside the syringe so that the straw does not show. *LESSON: The magnetic beads serves as the nucleocapsid and the doughnut magnet serves as the binding protein known as the base plate in a phage virus. The tablet serves as the*

trigger mechanism and the balloon serves as a potential energy source that will drive the injection motion. Real viruses are considered to be in an unstable, "spring-loaded" state just like this model.



12) To make the "target cell", tape a doughnut magnet onto the aluminum foil. Make sure NOT to cover the hole in the magnet with the tape. Then cover the 50mL beaker with the foil as shown. *LESSON: The magnet serves as a surface receptor on the cell that the virus likes to bind to, and the foil acts like the cell membrane that the virus must puncture through.*


13) Fill the water bucket with water and place the "target cell" beaker setup inside. Open the foil a little to let all air bubbles escape the beaker, and then reseal the beaker. Attach the virus model to the magnet receptor on the target cell. Some dye may leak at this time due to diffusion. *Lesson: Viruses target certain receptors on cells, which governs the virus tropism, or ability to infect certain hosts. Humans and birds have different receptors on*

their lung cells, which is why the avian flu has difficulty infecting humans. In this activity, an incorrectly magnetized (or demagnetized) magnet can be used instead as the receptor to show how improper binding leads to unsuccessful virus infection.



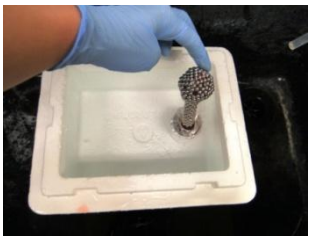

14) Tilt the beaker and the virus over gently so that the entire virus is soaked under water. The Alka-Seltzer tablet should start to dissolve. Start a timer.

15) Observe the virus acting. When the tablet dissolves, the model should inject the dye into the beaker. Stop the timer when this happens. *LESSON: The lag time between activation and injection is caused by the delay in activation mechanism. Lag time data of viruses can be used to make inferences on the mechanistic steps involved in a virus entering a cell.*


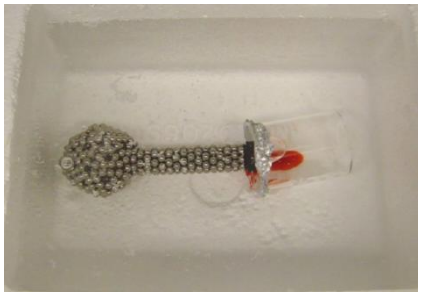

16) Record the "lag time" between virus activation (water submersion) and the actual injection event. Collect a class data to get a lag time distribution. *LESSON: In real research, lag times are collected in the same exact manner. The lag time distribution changes based on different environmental conditions and virus strains. Mathematical*

equations can be fitted to distributions to extract rate information.

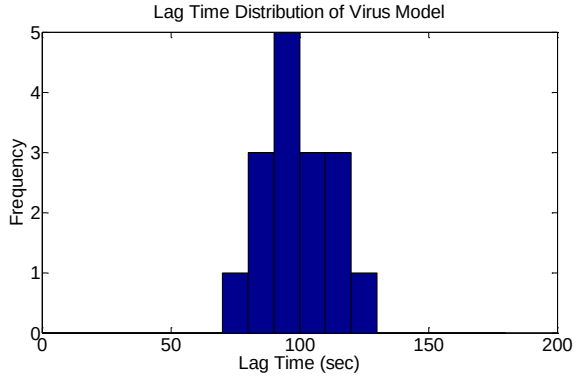

Lab Day 2: Building and testing antiviral strategies (45min)

1) Students should come up with their own antiviral strategies. Past examples were coating the tablet with thick syrup, using colder water, or jamming the binding site with another magnet.

2) Repeat the experiment of Day 1 with their antiviral strategy, and record the lag times. Compared the new lag times to the normal virus model's lag time from Day 1 of this activity.

3) Discuss other ways to deactivate the virus. Ex: Melt the rubber balloon, use a weaker or blunt end straw, etc. Talk about how these relate to real antiviral solutions being researched today. Ex: Antibodies, vaccine, enzyme inhibitors.

4) Assess students' understanding of viruses with the questions in the assessment. Use the model to help clarify.